



The Influence of Sheet Conditions on the Formability of Titanium Alloys at Room Temperature

A thesis submitted in fulfilment of the requirements for the degree of
Doctor of Engineering
In Advanced Manufacturing: Forging and Forming

Department of Design, Manufacturing and Engineering Management, University of
Strathclyde

Kwame Sefakor James

June 2021

Abstract

Titanium is the material of choice for use in most high value engineering components due to their good physical and chemical properties. However, their adoption are hindered by their poor room temperature formability as a result of the nature of their crystallographic structure and their high susceptibility to surface inhomogeneity. The main gaps in knowledge identified were the non-availability of data and research on the impact of machining induced edge conditions on the room temperature forming tendencies of titanium alloys. In addition, the availability of literature on the potential influence of post-processing induced surface defects on titanium sheet forming capabilities at room temperature was scanty. To assess these issues, statistical predictive numerical models and experimental trials have been undertaken in this research work, to examine the influence of titanium sheet conditions on their room temperature formability.

The hole expansion test (HET) and uniaxial tensile tests were conducted on titanium sheets machined with either laser, electric discharge machining (EDM) or abrasive water jet (AWJ) machining. The goal was to examine the impact of the machining induced edge surface defects on the edge formability of titanium at room temperature. The research found that titanium edges machined with EDM exhibited high edge forming performance, followed by the AWJ machined edges with the laser machined edges performing the least. The performance trends observed were attributable to the influence of the machining induced edge surface micro feature alterations. Forming parameters such as the machining method, tool geometry, machining parameters and the metallographic properties of titanium were found to influence the edge forming performance of titanium. This research work proposed the GOM Atos metrology as a supplementary method for characterising the edge forming performance of materials, based on the principle of sheet thinning being an indicator of formability. For the uniaxial tensile test trials, the machining methods and machining parameters were found to have no significant impact on the deformation behaviour of titanium. Digital image correlation (DIC) evaluation results showed that the strains were concentrated within the bulk material and away from the machined edges during the tensile deformation process. Also, this research proposed a novel statistical numerical regression model expression for predicting the edge forming performance of titanium alloys for edges prepared with AWJ and deformed with a Nakajima punch. The proposed model expression showed an average absolute error of 8.8% and a correlation coefficient of 0.9884 between the experimental and the predicted values.

Sheet metal surface defects in the form of indents and scratches are sometimes introduced during either transportation, storage or handling on the workshop floor. An approach was proposed to compute the localised strain evolution at an indent defect micro-surface of titanium sheets during uniaxial tensile deformation. The approach entails the use of a notched tensile sample, scanning electron microscope (SEM) and a Matlab based DIC system for offline strain measurement. A notched tensile sample was employed to ensure that only regions of high strain concentration was captured. The results found that during the tensile deformation process, the emergent localisation of deformation led to the formation of bands, which assembled at the sharp defect edges. These bands formed at the tip of the indent defect hindered the plastic flow by acting as an initiation zone for early crack nucleation resulting in reduced localised fracture strain values at micro scale. Further studies was carried out to assess the impact of longitudinal scratches on the bendability of titanium alloys. For the press brake forming trials, only scratches oriented along the sheet rolling direction as well as sheets with thickness of 1.6mm were considered. The results showed that scratch profiles with a depth between $-1\mu\text{m}$ to $-18\mu\text{m}$ and pile up height between $1\mu\text{m}$ to $16\mu\text{m}$ could be employed in a press brake forming operation. However, scratch defects with threshold values beyond depth ranges of $-18\mu\text{m}$ to $-35\mu\text{m}$ and a pile up height between $16\mu\text{m}$ to $35\mu\text{m}$ could be rejected for use in a given press brake forming operation. Failure of the coupons during the press brake forming trials were found to be initiated from the scratch defect sites in their role as stress raisers.

Based on the achieved research objectives, suggestions for further studies were proposed and the major industrial relevance as well as the project limitations explained.

Acknowledgement

I wish to express my sincere gratitude to the Advanced Forming Research Centre (AFRC) as well as the Department of Design, Manufacturing and Engineering Management (DMEM) of the University of Strathclyde for sponsoring this Engineering doctorate (EngD) project. I also wish to acknowledge the Titanium Metals Corporation (TIMET) for material donation throughout this project.

My utmost appreciation goes to my supervisors; Prof. Paul Blackwell (First supervisor) and Dr. Evgenia Yakushina (Second supervisor) for their support and guidance throughout this project. Your constructive criticisms, encouragements and sheer commitment contributed immensely towards the success of this EngD project.

A special mention goes to Dr. Dorothy Evans for giving me this special opportunity to undertake my doctoral research at the University of Strathclyde. Your support and encouragement has helped in making this journey a success.

I am thankful to the entire staff of the AFRC and DMEM for their support during this project. I am particularly grateful to Dr. Shanmukha Moturu and Dr. Giribaskar Sivaswamy for their advice and support during this project. A special mention also goes to Liza Hall, Ryan O'Neil, Jacqueline Schramm and all the laboratory technicians who contributed in diverse ways towards the success of this project.

I wish to thank my colleagues both at the AFRC and DMEM for their support and motivation. A special mention also goes to my badminton team members. I am very grateful for the opportunity to train with you and I will always relish our healthy competitive badminton sessions.

Finally, I wish to express my utmost gratitude to my family for their relentless support and encouragement during this doctoral journey.

Declaration of authenticity and author's right

“This thesis is the result of the author’s original research. It has been composed by the author and has not been previously submitted for examination which has led to the award of a degree.”

“The copyright of this thesis belongs to the author under the terms of the United Kingdom copyright acts as qualified by the University of Strathclyde regulation 3.50. Due acknowledgement must always be made of the use of any material contained in, or derived from this thesis.”

Signed: 

Dated: 29/06/2021

Proclamation of academic honesty

“I declare that this submission is entirely my own original work. I declare that, except where fully referenced direct quotations have been included, no aspect of this submission has been copied from any other source. I declare that all other works cited in this submission have been appropriately referenced.

I understand that any act of academic dishonesty such as plagiarism or collusion may result in the non-award of my degree.”

Signed: 

Dated: 29/06/2021

Previously published works

The underlisted publications were undertaken by the candidate in contribution to the application for an Engineering Doctorate degree;

- Kwame, J. S., Yakushina, E. & Blackwell, P., 2019. Effect of edge conditions on the formability of commercially pure titanium sheet (Grade 2) at room temperature. In: *MATEC Web of Conferences*, 321(04027). pp. 1-7. <https://doi.org/10.1051/matecconf/202032104027>.
- Kwame, J. S., Yakushina, E. & Blackwell, P., 2021. Effect of machining induced microstructure changes on the edge formability of titanium alloys at room temperature. In: Daehn, G. et al., (eds.), *Forming the Future: The Minerals, Metals & Materials Series*: The Minerals, Metals & Materials Society. https://doi.org/10.1007/978-3-030-75381-8_223.
- Kwame, J. S., Yakushina, E. & Blackwell, P., 2020. Examining failure behaviour of commercially pure titanium during tensile deformation and hole expansion test. *Journal of Materials and Applications*, 9(1), pp. 32-37. <https://doi.org/10.32732/jma.2020.9.1.32>.
- Kwame, J. S., Yakushina, E. & Blackwell, P., 2020. Impact of machining-induced surface defects on the edge formability of commercially pure titanium sheet at room temperature. *SN Applied Sciences*, 2(1999), pp. 1-14. <https://doi.org/10.1007/s42452-020-03839-z>. [Part of a topical collection for; Engineering: Effects of advanced materials, design and manufacturing techniques on the engineering applications. ISSN: 2523-3963 (Print) 2523-3971 (Online)].
- Kwame, J. S., Yakushina, E. & Blackwell, P., 2021. Influence of sheet conditions on in-plane strain evolution via ex-situ tensile deformation of Ti-3Al-2.5V at room temperature. *Journal of Materials and Applications*, 10(1), pp. 15-26. <https://doi.org/10.32732/jma.2021.10.1.15>.
- Kwame, J. S., Yakushina, E. & Blackwell, P., 2020. Prediction of hole expansion ratio of titanium alloys using R programming. *Journal of Modeling and Optimization*, 12(2), pp. 125-137. <https://doi.org/10.32732/jmo.2020.12.2.125>.
- Kwame, J. S., Yakushina, E. & Blackwell, P., 2021. The influence of longitudinal scratch defect on the bendability of titanium alloy. *Journal of Material Sciences & Manufacturing Research*. SRC/JMSMR-119, 2(2), pp.1-4.

The author of this thesis as an individual EngD student performed the research and obtained the results published above. For each publication output, the co-authors contributed via general advise and editorial guidance with the same contribution directed towards the EngD thesis compilation.

Signed: 

Dated: 29/06/2021

Abbreviations

	AFRC	Advanced forming research center
	AWJ	Abrasive waterjet machining
	ASM	American society for metals
	ASTM	American society for testing and materials
	AMP	Advanced machining processes
	AISI	American iron and steel institute
A	AFM	Atomic force microscopy
	AECG	Abrasive electro-chemical grinding
	ANSI	American national standards institute
	ANN	Artificial neural network
	AHS	Advanced high strength
	ANOVA	Analysis of variance
	AIM	Advisor in metals
	BCC	Body-centered cubic
B	BHF	Blankholder force
	BUE	Built-up edge
	BS	British standard
	CP-Ti	Commercially pure titanium
	CVD	Chemical vapour deposition
C	CNC	Computer numerical control
	CI	Confidence interval
	C_HET	Hole expansion test with Conical punch
	CCD	Charge-coupled device
		Design, manufacturing and engineering
	DMEM	management
D	3D	Three dimensional
	DIC	Digital image correlation
	2D	Two-dimensional
	EDM	Electric discharge machining
E	EPT	Electric pulse treatment
	ELI	Extra low interstitial
	EngD	Engineering doctorate

	EBSD	Electron backscatter diffraction
	ECAP	Equal channel angular pressing
	FCC	Face-centered cubic
F	FLDs	Forming limit diagrams
	FEM	Finite element modelling
	FLC	Forming limit curve
G	GTN	Gurson-Tvergaard-Needleman
	HET	Hole expansion test
H	HCP	hexagonal close packed
	HAZ	Heat affected zone
	HER	Hole expansion ratio
	IDR	Initial damage region
I	ISF	Incremental sheet forming
	ISO	International organisation for standardisation
	IPF	Inverse pole figure
J	JIS	Japanese industrial standard
L	LFR	Limiting forming ratio
M	MZ	Melt zone
N	NAK_HET	Hole expansion test with a Nakajima punch
P	PCD	Polycrystalline diamond
	PMMA	Polymethyl methacrylate
	RCR	Rough cutting region
R	RG	reliability-guided
	RD	Rolling direction
	RSS	Residual sum of squares
	S-N Curve	stress versus the number of cycles to failure curve
	SPIF	Single point incremental forming
S	SCR	Smooth cutting region
	SEM	Scanning electron microscopy
	SE	Secondary electron
	SST	Total sum of squares
	SSReg	Regression sum of squares

	StDev	Standard deviation
	TEM	Transmission electron microscopy
T	TIMET	Titanium metals corporation
	TRIP	Transformation-induced plasticity
	TSU	Tilt swivel unit
	USM	Ultrasonic machining
U	UNS	Unified numbering system
	UTS	Ultimate tensile strength
W	WEDM	Wire electro- discharge machining
X	XRD	X- ray diffraction
	ZNCC	Zero- mean normalised cross correlation
Z	ZNSSD	Zero-normalised sum of squared differences

Symbols

σ	Tensile stress
\bar{y}	Mean of y
y_i	i^{th} point of y
\hat{y}_i	i^{th} point on the straight line of best fit
N	Sample size
k	Number of predictor variable
R_{DS}	Deformed sheet surface roughness
R_0	Undeformed sheet surface roughness
m	Material constant
ε_s	Equivalent strain
d	Grain size
R_a	Arithmetic average height
R_q	Root mean square roughness
$R_{z(ISO)}$	Ten- point height
R_{pm}	Mean height of peaks
R_{vm}	Mean depth of valley
R_{Ku}	Kurtosis
R_{Sk}	Skewness
α / β	Alpha/ beta phase
d_f	Mean final hole diameter
d_0	Initial hole diameter
D_1	Random final diameter 1 edge with crack width
D_2	Random final diameter 2 edge with crack width
d_{max}	Maximum inside diameter of fully flanged edge
COP_n	n^{th} Crack opening distance
$D_{corrected}$	Final hole diameter after correction
σ_e	Stress in the elastic zone
E	Elastic modulus
ε_e	Elastic strain
σ_y	Yield strength
K	Linear hardening parameter

n	Strain hardening exponent
ε_0	Initial strain
ε_p	Plastic strain
EI	Erichsen index number
t	Material thickness
R^2	Coefficient of determination
R^2_{Adj}	Adjusted R^2
R	Correlation coefficient
S_v	Maximum pit height
F_L, θ	Vertical plane angle of loading
F_L, φ	Horizontal plane angle of loading
ε_1	Major strain
ε_2	Minor strain
β_{\S}	Regression coefficient
\S	Integer
δ_{abs}	Average absolute error
HER_{Exp}	Experimental HER
HER_{Pre}	Predicted HER
$\overline{HER_{Exp}}$	Average experimental HER
$\overline{HER_{Pre}}$	Average predicted HER
HER_{exp}^i	i^{th} experimental HER
HER_{pre}^i	i^{th} predicted HER
\mathbf{p}	Vector for displacement mapping function
M	Subset dimensions in pixels
(x, y)	Reference subset
x', y'	Target subset
$f(x, y)$	Grey level intensity at reference coordinate
$g(x', y')$	Grey level intensity at target coordinate
ε_{global}	Global engineering strain
Z	Integer for order of diffraction band
$\Delta\mathbf{k}$	Diffraction vector
hkl	Lattice plane integers

d_{hkl}	Interplanar spacing
\mathbf{k}	Wave vector
\mathbf{h}	Reciprocal lattice vector
\mathbf{g}	Diffracting vector
λ	Electron wavelength
R_{Ani}	Anisotropic coefficient
lm	Linear model function
y	Response variable
x	Predictor variable
p	Null hypothesis significance test probability
\mathbf{h}_{hkl}	Reciprocal vector
a_4, b_4	Rigid body motion terms
a_1, a_2, b_1, b_2	Elongation terms
a_3, b_3	Shearing terms
g_1	Grey values of reference images
g_2	Grey values of target images
(x_t, y_t)	Transformation of (x, y)
C	Correlation coefficient
$u(x, y)/v(x, y)$	Homogenous displacement fields for one pattern
u, v	Displacement components
$\Delta x, \Delta y$	Distance from subset centre
f_m, g_m	Ensemble averages for reference and target subsets
	Vectors apropos preferred displacement mapping
\vec{P}	parameters
F	Force

Table of Contents

Abstract.....	i
Acknowledgement	iii
Declaration of authenticity and author’s right	iv
Proclamation of academic honesty	v
Previously published works	vi
Abbreviations.....	vii
Symbols.....	x
List of figures.....	xx
List of tables.....	xxviii
Chapter 1	1
Introduction.....	1
1.1 Commercially pure titanium: properties and composition.....	1
1.2 Cold formability of titanium	4
1.3 Machining and forming as manufacturing processes of sheet metals.....	6
1.4 Research background and problem statement.....	7
1.5 Research aim	9
1.6 Research objectives	10
1.7 Thesis structure	11
1.8 Programme of work flowchart	12
Chapter 2.....	14
Literature review.....	14
2.1 Sheet metal surface asperities and limiting strains.....	14
2.2 Surface defects in formed parts and optimisation processes.....	19
2.3 Machinability of Titanium	29
2.4 Effect of alloying and mechanical properties on machinability.....	37
2.5 Impact of surface roughening and defects on fatigue properties	38

2.6 Surface roughness and amplitude parameters	39
2.7 Types of Machining Methods	42
2.8 Electric discharge machining	42
2.8.1 Impact of EDM machining parameters on material surface integrity	43
2.8.2 EDM induced microstructural changes	47
2.9 Abrasive water jet machining	49
2.9.1 Effect of AWJ machining parameters on surface morphology	53
2.9.2 AWJ induced microstructural changes.....	55
2.10 Laser machining process	55
2.10.1 Effect of laser machining parameters on surface morphology.....	57
2.10.2 Laser cutting induced microstructural changes	59
2.11 Sheet metal edge formability.....	62
2.11.1 Sheet hole flanging operation.....	62
2.11.2 Testing methods for examining sheet edge formability	65
2.11.3 Influence of machining on edge formability	67
2.11.4 Edge failure and limit strain evolution	71
2.11.5 Modelling and numerical predictions of sheet edge forming performance	74
2.12 Summary	76
Chapter 3.....	77
Experimental approaches and analysis methods.....	77
Overview	77
3.1 Machining, mechanical testing and measurements	77
3.1.1 Approach adopted for machining samples for hole expansion test and tensile test....	77
3.1.2 Dimensioning of tensile test sample.....	79
3.1.3 Uniaxial tensile test	79
3.1.4 Dimensioning of hole expansion test samples	80
3.1.5 Hole expansion test and Erichsen cupping test	81

3.1.6 GOM Atos metrology.....	84
3.1.7 Speckle pattern fabrication.....	86
3.2 Results characterisation and analysis methods.....	87
3.2.1 Image processing during ex-situ analysis of Ti-3Al-2.5V	87
3.2.2 Statistical evaluation: ANOVA analysis	91
3.2.3 Regression model development in R programming.....	93
3.2.4 Experimental data exploration and regression model expressions.....	93
3.2.5 Model predictive power assessment.....	97
3.3 Summary	100
Chapter 4.....	101
Effect of machining induced edge defects on the tensile deformation of CP-Ti sheet at room temperature	101
Overview	101
4.1 Experimental procedure	101
4.1.1 The material.....	101
4.1.2 Microstructure characterisation and chemical composition.....	101
4.1.3 Edge preparation methods and characterisation.....	102
4.1.4 GOM Atos measurement.....	104
4.1.5 ANOVA analysis.....	105
4.1.6 Uniaxial tensile test	105
4.2 Results and Discussion.....	105
4.2.1 Machining induced edge defects	105
4.2.2 One-way ANOVA analysis of edge roughness values.....	106
4.2.3 Effect of machining parameters on tensile deformation behaviour	108
4.2.4 Thinning evolution analysis	112
4.2.5 Failure Analysis.....	114
4.3 Summary	118

Chapter 5.....	120
Effect of machining on the edge formability of commercially pure titanium sheet	120
Overview	120
5.1 Experimental procedure	120
5.1.1 The material and material characterisation	120
5.1.2 Mechanical properties	121
5.1.3 Hole expansion test	122
5.1.4 Tool Geometry and sheet loading condition	122
5.1.5 Material edge preparation.....	123
5.2 Results and discussion.....	124
5.2.1 Machining induced edge surface defects	124
5.2.2 Impact of machining on HER: Hemispherical punch	127
5.2.3 Effect of different surface finishes on the HER: Hemispherical punch	128
5.2.4 Edge forming limit evaluation	129
5.2.5 Effect of tool geometry on HER	131
5.2.6 Assessment of edge formability using GOM Atos measurement	132
5.2.6.1. GOM Atos measurement after HET with Conical punch	134
5.2.6.2. GOM Atos measurement after HET with Hemispherical punch	135
5.2.7 Failure behaviour of CP-Ti (Grade 2) during uniaxial tensile deformation and HET	137
5.2.8 Hole edge fracture initiation.....	141
5.3 Summary	146
Chapter 6.....	148
Effect of machining on the edge formability of an alloyed and unalloyed titanium grade ...	148
Overview	148
6.1 Experimental procedure	148
6.1.1 The materials	148

6.1.2 Material edge surface preparation	149
6.1.3 Hole expansion test	152
6.1.4 Uniaxial tensile test and Mechanical properties.....	152
6.2 Results and Discussion.....	153
6.2.1 Machining induced edge surface defects	153
6.2.2 Comparison of critical surface features and parameters after machining	154
6.2.3 Edge forming performance: Conical punch	156
6.2.4 Thinning evolution after HET: Hemispherical punch.....	158
6.2.5 Failure nucleation during HET.....	160
6.3 Summary	165
Chapter 7.....	167
Statistical numerical prediction of the edge forming performance of titanium alloys	167
Overview	167
7.1 Experimental procedure	167
7.1.1 Edge preparation method and model limitation	167
7.1.2 The materials and mechanical properties	168
7.1.3 Hole expansion test and Erichsen cupping test	170
7.1.4 Model development in R programming	171
7.1.5 Model description.....	173
7.1.6 Model performance assessment criteria	175
7.2 Results and Discussion.....	177
7.2.1. Formability of titanium alloys	177
7.2.2 Forming strains after the Erichsen cupping test	178
7.2.3 Thinning evolution after Erichsen cupping test	179
7.2.4 Model predictability assessment and regression model equations.....	180
7.2.5. Cross-validation trial for predicting HER of Ti-21S.....	181

7.2.6 Summary of generated regression model equations and model coefficient suitability	184
7.2.7 Model predictability analysis	185
7.3 Summary	187
Chapter 8.....	189
Supplied sheet surface conditions and the impact of surface defects on the formability of Ti-3Al-2.5V	189
Overview	189
8.1 Localised strain measurement and the DIC approach.....	189
8.2 Press brake forming.....	191
8.3 Experimental procedure	192
8.3.1 The material.....	192
8.3.2 Surface preparation and mechanical properties of the ex-situ tensile material.....	192
8.3.3 Nature of the surface defects on the as-received sheet.....	193
8.3.4 Surface scratch profile classification for the press brake forming trials.....	195
8.3.5 Bending test trials.....	197
8.3.6 Ex-situ uniaxial tensile test and strain analysis of a notched tensile sample	198
8.3.7 Digital image correlation.....	199
8.4 Results and discussion.....	201
8.4.1 Effect of longitudinal scratch defect on the sheet bendability	201
8.4.2 Crack nucleation during the press brake forming trials	203
8.4.3 Evaluation of localised strain evolution at indent and defect-free micro-surfaces ...	203
8.4.4 Localised strain evolution at defect-free micro-surface	204
8.4.5 Localised strain evolution at indent defect micro-surface	208
8.4.6 Damage evolution of the notched tensile sample.....	212
8.5 Summary	214
Chapter 9.....	216
Conclusions, recommendations and contributions to knowledge.....	216

9.1 Main conclusions.....	216
9.2 Recommendations and future works	217
9.3 Contributions to knowledge and industrial relevance	218
9.4 Project challenges and limitations.....	220
References.....	221
Appendices.....	246
Appendix A	246
A1 Metallurgical surface preparation.....	246
A2 Microscopy analysis	249
A2.1 Microstructure characterisation	249
A2.2 Surface profile parameter measurement.....	250
A3 Fundamental principles of EBSD.....	252
A4 Fundamental principle of DIC in GOM Aramis	254
A5 Fundamental principle of DIC in Ncorr version 2.1.1 software.....	256
A5.1 Displacement mapping	257
A5.2 Correlation function	258
Appendix B	259
B1 Heat treatment cycle of D2 tool steel billet for fabricating the HET tool set.....	259
B2 Tool set Fabrication	261
B3 GOM Atos analysis of the tool integrity before HET trials	262
B4 GOM Atos analysis of the tool integrity after HET trials	265
B5 Engineering drawing of the tool set design	267
Appendix C	270
C1 GOM Atos measurement of tensile sample thinning.....	270
Appendix D	271
D1 Prediction of HER using the proposed regression model expression	271

List of figures

Figure 1. 1 CP-Ti S-N curve	2
Figure 1. 2 JIS Grade 1 CP-Ti exhibiting lower workability after cold working compared to thermally activated counterparts	3
Figure 1. 3 Ultra-fine grained micrograph of CP-Ti grade 2 after ECAP	3
Figure 1. 4 Roll formability of Ti-6Al-4V at room temperature	4
Figure 1. 5 Attained finished surface quality of CP-Ti formed under various friction conditions	5
Figure 1. 6 Multi-stage cold deep drawing of pure titanium after intermediate annealing	6
Figure 1. 7 Schematic of the HET	7
Figure 1. 8 Programme of work flowchart.....	13
Figure 2. 1 Failure at limit strain after in-plane biaxial stretching of Cu sheet	14
Figure 2. 2 The limit strain in balanced biaxial tension as a function of thickness of steel sheet	15
Figure 2. 3 Changes in Lead sheet metal thickness examined in plane transverse to forming groove	16
Figure 2. 4 Enhancement of forming limit by reduction of surface roughening	17
Figure 2. 5 Forming limit strains attained via surface roughness polishing of aluminium sheet and foils.....	18
Figure 2. 6 Response of sheet forming limit strain to defect width.....	19
Figure 2. 7 Produced and rejected extruded parts in tons with specific defect zones.....	20
Figure 2. 8 Typical defects during SPIF process	23
Figure 2. 9 Defects and their impact on AA-1060 aluminium sheet formability	24
Figure 2. 10 Response of blank motion and BHF on wrinkle control and Cu-alloy deep drawability	25
Figure 2. 11 Variation of BHF with punch displacement to avoid failure in zinc-coated and phosphated steel sheets	26
Figure 2. 12 Limiting dome height of TC 1 Ti- sheet metal enhanced by 31.8% after double sided bulging pressure.....	27
Figure 2. 13 Effect of metallurgical variable on defect formation in Aluminium alloys during forming.....	27
Figure 2. 14 Limited formability of AA6061 due to orange peel defect	28

Figure 2. 15 Influence of different tool diameters on the nature of fracture at the end of groves in AA 7075-O aluminium sheet	28
Figure 2. 16 Schematics of mechanism of shear localised chip formation in titanium alloy ..	31
Figure 2. 17 Chip formed after orthogonal machining of Ti-6Al-4V	32
Figure 2. 18 3D reaction of surface roughness to approach angle and feed rate	33
Figure 2. 19 3D reaction of surface roughness to cut depth and feed rate.....	33
Figure 2. 20 Surface morphology of WT1-0 titanium when cut with different machining methods	34
Figure 2. 21 Typical stress-strain graph of Ti-22Al-27Nb sheet after EPT.....	34
Figure 2. 22 Microstructure effect on chip formation in titanium alloys.....	36
Figure 2. 23 Variation of fatigue crack nucleation site with surface integrity	38
Figure 2. 24 Surface roughness response to fatigue behaviour	39
Figure 2. 25 Surface roughness features	40
Figure 2. 26 Response of steel surface roughness and texture to EDM cutting parameters....	44
Figure 2. 27 Influence of pulse on-period on tool steel surface roughness at various cutting speeds (pulsed current 10A).....	45
Figure 2. 28 Schematic of a typical surface layer after EDM cutting.....	48
Figure 2. 29 Surface layers after EDM machining of AISI P20 steel.....	48
Figure 2. 30 Recast layer thickness at various EDM conditions	49
Figure 2. 31 Surface effect after typical AWJ cutting	50
Figure 2. 32 Surface texture features	50
Figure 2. 33 Macroscopic features of AWJ machined surface	51
Figure 2. 34 Microscopic attributes of three cutting zones on the AWJ cut surface of Al 7075-T6 alloy	52
Figure 2. 35 Two cutting zones of AWJ machined surface	52
Figure 2. 36 Surface roughening versus assessed depth for varying traverse speeds.....	54
Figure 2. 37 Comparison between laser assisted cutting and traditional cutting effects on tool wear.....	56
Figure 2. 38 SEM of the impact of pulsed laser cut on titanium surfaces	56
Figure 2. 39 3D surface morphology after laser machining of low carbon steel.....	57
Figure 2. 40 Spot overlap response to cutting speed during nickel-based superalloy laser cutting	58
Figure 2. 41 Melt thickness increasing with cutting speed for varying gas velocities	60

Figure 2. 42 SEM of TC1 titanium alloy with microstructural changes and hardness evolution after laser cutting.....	61
Figure 2. 43 Micrograph of HAZ after laser cutting of low carbon steel	61
Figure 2. 44 Regression model showing response of machining parameters	62
Figure 2. 45 Nature of lip at hole edge with varying hole diameter of Ferrite- Bainite duplex steel plate during hole flanging.....	63
Figure 2. 46 Flange thickness with 0 and 1000rpm spindle speed	63
Figure 2. 47 Tool influence on hole flanging strategies	64
Figure 2. 48 Correction for the manual monitoring of crack opening during HET.....	66
Figure 2. 49 Hole surface integrity of DP 980 steels and their respective failure mode after HET	68
Figure 2. 50 Hole edge of CP800 after HET.	69
Figure 2. 51 Optical micrograph after sectioning bainitic ferrite matrix steel.....	69
Figure 2. 52 Impact of burr direction on HET and fracture evolution in dual phase steel sheets	70
Figure 2. 53 Influence of punch geometry on the crack position in dual and complex phase steels.....	71
Figure 2. 54 Attained strain path after HET	72
Figure 2. 55 Edge fracture types for various steels after HET.....	72
Figure 2. 56 Attained tensile fracture strain with varying stress state	73
Figure 2. 57 Load curve drop considered as edge- stretch limit indicator.....	74
Figure 3. 1 Dimensioning of the tensile test specimen	79
Figure 3. 2 Uniaxial tensile test experimental set up	80
Figure 3. 3 Dimensioning of the hole expansion test specimen	81
Figure 3. 4 BUP testing machining with an accompanying DIC installation	82
Figure 3. 5 Tool geometries utilised for HET of titanium alloys.....	83
Figure 3. 6 Spherical punch for cupping test trial.....	83
Figure 3. 7 Test termination criteria during HET and Erichsen cupping test	84
Figure 3. 8 GOM Atos set-up for tensile specimen measurement.....	85
Figure 3. 9 SEM random grey intensity pattern of Ti-3Al-2.5V	86
Figure 3. 10 Constructive speckle pattern of the HET sample	87
Figure 3. 11 Ncorr graphic user interface	88

Figure 3. 12 DIC analysis	89
Figure 3. 13 Ncorr graphic user interface for unit conversion during displacement formatting	90
Figure 3. 14 Plane fitting for strain radius 15 with Lagrangian view option.....	90
Figure 3. 15 Flowchart of the one-way ANOVA	91
Figure 3. 16 Flowchart of ANOVA analysis with post-hoc comparisons	92
Figure 3. 17 Scatter plot for exploring the relationship between the response and predictor variables	94
Figure 3. 18 Graphic user interface for model expression A	95
Figure 3. 19 Statistical parameters for model expression A	96
Figure 3. 20 Graphic user interface for model expression B	97
Figure 3. 21 Statistical parameters for model expression B	97
Figure 4. 1 EBSD micrograph of the as-received CP-Ti (Grade 2) sheet.....	102
Figure 4. 2 3D surface morphology of the AWJ machined edges	103
Figure 4. 3 3D surface morphology of the EDM machined edges	104
Figure 4. 4 GOM Atos measurement of thinning along gage section	104
Figure 4. 5 SEM micrograph of machined edges	106
Figure 4. 6 Mean edge roughness after AWJ cutting.....	107
Figure 4. 7 Mean edge roughness after EDM cutting	108
Figure 4. 8 Tensile response of AWJ machined edges with different cut edge quality.....	109
Figure 4. 9 Tensile response of EDM machined edges with different cut edge quality	110
Figure 4. 10 Plot of width strain verses thickness strain.....	111
Figure 4. 11 EDM and AWJ fabricated edges deformed in three sheet directions.....	111
Figure 4. 12 Thickness variation for EDM and AWJ test samples.....	114
Figure 4. 13 Deformation mode after plastic deformation	115
Figure 4. 14 True strain evolution with deformation period.....	116
Figure 4. 15 Fractograph of crack edges after tensile testing	118
Figure 5. 1 Microstructure of supplied sheet; EBSD image	121
Figure 5. 2 True stress-strain curve.....	122
Figure 5. 3 Schematic of the HET set-up.....	122
Figure 5. 4 Schematics of tool geometry and sheet loading condition	123

Figure 5. 5 Alicona micrograph of edge surface finishes after AWJ cutting	124
Figure 5. 6 Alicona micrograph of EDM cut edge surface.....	125
Figure 5. 7 Optical micrograph of CP-Ti (Grade 2) machined edges.....	125
Figure 5. 8 3D surface morphology of machined edges	126
Figure 5. 9 HER of CP-Ti (Grade 2) fabricated with either laser, EDM or AWJ	127
Figure 5. 10 Dome height evolution after HET	128
Figure 5. 11 HER for various edge surface finishes with hemispherical punch.....	128
Figure 5. 12 Major and minor strain evolution during HET with hemispherical punch	130
Figure 5. 13 Edge forming limit for the various machining methods.....	130
Figure 5. 14 Effect of tool geometry on HER of unfinished edge quality.....	132
Figure 5. 15 Data loss due to extreme deformation of an EDM fabricated edge	133
Figure 5. 16 Thinning evolution analysis after HET with conical punch.....	135
Figure 5. 17 Thinning evolution analysis after HET with hemispherical punch.....	137
Figure 5. 18 Strain displacement in the plastic region for a 45 ⁰ oriented sample.....	138
Figure 5. 19 Deformation mode analysis	139
Figure 5. 20 Multiple localised necking sites during HET	140
Figure 5. 21 Nature of thinning distribution at failure for CP-Ti (Grade 2).....	140
Figure 5. 22 SEM analysis of the failure process of the laser cut surface	143
Figure 5. 23 SEM analysis of the failure process of the AWJ cut surface	144
Figure 5. 24 SEM analysis of the failure process of the EDM cut surface.....	145
Figure 6. 1 Micrograph of as-received Ti-3Al-2.5V sheet	148
Figure 6. 2 AWJ machined edge surface morphologies	149
Figure 6. 3 EDM machined edge surface morphologies.....	150
Figure 6. 4 Edge surface integrity of Ti-3Al-2.5V examined over 1.6cm distance.....	151
Figure 6. 5 Tensile properties of CP-Ti (Grade 2) and Ti-3Al-2.5V	152
Figure 6. 6 Surface morphology of the machined edges of Ti-3Al-2.5V	153
Figure 6. 7 SEM images for EDM surface crack density estimation.....	155
Figure 6. 8 Edge formability of CP-Ti (Grade 2) and Ti-3Al-2.5V alloys assessed with conical punch.....	157
Figure 6. 9 Machining induced surface microstructure changes	157
Figure 6. 10 Failure mode during HET of AWJ cut edge of Ti-3Al-2.5V	161
Figure 6. 11 AWJ edge crack behaviour of Ti-3Al-2.5V	162

Figure 6. 12 Failure behaviour in AWJ machined edge of CP-Ti (grade 2).....	163
Figure 6. 13 EDM cut edge failure initiation process during HET of Ti-3Al-2.5V	164
Figure 7. 1 Stress-stain curves for the titanium alloys examined	169
Figure 7. 2 Schematic of the Erichsen cupping test.....	170
Figure 7. 3 HER prediction flowchart.....	172
Figure 7. 4 R code user interface in R studio window	174
Figure 7. 5 HER and EI assessment of titanium alloys.....	178
Figure 7. 6 Major strain evolution during Erichsen cupping test	179
Figure 7. 7 Thinning evolution during Erichsen test	180
Figure 7. 8 Generated regression model equation coefficients for all six tested samples	181
Figure 7. 9 Generated regression model equation coefficients based on 5 experimental data sets minus Ti-21S.....	182
Figure 7. 10 R code window interface for predicting HER of Ti-21S.....	183
Figure 7. 11 Plot of the experimental and predicted HER	186
Figure 8. 1 Ti-3Al-2.5V alloy	192
Figure 8. 2 Examples of different forms of post-processing defects on sheet surfaces.....	193
Figure 8. 3 Surface profilometry analysis at full-length measurement (1.6cm)	195
Figure 8. 4 Scratch characteristics profile parameters	196
Figure 8. 5 Experimental set-up for the press brake forming trials	197
Figure 8. 6 Test sample dimensions.....	198
Figure 8. 7 Zones examined during ex-situ tensile testing	198
Figure 8. 8 Seed placement matching for reference and current images	201
Figure 8. 9 Coupons after press brake trial	202
Figure 8. 10 Crack nucleation process	203
Figure 8. 11 Standard force- travel curve for the interrupted tensile deformation	204
Figure 8. 12 SEM and DIC strain maps at the defect free micro surface	206
Figure 8. 13 Strain concentration at heavily deformed bands during in-situ SEM tensile test of ferrite-pearlite two- phase steels	207
Figure 8. 14 DIC parameters for localised phase strain evolution.....	207
Figure 8. 15 Localised strain evolution in α phases and the emergent band regions.....	208
Figure 8. 16 SEM and DIC strain maps at the indent defect micro surface	210

Figure 8. 17 Localised and global strain evolution at micro-surface conditions	212
Figure 8. 18 Damage nucleation after 1.7% global strain.....	213
Figure A. 1 Apparatus for sample cutting and mounting for onward metallurgical preparation	246
Figure A. 2 Apparatus for metallurgical surface preparation	248
Figure A. 3 Characteristic surfaces of CP-Ti (Grade 2) after electropolishing	249
Figure A. 4 Prepared specimen for fractography analysis in SEM.....	250
Figure A. 5 Alicona 3D InfiniteFocus optical microscope	251
Figure A. 6 Schematic of EBSD set-up	252
Figure A. 7 Illustration of Bragg's law	253
Figure A. 8 Random grey level on HET test sample	254
Figure A. 9 Positions of reference and target image patterns	255
Figure A. 10 Fundamental principles of DIC	256
Figure A. 11 Position of deformed and undeformed subsets.....	257
Figure B. 1 Heat treatment cycle adopted for the D2 tool steel.....	260
Figure B. 2 Schematic of the tool set-up and dimensioning	261
Figure B. 3 Manufactured die set with conical punch for HET trials.....	262
Figure B. 4 GOM Atos measurement of the bottom die prior to the HET	263
Figure B. 5 GOM Atos measurement of the top die prior to the HET	264
Figure B. 6 GOM Atos measurement of the conical punch prior to the HET	264
Figure B. 7 GOM Atos measurement of the bottom die after HET.....	265
Figure B. 8 GOM Atos measurement of the top die after HET	266
Figure B. 9 GOM Atos measurement of the conical punch after HET.....	266
Figure B. 10 AFRC approved engineering drawing of the top die	267
Figure B. 11 AFRC approved engineering drawing of the conical punch.....	268
Figure B. 12 AFRC approved engineering drawing of the bottom die.....	269
Figure C. 1 GOM Atos measurement of thinning along a tensile sample gage section	270
Figure D. 1 R-script computation on the user interface for Ti-6Al-4V	271

Figure D. 2 R-script computation on the user interface for Ti-3Al-2.5V ($t=1.6\text{mm}$).....	272
Figure D. 3 R-script computation on the user interface for Ti-3Al-2.5V ($t=1.25\text{mm}$).....	273
Figure D. 4 R-script computation on the user interface for CP-Ti (Grade 2).....	274
Figure D. 5 R-script computation on the user interface for Ti-35A	275

List of tables

Table 2. 1 Classification of defects in sheet metal forming.....	20
Table 2. 2 Defects in formed parts; derived from.....	21
Table 2. 3 Thermal conductivity with increasing temperature of titanium.....	29
Table 2. 4 Issues inhibiting the machinability of titanium, derived from.....	30
Table 2. 5 Major surface defects during titanium machining	35
Table 2. 6 Surface roughness amplitude parameters	40
Table 2. 7 Impact of EDM process variables on surface asperities	46
Table 2. 8 Test methods utilised to assess cut-edge formability.....	67
Table 3. 1 Comparison of model predictability using cross-validation method	98
Table 3. 2 Comparison of statistical parameters	99
Table 4. 1 Alloying constituents of CP-Ti (Grade 2).....	102
Table 4. 2 Grouping information using the Tukey method for AWJ cut quality.....	107
Table 4. 3 Grouping information using the Tukey method for EDM cut quality	108
Table 4. 4 Tukey Pairwise Comparisons for UTS and yield strength values	112
Table 4. 5 GOM Atos measurement of thinning evolution after tensile testing	113
Table 4. 6 Global strain distribution prior to fracture (after 90% deformation).....	117
Table 5. 1 Mechanical properties of CP-Ti (Grade 2) at room temperature.....	121
Table 5. 2 Thinning evolution with HER and edge surface finish after HET with conical punch	134
Table 5. 3 GOM Atos metrology measurement of samples deformed with hemispherical punch	136
Table 6. 1 Surface texture measurement of AWJ machined edges.....	155
Table 6. 2 Comparison of thinning evolution of AWJ fabricated edges after HET with hemispherical punch	158
Table 6. 3 Comparison of thinning evolution of EDM fabricated edges after HET with hemispherical punch	159

Table 7. 1 Chemical composition of titanium alloys	168
Table 7. 2 <i>p</i> -value span for levels of significance	175
Table 7. 3 Formability assessment at room temperature	177
Table 7. 4 <i>p</i> -value and R^2_{Adj} of generated regression model coefficients.....	184
Table 7. 5 Generated regression model equations	185
Table 7. 6 Comparison of experimental and predicted HER	186
Table 8. 1 Micrographs of defect types observed on the as-supplied Ti-3Al-2.5V sheets	194
Table 8. 2 Three ranges of scratch profiles examined during the press brake forming	196
Table 8. 3 Press brake forming trials for different longitudinal scratch profiles.....	202
Table B. 1 Heat treatment steps for hardening the D2 tool steel billet.....	260

Chapter 1

Introduction

1.1 Commercially pure titanium: properties and composition

For several years, titanium and its alloys have formed an essential facet of high value engineering performance endeavours. They are widely utilised in the aerospace industry by virtue of their structural efficiency (due to their high strength to low weight ratio) and high corrosion resistance tendencies (due to their enormous passivation capability) (Boyer, 1996). For a large modern commercial aircraft, about 7% of the airframe structural weights and about 36% of the engine structural weights (by volume the most abundant material in the engine) are fabricated from titanium (Peters, et al., 2003). The decision to select either an unalloyed, α , near α , $\alpha+\beta$ or metastable β grade titanium relies on either the forming technique desired, cost considerations, service prerequisite or the mechanical properties required. The unique presence of highly soluble interstitial oxygen and nitrogen in titanium differentiates them from other metals. These soluble interstitial elements pose issues such as high temperature oxidation and alpha casing thereby impeding their ductility as well as fatigue strength, which would otherwise be absent in other metals (Beal, et al., 2006).

The most common commercially pure titanium (CP-Ti) grades available, have various quantities of interstitial impurities added (C, O, N, Fe, H) with the enhanced CP-Ti grades having extra constituent elements like Palladium and Ni-Mo inclusive (ASM Metals Handbook, 1996). For CP-Ti, the variation in yield strength is attributable to changes in grain size and the quantity of interstitial impurity available (Beal, et al., 2006). The tensile strength and ductility of CP-Ti are also responsive to the amount of oxygen present (Beal, et al., 2006). The interstitial impurities enhance the mechanical properties of CP-Ti without decreasing the ductility, with an increase in Fe content leading to refinement of α grains (equiaxed) and reduced strain hardening (Simbi & Scully, 1996). Increase in interstitial element (equivalent oxygen) also results in the increase in yield stress of CP-Ti, Figure 1.1*a*. Fatigue life of CP-Ti is a function of the amount of interstitial element present, the level to which the material is cold worked as well as the grain size, Figure 1.1*b* (ASM Metals Handbook, 1996). CP-Ti with lower amount of interstitial elements (higher purity) have reduced hardness, lower strength as well as lower transition temperature in comparison with the ones with lower purity (Beal, et al., 2006).

An increase in the interstitial impurities of CP-Ti does not affect the deformation texture (Simbi & Scully, 1996).

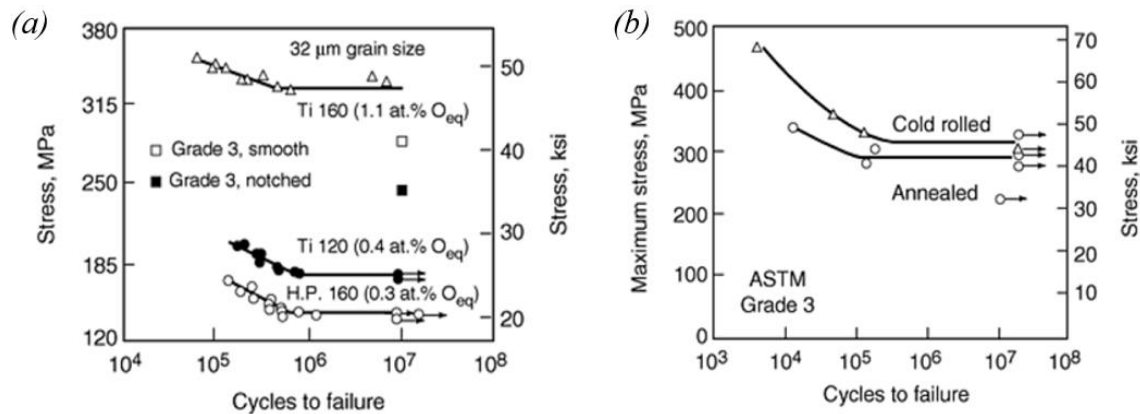


Figure 1. 1 CP-Ti S-N curve (ASM Metals Handbook, 1996)
Influence of (a) equivalent oxygen, (b) cold work

Since the reduction in grain size has been established to improve the strength of CP-Ti, pre-treatment with severe plastic deformation methods have also been adopted to enhance the strength and hardness (Sergueeva, et al., 2001) as well as the fatigue strength (Semenova, et al., 2009) of CP-Ti. Other unconventional manufacturing techniques like the additive manufacturing method (selective laser melting) is also reported to improve the strength as well as hardness of CP-Ti without altering the ductility (Attar, et al., 2014).

Generally, the nature of the unit cells of hexagonal close packed (HCP) based materials makes them susceptible to texturing during rolling. This results in the emergent deformation modes being a function of the loading orientation. CP-Ti is very anisotropic with the development of texture mainly the outcome of plastic deformation. An increase in the rolling reduction (50% deformation) of CP-Ti impacts on the tensile property anisotropy due to the development of strong basal texture with further loading leading to the formation of mechanical fibering (Nasiri-Abarbekoh, et al., 2012). The deformation modes obtained after the texture formation influences the tensile property anisotropy which are manifested through the emergent dimple shape and size, as well as how the dimples are distributed (fracture mechanism) (Nasiri-Abarbekoh, et al., 2012). Normally at high strain rate deformation, a weak deformation texture is obtained during compression of CP-Ti at room temperature via quasi-static and dynamic loading conditions (Gurao, et al., 2011). Severe plastic deformation techniques like equal channel angular pressing (ECAP) used to plastically work CP-Ti Grade 2 at room temperature also results in substantial mechanical anisotropy because of strong texture formation (Jäger, et al., 2015).

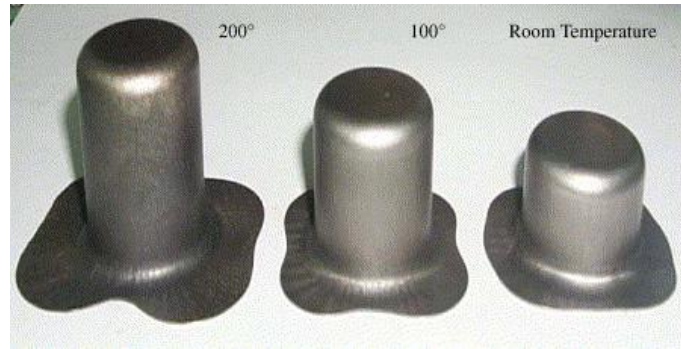


Figure 1. 2 JIS Grade 1 CP-Ti exhibiting lower workability after cold working compared to thermally activated counterparts (Chen & Chiu, 2005)

Commercially pure titanium and near commercially pure alloys possess α -phase grained microstructure with HCP crystal structure which results in fundamental challenges in cold working them. Some basic macroscopic plastic attributes which hinder the formability of materials with HCP crystal structure includes; high anisotropy level, high anisotropic work hardening and yielding (Jurendić & Gaiani, 2013). According to Chen and Chiu, the limited level of JIS Grade 1 CP-Ti formability at room temperature are attributable to its HCP structure which results in low ductility (Chen & Chiu, 2005). Their work revealed that thermal activation is required to enhance the ductility and formability of JIS Grade 1 CP-Ti, Figure 1.2.

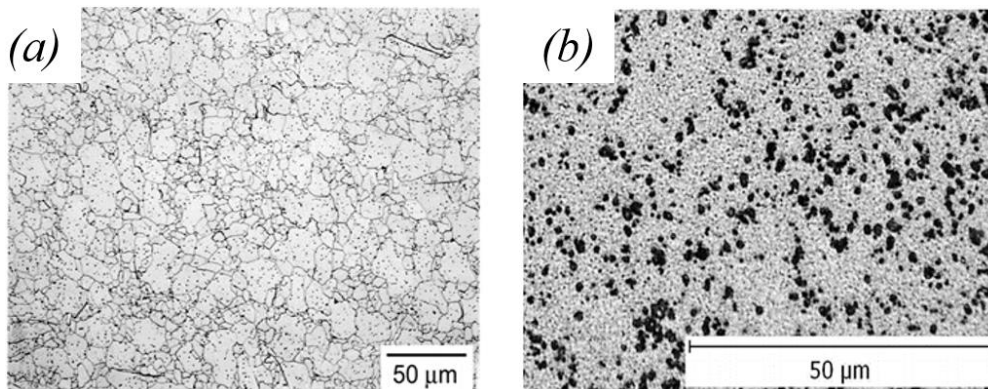


Figure 1. 3 Ultra-fine grained micrograph of CP-Ti grade 2 after ECAP (Greger, et al., 2011)

(a) Original micrograph, (b) micrograph after 8passes of ECAP

Nevertheless, some severe plastic deformation methods have also been shown to improve the mechanical properties of HCP crystal structured materials. Greger et al., in their research while adopting ECAP and cold drawing of CP-Ti (Grade 2) revealed that plastic deformation of the material is mainly by way of continuous shear deformation (Greger, et al., 2011). According to their work, the mechanical properties of the material are improved by virtue of the ECAP grain refinement phenomenon, Figure 1.3.

1.2 Cold formability of titanium

Cold forming of materials form a very significant facet of manufacturing processes owing to their tendency to reduce scrap, reduce production cost and the possibility of attaining intricate formed shapes. For this reason, cold forming technologies are extensively employed in both aviation and high-end automobile sectors for fabricating parts. Titanium alloys adopted in a particular forming operation can be chosen based on either the required operating temperature, forming process or even the production cost (Antunes, et al., 2018). Various titanium alloys utilized in the aerospace sector have been identified to be cold formable. Special titanium alloys like the Ti-15V-3Cr-3Al-3Sn are fabricated for use in the aerospace and other industries not only because of their low production cost, but also for their adoption in areas where cold workability and high strength are required (Rosenberg, 1983). Ti-15V-3Cr-3Al-3Sn beta alloys are employed in aerospace brake applications and can be both cold worked as well as heat treated to strength of about 1GPa (Boyer, 1992).

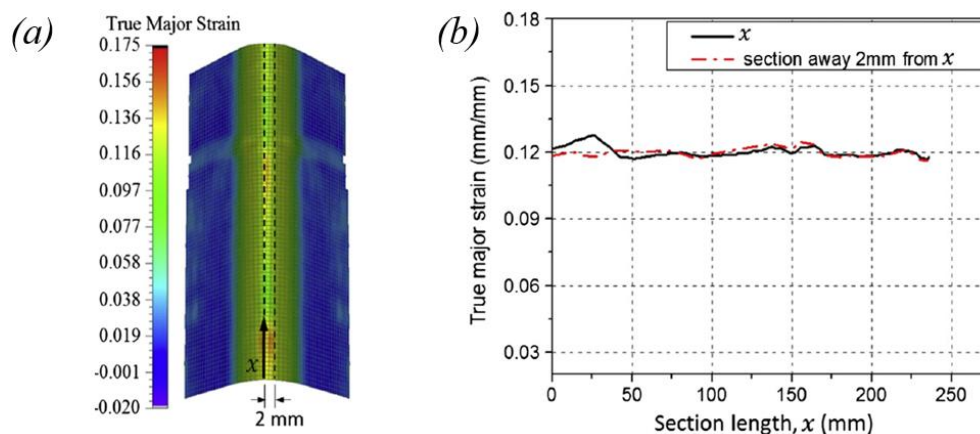


Figure 1.4 Roll formability of Ti-6Al-4V at room temperature (Badr, et al., 2015)
(a) Strain distribution over sheet surface, (b) true major strain distribution over section length
CP-Ti and most ductile metastable beta titanium alloys (Ti-15V-3Sn-3Cr-3Al and Ti-3Al-8V-6Cr-4Zr-4Mo), can be cold worked to a limited degree. For Ti-8Al-1Mo-1V alloy sheets employed in cold forming, only shallow shapes can be attained when using standard forming methods. For that, larger bend radii must be employed with shallower stretch flanges (Beal, et al., 2006). CP-Ti (Grade 1) normally have excellent drawing tendencies. The other grades of CP-Ti usually requires higher forming forces, lower forming speed and higher corner radius to plastically work them (Adamus, 2006). For cold stamping of titanium alloys however, intermediate annealing as well as stress relief annealing are usually employed under vacuum conditions (Adamus, 2006). The poor drawability of titanium alloys are also attributable to their high yield strength and high yield-to-tensile ratio values (Adamus, 2006). Studies

conducted by Badr et al., on the possibility of forming Ti-6Al-4V at room temperature showed that the tendency of stamping or deep drawing the material is cumbersome due to the high springback and low material hardening tendencies (Badr, et al., 2015). Their work however showed that there is the possibility of forming Ti-6Al-4V at room temperature via roll forming into ‘*simple longitudinal sections*’ with minimized shape defects compared to other high strength materials, Figure 1.4.

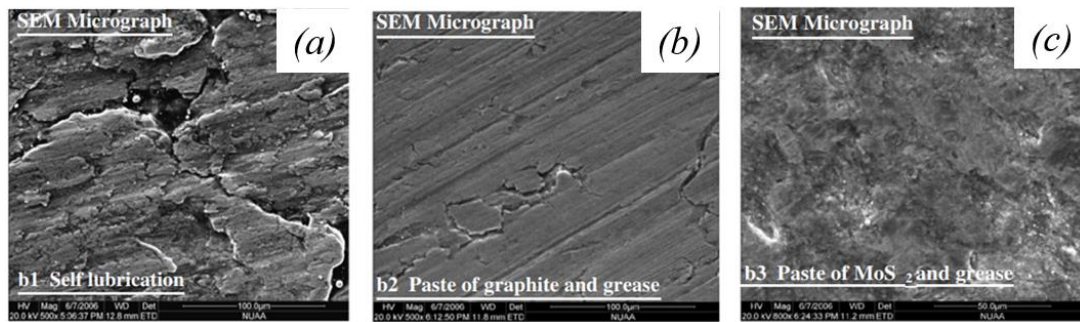


Figure 1. 5 Attained finished surface quality of CP-Ti formed under various friction conditions (Hussain, et al., 2008)

(a) Self-lubrication, (b) Paste of graphite and grease, (c) Paste of MoS₂ and grease

Pure titanium is also documented to be cold workable effectively using incremental sheet forming (ISF) technique. Work done by Hussain et al., on the formability of CP-Ti sheet using cold ISF process showed that the process parameters play a massive role in the cold formability of the material (Hussain, et al., 2008). According to their work, the major obstacle that hinder the attainment of optimum formability of CP-Ti during cold ISF process is the friction that occurs at the tool/ blank interface. This occurrence depending on the type of lubricant employed, have a major impact on the attained finished surface quality after cold ISF, Figure 1.5.

Some works also focused on the micro level mechanisms governing the cold working of titanium. Zhang et al., in their work on the microstructure evolution during cold deep drawing of CP-Ti sheet showed that the attained plastic strain during the entire deformation process are accommodated by deformation twinning and dislocation slip (Zhang, et al., 2012).

Pure titanium generally shows good ductility during cold working processes due to their high normal anisotropy but exhibit limited workability in severe forming processes. The normal practice utilized mostly is to adopt thermal activation methods to alter the material properties in order to provoke the material flow (Ogawa, 2007). Harada and Ueyama, in their work studied

the cold formability of pure titanium (Grade 2) at ambient temperature during multi-stage deep drawing (Harada & Ueyama, 2015). Their work showed that utilizing heat oxide coating to shield the material from direct contact with the dies and ironing while adopting intermediate heat treatment results in the attainment of optimum multi-stage cold deep drawability of the material, Figure 1.6.



Figure 1. 6 Multi-stage cold deep drawing of pure titanium after intermediate annealing (Harada & Ueyama, 2015)

1.3 Machining and forming as manufacturing processes of sheet metals

Metal forming mostly entails the working of metals into desired shapes as a result of plastic deformation via the application of a force (Dixit, et al., 2011). Thus, material removal are not undertaken during metal forming processes. Other methods like the laser forming techniques can also be employed to plastically deform metals via the aid of a heat gradient (Geiger & Vollertsen, 1993); (Siqueira, et al., 2016). For sheet metal forming processes, a sheet with low volume to surface area ratio and thickness designation lower than 6mm is utilised (Dixit, et al., 2011).

Furthermore, machining adopted as manufacturing processes are mainly for material removal purposes. Machining mostly results in the alteration of material cut surface properties and in other cases properties just beneath the cut surface. Conventional machining techniques like turning and milling largely entails material removal by way of chip formation. Wedge shaped tools are mostly utilised to subject the workpiece to shearing, bending and compression. Conventional cutting method mostly entails direct contact between the tool and the workpiece during the machining process. On the other hand, the quest to enhance machining precision coupled with the drive to improve the machinability of difficult-to-cut materials has necessitated the adoption of non-conventional machining methods. For non-conventional cutting methods, no direct contact exist between the cutting means and the workpiece during the machining process. Non-conventional machining methods involves the use of other means

including; abrasive particles, water, chemicals, heat action, electrons, laser, etc. to machine parts (Dixit & Dixit, 2008). Non-conventional machining processes (e.g. ultrasonic machining, electrochemical machining, laser beam machining, etc.) are adopted extensively by the metal working industry due to their versatility in usage and superior surface finish compared to conventional machining methods (Dubey & Yadava, 2008).

For manufacturing processes like sheet metal hole flanging operation, machining and sheet forming processes are adopted as an integrated forming process for the onward fabrication of parts. The hole flanging operation entails machining preceding the forming process. Hole flanging are adopted mostly in the automotive, aerospace and aeronautic industry for forming sheet metals with pre-fabricated holes to make various shapes of flanges (Cui & Gao, 2010). Hole flanging usually adopts press working to toughen and enhance hole edges, permits thread cutting in components as well as joint formation for the assembly of tubes to other formed parts (Silva, et al., 2013). The extent of edge flangeability of sheet metals after a particular choice of machining are assessed using the hole expansion test (HET). A schematic set-up of the HET is shown in Figure 1.7.

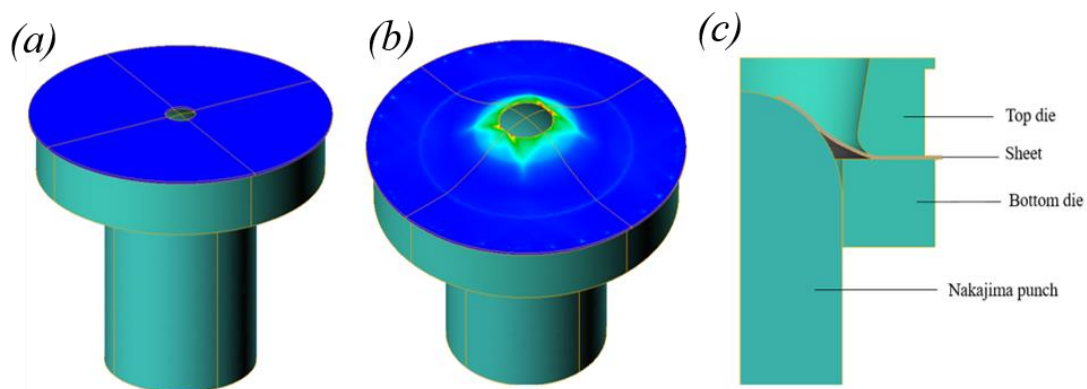


Figure 1. 7 Schematic of the HET
 (a) clamping and (b) deformed positions, (c) cross-sectional view after the HET

1.4 Research background and problem statement

Titanium is the material of choice for the aerospace industry due to their good physical and chemical properties. However, their wide adoption is limited by virtue of their poor room temperature formability (due to the nature of their crystallographic structure) (Jurendić & Gaiani, 2013) and their high sensitivity to notches which makes them susceptible to cracking and tearing during cold working (Beal, et al., 2006). Therefore, there is the need to continuously explore various ways of attaining optimum formability of titanium at room temperature.

Manufacturing processes sometimes involves the assembly of parts produced from hole flanging operations with other fabricated parts to form new components. For sheet hole flanging operations, a pre-fabricated hole is required in the sheet metal prior to the forming process. Various machining methods are commercially utilised to cut sheet metals (El-Hofy, 2014). For that, unique edge surface morphologies are produced by different machining methods. The integrity of the hole edges prepared after machining for hole flanging operation is a crucial parameter to consider when assessing the edge forming performance of sheet metals. Research conducted on ultra-high strength steels revealed that the macroscopic unevenness of the sheared edges coupled with its hardness influences the edge forming performance of the material (Mori, et al., 2010). Xu et al., in their work on the adoption of EDM, laser and punching to prepare dual phase steels for hole flanging operation also revealed varied edge forming performances of the material (Xu, et al., 2012). According to Schneider et al., the damage produced on the edge surface of dual-phase and ferritic-bainitic steels after shear cutting reduced their edge formability (Schneider, et al., 2016). Most research activities undertaken to assess the impact of edge preparation methods on sheet edge formability have been conducted on steels. However, no research has been previously conducted to examine the impact of edge preparation methods on the edge forming performance of titanium alloys. Also, the effect of varying machining parameters on sheet metal edge surface integrity have been extensively documented in literature (Lee, et al., 2004); (Miraoui, et al., 2014). However, limited research has been previously conducted to ascertain the impact of varying machining parameters on the edge formability of sheet metals.

Additionally, the difficulty in machining titanium and its alloys are well documented (Churi, et al., 2007). This difficulty in their machinability are attributable to their inherent material properties like low thermal conductivity; (21-22W/mK for pure titanium and 5.5-25W/mK for $\alpha/\beta/\alpha+\beta$ Ti at 0-800⁰C) compared to steel (60-30W/mK) and aluminium alloys (170-240W/mK at 0-600⁰C) (Veiga, et al., 2013) as well as their high temperature strength and low elastic modulus (Colafemina, et al., 2007). The reduction in elastic modulus of titanium makes it more prone to deflection and vibration during cutting (Veiga, et al., 2013). The extent of machinability of titanium has also been shown to be a function of their alloying constituent (Yang & Liu, 1999). Therefore, there is the need to examine the nature of edge surface defects produced in pure titanium and its alloyed counterparts when machined with different cutting methods, as well as the impact of the quality of edge surface finishes produced on their edge forming performance at room temperature.

Furthermore, post-processing surface defects in the form of grooves, scratches and indents are mostly introduced on sheet metal surfaces during either transportation, storage or handling of sheet metals. Works previously done on the impact of post-processing induced defects are limited to their consequence in relation to production cost. Qamar et al., conducted a research on aluminium by focusing on production cost accrued as a result of the elimination of surface defects and rejected parts (Qamar, et al., 2004). Their work mainly focused on surface finish defects, post extrusion defects as well as other material and tool related defects. However, research directed at examining the impact of post-processing defects inherent on sheet surfaces on their formability has not been previously investigated. Considering the high sensitivity of titanium to surface inhomogeneity (Yuri, et al., 2003), there is therefore the need to examine the nature of post-processing defects present on titanium sheet surfaces, their distribution, orientation and depth, as well as their influence on the room temperature formability of titanium alloys.

Research directed at addressing the above-mentioned gaps in titanium formability will help;

- Improve the room temperature formability of titanium via optimization of surface conditions.
- Contribute towards comprehending the effect of sheet metal surface defects produced post manufacturing on the material forming limit strain evolution.
- Clarify the requirements of supplied sheet conditions.
- Generate the requisite experimental data which could be linked to material models to understand the forming behavior of titanium at room temperature.
- Explore various ways of attaining optimum room temperature formability of titanium, which aligns with the key interest of the aerospace industry.

Hole flangeability, stretch flangeability and edge formability are used interchangeably in this EngD research.

1.5 Research aim

This EngD project aims at understanding the effect of post-manufacturing induced sheet metal surface defects (i.e. induced either post machining or via inadvertent sheet surface damage) on the room temperature formability of titanium alloys.

1.6 Research objectives

The main objectives of this EngD project includes;

- Assess the impact of EDM, AWJ and laser cutting on the edge formability of a pure titanium grade. Also, examine the influence of varying machining parameters on the edge surface integrity evolution as well as the impact of forming parameters on the edge formability of a pure titanium grade. In addition, compare the edge forming performance trends with their alloyed counterpart.
- Evaluate the edge formability limit strain diagram of a pure titanium grade for edge surfaces prepared with either laser, EDM or AWJ machining.
- Establish how the examined cutting techniques alter the edge related failure modes and failure nucleation process in titanium alloys after the edge forming process.
- Ascertain if uniaxial tensile test samples fabricated with either EDM or AWJ have any significant impact on the room temperature uniaxial tensile properties of a pure titanium grade.
- Examine the main differences and similarities in the failure behavior of a pure titanium grade, when tested after HET and uniaxial tensile deformation, taking into account the similarity in stress state observed during conventional tensile deformation and those obtained at the hole edge after HET.
- Based on the knowledge gained from the response of the edge preparation methods of titanium to the edge forming parameters, formulate a statistical numerical model expression, capable of generating regression model equations for the onward prediction of the edge forming performance of titanium alloys.
- Assess the impact of indent surface defects on the localized strain evolution as well as the nature of deformation attained during uniaxial tensile deformation of titanium alloys at micro scale.
- Establish via experimental trials the threshold values of scratch characteristic parameter profiles which could be considered acceptable during sheet metal selection processes for press brake forming of titanium alloys.

1.7 Thesis structure

The EngD thesis has been structured as follows;

- An opening abstract which provided a general overview of the work including the project background, experimental techniques as well as some of the results derived from the work.
- Chapter 1; Contains an introductory chapter detailing the general rationale behind the project and the major research questions addressed in this work. It also included the main project aims and objectives.
- Chapter 2; Entails an extensive literature review on the major themes identified. This chapter also detailed some works that have been done in the areas of interest, which could serve as a background knowledge for this research. The literature review also provided an avenue for identifying the knowledge gaps. The major criteria for journal and scholarly text selection utilised for the literature survey were generally based on selected impact factor of the journals, the pedigree of the publishers, visibility and citations.
- Chapter 3; Contains the experimental methods and the analysis approaches used in this work. It majorly dwelled on the mechanical testing and measurement approaches as well as detailing the results characterisation and analysis methods.
- Chapter 4; Explains the impact of preparing uniaxial tensile test samples with either EDM or AWJ machining on the room temperature tensile deformation of CP-Ti (Grade 2). This chapter examined the nature of the edge defects produced after AWJ and EDM machining to ascertain if the defects produced influence the failure mode evolution and the room temperature tensile properties of the material.
- Chapter 5; Details experimental works to examine the impact of laser, EDM and AWJ machined sheet edges on the edge formability of CP-Ti (Grade 2) at room temperature. The chapter also introduced supplementary techniques for characterising the material edge formability performance.
- Chapter 6; Details experimental trials to examine the impact of AWJ and EDM machining on the edge surface integrity as well as the edge forming performance of Ti-3Al-2.5V. The results were compared to those of CP-Ti (Grade 2).

- Chapter 7; Based on the knowledge acquired from the response of titanium alloys to the edge forming parameters, a predictive statistical numerical model expression was proposed and discussed in this chapter.
- Chapter 8; Details an experimental approach to compute the localised strain evolution at an indent defect micro-surface of Ti-3Al-2.5V during uniaxial tensile deformation. This chapter also assessed the morphology of the characteristic profile of longitudinal scratch defects oriented along the sheet rolling direction and their impact on the bendability of Ti-3Al-2.5V.
- Chapter 9; Comprises concluding remarks on the major findings of the EngD research. Recommendation for future works were detailed in this chapter and the research questions were fully revised and addressed. Major contributions to knowledge and the industrial relevance of the project were also discussed in this chapter. The main EngD project challenges and the limitations were addressed in this chapter.
- Appendices; Entails some experimental apparatus and processes undertaken in this project. It also details the fundamental principles governing some experimental techniques adopted in this EngD research. The heat treatment regime followed to prepare the tool materials were detailed in this chapter. The procedure for the tool set fabrication including the assessment of the tool dimensional integrity, before and after the experimental trials were detailed in this section.

1.8 Programme of work flowchart

The main routes followed to execute the research objectives in order to address the major research questions are shown in the EngD project programme of work flowchart in Figure 1.8. Overall, experimental trials and formulated predictive statistical numerical model expressions were utilised in this EngD research to address the knowledge gaps identified.

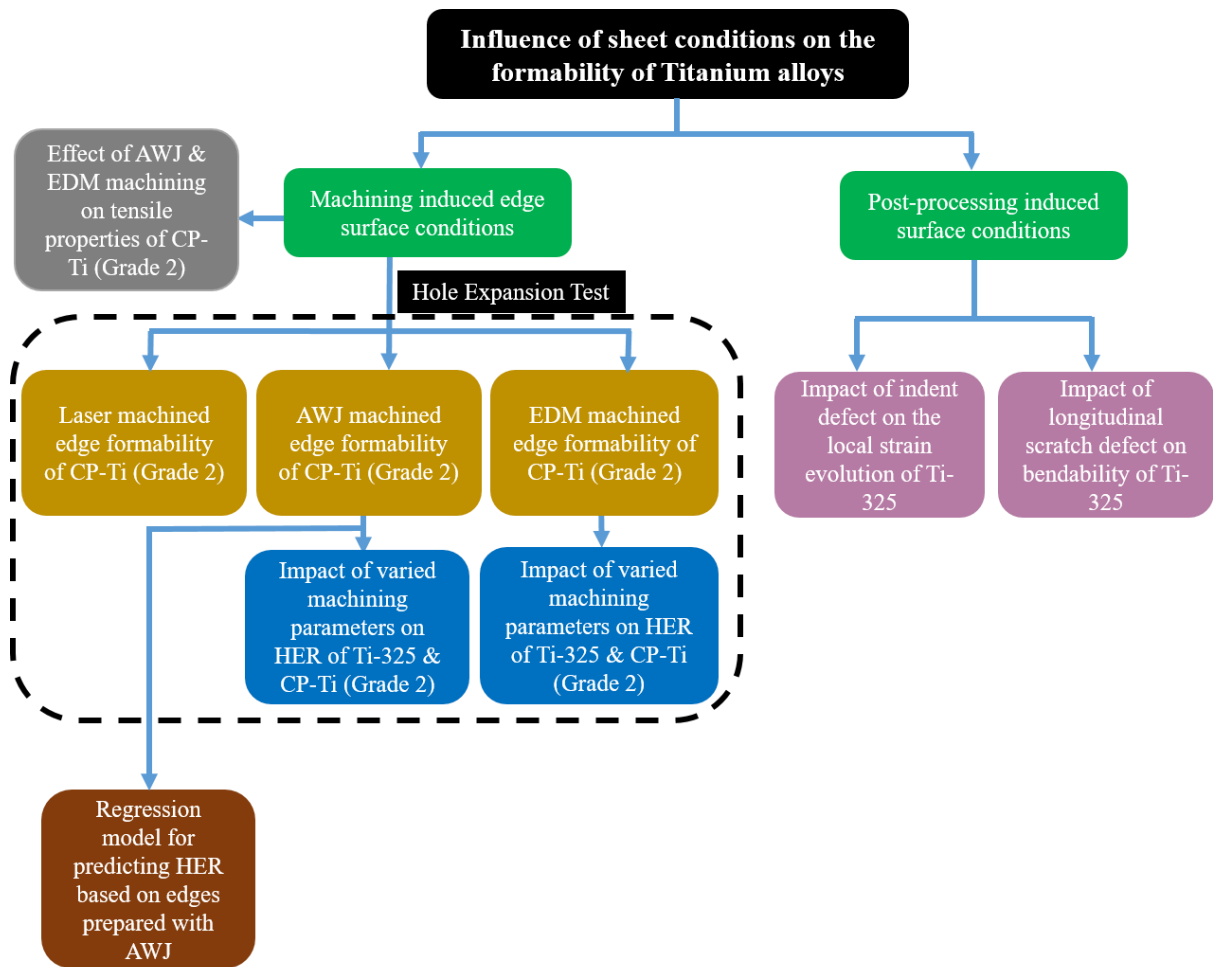


Figure 1. 8 Programme of work flowchart

Chapter 2

Literature review

2.1 Sheet metal surface asperities and limiting strains

Sheet metal forming process is an extremely important facet of the design and manufacturing industry. Knowledge of forming parameters and their influence on the formability of sheet metals is paramount to the forming and design process. Therefore, research directed at the forming tendencies of metals is necessary to ascertain their applicability in a particular sheet metal forming operation. This quest is also founded in the need to estimate and comprehend the limiting strains achieved during forming operations especially in the cold working industry. Surface roughening during sheet metal forming is detrimental to the surface integrity of the final product and provides a nucleation site for strain localization (Wilson, et al., 1981), Figure 2.1.

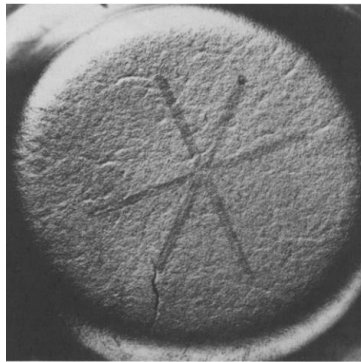


Figure 2. 1 Failure at limit strain after in-plane biaxial stretching of Cu sheet (Wilson, et al., 1981)

The increase in surface roughness with deformation in thin sheet metals are essential in examining the strain limit and the strain instability. Fukuda et al., in their work to determine the roughening of the free surface of mild steel experimentally showed that by putting them through plastic deformation under varying strain ratios, the surface roughening was linearly responsive to the equivalent strain (Fukuda, et al., 1974). To some extent, surface roughening can be considered as a microstructural consequence of slip activities happening during plastic deformation resulting in necking and ultimately failure at higher strains (Jain, et al., 1996). The relationship between the surface roughening of a sheet metal, the equivalent strain and the average grain size can be expressed as (Ogórek & Stachowicz, 2005);

$$R_{DS} = R_0 + m\varepsilon_s d^{0.5} \quad (2.1)$$

Where: R_{DS} = deformed sheet surface roughness; R_0 = undeformed sheet surface roughness; m = material constant; ϵ_s = equivalent strain; d = average grain size

According to Zhao et al., the nature of strain homogeneity observed in aluminium oligocrystal is attributable to the history of its grain topography and microtexture (Zhao, et al., 2008). According to their work, the manner in which the surface roughness evolves are attributable to the nature of the micro strain localization as well as the intra-grain interaction.

A theoretical analysis of stretch forming technique on thin sheet anisotropic metals (ASTM 1080 steel, Al-2024 and 70/30 Brass) also shows that the plastic instability strains reduce with decreasing thickness to grain size ratio (Al-Qureshi, et al., 2005). According to their work, the surface roughness values are linearly responsive to the limit strains of the sheet metals.

Sheet metal surface defects are also considered as lower thickness point of sheet metals and these non-homogeneities (surface asperities and roughness) influence the strain limit of components. According to a work on the influence of thickness of AA1100 aluminum sheet on its in-plane stretch-forming limit, the roughness of the sheet was linearly responsive to its effective strain with a reduction in the sheet thickness producing reduced forming limit (Fukui & Nakanishi, 1988). Sheet metal surface defects could be produced from the development of minute pre-existing imperfection available in the sheet (local thickness variation) (Marciniak & Kuczyński, 1967).

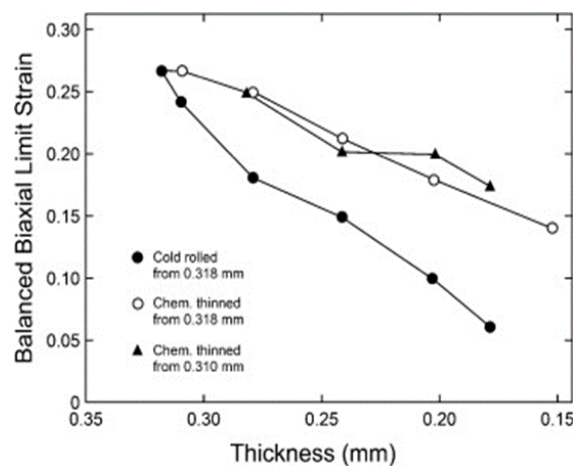


Figure 2. 2 The limit strain in balanced biaxial tension as a function of thickness of steel sheet (Raghavan & Garrison-Jr, 2010)

For stretch forming of thin metals (steel, aluminum and brass sheets, <1mm of initial thickness), surface roughness results in non-uniformity in thickness during deformation and plays a vital role in the nucleation of tensile instability and measured values of limit strains

(Tadros & Mellor, 1978). According to studies by Raghavan and Garrison-Jr, for balanced biaxial stretching however, the limit strain decreases with decreasing thickness as the strength of the material is held constant for steel sheets (Raghavan & Garrison-Jr, 2010), Figure 2.2. It was inferred from their work that the thinning in the balanced biaxial stretching is responsive to defects in the steel material.

Strain localization can also be attributed to the process of loss of stability (grooves in the form of defects and variation in thickness, Figure 2.3) running in a direction perpendicular to the larger principal stress during stretch forming of Lead sheet metals (Marciniak & Kuczyński, 1967).

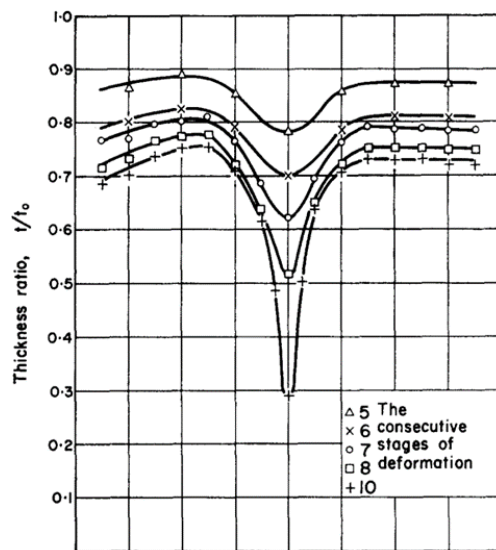


Figure 2. 3 Changes in Lead sheet metal thickness examined in plane transverse to forming groove (Marciniak & Kuczyński, 1967)

According to Hiroi and Nishimura, surface defects are the main sources of the initial inhomogeneity of sheet metal thickness, and there exists a critical depth of surface defect (2 and 0.5% of thickness for soft and hard aluminium sheets respectively) up to which, fracture is not produced and the forming limit does not reduce (Hiroi & Nishimura, 1997).

According to Becker, in addition to the linear responsiveness of surface roughening to strain and grain size, the impact of small-scale strain localization at the surface also contributes enormously to surface roughening in AA-6111-T4 aluminium sheet (Becker, 1998). Becker on the same material also reported that parameters (strain hardening, crystallographic texture and material homogeneity) that influence on strain localization, by extension also affect the surface roughening during sheet metal forming.

Furthermore, studies conducted by Osakada and Oyane on the relationship between surface roughening and strain was done on various metals with different crystallographic structures, (HCP: Zn and Mg; FCC: Cu, 52S-Al, 70-30 Brass, 52S-Al and 18-8 Stainless steel; BCC: Fe (0.03%C) and 13Cr Stainless steel) (Osakada & Oyane, 1971). Results showed that surface roughening tendencies was lowest for metals with BCC structures and highest for HCP structures with intermediate results for metals with FCC structures. Their research concluded that surface roughening rate increases linearly with strain and are responsive to the deformation mode, position of relevant surface (variations in surface area with deformation), grain size and metal crystal structure (Osakada & Oyane, 1971).

Forming limit diagrams (FLDs) are vital in estimating the limit strains at a point in a sheet metal and recounts how principal surface strain at highly localized zone of thinning or necking becomes visible in the surface of the sheet metal (Chow & Jie, 2004). It was reported that if the surface asperities which causes the localised necking during a forming process is reduced, the subsequent strain to the onset of a localised necking is appreciably increased, and as a consequence, the forming limit strain is expected to increase compared to ordinary forming processes. Takakura et al., in their work studied the enhancement of forming limit of soft aluminium and copper sheet metals by reducing the surface roughening with plastic strain, which led to the onset of localised necking (Takakura, et al., 1987). Their result shows that the forming limit is enhanced in the stretch-forming zone at regions where the minor and major strains are positive in the sheet plane, Figure 2.4.

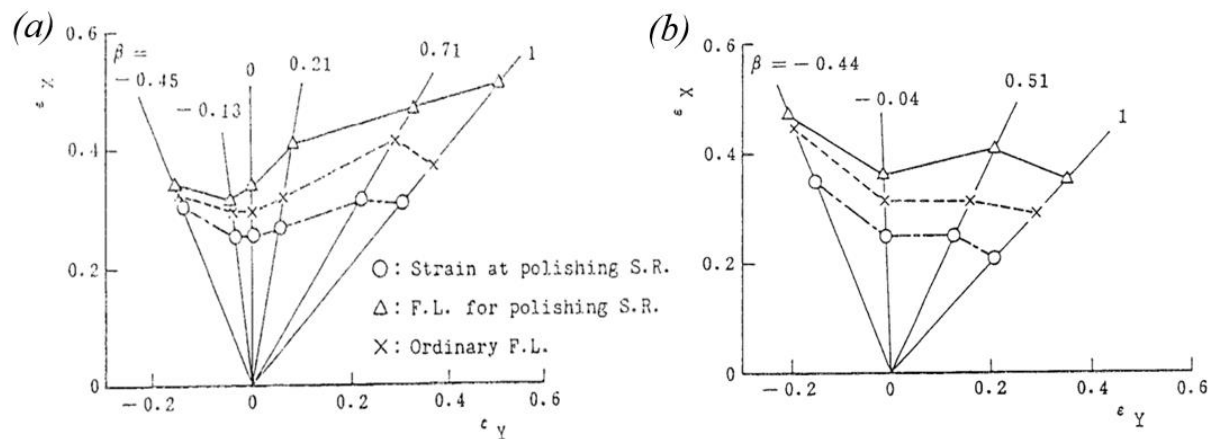


Figure 2. 4 Enhancement of forming limit by reduction of surface roughening (Takakura, et al., 1987)

Enhanced FLD attained by intermediate polishing of (a) soft Aluminium and (b) Cu sheet metal

The inception of necking of sheet limit strains during stretching is cumbersome to predict. According to Yamaguchi et al., the forming limit of aluminium sheet and foils can be enhanced during balanced biaxial stretching by reducing the surface roughness via inter-stage method of polishing (Yamaguchi, et al., 1995), Figure 2.5. Ideally, this process is attained during stretching process at strains just before the start of localised necking. According to their work, forming limit strains normally reduce with reduction in sheet thickness. However, surface roughness reduction during the forming process via polishing appreciably enhances the forming limit of aluminium sheet with 0.1-0.2mm thickness to attain limit strains of about 1.4× bigger than their unpolished counterpart undergoing the same forming process.

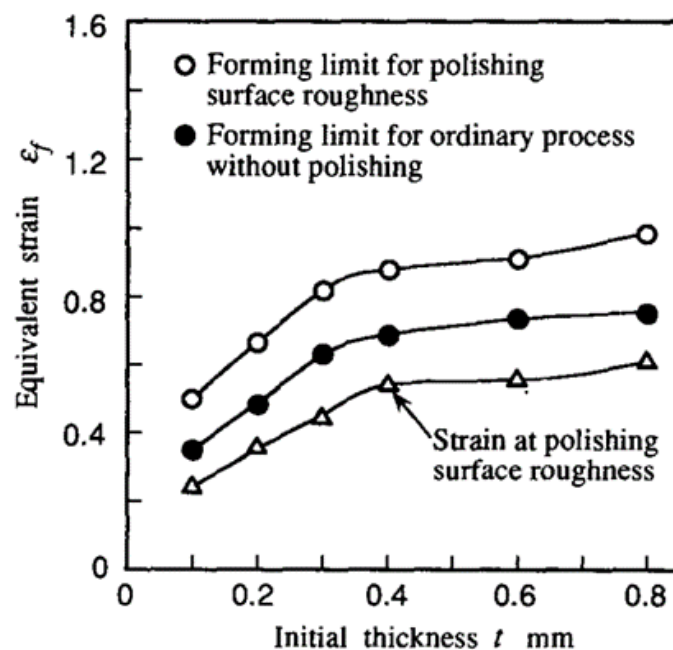


Figure 2. 5 Forming limit strains attained via surface roughness polishing of aluminium sheet and foils (Yamaguchi, et al., 1995)

McCarron et al., in their work studied the impact of geometrical defects, introduced by electropolishing grooves into steel sheet surfaces on their formability during biaxial stretching (McCarron, et al., 1988). Their results showed that for the most critical defects (grooves), localised necking was observed due to the defect strain states changing to plane strain. Their studies also showed that sheet homogeneity improves the formability of the material since the changes in the sheet forming limit strain are a function of the attained groove depths, Figure 2.6.

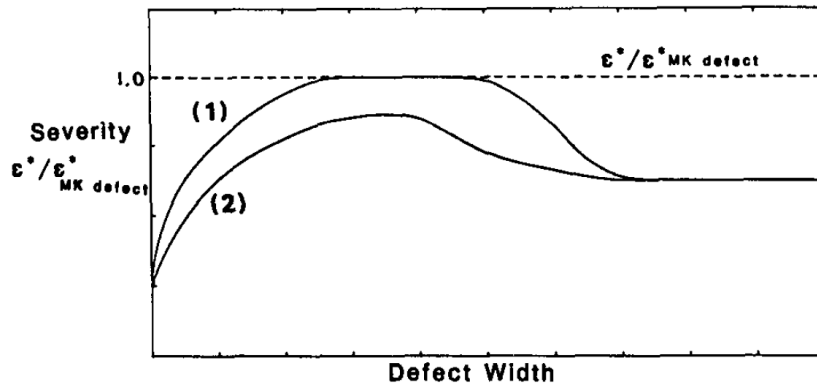


Figure 2. 6 Response of sheet forming limit strain to defect width (McCarron, et al., 1988)

Cases (1): long defects, (2) short defects

2.2 Surface defects in formed parts and optimisation processes

Surface defects may be introduced into materials at various stages of fabrication including production and casting, heat treatment, hot slab rolling as well as cold strip rolling. During manufacturing, the nature of the surface defects introduced in materials are generally in the form of holes, blowholes, scars, edge cracks, inclusions and aluminium oxide lines. For other activities like technological operations, surface defects introduced into materials are in the form of thermal cracks, hangnails, shell surfaces, scales, rolls squeezes and scratches. These surface defects encountered during these technological operations result in the reduction of the mechanical properties of materials (Mišičko, et al., 2009). Other sources of surface defects seen in sheet metals after fabrication are usually some marks on the press tooling or rollers which are conveyed onto the sheet surface which produces differing effect on the attained surface finish (Wilby & Neale, 2009).

Existence of defects in sheet metal during forming provides all sort of difficulties in the design and manufacture of components. These issues are usually dealt with by employing the most economically efficient approach of either optimizing the sheet formability via controlling the defects or by improving the forming process itself. *'No matter whether deliberately created or inadvertently induced, notches and defects invariably exist in engineering components'* (Atzori, et al., 2003).

According to AutoForm, the major manufacturing obstacle causing delays in product development processes is the surface defect optimization (AutoForm News, 2015). The cost of producing materials with defects attributable to the production method employed and its

consequence on productivity is massive and could have detrimental effect not only on production but also on the integrity of formed products. According to Qamar et al., the potency of an aluminium extrusion plant during processing is a function of the extent to which surface defects can be drastically reduced (Qamar, et al., 2004). According to their work, rejected parts are usually linked to surface finish defects, post extrusion defects and other material and tool related defects. Their work also showed the press area defects in tonnage of the rejected extruded finished products as the most rejected over a 9-year period, Figure 2.7.

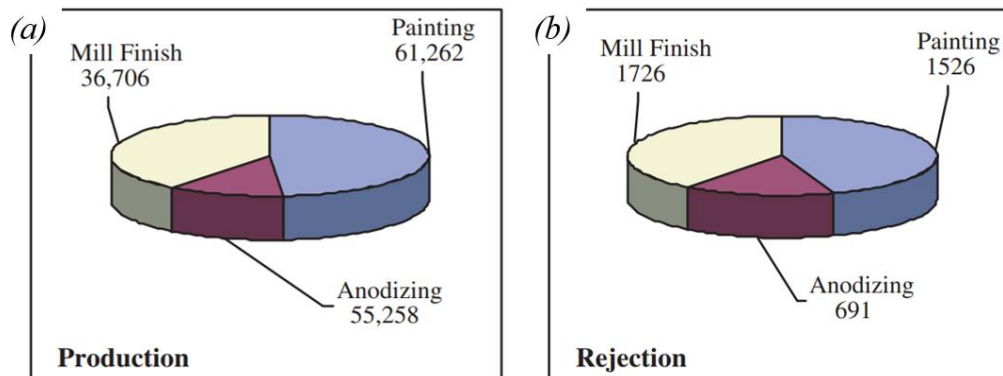


Figure 2. 7 Produced and rejected extruded parts in tons with specific defect zones (Qamar, et al., 2004)

(a) Total extruded production (b) total rejected extruded part

Defects observed in sheet metal forming can be categorised into three major groups, Table 2.1 (Levaillant & Chenot, 1992);

Table 2. 1 Classification of defects in sheet metal forming (Levaillant & Chenot, 1992)

Type	Impact	Major cause
Material dependent defect	extreme local thinning, crack, cavities in microstructure, Orange peel surface	Amount of deformation
Surface defect	Scratches	Bad friction condition
Mechanics dependent	Wrinkles, buckles	In-plane compression stress

Surface defects normally observed in sheet metals utilised for automobile body panels appear in the form of depressions, elevations, bimps, orange peel- like or local thinning, and are

manifested as minute deviations from the nominal surface panel with changing size and depth (Andersson, 2009). However, the ultimate defect in a formed sheet metal is the development of cracks, which destroys its structural integrity. The onset of surface cracking is a function of the inherent ductility of the component and the local stress, which are defined by the process variables. Defects during metal forming processes are undesirable due to the unsatisfactory appearance of product surfaces and the adverse effect they have on the strength and formability of components (Hayashi & Nakagawa, 1994). Defects may also be as a result of local necking, thinning, buckling or wrinkling in the region of compressive stress (Dieter, 1961). Other forms of defects may arise by virtue of the failure to maintain dimensional tolerance due to springback (Dieter, 1961). Kim et al., in their research on the hydroforming technique of aluminium tubes showed that the surface defects normally observed are buckling and wrinkling mainly because of plastic instability. According to their work, the severity of the wrinkles produced during this process generates stress distributions resulting in cracks from the die lines (Kim, et al., 2007). According to Wang et al., wrinkling and tearing are the main causes of failure during deep drawing of sheet metal parts (Wang, et al., 1994). According to their work, wrinkling is as a consequence of acting extreme compressive and tensile stresses resulting in fracture. Various sheet metal surface defects encountered in formed parts and how they could be avoided are enumerated in Table 2.2.

Table 2. 2 Defects in formed parts; derived from (Dieter, 1961)

Surface Defect	Description	Remedy
Wrinkling of flange/edge of cup	From buckling of sheet as a result of high circumferential compressive stress	Use sufficient hold-down pressure to suppress the buckling
Orange peel effect	Pronounced surface roughness in the region, which had undergone appreciable deformation. Mostly occurs in sheet metals with large grain size	Use finer grain sized sheet metal so that the grains deform more nearly as a whole.

Stretcher strains (worms)	<p>Surface defects found usually in low carbon steel sheet. Defect appears as a flame-like pattern of depressions in surface.</p> <p>Depressions appear first along the plane of maximum shear stress and as deformation proceeds, they spread and bond together to form the uniform rough surface.</p>	<p>Give sheet steel small cold reduction (0.5-2% reduction in thickness). Such a temper-rolling treatment cold works the metal to eliminate the yield point.</p>
Earing	<p>In deep drawing of cup, directionality shows in phenomenon called earing as wavy edge on top of the cup. Heights of ears vary directly with the degree of preferred orientation in the sheet.</p>	<p>Allowance for trimming ears from cup must be made when determining the size of the blank.</p>
Separation of cup bottom at location of greatest thinning near punch radius	<p>Occurs in deep drawing of cup</p>	<p>Reduce the thinning by using larger punch radius or decreasing the punch load required for the drawing operation.</p>
Radial cracks in flange/edge of cup	<p>Occurs in metals with insufficient ductility to withstand large amount of circumferential shrinking required in the region of the blank.</p>	<p>Redrawing with annealing.</p>

Microstructural activities have also been identified to be associated with the origination of surface defects in sheet metal processing. According to Zhao et al., surface roughness generated from microstructure can be classified as orange peel and ridging (Zhao, et al., 2004). According to their work, defects in sheet metals are generated as a result of;

- Heterogeneity of polycrystalline materials having grains exhibiting anisotropic elastic and plastic trends.
- Varying crystallographic orientation resulting in obstruction of grain boundary.
- Unsuitable deformation produced as a result of merger between surrounding grains.

During single point incremental sheet forming (SPIF) process of aluminium, the main defects observed are the generation of wall defects and the pillow defect (Hussain, et al., 2014). These defects are dependent on the stress ratio registered at the contact between the blank and the tool as well as the central bottom area of the component (Hussain, et al., 2014), Figure 2.8.

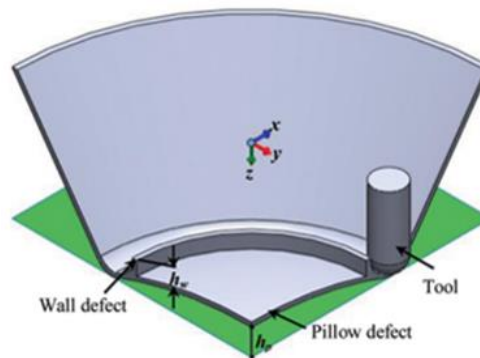


Figure 2. 8 Typical defects during SPIF process (Hussain, et al., 2014)

According to Hussain et al., common defects found during the SPIF of aluminium are bulge (pillow defects), squeezed out wall and corner-fold defects and these have severe impact on the formability as well as the geometrical accuracy of aluminium sheet components during the forming process (Hussain, et al., 2011), Figure 2.9.

One of the notable defects observed during press forming is wrinkling. Undesirable pressing could emerge as a consequence of instability in compression (wrinkling) to generate dimensional inaccuracies and unsuitable finished parts. Wrinkling in press forming is mainly due to elastic recovery happening during the unloading regime. Some studies have attributed the growth of wrinkles in sheet metals during press forming to the influence of material mechanical properties. Szacinski and Thomson in their work utilised the handkerchief test (Yoshida test) to study the impact of various sheet metals' (mild steel, titanium, brass, copper

and stainless steel) mechanical properties on their wrinkling tendencies. Their work showed that the initiation of wrinkles are enabled by strain rate, normal plastic anisotropy and yield strength. Their work also observed that wrinkles are impeded by Lüders strain, work hardening and positive strain rate sensitivity (Szacinski & Thomson, 1984).

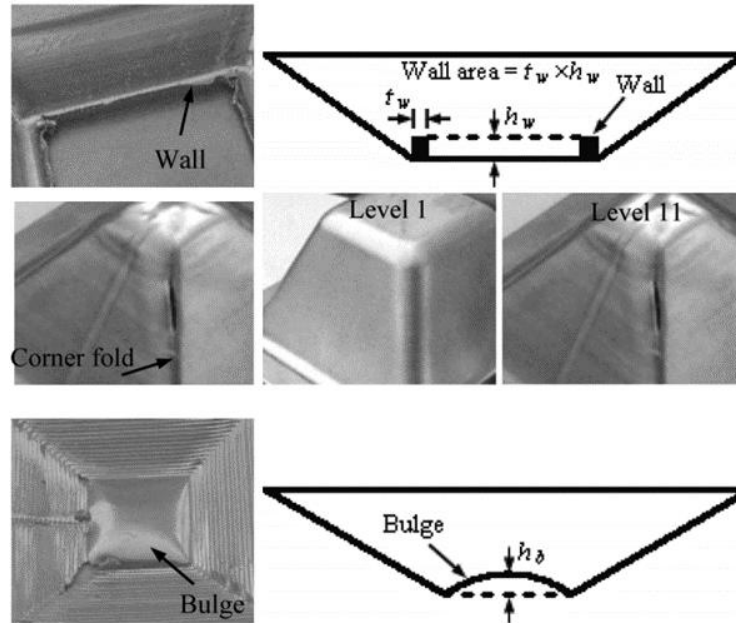


Figure 2. 9 Defects and their impact on AA-1060 aluminium sheet formability (Hussain, et al., 2011)

According to Szacinski and Thomson, the thriving and elimination of plastic wrinkles observed in carbon steels, austenitic stainless steels, aluminium and its alloys, titanium, copper, and 70–30 brass, together with the extent of wrinkles generated by elastic recovery are linearly responsive to the yield strength and the work hardening exponent of the metals during press forming (Szacinski & Thomson, 1991).

Various works have also shown that the effect of surface defects could be suppressed by adopting various optimisation methods. Work on the surface roughness morphology of cold rolled steel sheets treated with three coarsening processes (shot blasting texturing, electro-discharge texturing and laser texturing) before and after stamping showed that the sheets with uniform dispersion of micro-pits, large concave valley and smooth convex hull exhibited good forming performance (Tang, 2013). This implies that uniform distribution of surface asperities normally influences the forming properties positively.

Badr et al., after exploring the impact of various roll forming techniques on the quality of shapes attained during cold working of Ti-6Al-4V observed that the main defects obtained are

shape defects (bow and springback) (Badr, et al., 2018). Their work also showed that the shape defects during roll forming could be minimized by employing a constant radius forming technique.

Forming process designs like blank holding force (BHF) control technique and blank shape (die shape optimization) are crucial for the improvement of the quality of formed parts. Die shape optimization for sheet metal forming processes have also been reported to improve stamping qualities by minimizing the risk of rupture, wrinkles and unstretched areas (Shi, et al., 2004). Research work has also been done on the feasibility of developing an algorithm to establish a balance between the attainment of low BHF and the blank motion in order to study the effect of the temporal sustenance of wrinkles on the deep drawability of copper alloys (Yagami, et al., 2007). Their work showed that identifying the required wrinkle height to ignore at recoverable regions ($Cu < 200\mu m$) and the ones to reduce, will go a long way to minimising the extent of '*ductile damage accumulation*', thereby improving the deep drawability of copper alloys, Figure 2.10.

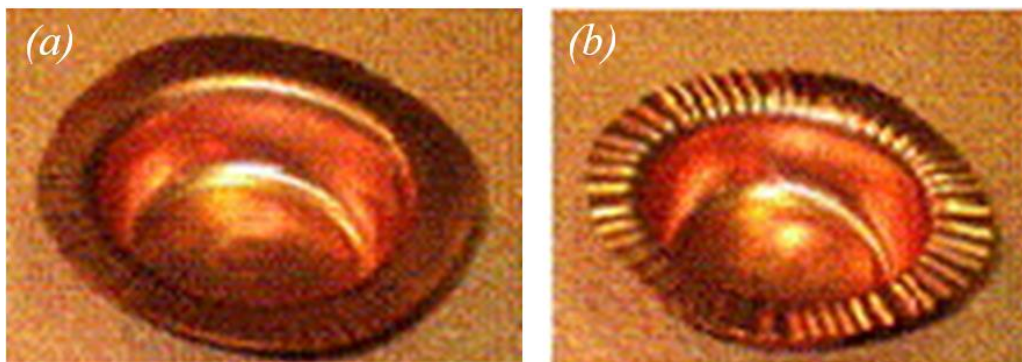


Figure 2. 10 Response of blank motion and BHF on wrinkle control and Cu-alloy deep drawability (Yagami, et al., 2007)

(a) Deep drawn sheet after wrinkle height reduction, (b) Deep drawn sheet with outgrown wrinkle height

Controlling the BHF is an essential criterion to resist wrinkling tendency as well as avoiding tearing of a blank sheet thereby enhancing the formability by improving part quality and increasing draw depth, Figure 2.11 (Obermeyer & Majlessi, 1998); (Ahmetoglu, et al., 1995). Furthermore, numerical methods proposed in some works are also utilised in optimising the onset of wrinkles around the die wall in unsupported regions of high strength steel (Wang, et al., 1994). According to Tomita and Shindo, the onset of wrinkling can be predicted by assuming the wrinkles to be the bifurcation of plane stress deformation to an out-of-plane bending type deformation (Tomita & Shindo, 1988). Their work also suggested that the growth

of wrinkles could be traced in terms of 3D shell analysis. Kim and Son, in their work showed that wrinkle limit diagrams could be employed to estimate various conditions responsible for the initiation of wrinkles in anisotropic materials exposed to biaxial plane stress (Kim & Son, 2000).

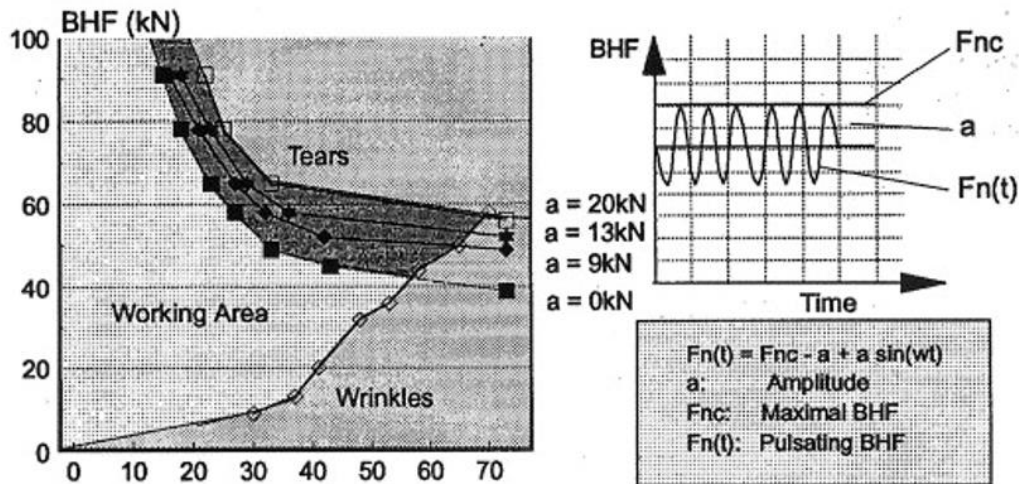


Figure 2. 11 Variation of BHF with punch displacement to avoid failure in zinc-coated and phosphated steel sheets (Obermeyer & Majlessi, 1998)

Numerical analysis conducted by Lee et al., on the evaluation of stress during aluminium extrusion process has shown that a rigorous stress analysis of the forming process plays a vital role in the estimation of the nucleation of sheet forming defects in the form of (Lee, et al., 1977);

- The inception of interior or surface fractures (cracks).
- Inception of local instabilities resulting in local strain peaks, as well as
- Generation of excess residual stress.

According to Song et al., high-density electropulsing treatment meted out on titanium alloys has the tendency of improving their workability tremendously by way of imposing thermal compressive stresses (Song, et al., 2007). According to their work, defects like micro-cracks, cavities and voids as well as others forms of impurities present on TC4 titanium alloys can be sealed during this treatment by way of thermal expansion caused by the electric current, thereby improving the cold formability of the titanium sheet metal.

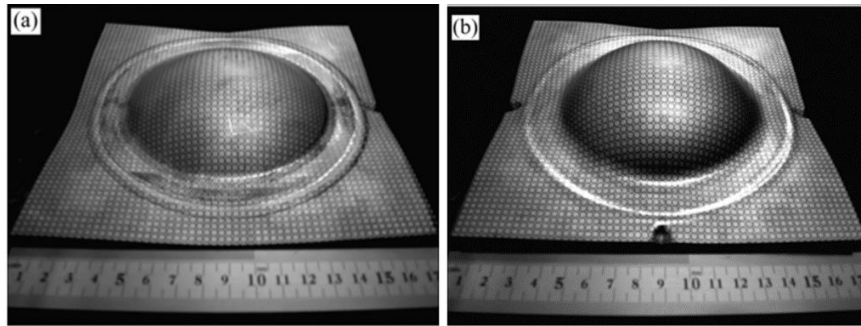


Figure 2. 12 Limiting dome height of TC 1 Ti- sheet metal enhanced by 31.8% after double sided bulging pressure (Wang, et al., 2008)

(a) Traditional one-sided pressure bulging, (b) Double-sided pressure bulging

Double-pressure mechanism adoption during pressure bulge testing has also been reported to be very instrumental towards the enhancement of the formability of titanium alloys at room temperature (Wang, et al., 2008). According to their work, the hydrostatic pressure adopted in this technique is capable of restricting micro-crack growth in TC1 titanium alloys, thereby minimising their non-equilibrium development. This serves as an impediment to failure hence improving the workability of the titanium sheet metal, Figure 2.12.

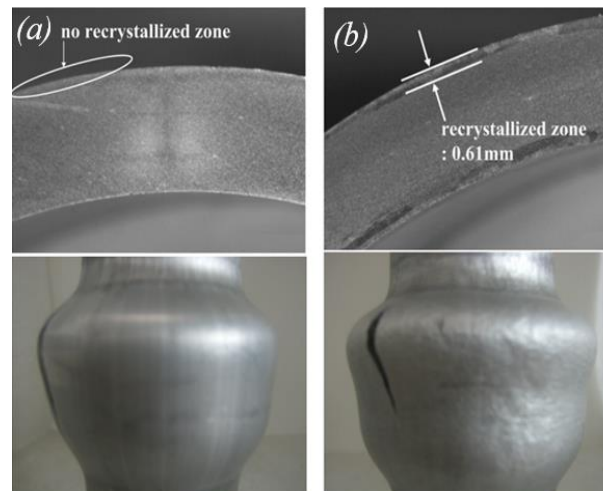


Figure 2. 13 Effect of metallurgical variable on defect formation in Aluminium alloys during forming (Kim, et al., 2007)

(a) No presence of orange peel in AA6082 alloy, (b) presence of orange peel in AA6061 alloy
 Adoption of conventional metallurgical methods have also been suggested to be an effective means of optimising the impact of defects during sheet metal forming. Research conducted by Kim et al., on the extrusion of AA6082 and AA6061 aluminium alloys has shown that higher volume fraction of alloying elements in AA6082 (Mn and Cr) plays a vital role in obstructing grain growth and recrystallization from occurring in this alloys thereby effectively suppressing

the nucleation of orange peel defect during extrusion. Conversely, the presence of lower alloying elements coupled with the presence of recrystallized regions in AA6061 resulted in the generation of orange peel during the forming process (Kim, et al., 2007), Figure 2.13.

Kim et al., also recognised that AA6061 aluminium with coarse grains also have the tendency of developing mottled surface after pressing process. The high variations in the response of the grains to plastic deformation can be ascribed to the random nature of the grain orientation. This phenomenon largely results in the non- uniformity of their surfaces thereby introducing the orange- peel defect in the material (Kim, et al., 2007), Figure 2.14.

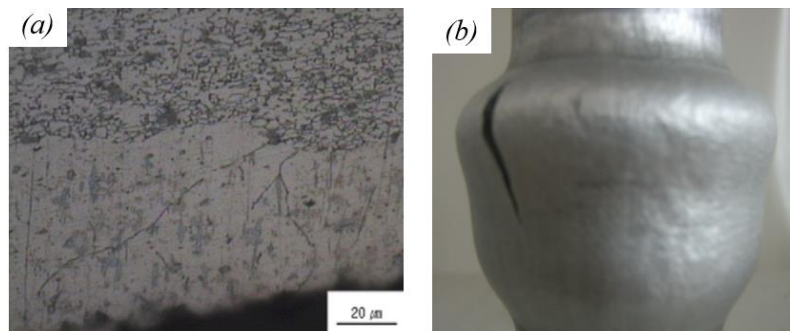


Figure 2. 14 Limited formability of AA6061 due to orange peel defect, (a)AA6061 edge surface with coarse grains, (b) AA6061 tube with orange peel (Kim, et al., 2007)

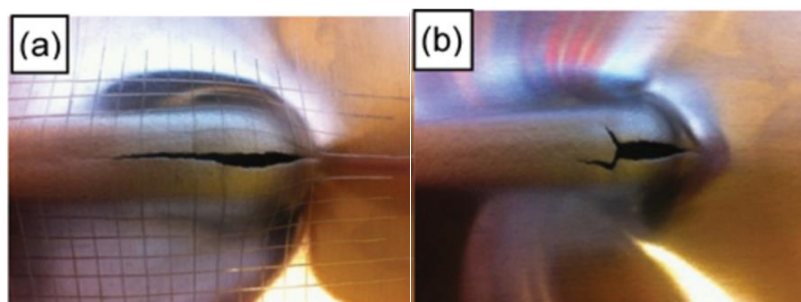


Figure 2. 15 Influence of different tool diameters on the nature of fracture at the end of grooves in AA 7075-O aluminium sheet (Li, et al., 2014)

(a) 30mm large ball tool producing monodirectional failure, (b) hemispherical tool producing bi-directional failure

A research conducted by Li et al., on the impact of contact interface on the ISF of AA7075-O aluminium sheet metal shows that an increase in the tool diameter is responsive to the fracture depth at the end of the grooves (Li, et al., 2014), Figure 2.15. Their work also showed that higher values of tool diameter results in the enhancement of the formability of aluminium

alloys with the limitation of geometrical complexity. Their research concluded that rolling contact situations results in the least local damage and scratches on the surface of the AA7075-O aluminium sheet metal (Li, et al., 2014).

Industrially, the high cost incurred in correcting post- production surface defects has led to the formulation of various optimization techniques such as; the one-shot deflectometry technique based on the Fourier- transform method (Sárosi, et al., 2010), development of a genetic algorithm which relies on extreme machine learning (Tian & Xu, 2017), convolutional neural network system for recognition and detection (Tao, et al., 2018) and an image thresholding method based on automated vision systems (Lohade & Chopade, 2016). These optimization systems were designed to aid in the inspection and detection of surface defects on sheet metal surfaces during production.

2.3 Machinability of Titanium

Titanium alloys are extensively utilised in the aviation sector largely on account of their high level of strength to weight ratio, elevated fatigue strength, elevated temperature strength, high fracture toughness and corrosion resistance (Pervaiz, et al., 2014). However, the difficulty in machining posed by titanium makes it cumbersome to work its parts (Churi, et al., 2007). The poor machinability of titanium is attributable to their low values of thermal conductivity, strength at extreme temperature as well as reduced elastic modulus (Colafemina, et al., 2007). Thermal conductivity plays a massive role in the machining capability of metals. The rise in thermal conductivity with increasing temperature enhances cutting by way of the heat removal rate as well as the amount of machining force required (Veiga, et al., 2013). Titanium and its alloys exhibit low machinability as a result of their poor thermal conductivity (see Table 2.3) compared to steels (60-30W/mK) and aluminium alloys (170-240W/mK at 0-600⁰C) (Veiga, et al., 2013). The thermal conductivity of CP-Ti remains stable with increasing temperature compared to its alloyed counterparts, Table 2.3.

Table 2. 3 Thermal conductivity with increasing temperature of titanium (Veiga, et al., 2013)

Temperature [°C]		0	200	400	600	800
k [W/m.K]	Pure-Ti	22	21	21	21	-
	$\alpha / \alpha+\beta / \beta$	5.5-8.0	8.0-12.0	10.0-17.0	12.5-21.0	15.0-25.0

Hence, titanium when arranged according to decreasing order of machinability will follow the trend from CP-Ti, α -Ti, α + β -titanium and finally β -titanium being the most laborious to machine (Yang & Liu, 1999). In terms of mechanical properties, a decline in elastic modulus also makes parts more prone to deflection and vibration during cutting hence unappealing (Veiga, et al., 2013).

Various researches have been conducted on the possibility of cutting titanium and its alloys (Veiga, et al., 2013); (Armendia, et al., 2010); (Arrazola, et al., 2009); (Ezugwe, et al., 2003). Titanium susceptibility to surface deterioration during cutting results in poor surface finish. Titanium also sticks fervently to common tool materials thereby producing high friction and also provoking the possibility of damaging the surface as a consequence of deformation as well as the formation of built-up edge (BUE) (Ramesh, et al., 2008). Other issues that impede the machining potential of titanium and its alloys are summarised in Table 2.4.

Table 2. 4 Issues inhibiting the machinability of titanium, derived from (Donachie, 1988)

Factors	Description
Poor heat conduction	Heat produced during machining does not penetrate into the material but stays on the edges and surface of the tool
Chemical reactivity	Titanium's immense ability to react chemically with machining tools at working temperature results in issues like galling, welding as well as quick deterioration of the machining tool. Its high affinity to oxygen and nitrogen could also grant the hardening of the surface.
Easy surface integrity deterioration	Grinding and other methods makes titanium susceptible to surface damage which affects its fatigue properties
Strain hardening	Non- existence of BUE due to strain hardening features of titanium alloys. Due to the absence of BUE, a massive shearing angle is produced leading to several

	mechanisms which results in quick tool deterioration.
--	---

According to Pramanik and Littlefair, improvements in the fabrication of titanium alloys relies mainly on surmounting the complexities related to ingrained alloy properties (Pramanik & Littlefair, 2015). According their the work, vibration analysis kit, hybrid machining, high pressure coolants, thermally enhanced machining, cryogenic cooling as well as the utilisation of conductive cutting tool holders improves the machinability of titanium alloys.

Chips formed during the cutting of titanium and its alloys follows the discontinuous chip principle and are characterised by serration, shear localization, discontinuity, segmentation and cyclic attributes. Hardened steels also show similar traits under the same chip principle when machined under certain cutting conditions (Yang & Liu, 1999). For the formation of shear-localised chips in titanium alloys, different surfaces partake in the formation process, Figure 2.16 (Komanduri, 1982).

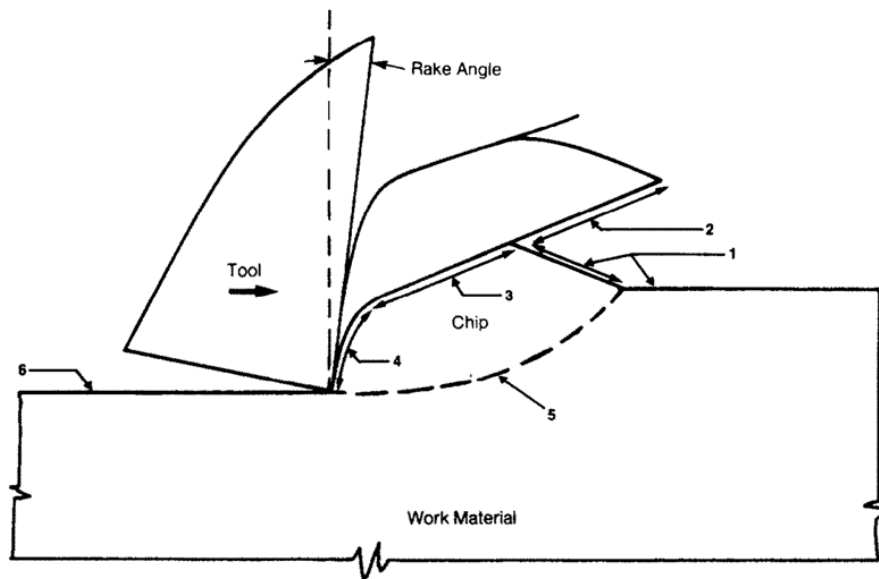


Figure 2. 16 Schematics of mechanism of shear localised chip formation in titanium alloys (Komanduri, 1982)

1. As-received material surface.
2. Aspect of sheared surface by catastrophic failure which are detached from the following parts as a results of intense shear.

3. Catastrophic shear resulting in intense shear band produced at the upsetting level of parts being made.
4. Intensely sheared surface of part in touch with the tool and eventually sliding on surface of tool.
5. Primary shear region which experiences intense localised deformation.
6. Final cut surface.

The widely agreed chip formation mechanism for titanium and its alloys is attributable to thermoplastic instability as well as adiabatic shear banding (Veiga, et al., 2013), Figure 2.17.

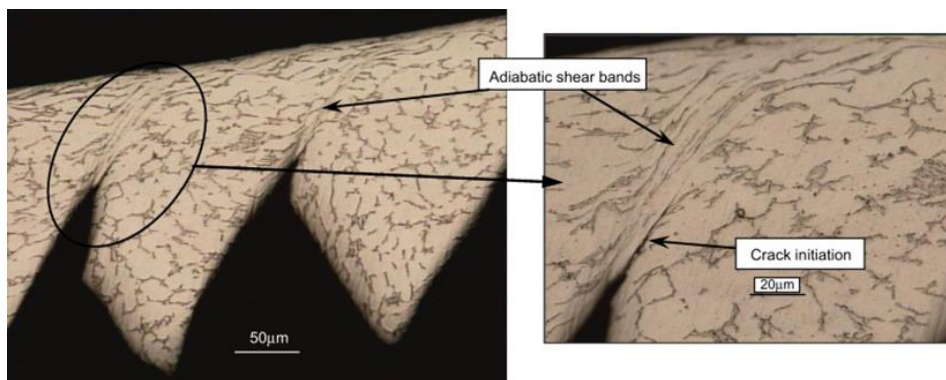


Figure 2. 17 Chip formed after orthogonal machining of Ti-6Al-4V (Calamaz, et al., 2008)

The roughness of a component surface is instrumental in evaluating the machining accuracy and machined surface integrity. Even though many conditions affect the quality of machined component surfaces, machining parameters have been shown to have a drastic effect on the roughening of machined component's surface. The deployment of polycrystalline diamond (PCD) cutting insert to cut titanium (Grade-5) alloy revealed that there was an increase in the roughening of the surface as the machining tempo increased with the feed rate, but declined with decreasing approach angle as well as the cut depth, Figure 2.18 (Chuahan & Dass, 2012). According to their work, this could be credited to the increase in the chip friction effect, which resulted in the nose radius of the tool having a higher stress and temperature.

Machining test carried out using chemical vapour deposition (CVD)-coated carbide insert to machine $\alpha+\beta$ titanium alloy (Grade 5) also showed that the roughening observed at the surface was linearly responsive to the feed rate increase but declined with the cut depth (Ramesh, et al., 2008), Figure 2.19. This observation was attributable to the increase in thermal loading as well as machining tool vibration. Their results also inferred that feed rate is the major determinant of surface roughness in titanium alloys.

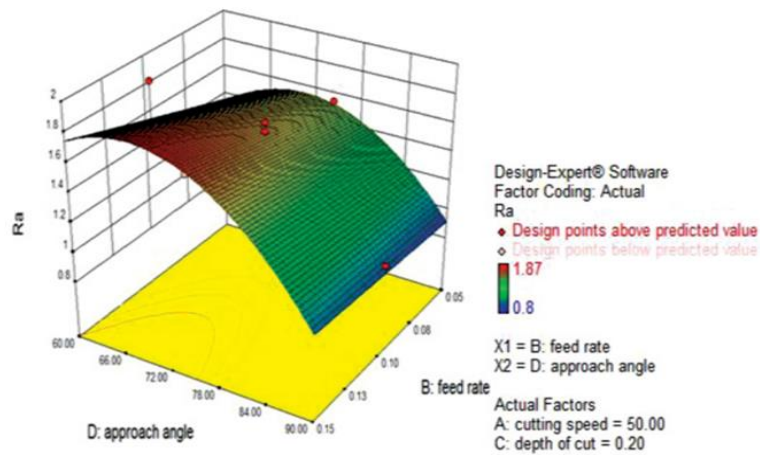


Figure 2. 18 3D reaction of surface roughness to approach angle and feed rate (Chuah & Dass, 2012)

Fuzzy modelling technique adopted to study machining parameters in Ti-6Al-4V titanium alloys showed that the surface finish increased with rising speed of cut due to the absence of BUE formation at higher speed (Ramesh, et al., 2008). According to their work, an increase in the feed rate resulted in an increase in roughness of the part surface on the score of generation of more heat.

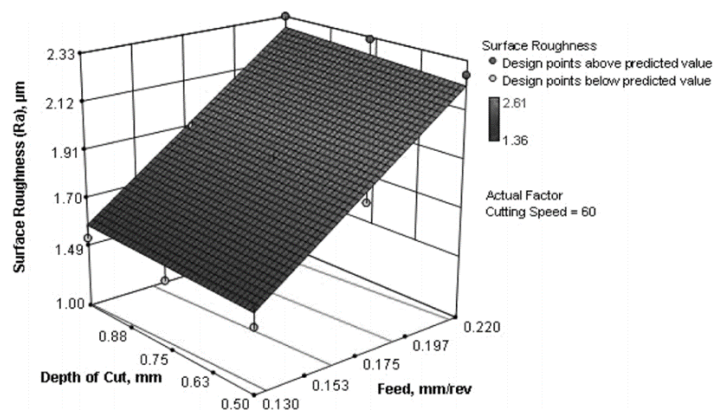


Figure 2. 19 3D reaction of surface roughness to cut depth and feed rate (Ramesh, et al., 2008)

Turning test with straight grade cemented carbide tool conducted on Ti-6Al-4V showed that the roughness of the surface increased as the cutting speed increased until the tool life is terminated (Che-Haron & Jawaid, 2005).

Furthermore, some research works have also demonstrated that utilising different cutting techniques to machine titanium alloys results in varied impact on their surface qualities. A work done by Adamus on the machinability of WT1-0 titanium (Russian grade) sheet using guillotine, laser and AWJ cutting methods revealed varying surface integrity (Adamus, 2007).

The work reported that AWJ machined titanium surface is characterised by tracks produced by virtue of the path travelled by the water jet which drives the abrasive dust via the material. Surfaces produced using guillotine possess scratch- like tracks, which are formed parallel to the cutting force direction. The work also showed that the laser cut surface compared to the other two methods studied produced a smoother surface quality, Figure 2.20.

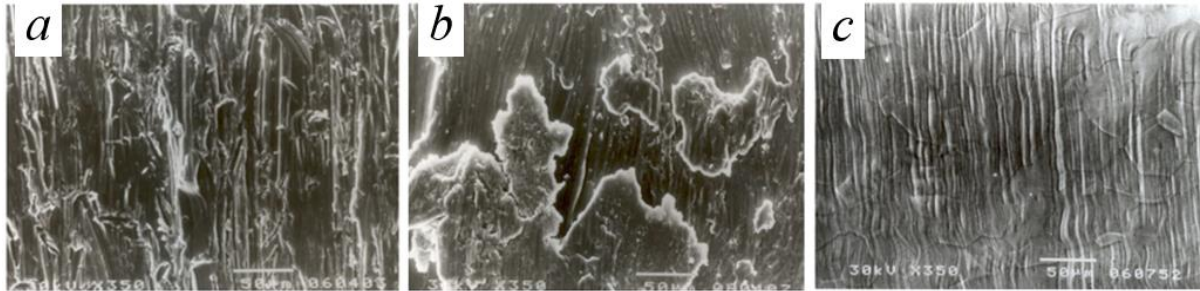


Figure 2. 20 Surface morphology of WT1-0 titanium when cut with different machining methods (Adamus, 2007)

Surface quality after (a) AWJ, (b) laser cutting, (c) guillotine cutting

The idea of altering the properties of titanium before cutting to enhance their machinability has been explored by some researchers. The electric pulse treatment (EPT) has been reported to be suitable for enhancing the properties of titanium alloys for the onward ease in machining tendencies.

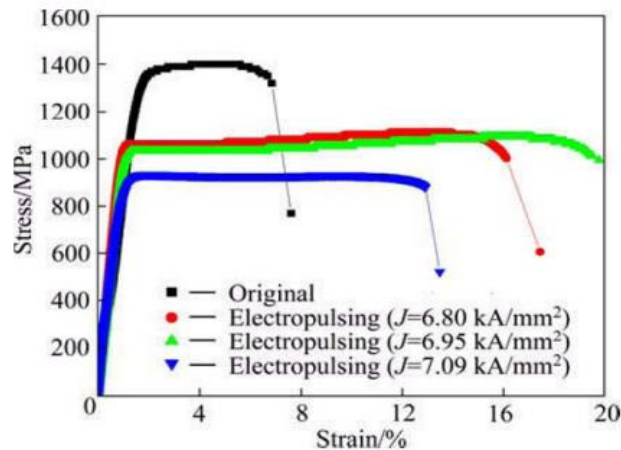


Figure 2. 21 Typical stress-strain graph of Ti-22Al-27Nb sheet after EPT (Song, et al., 2013) According to Ye et al., the EPT treatment of Ti-6Al-4V alloy strips if employed in the solid solution state, results in the enhancement of its elongation to failure drastically at peak by 225% whilst maintaining the tensile strength almost constant (only 6.5% decrease) juxtaposed that of the untreated alloyed strips (Ye, et al., 2015). According to Song et al, EPT treatment of Ti-

22Al-27Nb sheet has the ability to increase the workability and enhance the plastic tendencies of the titanium alloy, Figure 2.21 (Song, et al., 2013).

Some works have also examined the machinability of EPT treated titanium alloys. According to Wu and To, EPT treatment can be used to alter the mechanical attributes of Ti-6Al-4V in order to enhance their machinability during ultra-precision cutting (Wu & To, 2016). According to their work, machinability of the titanium alloy is improved when the current density as well as the EPT frequency is increased. Their work also inferred that EPT treatment is a suitable technique for reducing the machining force as well as enhancing the quality of machining in titanium alloys.

Machining results in surface defects in the form of local changes in the microstructure on the machined surfaces and sometimes those beneath the cut surfaces. Some common surface integrity defects encountered when cutting titanium alloys are summarised in Table 2.5.

Table 2. 5 Major surface defects during titanium machining; derived from (Pervaiz, et al., 2014)

Defect	Description
Carbide cracking	Carbide particles from coating remove during machining and rubs against the newly generated machined surface. Residual cavities as well as cracks introduced on the surfaces of machined parts are as a result of carbide cracking.
Microstructure changes	Various material property mechanisms interact during cutting. Microstructure of components change resulting in variations in material property.
Occurrence of white layer	Occurs where the hardness features of the machined surface of a material is greater than that of the full volume. The layer is found to be normally brittle as well as hard and has massive effect on the fatigue life of parts due to them promoting crack growth.

Work hardened layer formation	Strain hardened layers are formed due to the machining process. The occurrence of this phenomenon on the surface layer of a component makes its fabricability cumbersome due to the hard layer.
Residual stress	As a result of high load applied to surfaces during cutting thereby increasing temperature in the cutting zone. Residual stress creates conditions for crack nucleation and growth hence having a massive impact on the fatigue strength of parts.

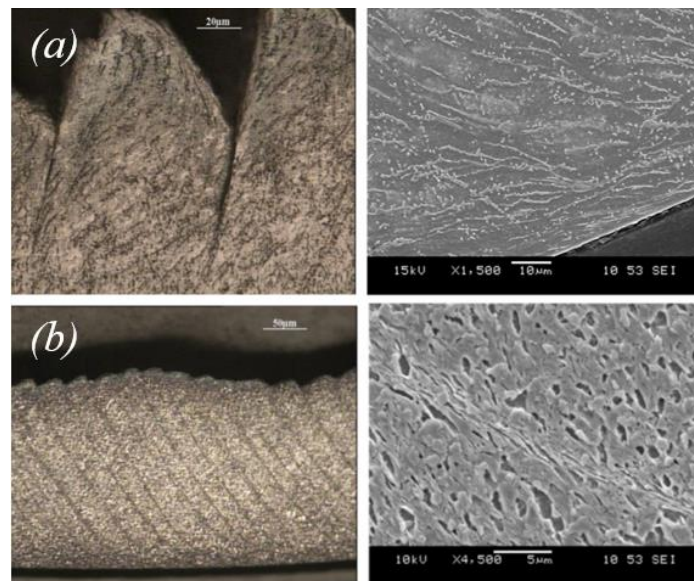


Figure 2. 22 Microstructure effect on chip formation in titanium alloys (Nouari & Makich, 2013)

Nature of chips obtained in (a) Ti-6Al-4V and (b) Ti-555

Some works have also shown that the nature of titanium microstructures could have a significant impact on the tool wear mode attained during a given machining process. Nouari and Makich conducted research on the impact of the microstructures of Ti-6Al-4V and Ti-555 alloys on tool wearing of cemented cutting (Nouari & Makich, 2013). Their work showed that the wear mode observed in Ti-555 is characterised by abrasion wear as a result of its fine

microstructure (grain size; 1 μ m). According to their work, the wear mode observed in Ti-6Al-4V were adhesion and diffusion modes after which coating delamination process occurred due to its coarse size microstructure (grain size; 10 μ m). These variations also influence the nature of chip formation evolution in both materials, as shown in Figure 2.22.

Notable failure modes encountered when cutting titanium alloys includes (Ezugwu & Wang, 1997);

- Flank wear (due to dissolution-diffusion, attrition and plastic deformation which are a function of the machining condition and tool material).
- Crater wear (factors same as flank wear).
- Notch wear (as a result of fracture process and/or chemical reaction).
- Chipping and
- Catastrophic failure.

2.4 Effect of alloying and mechanical properties on machinability

Different types of materials respond disparately to various machining methods due to variations in their chemical composition and mechanical properties. Leskovar and Grum in their work examined the impact of alloying on the machinability of steels in terms of chip formation, machining force, wear and roughness (Leskovar & Grum, 1986). Their work indicated that the addition of Mg, S, P and Pb are favourable while the addition of Si, Al, Ti, O, Ni and Co are detrimental to the machining ability of steels. Aluminium alloys are faster to machine and can be machined more economically compared to pure aluminium due to the complex nature of their metallurgical structure (ASM Handbook: Machining, 1989). According to Zheng and Liu, when considering the impact of material properties on their machinability, optimum machining capability are attained when there are reduced effects of ductility, strain hardening and abrasiveness (Zheng & Liu, 2015). According to Şeker et al., ductile irons due to their superior strength, ductility and toughness properties have poor machinability compared to flake graphite cast iron (Şeker, et al., 2003). Studies with Ti-4.5Al-4Cr-0.5Fe-0.15C employed as a base alloy with decreasing Al and Cr content revealed that substituting Cr with Mo and/or Fe enhances the machinability of the material (Murakami, et al., 2011). According to Arrazola et al., near β alloys (Ti555.3) are more laborious to machine compared to Ti-6Al-4V due to their equivalent

Mo content and the differences in microstructure. The equivalent Mo of the near β alloys examined was almost 8 times higher than those used for the Ti-6Al-4V alloy (Arrazola, et al., 2009). According to their research, the equivalent Mo content enhances the tensile strength and hardness under aging conditions.

2.5 Impact of surface roughening and defects on fatigue properties

Defects produced during cutting processes act as stress inducers thereby reducing the fatigue and fracture resistance of parts. Surface roughness has a strong correlation to fatigue resistance. Rough surfaces are usually characterised by many notches, which provides an enabling condition for fatigue crack nucleation, propagation and growth.

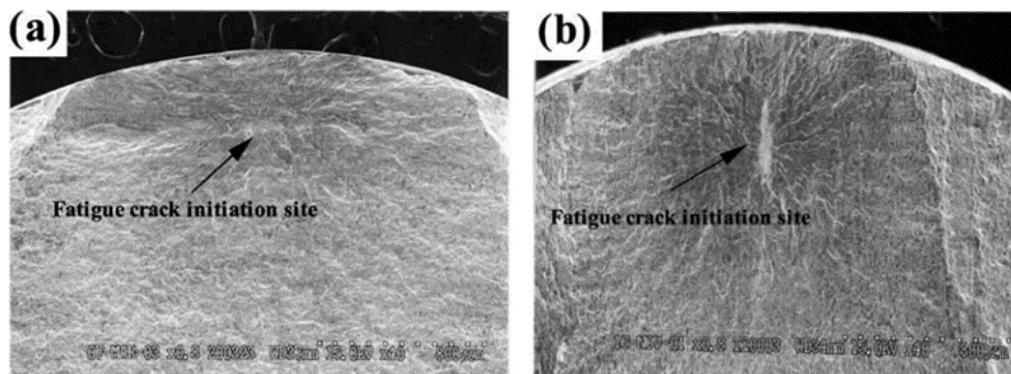


Figure 2. 23 Variation of fatigue crack nucleation site with surface integrity (Yuri, et al., 2003)

(a) Surface produced with #600 emery paper, (b) Surface produced with #100 emery paper

The consequence of surface roughness on fatigue properties have been researched in several works (Yuri, et al., 2003); (Alang, et al., 2011); (Suresh & Ritchie, 1982). Different surface finishes produced by various machining processes have appreciable effect on the fatigue performance of components. Fatigue failure depends on surface integrity hence any factor which influences the fatigue strength of the surface also changes the fatigue properties.

The effect of surface conditions on the fatigue behaviour is a result of the overriding impact of surface roughness. Work done by Yuri et al., on Ti-5Al-2.5Sn ELI alloy revealed that the variation in location of fatigue crack nucleation site in the material is a function of the nature of the surface integrity and fatigue strength values produced, Figure 2.23 (Yuri, et al., 2003). According to their work, samples with notched surfaces (rougher surfaces) produce lower fatigue strength compared to the other lower surface roughness samples.

Alang et al., in their work also examined the impact of surface roughness (prepared with emery paper grit #600, #400 and #100) on the fatigue life of carbon steels after cantilever rotating bending fatigue test (Alang, et al., 2011). Their work observed that the amount of crack nucleation zones are highest for rougher surface specimen thereby acting as stress raisers leading to the reduction in crack initiation life. Their results also revealed that the number of cycles to failure observed for surfaces with finer roughness are higher compared to those observed for samples with coarser surface roughness, Figure 2.24.

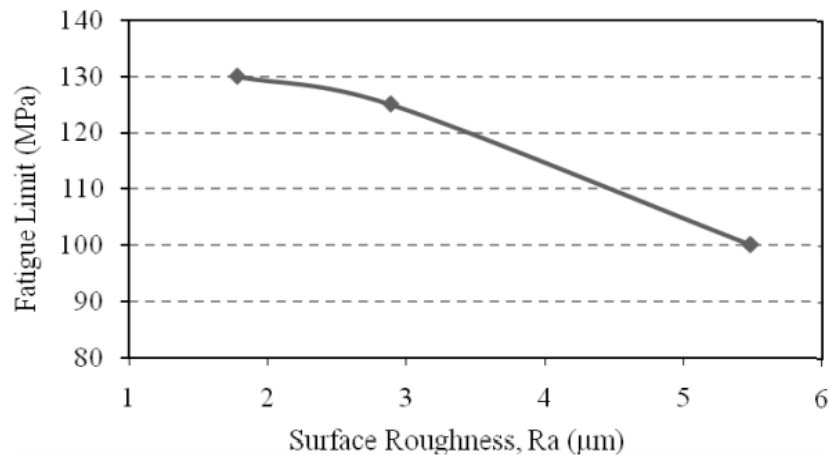


Figure 2. 24 Surface roughness response to fatigue behaviour (Alang, et al., 2011)

Generally, poor surface quality may result in notch- effect crack initiation and subsequent reduction in the fatigue strength of notch-sensitive materials. Factors that promote component surface fatigue response includes (Dieter, 1961);

- i. Stress raisers.
- ii. Variations in fatigue strength of part surface.
- iii. Variations in component surface residual stress.
- iv. Surfaces subjected to oxidation and corrosion.

2.6 Surface roughness and amplitude parameters

For a given machined part, the surface integrity is an intrinsic behaviour which is a consequence of the cutting conditions. They also constitute the prime denotation for describing the appearance of processed surfaces of components. Generated machined surfaces can be described by their texture. The surface texture of machined surfaces are normally expressed by way of their roughness and waviness. Three features are prescribed to define surface states

(Suraratchai, et al., 2008); geometrical parameters (surface roughness), mechanical parameters (residual stress) and metallurgical parameters (microstructure). These surface states vary depending on the machining conditions and parameters.

The quality of the surfaces produced after machining is of major interest in most manufacturing processes. The integrity of surfaces produced after machining is visibly depicted by its surface roughness morphology. Surface roughness is characterised by waviness, ridges and valleys, which provides quantitative knowledge of the texture of the related surface, Figure 2.25 (Liu, et al., 2014). Surface roughness can serve as an indicator for part mechanical performance since it can provide information about the nature of component failure. The degree of surface roughening can be evaluated based on the profile of the surface.

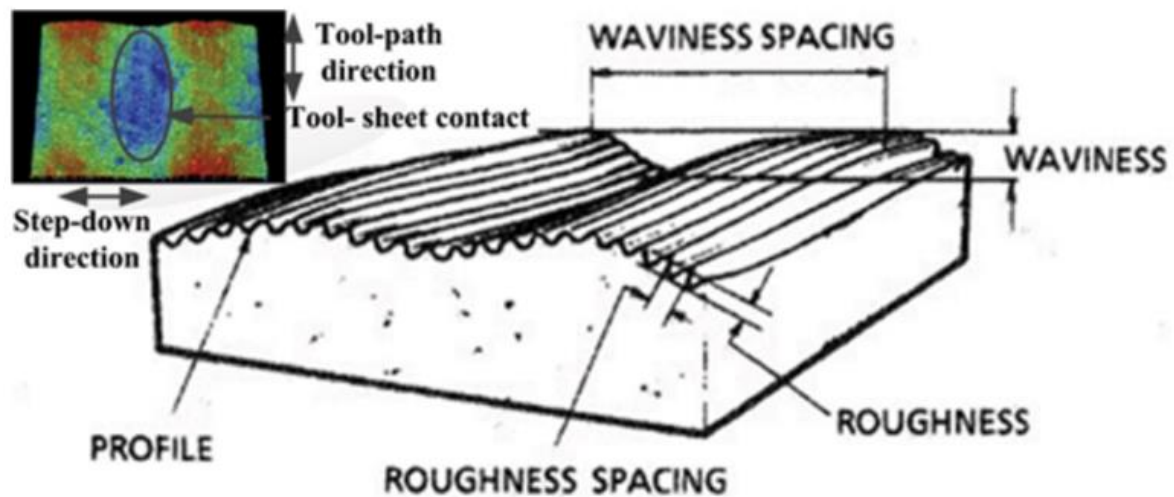


Figure 2. 25 Surface roughness features (Liu, et al., 2014)

Usually, the topography of surfaces are accounted for by determining the amplitude parameters, and are described by the vertical features of the surface variations (Gadelmawla, et al., 2002). Some amplitude parameters are described in Table 2.6.

Table 2. 6 Surface roughness amplitude parameters, extracted from (Gadelmawla, et al., 2002)

Designation	Description	Equation
R_a	Arithmetic average height: other times called centre line average is a largely adopted measure for quality control	$R_a = \frac{1}{l} \int_0^l y(x) dx$ $R_a = \frac{1}{n} \sum_{i=1}^n y_i $

R_q	Root mean square roughness: shows the surface height distribution standard deviation. It utilises statistical techniques to define the surface roughness	$R_q = \sqrt{\frac{1}{l} \int_0^l \{y(x)\}^2 dx}$ $R_q = \sqrt{\frac{1}{n} \sum_{i=1}^n y_i^2}$
$R_{z(ISO)}$	Ten- point height: height disparity between midpoint of 5 tallest peaks and 5 shortest valleys down the computed length of profile	$R_{z(ISO)} = \frac{1}{n} \left(\sum_{i=1}^n P_i - \sum_{i=1}^n V_i \right)$
R_{pm}	Mean height of peaks: mean of maximum height of peaks (R_p) gotten for individual sampling length of measured length	$R_{pm} = \frac{1}{n} \left(\sum_{i=1}^n R_{pi} \right)$
R_{vm}	Mean depth of valley: mean of maximum depth of valley (R_v) gotten for each sampling length of the assessment length	$R_{vm} = \frac{1}{n} \left(\sum_{i=1}^n V_i \right)$
R_{Ku}	Kurtosis: describes the preciseness of the probability density of the profile	$R_{Ku} = \frac{1}{R_q^4} \int_{-\infty}^{\infty} y^4 p(y) dy$
R_{Sk}	Skewness: utilised to assess the symmetry of the profile about the midpoint line	$R_{Sk} = \frac{1}{R_q^3} \int_{-\infty}^{\infty} y^3 p(y) dy$

2.7 Types of Machining Methods

For a given machined part, the quality of the surface produced is essential to ascertaining the service life, which are normally hindered by factors such as fatigue failure. The advent of difficult-to-machine novel engineering materials coupled with the quest for better surface finish, cumbersome design prerequisites as well as complex and intricate part fabrication requirements has limited the reliance on traditional machining (milling, boring, turning, slotting, grinding, etc.) routes. This has resulted in the pursuit of modern approaches capable of addressing the shortfalls in employing traditional cutting methods.

Non-conventional machining techniques also referred to as advanced machining processes (AMPs), are adopted to address the deficiencies encountered when using traditional machining methods. For non-conventional machining techniques, contact is non-existent between the cutting means and the components. In recent times, AMPs deployed in industry includes; electro discharge machining, beam machining and its subsidiaries, electrochemical machining, laser and electron beam machining, chemical machining processes and its subsidiaries, ultrasonic machining (USM), abrasive waterjet cutting technique and the associated likes (Dubey & Yadava, 2008).

This EngD research focused mainly on three non-conventional machining techniques; electric discharge machining, abrasive water jet cutting and laser machining methods. These machining methods were used mainly due to their wide adoption in industry and their ability to produce better surface finish qualities compared to traditional machining.

2.8 Electric discharge machining

During electric discharge machining (EDM), the tool electrode and the component are not in contact but immersed in a dielectric. The discharge energy produced in the form of a spark transfers very high temperature onto the surface of the component at the point of contact. Surfaces produced by EDM are characterised by numerous discrete discharges acting along the tool electrode and the component surface. EDM technique is used in a vast range of conductive materials. The main surface defects observed after EDM machining are shallow craters, pockmarks, voids, globules of debris, uneven fusing structure and cracks (Zeilmann, et al., 2013).

Some works have attributed the surface defect evolution encountered during EDM cutting to the influence of thermal gradient (Rebeloa, et al., 1998); (Lin, et al., 2001); (Lee & Li, 2003). According to Rebeloa et al., the predominant feature of an EDM cut surface of a martensitic steel is micro-cracks, which are produced as a consequence of the evolution of extreme thermal stresses outweighing the ultimate tensile strength of the material (Rebeloa, et al., 1998). According to Lin et al., the poor surface integrity of EDM machined 6061Al/Al₂O₃p/20P aluminium metal matrix composites are attributable to the incomplete flushing away of molten parts resulting in their re-solidification to form discharge craters. Their work inferred that micro-cracks and pores in EDM machined surfaces are attributable to high temperature gradient (Lin, et al., 2001). According to Lee and Li, crack formation in tungsten carbide during EDM cutting is the manifestation of extreme thermal stresses acting, greater than the fracture strength and plastic deformation of the component (Lee & Li, 2003).

2.8.1 Impact of EDM machining parameters on material surface integrity

The quality of surfaces produced by EDM machining method are documented to be a function of the parameters selected for the surface preparation. Surface roughness produced after EDM cutting of AISI D2 tool steel (Guu, et al., 2003) and Ti-6Al-4V (Hascalik & Caydas, 2007), are responsive to the intensity of the spark produced as well as the craters size produced during the cutting process at various ranges of pulse time and discharge current. According to Zeilmann et al., variations in surface morphology in terms of the surface roughness attained for steels after EDM cutting evolves with varying machining parameters due to the extent of heat produced by the electric discharge on the part surface (Zeilmann, et al., 2013), Figure 2.26. According to their work, surface roughness increases with increasing pulse-on current and duration.

Typical evaluation of surfaces after EDM of carbon steel (AISI-I 045) and tool steel (AISI-D2) by Taguchi Approach also revealed that roughness of the surface is influenced by the pulse-on current and duration as well as the material type (Lee & Yur, 2000). According to Lee et al., EDM cutting of AISI 1045 carbon steel using copper–tungsten electrode as a tool revealed that the surface roughness increases with increasing pulse-on current as well as the pulse-on duration but deteriorates for prolonged pulse-on duration (Lee, et al., 2004).

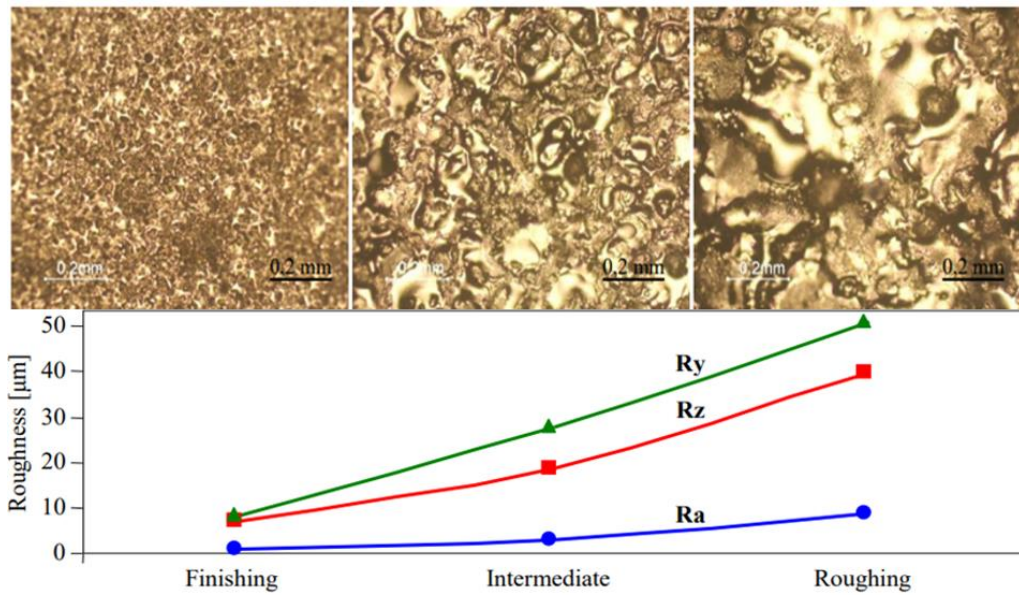


Figure 2. 26 Response of steel surface roughness and texture to EDM cutting parameters (Zeilmann, et al., 2013)

According to Guu, the roughening of an AISI D2 tool steel surface produced after EDM method is responsive to the power applied but the technique induces tensile residual stress onto the machined part (Guu, 2005). According to the work, using an atomic force microscopy (AFM) technique on the EDMed part revealed that the roughness of the surface produced and the micro-crack depths on the surface were as a result of the power input. According to Rebeloa et al., EDM machining of martensitic steels shows that the surface roughness and the crack density on the surface increases with increasing pulse energy (Rebeloa, et al., 1998). A new rotary EDM machining technique for fabricating difficult-to-machine cylindrical AISI D2 tool steel also showed that the roughness of the surface deteriorated with increasing rotation speed and pulse on duration (Guu & Hocheng, 2001). Their work concluded that component turning could minimise the formation of micro-voids and defects on the EDM machined surfaces, Figure 2.27. According to Zeid, EDM machining of AISI D6 tool steel results in the surface cracks depth increasing with increasing discharge energy. Their work also showed that the depth of cracks are synonymous with the material thickness realised for each cutting damage. The roughening conditions are also revealed to correspond to high current fixture and pulse on period leading to further surface defects and ultimately to a substantial decrease in the fatigue life of the material (Zeid, 1997).

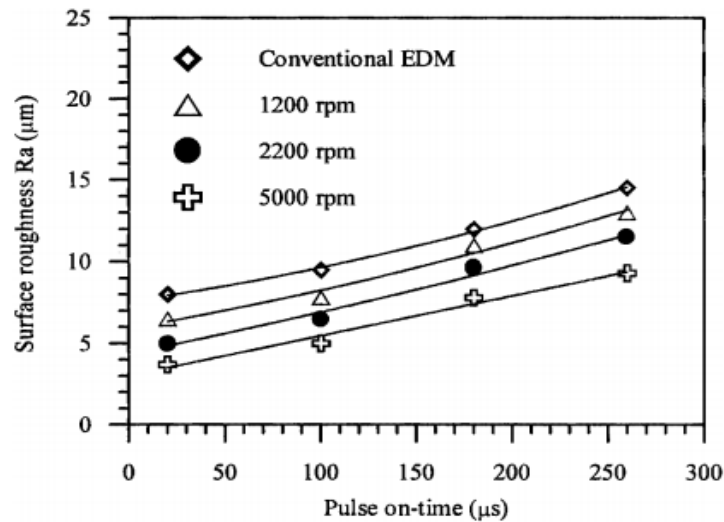


Figure 2. 27 Influence of pulse on-period on tool steel surface roughness at various cutting speeds (pulsed current 10A) (Guu & Hocheng, 2001)

According to Guu et al., EDM machining of AISI D2 tool steel induces defects (pinholes, micro-voids and craters) onto the surface layer, which appear as ridged surfaces thereby causing damage across the top face layer (Guu, et al., 2003). According to their work, roughening of the material increases with increasing pulse current and period. According to Merdan and Arnell, the depth of micro cracks formed at the surface of a die steel, increase with the pulse energy during an EDM process (Merdan & Arnell, 1989). According to Kumar et al., in their work on the density values of top face crack at different peak current-pulse on duration of pure titanium during wire EDM showed that the highest values of these variables created excessive thermal state in the cutting region and subsequent swift cooling, which resulted in high crack densities (Kumar, et al., 2013).

The dielectric forms a very vital facet of an EDM set up. Some researchers have reported on the significant roles that a dielectric plays in the edge surface quality evolution of EDM machined surfaces (Yan, et al., 2005); (Lin, et al., 2000); (Chen, et al., 1999). According to Lin et al., the surface roughness of Ti-6Al-4V when EDM is combined with ultrasonic machining (USM) process whilst utilising kerosene as a dielectric is more effective compared to the adoption of distilled water due to the superior cooling rate of water (Lin, et al., 2000). According to Chen et al., a large quantity of detritus and micro cracks are obtained when distilled water is used as a dielectric compared to kerosene during an EDM machining of Ti-6Al-4V alloy (Chen, et al., 1999). According to their work, EDM surfaces usually have flaws of micro cracks and pores occurring mainly as a result of the massive temperature gradients observed during the process. These surface defects result in abysmal surface quality and

reduced service life of parts. Yan et al., in their work studied how to improve the surface of pure titanium by utilising urea mixture placed in water to serve as a dielectric in an EDM process (Yan, et al., 2005). According to their work, when the urea mixture was employed as the dielectric, a deterioration of the surface roughening occurred with an increase in peak current. Although a surge in the peak current proliferated the discharge energy and the impulsive force, additional flowing material was removed hence triggering deeper and a more colossal discharge craters. Thus, the surface roughening became scratchier.

The nature of the wire used in EDM processes have also been shown to have a significant impact on the attained surface quality of titanium alloys. Farnaz et al., in their work demonstrated the effect of brass and Zn coated brass wire on the surface quality of Ti-6Al-4V alloy. According to their work, the better surface quality produced by the Zn coated brass wire after EDM machining are attributable to their high thermal conductivity as well as the low melting temperature of Zn employed for the coating (Farnaz, et al., 2013).

Table 2.7 describes the surface morphology response of various materials to varying pulse current and the pulse duration time during EDM machining.

Table 2. 7 Impact of EDM process variables on surface asperities

Material	EDM Parameter	Surface asperity response
Tungsten carbide (Lee & Li, 2001)	Increasing pulse current and duration	Increased surface roughness
Fe-Mn-Al alloy (Guu & Hou, 2007)	Increased pulse current and duration	Increased surface defects (micro-cracks, micro-voids, machined damage)
Tool steel (Kiyak & Cakir, 2007)	Increased pulse time and current	Increased surface roughness
Tool steel (Keskin, et al., 2006)	Increased discharge duration	Increased surface roughness

According to Lee and Li, the density of cracks increase with increasing peak current and pulse period during an EDM machining of tungsten carbide (Lee & Li, 2003).

Hascalik and Caydas in their work also studied ways of improving the surface roughening of an EDM machined Ti-6Al-4V surface in order to enhance its surface integrity (Hascalik & Caydas, 2007). According to their work, poor edge quality results in lower formability capacity. Hence, using abrasive electro-chemical grinding (AECG) to post-treat an EDM surface significantly enhances the surface roughening and removes EDM destructions entirely by adjusting the cutting parameters (Hascalik & Caydas, 2007).

2.8.2 EDM induced microstructural changes

Microstructure of EDM machined surfaces are complex, varied depending on the material and differs from that of the bulk materials. However, they are typically classified into three distinct sections; the outermost part that melts (white layer), the intermediate heat affected zone (HAZ) layer in which the heat is quite not elevated amply to melt but effectively induces microstructure transformation and the parent material. Several research works have shown that significant microstructure transformation occurs on the surface and subsurface layer of various materials after EDM machining (Cusanelli, et al., 2004); (Ghanem, et al., 2002); (Ghanem, et al., 2003); (Strasky, et al., 2011). Research has also shown that, the metallurgical transformation of the surface layer results in the reduction of the fatigue performance of EDM machined parts (Strasky, et al., 2011); (Ghanem, et al., 2002). According to Kumar et al., a typical surface layer after EDM machining consist of, Figure 2.28 (Kumar, et al., 2009);

- Upper white layer which at high speed crystalizes from cooled liquid.
- The upper melt zone with depth which is a function of the pulse energy and machining time.
- Beneath the top layer zone is the region of chemically impacted layer with variation in chemical constituent and likely phase transformation.
- Below this region is an observed zone of plastic deformation accompanied by micro and macro strains marked by the existence of slip, twins as well as phase variation.

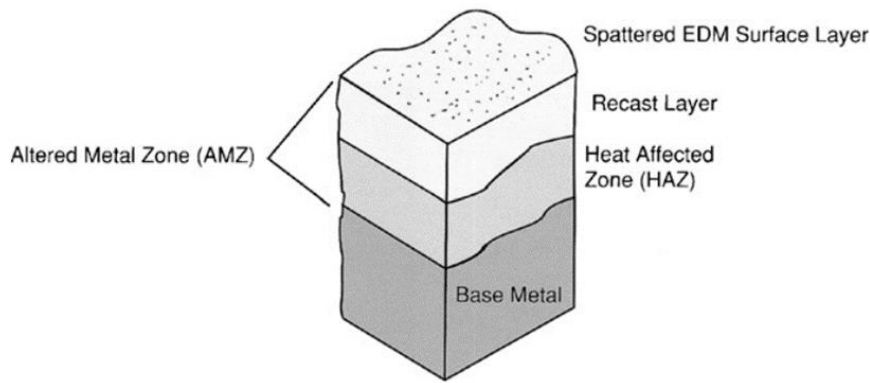


Figure 2. 28 Schematic of a typical surface layer after EDM cutting (Kumar, et al., 2009)

According to Zeilmann et al., the constituents of recast layers in steel materials after EDM machining are usually iron carbide in various forms, dispersed over the austenitic matrix and completely isolated from the base material as well as the electrode type, Figure 2.29 (Zeilmann, et al., 2015).

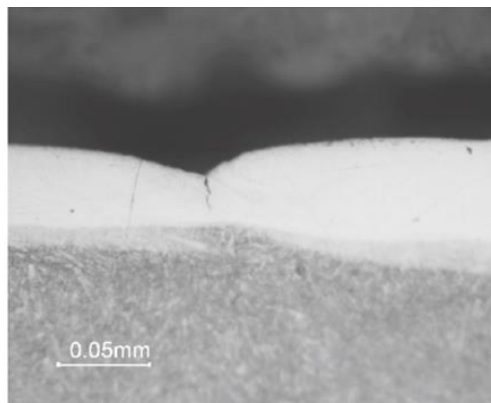


Figure 2. 29 Surface layers after EDM machining of AISI P20 steel (Zeilmann, et al., 2015)

To guarantee the enhancement of the surface roughening properties, it is important to understand the impact of the machining parameters on the microstructure transformation in the white layer and the subsurface of EDM machined components. According to Guu et al., the thickness of the recast layer of an EDM machined surface of AISI D2 tool steel increases with increasing pulse on duration and current (Guu, et al., 2003), Figure 2.30. According to Merdan and Arnell, the depth of an EDM machined damage observed in die steels can be equated to the thickness of their recast layer (Merdan & Arnell, 1989). According to Ekmekci, the major element material properties and white layer constituents of steels after EDM machining have a peculiar effect on crack generation, which results in varying crack focal point layouts on the surface and perforating depths in the substrate (Ekmekci, 2009). According to their work, crack

perforation depth is commensurate with the registered pulse energy and the cracks inside the white layer are generated mainly as a result of the non-homogeneity of the white layer.

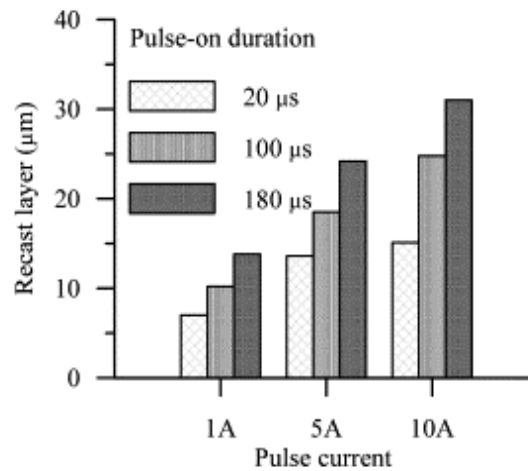


Figure 2. 30 Recast layer thickness at various EDM conditions (Guu, et al., 2003)

2.9 Abrasive water jet machining

Another commercially adopted non-traditional cutting technique for fabricating sheet metals is the abrasive water jet (AWJ) machining. It involves cutting a component via utilising a thin water jet operated under high pressure and the incorporation of abrasive slurry for nicking the target component by way of erosion. The cut surfaces obtained are by interactions with abrasive particles transported in an extremely high-pressure water jet.

AWJ machined surfaces generally can be grouped according to the surface texture (exterior) as well as the surface integrity (interior), Figure 2.31, and the size of the abrasive particles play a vital role in the morphology of the attained surface finish (Hashish, 1991).

There are three main mechanisms observed during the AWJ machining of metals (Arola & Ramulu, 1997);

- Plowing
- Rubbings
- Microchip formation.

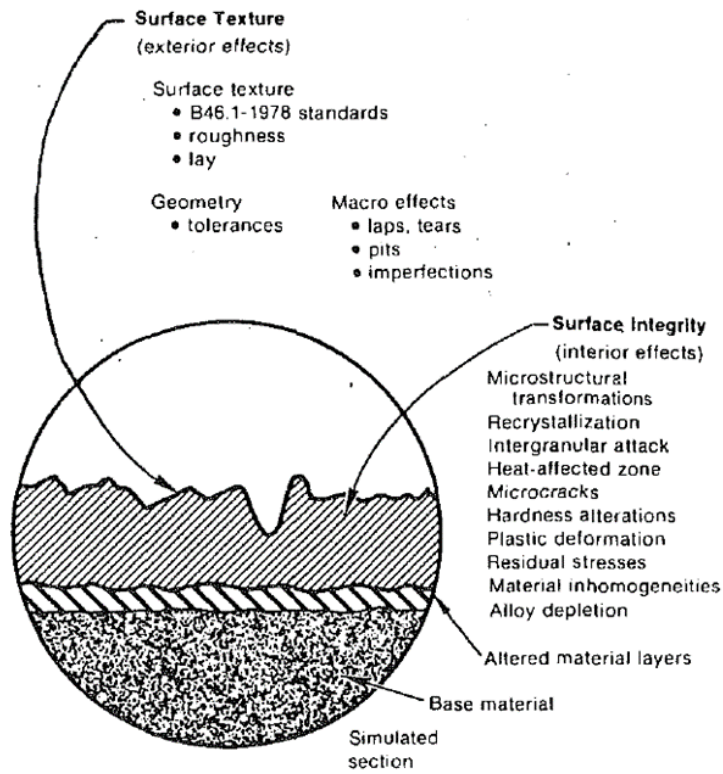


Figure 2. 31 Surface effect after typical AWJ cutting (Hashish, 1991)

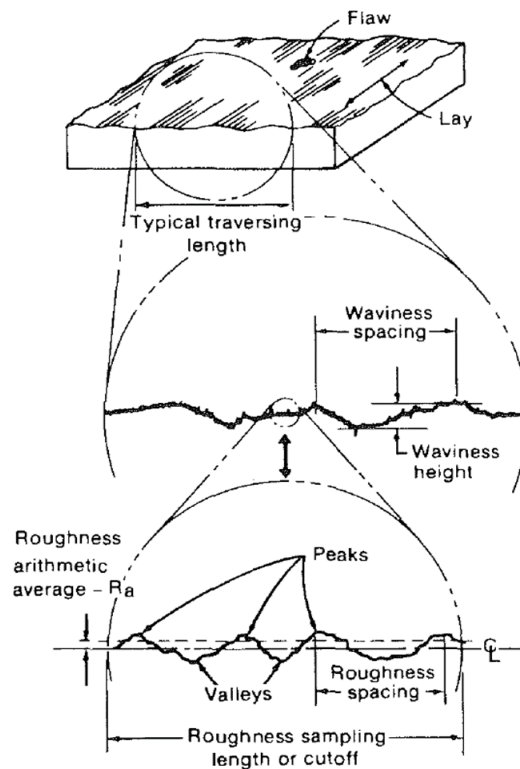


Figure 2. 32 Surface texture features (derived from ANSI B46.1-1978) (Hashish, 1991)

The pre-eminence of any of the mechanisms is influenced by the mechanical attributes of the components and the angle through which the abrasive is directed.

Generally, surface texture features are based on the surface roughness (peaks, valleys and spacing) as well as their waviness (height and spacing) which describe generic features based on ANSI B46.1-1978 standards of a typical traversing length of a cut component, Figure 2.32 (Hashish, 1991).

Furthermore, for AWJ machined surfaces low cut depths are normally characterised by cutting wear. With increased cutting depth, the material removal mechanism transforms and are described by the deformation wear which occurs via cyclic cutting actions resulting in wavy surface texture which distinguishes the two wear zones (Arola & Ramulu, 1997), Figure 2.33.

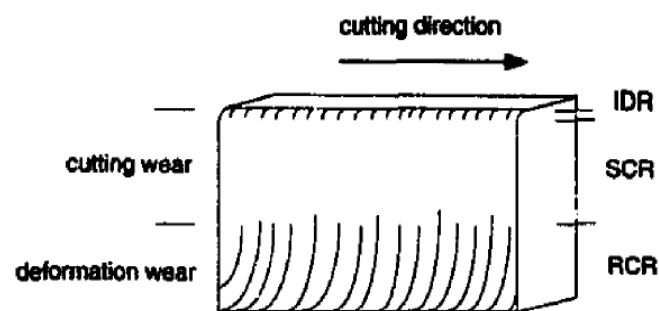


Figure 2. 33 Macroscopic features of AWJ machined surface (Arola & Ramulu, 1997)

According to Hashish, a cutting wear is formed when abrasive particles hit the cut surface at an insubstantial angle whereas the deformation wear occurs when the abrasive particles are incident at a higher impact angle (Hashish, 1984).

Ramulu et al., in their work on AWJ machinability of AA 7075-T6 aluminium alloy identified three distinct macroscopic regions (Ramulu, et al., 2000);

- IDR (initial damage region)
- SCR (smooth cutting region)
- RCR (rough cutting region)

Ramulu et al., also revealed that the material removal mechanism after AWJ machining of the AA 7075-T6 aluminium alloy is shear deformation (Ramulu, et al., 2000). According to their work, the major distinction in the microscopic features are attributable to the material removal in the SCR and RCR zones due to amplification of the jet deflection with its angle increasing with depth. The IDR zone shows appreciable deformation tendencies due to the almost normal iteration impact of the abrasives on the jet periphery. The IDR zones exhibits the highest degree

of deformation with little or no disfiguring within the SCR and the RCR zones due to the minute grinding assault angles at those zones (Ramulu, et al., 2000), Figure 2.34.

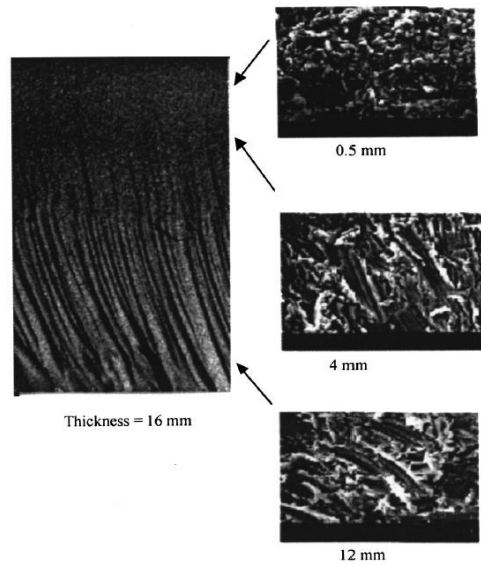


Figure 2. 34 Microscopic attributes of three cutting zones on the AWJ cut surface of Al 7075-T6 alloy (Ramulu, et al., 2000)

According to Chao et al., water jet machining produced for steel, stainless steel and titanium surfaces are partitioned into featureless and striation regions, where the striation effect is infinitesimal in the smooth region, Figure 2.35 (Chao, et al., 1995). Their work noted that the smooth region has an arbitrary isotropic texture with the height spread almost Gaussian. Their work also inferred that unavoidable vibration of the mechanical feature enormously affects striations provoked in the water jet cutting system.

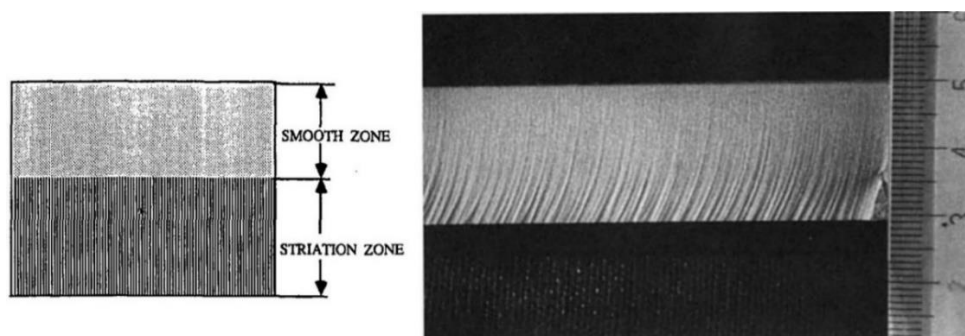


Figure 2. 35 Two cutting zones of AWJ machined surface (Chao, et al., 1995)

Material property response to AWJ machining have been explored in some works. An experimental studies on the material property response of metals (AISI 4340, Mo, Monel 400, AISI 304 and Ti-6Al-4V) to AWJ machining showed that strain hardening and subsurface deformation does occur after AWJ cutting of metals (Arola & Ramulu, 1997). Their work also

found that the degree of deformation is a function of the work hardening tendencies of the metals as well as the angle through which the abrasives are applied. Their work also showed that the plastic deformation depth is inversely proportional to the strength coefficient of the metals after AWJ cutting.

According to Tabatchikova et al., AWJ results in hardening of the surface layer near the cut surface of AMg6 alloy, with X-ray diffraction (XRD) results showing pronounced plastic deformation (Tabatchikova, et al., 2017). According to their work, transmission electron microscopy (TEM) results revealed structure transformation in the alloy with multiple slip bands and the presence of intermetallic phases after AWJ machining of the AMg6 alloy.

2.9.1 Effect of AWJ machining parameters on surface morphology

Machining parameters have significant impact on the edge surface integrity of materials after AWJ machining. The transverse cutting speed is registered in several works to influence the surface roughness tendencies of materials. A work done to experimentally assess the influence of transverse speed on the AWJ cutting of Inconel 718 nickel-based superalloy revealed that the surface roughening as well as the kerf taper ratio of the alloy increased with transverse speed but decreased with kerf width (Ay, et al., 2010). According to Begic-Hajdarevic et al., AWJ machining of aluminium revealed that the surface roughening is responsive to the abrasive mass flow rate and the transverse speed (Begic-Hajdarevic, et al., 2015). Thomas in a research on AWJ machining of high strength steels observed that the technique of garnet aggregate shot peening induces imperfections on the cut edge surface with their volume and profile having influence on the hardness of the cut edges (Thomas, 2009). Their work also concluded that the transverse machining speed is responsive to the cut-edge roughening attributes as well as the surface and near-edge microstructure of the high strength steels.

Transverse speed of AWJ machining is suggested in some works to influence the cut depth zone evolution of machined parts. Hascalik et al., in their work on the AWJ machining of Ti-6Al-4V alloy showed that the surface roughness remains constant with cut depth in the SCR zone (Hascalik, et al., 2007). According to their work, the transverse speed of AWJ increases with decreasing kerf width hence plays a massive role in ascertaining the depth of the SCR, Figure 2.36.

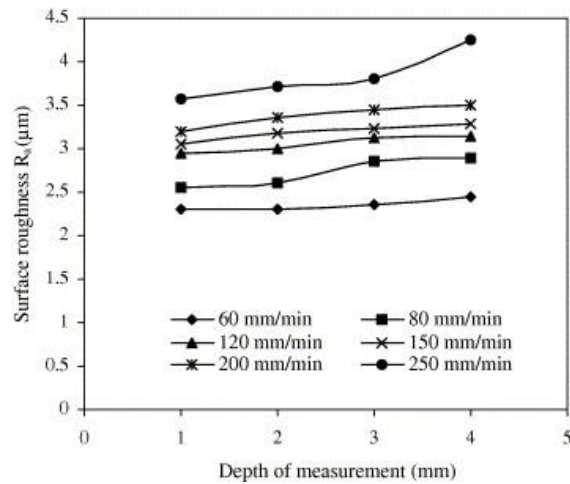


Figure 2. 36 Surface roughening versus assessed depth for varying traverse speeds (Hascalik, et al., 2007).

According to Chao et al., roughness parameters of steel, titanium and stainless steel after AWJ machining increases rapidly with increasing cutting depth and machining speed for striation region of the AWJ machined surface (Chao, et al., 1995). Their work also showed that for the smooth zone, the roughening parameters increase gradually with machining speed but have infinitesimal impact on the depth of cut.

Analytical studies done by adopting artificial neural network (ANN) in addition to a regression model to forecast parameters affecting surface roughening in AWJ cutting of AA7075 aluminium alloy showed that water jet pressure has the paramount impact on surface roughening with surface striation and waviness increasing with increasing jet pressure (Caydas & Hascalik, 2008).

Akkurt et al., in their work also studied AWJ machining in pure aluminium, AA-6061 aluminium alloy, brass-353 ($\alpha+\beta$ brass), AISI 1030 and AISI 304 steel materials (Akkurt, et al., 2004). According to their findings, the pressure of the AWJ produces negative effects with respect to surface roughening as the thickness of the component reduces. In addition, the surface roughness decreases with increasing sheet thickness. According to their work, high strength of materials command high machining force between the cutting means and the component interface. Hence, deformation effects of AWJ increases on thinner intersections and destroys the surface quality. Their work concluded that deformation effects of AWJ is responsive to pressure and the feed rate (Akkurt, et al., 2004).

2.9.2 AWJ induced microstructural changes

No HAZ is associated with surfaces machined with AWJ hence no microstructure transformation occurs during the cutting process. The cut surface is normally characterised by trails of wear and friction caused by the abrasive particles fired at extreme speed during the cutting period (Zhoa & Guo, 2014).

Generally, striation formation is one major feature of AWJ cutting. Several researches have been directed at understanding the mechanism of striation formation. However, the real origin of striation formation is still unclear but appears to vary between materials and the machining processes. According to Monno and Ravasio, striation production is a consequence of jet instability during the cutting process (Monno & Ravasio, 2005). Studies by Chen and Siores on alumina ceramics revealed that striation formation in AWJ is mainspring by the "*wavy abrasive particle kinetic energy distribution*" associated with the machined portion (Chen & Siores, 2003). According to Orbanic and Junkar, for AWJ machining of polymethyl methacrylate (PMMA), striation evolution is the outcome of perturbations on the cutting front, which causes the deflection of the jet flow (Orbanic & Junkar, 2008). According to Chen et al., sources of striation formation during AWJ cutting includes the manner of the step formations exclusive to the jet machining process, the dynamic features of the water jet as well as the vibration of the machining system (Chen, et al., 2003).

A comparative analysis of the quality of the cut surface produced between laser cutting and AWJ cutting are also examined in some works. Research conducted on titanium ASTM B265-99 (Zelenak, et al., 2012), carbon steel (Alsoufi, et al., 2016), epoxy pre-impregnated graphite woven fabric and fibre reinforced plastic (Shanmugam, et al., 2002) as well as on a review conducted by (Krajcarz, 2014) suggested that AWJ produces a better surface quality compared to laser machined surfaces.

2.10 Laser machining process

Laser cutting is a thermal non-contact machining process capable of cutting to high precision. The heating, melting and evaporation during the process influences the component surface. Surface roughness and material removal rates of laser cutting process improves tremendously compared to conventional machining (Attia, et al., 2010); (Xavierarockiaraj & Kuppan, 2014). Laser assisted cutting of tool steel SKD11 have significantly less impact on the tool wear

compared to traditional cutting with physical vapour deposition (PVD) coated ceramic tool (TiN) (Xavierarockiaraj & Kuppan, 2014), Figure 2.37.

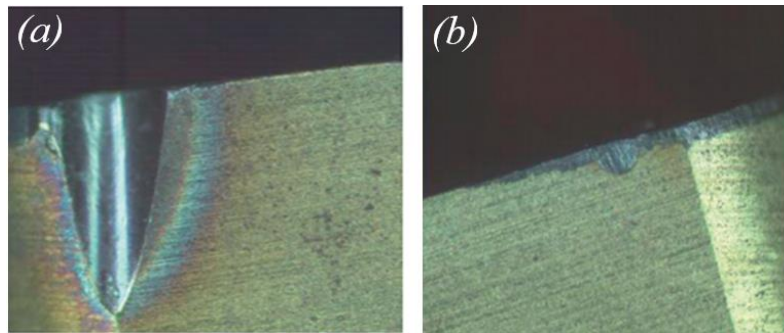


Figure 2. 37 Comparison between laser assisted cutting and traditional cutting effects on tool wear (Xavierarockiaraj & Kuppan, 2014)

(a) Traditional cutting effect on tool wear, (b) laser assisted cutting impact on tool wear Meurling et al., in their work on carbon and stainless steel sheets reported that mechanical machining results in lesser fatigue strength compared to laser machining, due to the presence of larger surface defects on the cut surface edges (Meurling, et al., 2001).

Ridges that emerge on a laser cut surface are as a result of the combined influence of laser pulses as well as high pressure assisted gas. According to Shanjin and Yang, employing air and nitrogen aided laser technique to machine titanium alloys could result in the occurrence of micro cracks as well as reduction in part surface quality (Shanjin & Yang, 2006). Their work attributed this impact to the oxygen and nitrogen embrittlement of the machined surface. According to their work, utilising argon produces surface with better quality finish, Figure 2.38.

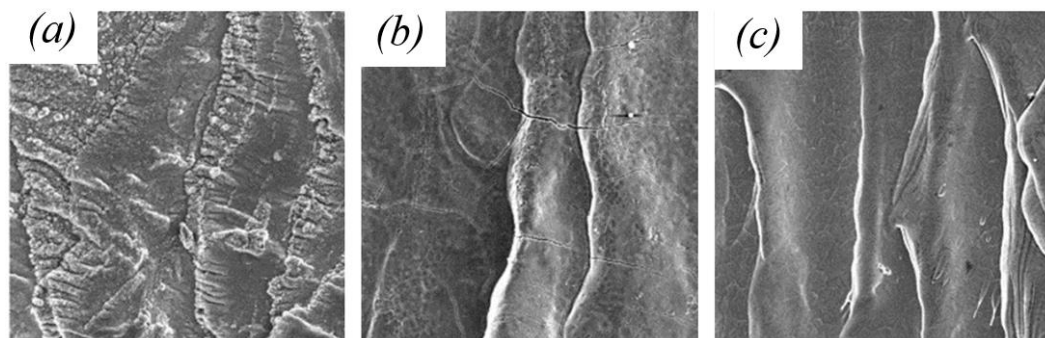


Figure 2. 38 SEM of the impact of pulsed laser cut on titanium surfaces (Shanjin & Yang, 2006)

Nitrogen-aided cut surface, (b) air aided laser cut surface, (c) argon aided cut surface

Generally, CO₂ laser mode of cutting can be classified as sublimating, melting or burning depending on the mechanism of material removal (Badoniya, 2018). The surface quality of a laser machined surface is usually described by; the cut component characteristics (such as micro crack generation and depth of HAZ) as well as the surface features (such as height of striations, roughness of surface and machined surface inclination) (Neimeyer, et al., 1993).

2.10.1 Effect of laser machining parameters on surface morphology

Laser cutting parameters have been reported to have a major effect on the quality of machined component surfaces attained. According to Stournaras et al., increasing the laser power and reducing the machining speed during CO₂ laser machining of AA5083 aluminium sheet results in an increase in the kerf width and HAZ (Stournaras, et al., 2009). Work done by Rajaram et al., on the quality of cut obtained after CO₂ laser machining of 4130 steels also revealed that the feed rate has a significant effect on the striation formation and surface roughness (Rajaram, et al., 2003). According to their work, the laser power has an impact on the attained kerf width and HAZ size. Their work also revealed that the kerf width increased with increasing cut distance as a result of heat accumulation in the 4130 steel component during laser cutting process.

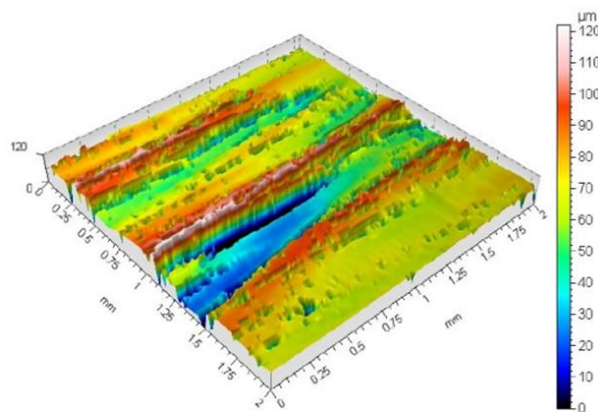


Figure 2. 39 3D surface morphology after laser machining of low carbon steel (Miraoui, et al., 2014)

According to Miraoui et al., laser beam diameter has negligible effect on surface roughness of steel plates however, higher laser power results in improved surface roughness (Miraoui, et al., 2014). Their work also observed micro-geometric variations across the machined surface after laser machining, Figure 2.39.

Neimeyer et al., in their work on mild steels observed that increasing machining speed results in the reduction of surface roughness values (Neimeyer, et al., 1993). Their work attributed the trend to the fact that the laser moves quicker than the emerging oxidation front thereby offering a steadier thermal input to sustain the melt. This occurrence according to their work retards the melt solidification, hence the smoother surface. Ghany and Newishy in their work on the laser cutting of austenitic stainless steels showed that an increase in the cutting frequency and speed results in the reduction of the attained kerf width and cut surface roughness (Ghany & Newishy, 2005). Thawari et al., in their work on the laser machining of nickel-based superalloys also observed that the laser machining quality in terms of the kerf width and surface roughness are a function of the spot overlap adopted during the machining process (Thawari, et al., 2005). Their work also revealed that the spot overlap decreases with increasing laser pulse energy and cutting speed, Figure 2.40.

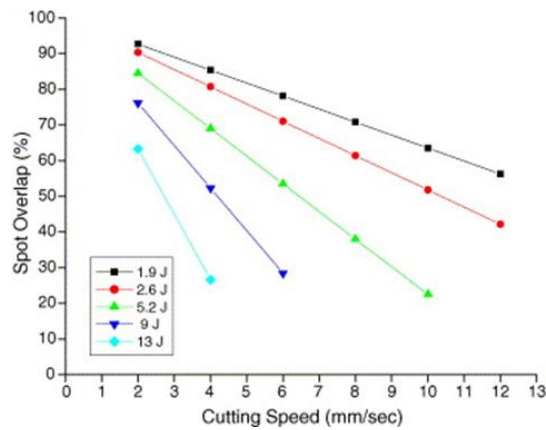


Figure 2. 40 Spot overlap response to cutting speed during nickel-based superalloy laser cutting (Thawari, et al., 2005)

Furthermore, research conducted on the laser cutting of low carbon steels showed that the obtained surface roughness values reduced with increasing laser power but increased with sheet thickness (Radovanovic & Dašić, 2006).

Work on the machining of AA5083 aluminium sheet material using CO₂ laser also showed that the deployment of gap pressure combines well with the pulsing frequency when ascertaining the surface roughness evolution as well as the machined surface morphology of the material (Stournaras, et al., 2009).

In addition, laser machined surfaces of mild and low-alloyed steels show distinct form of waviness and possess characteristic grooved pattern which are a function of the shape of the

focused beam, the machining speed, the molten part removal rate and hardening at the zone of machining (Radovanovic & Dašić, 2006).

A work conducted on the laser machinability of stainless steels showed that the microstructure evolution at the cut edge as well as the hardness values are influenced by the cutting parameters (Miraoui, et al., 2013). According to their studies, the hardness values of the machined surfaces are a function of the speed of cutting and the laser power. Their work also reported that the surface roughness featured the presence of cracks and periodic striations after laser cutting of the material.

2.10.2 Laser cutting induced microstructural changes

Striation formation is one of the key features of a laser cut surface and they have effect on the surface quality (roughness) and precision (kerf width) of the cut part. The presence of striations is undesirable since they act as stress raisers as well as also resulting in geometric variations. Kaebernick et al., in their research described a technique for the monitoring and control of striation by measuring the striation frequency to provide basic feedback for the improvement of surface roughness through pulse control during laser cutting (Kaebernick, et al., 1998).

The mechanism for striation formation have been studied in many works but no consensus have been reached on the true mechanism of its occurrence. Research conducted by Yilbaş on mild steel sheets revealed that a substantial amount of surface plasma occurs when using thicker sheets at high oxygen pressure resulting in the erosion of surfaces due to thermal effect. According to their work, an increase in the incident energy due to its obstruction by the plasma to reach the intended target surface, increases the removal rate of the molten melt from the kerf resulting in more surface plasma. The periodic nature of the process leads to stria formation around the kerf edge (Yilbaş, 1996). Vicanek et al., using theoretical model to study striation phenomenon stated that melt flow during laser machining is generally unstable. According to their work, the undulatory melt flow thus generates the roughening of the cut surface. Instability as a result of the oscillation generates frequency of alike order to the noticed pattern. With increasing cutting speed, the melt thickness increases, (Figure 2.41) since more molten materials are produced per unit time in the cutting kerf (Vicanek, et al., 1987). According to Schuöcker, the generation of striation on cut surfaces during laser cutting is due to the movement of liquid layer in the cutting direction and their oscillation causes a spatially periodic distortion of the cut edges (Schuöcker, 1986).

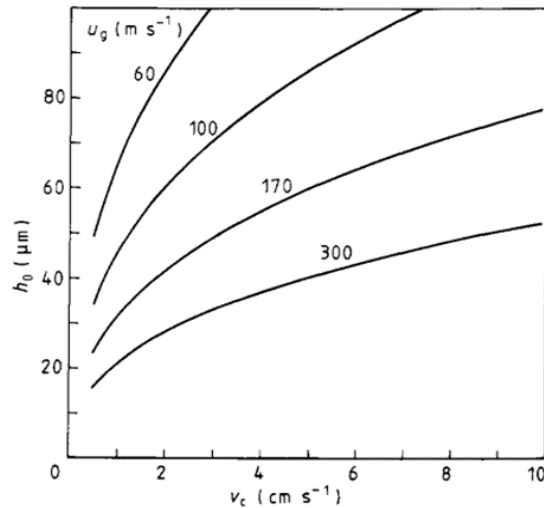


Figure 2.41 Melt thickness increasing with cutting speed for varying gas velocities (Vicanek, et al., 1987)

According to Kai and Lawrence, when the laser cutting speed is low, liquid film ruptures on the cutting front. With increasing speed, waves are produced on top of the cutting front in place of the film rupture. According to their work, each film rupture results in sudden increase of melt removal and thus accelerates the oxidation and melting. This resulted in the cyclic pattern formed on the cut edge (Kai & Lawrence, 1999). According to Schuöcker and Muller, periodic striation is caused by the fluctuation and oscillation of liquid layer usually formed at the momentary end of a cut kerf that induces spatial perturbations on the cut edges due to the movement of the liquid layer with the cutting speed (Schuöcker & Muller, 1987). According to Kim et al., striation formation in thin stainless steel tube is attributable to the ejection of molten metal and evaporation during the laser cutting process (Kim, et al., 2001).

One of the major features of laser machining is the occurrence of microstructural transformation effected on component surfaces. Laser cutting process entails a thermo-mechanical interaction between the laser cutting parameters and matter, resulting in the formation of the HAZs. Shanjin and Yang during studies on TC1 titanium alloy observed that laser cutting parameters have major effect on the melt zone (MZ), HAZ and the microhardness beneath the cut surface, Figure 2.42b (Shanjin & Yang, 2006). Since laser cutting is a thermal process, most of the heat melts or vaporizes on the cut surface and then gets blown away by an assisted gas. The remainder of heat transmits to the matrix and changes the microstructure of the surface material resulting in the formation of HAZ layer, Figure 2.42a (Shanjin & Yang, 2006).

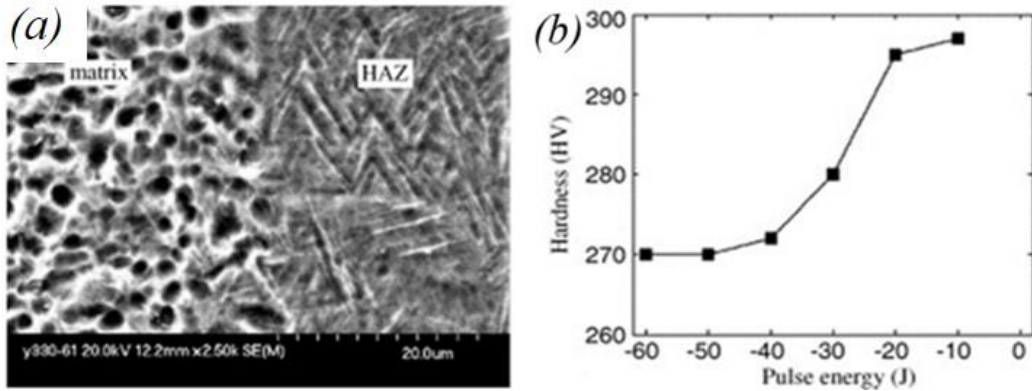


Figure 2.42 SEM of TC1 titanium alloy with microstructural changes and hardness evolution after laser cutting (Shanjin & Yang, 2006)

(a) Microstructure changes, (b) hardness variation across surface having HAZ

Research conducted by Miraoui et al., on the laser cutting of low carbon steel plates showed that the heat generated during the process after cooling results in a transformed microstructure, consisting of a white layer (melt zone) and HAZ, Figure 2.43 (Miraoui, et al., 2016). According to their work, the HAZ is responsive to the laser power and cutting speed. Their work also inferred that the HAZ may lead to undesirable effects like low fatigue resistance, surface cracking and distortions.

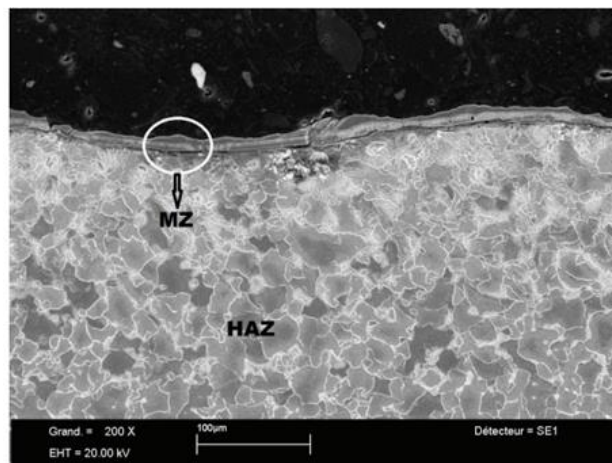


Figure 2.43 Micrograph of HAZ after laser cutting of low carbon steel (Miraoui, et al., 2016)

Rajaram et al., in their work on 4130 steels observed that the response of the feed rate and laser power to the width of HAZ depends on the material's ability to conduct heat (Rajaram, et al., 2003). Their research also utilised regression model to ascertain the response of machining parameters to kerf width, surface roughness, striation frequency and HAZ evolution, Figure 2.44.

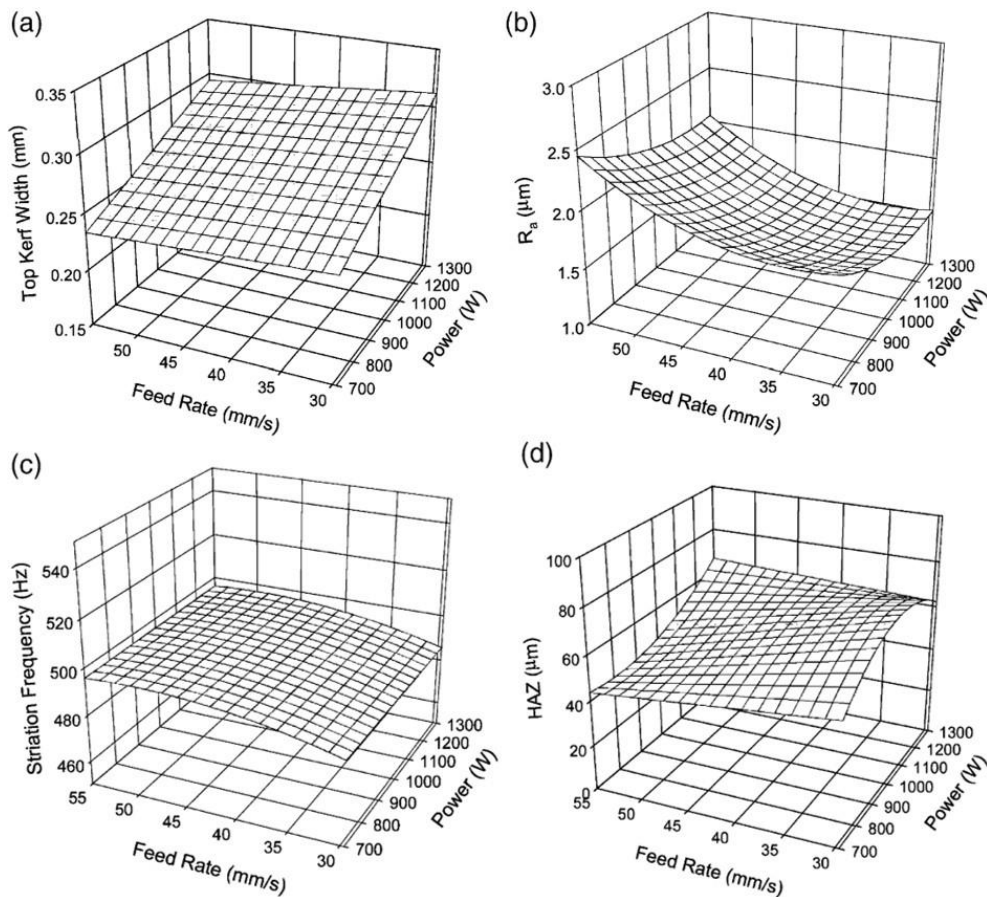


Figure 2. 44 Regression model showing response of machining parameters to (a) kerf width, (b) surface roughness, (c) striation frequency, (d) HAZ evolution during laser cutting of 4130 steels (Rajaram, et al., 2003)

2.11 Sheet metal edge formability

2.11.1 Sheet hole flanging operation

Hole flanging is a sheet metal forming technique widely adopted in the automobile, aerospace and aeronautic industry for plastically working sheets with pre-fabricated holes to make various shapes of flanges (Cui & Gao, 2010). The technique mostly utilises press working to toughen and enhance hole edges, enable thread cutting in parts as well as offer extra aid during the attachment of tubes to sheet components (Silva, et al., 2013). During the process, the displacement of the sheet metal around the pre-fabricated holes is usually by way of sheet stretching or even bending, and the nature of the circumferential strains introduced at the hole periphery are adequate enough to result in the material failure by tearing, fracturing or even necking (Wang & Wenner, 1974). According to Kacem et al., the major defects present during the hole flanging of aluminium alloys includes; orange peel, radial fracture and axial cracks

(Kacem, et al., 2013). Research work done by Hyun et al., on the extent of hole flanging attainable in transformation-induced plasticity (TRIP) steel and ferrite- bainite duplex steel plates also showed that the nature of the lip (shape and height) seen at the hole edge is a function of the hole diameter (Hyun, et al., 2002). Their work attributed this observation to the localised necking produced by the circumferential strains, Figure 2.45.



Figure 2. 45 Nature of lip at hole edge with varying hole diameter of Ferrite- Bainite duplex steel plate during hole flanging (Hyun, et al., 2002)

Incremental hole flanging, a technique which adopts ISF to perform hole flanging operations has also been studied in some works and thought to offer improved hole flangeability of sheet metals. According to Bambach et al., utilising incremental hole flanging to work mild steels provides twice as much limit hole expansion ratio compared to those obtained in traditional hole flanging operation (Bambach, et al., 2014).

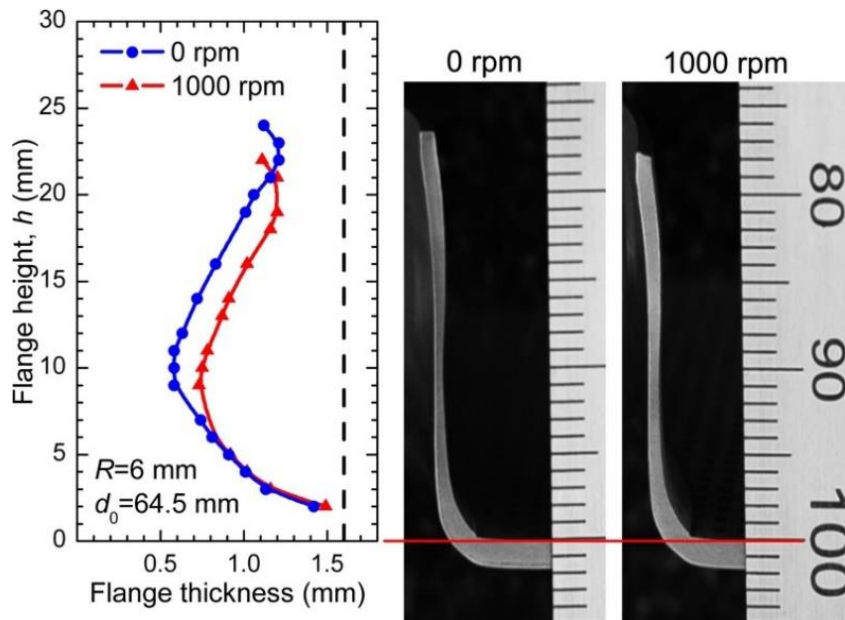


Figure 2. 46 Flange thickness with 0 and 1000rpm spindle speed (Borrego, et al., 2016)

Using pre-fabricated holes with high diameters during incremental hole flanging results in a new deformation mode which are normally absent in sheet metals with no pre-fabricated holes. This is attributable to the integration of in-plane stretching during plane strain conditions accompanied by bending at the perimeter of the flanges. This hinders the strain path growth towards the initiation of failure, hence offering an improved formability compared to the traditional hole flanging by press working (Centeno, et al., 2012).

Borrego et al., using SPIF to perform hole flanging operation on AA7075-O aluminium alloy showed that the tool size and bending ratio play a vital role in the failure mode evolution. Their work also indicated that the spindle speed have effect on the attained surface quality by offering a much regular flange thickness profile of the aluminium sheet, Figure 2.46 (Borrego, et al., 2016).

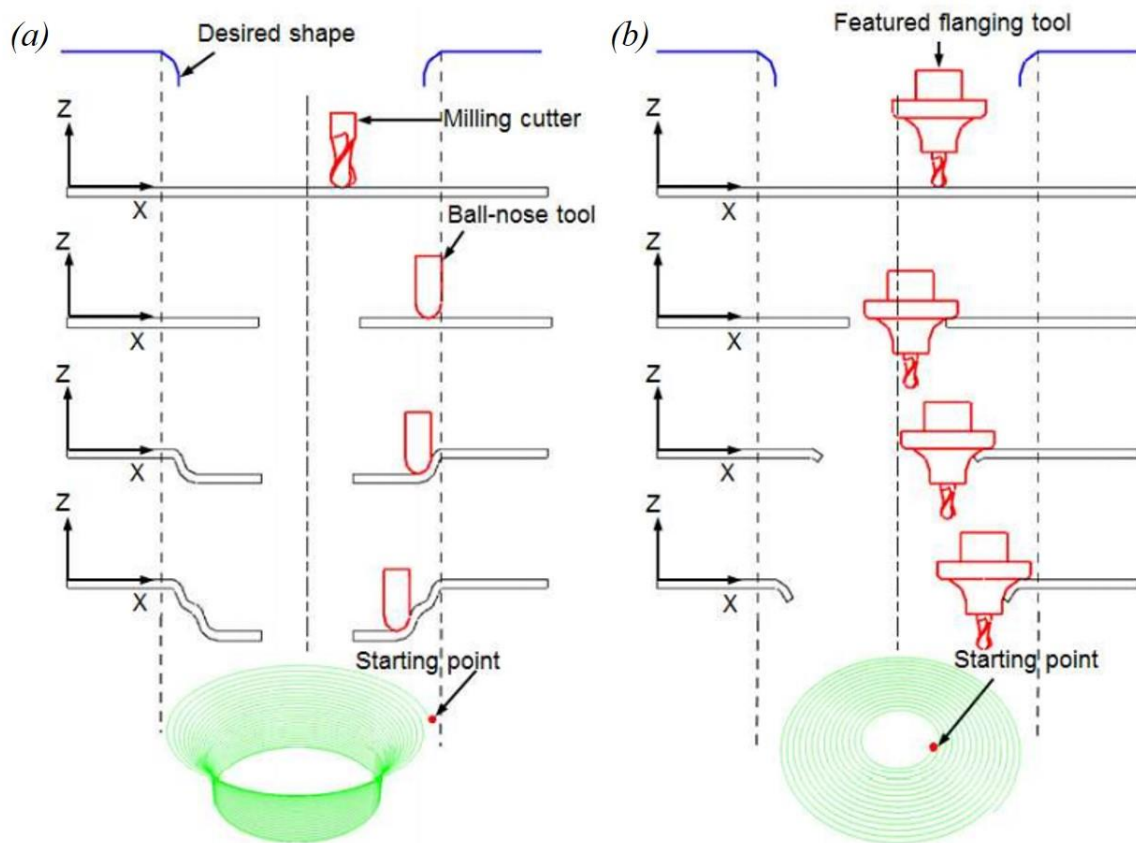


Figure 2. 47 Tool influence on hole flanging strategies (Cao, et al., 2016)

(a) Traditional ball nose tool path, (b) proposed new hole flanging tool path

Cao et al., in their work recognised that the major issue confronting traditional ISF is significant sheet thinning resulting in the uneven thickness distribution in formed components. Their work on AA5052 aluminium sheet metal proposed a new tool geometry and forming strategy,

capable of rectifying this anomaly during incremental hole flanging operations (Cao, et al., 2016). According to their work, utilising new flanging tools with special geometrical features (hyperbolic and cylindrical features) as opposed to the traditional ball nose tool, improves the hole flanging operation significantly. Their work also revealed that the tool path adopted in the hole flanging operation plays a vital role in attaining optimum flanged parts. According to their research, incorporating a milling cutter into the new tool to ensure that the initial hole is fabricated without tool replacement and moving the tool from the milled hole edge towards outside along the horizontal x-y plane improves the sheet thickness distribution, Figure 2.47*b*. This according to the work is opposed to the traditional ball nose tool path, where the tool movement is from the sheet periphery towards the milled hole edge with downward movement along a 3D profile, layer by layer in the z-direction, Figure 2.47*a* (Cao, et al., 2016).

Other metrics are proposed in some works to be applicable in assessing the hole flanging performance in materials. Montanari et al., in their work proposed the circle grid analysis integrated with plasticity as a means of tracing the history of deformation in AA1050-H111 aluminium alloy subjected to incremental hole flanging (Montanari, et al., 2013).

2.11.2 Testing methods for examining sheet edge formability

The hole expansion test (HET) governed by ISO 16630:2017, is normally utilised to characterise the edge formability of sheet metals. The hole expansion ratio (HER) defines the extent of edge formability of sheet metals and are computed by considering the initial and final diameters of the pre- fabricated hole after HET (Karelova, et al., 2009);

$$HER = \frac{d_f - d_0}{d_0} \times 100\% \quad (2.2)$$

Where; d_f – mean final hole diameter after testing; d_0 – initial hole diameter

The higher the HER value, the higher the edge formability of materials. Ideally, the HET is terminated upon the onset of hole edge through-thickness crack with the aid of cameras. However, for test conducted relying on visual inspection of the crack inception, this determination can be cumbersome. Therefore, the cracks which emanate after the test termination can be compensated for by correcting equation (2.2), Figure 2.48 (Larour, et al., 2014);

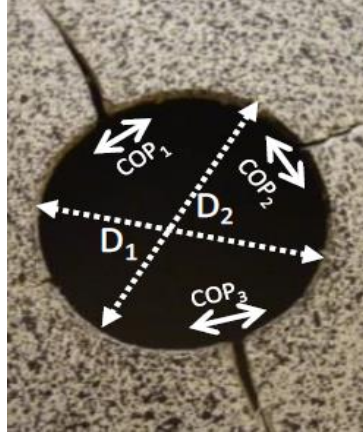


Figure 2. 48 Correction for the manual monitoring of crack opening during HET (Larour, et al., 2014)

$$D_{corrected} = \frac{\left(\frac{D_1+D_2}{2}\right)\pi - \sum_1^n COP_n}{\pi} \quad (2.3)$$

Given that, $d_f = D_{corrected}$ after accounting for the corrections in the crack width, then;

By putting equation (2.3) into equation (2.2)

$$HER = \frac{D_{corrected} - d_0}{d_0} \quad (2.4)$$

Where: COP_n – n^{th} crack opening distance; $D_{corrected}$ – final hole diameter after correction, D_1 – random final diameter 1 edge with crack width, D_2 – random final diameter 2 edge with crack width.

Schneider et al., in their work on dual-phase and ferritic-bainitic steel grades developed a technique based on the GOM Aramis strain data to propose a crack-criteria for user-independent crack-time detection. Their work also identified equation (2.3) as an appropriate mathematical relation for correcting crack attained during HET (Schneider, et al., 2016).

The limiting forming ratio (LFR) is also a very vital indicator for quantifying the inception of cracks during sheet hole flanging and it describes the value beyond which the material fails (Silva, et al., 2013);

$$LFR = \frac{d_{max}}{d_0} \quad (2.5)$$

Where; d_{max} – maximum inside diameter of a fully flanged edge

Schneider et al., in their review paper described various test types identified to be useful in characterising the edge surface formability of sheet metals, Table 2.8 (Schneider, et al., 2015).

Table 2. 8 Test methods utilised to assess cut-edge formability; extracted from (Schneider, et al., 2015)

Method of Testing	Name of Test
Circular hole expansion with conical punch	HET, ISO 16630:2017
Circular hole expansion with hemispherical punch	Hole expansion with Nakajima punch
Circular hole expansion with flat bottom punch	KWI- test
Cut- edge bending in sheet plane	In-plane bending test
	Side bending test
	Double bend test
Cut- edge bending out of sheet plane	Hutchinson bend test
	HAB- test
	90 ⁰ flanging test
Cut-edge bending and tension out of sheet plane	Analysis of edge-crack-sensibility
	Diabolo test
Flanging of cut-edge	Hole flanging test
Tension of specimen with cut-edge notch	Strip tensile test
	Half-a-dog bone tensile test
Tension of specimen with cut-edge hole	Hole tensile test

2.11.3 Influence of machining on edge formability

One of the major concerns, which arise when dealing with sheet metals with pre-fabricated holes during forming, is the condition of their machined surfaces. Different machining methods are commercially adopted to prepare sheet metals in industry, with each cutting method producing specific edge micro features. Research work carried out by Thipprakmas, et al. has also shown that the quality of the cut edge surface of sheet metals play a massive role in the attainment of optimum edge flangeability of sheet metals (Thipprakmas, et al., 2007). Mori et

al., in their work on ultra-high strength steels also showed that the macroscopic unevenness of the sheared edges coupled with its hardness influences the limiting expansion ratio and the stretch flangeability of the steel sheets (Mori, et al., 2010).

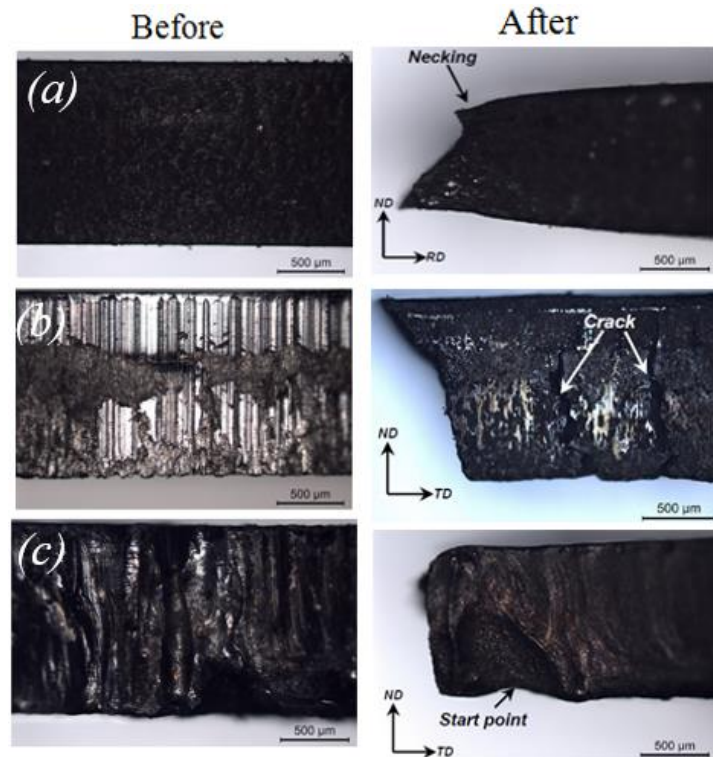


Figure 2. 49 Hole surface integrity of DP 980 steels and their respective failure mode after HET (Xu, et al., 2012)

(a) EDM hole surface quality before and after HET, (b) Punching hole surface quality before and after HET, (c) Laser hole surface quality before and after HET

Research done by Xu et al., on the effect of EDM, laser machining and punching on the surface integrity of pre-fabricated holes in DP 980 steels (dual phase grade) after hole expansion test showed that EDM gave the highest hole expansion ratio with punching producing the least (Xu, et al., 2012). According to their work, punching produced surface deformation with the most damage to the pre- punched hole surface with EDM producing a more uniform surface. Their work also inferred that the cutting methods influence the nature of failure modes due to the variations in surface quality, Figure 2.49. Karelova et al., in their work also studied the effect of hole surface quality (edge conditions) produced after hole punching, hole drilling and wire cutting on the hole expansion of dual and complex phase advanced high strength (AHS) steels (Karelova, et al., 2009). Their work reported that for identical hole edge conditions, complex-phase grade (CP800) exhibited higher edge formability compared to dual-phase grade (DP800),

Figure 2.50. Their work also revealed that defects produced by virtue of punching and drilling had damaging impact on the edge formability of both materials.

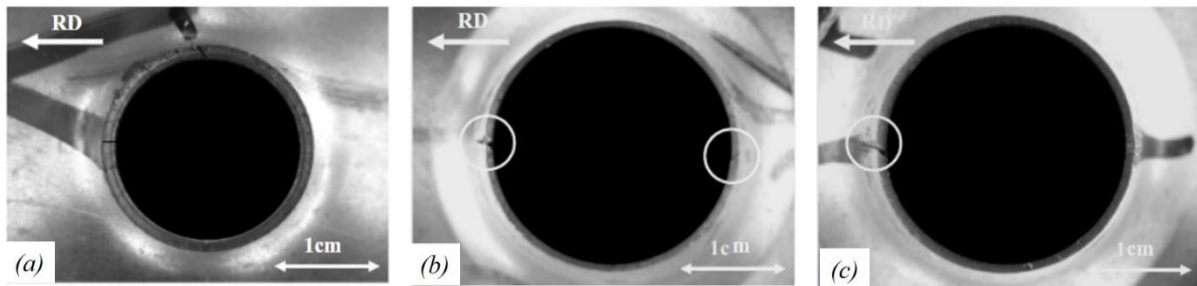


Figure 2. 50 Hole edge of CP800 after HET (Karelova, et al., 2009).

(a) Randomly distributed crack for punched edge, (b) two major cracks for drilled edge, (c) one crack for wire cut edge

Nagasaka et al., in their studies examined the influence of laser cutting and mechanical punching on the edge formability of ultra-high strength TRIP-aided steel sheets with bainitic ferrite matrix after austempering (Nagasaka, et al., 2010). Their work found that laser cutting produces enhanced stretch flangeability compared to edges prepared from mechanical punching due to its effect on the microstructure and the integrity of the surfaces produced, Figure 2.51.

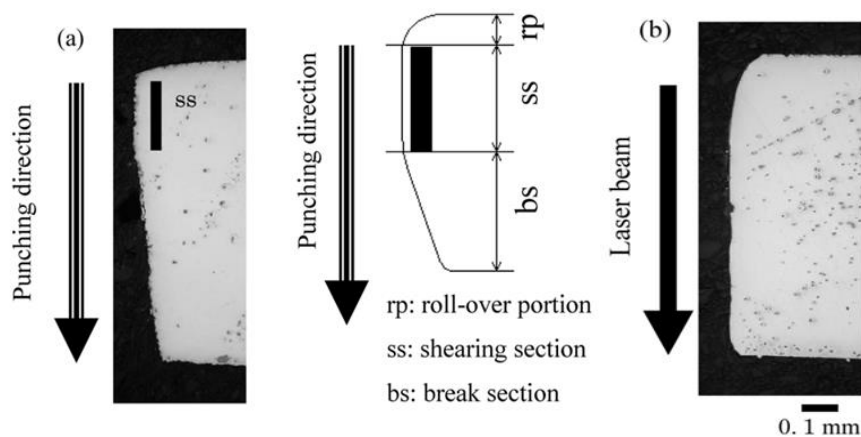


Figure 2. 51 Optical micrograph after sectioning bainitic ferrite matrix steel (Nagasaka, et al., 2010)

(a) Micrograph after mechanical punching showing three sections, (b) micrograph after laser cutting showing no variation in sections

Tsoupis and Merklein, in their work to study the edge crack sensitivity of DP800 steel and AA5182 aluminium alloy showed that loading conditions have a significant influence on the edge crack sensitivity of the sheet metals (Tsoupis & Merklein, 2016). Their work also showed

that cutting by punching decreases the hole expansion ratio due to its impact on the formability of the material edges.

The manner in which punched edge of blanks are positioned with respect to the punch direction are also thought to have adverse effect on the nature of crack inception and growth as well as the HER of materials. Zhang et al., in their work compared the hole expansion evolution of dual phase steel sheets studied under burr up and burr down placement conditions, Figure 2.52 (Zhang, et al., 2007). According to their work, the distinct features of the sheet edge condition and their positioning with respect to the applied deformation force, plays a vital role in the failure mode of the material during the test.

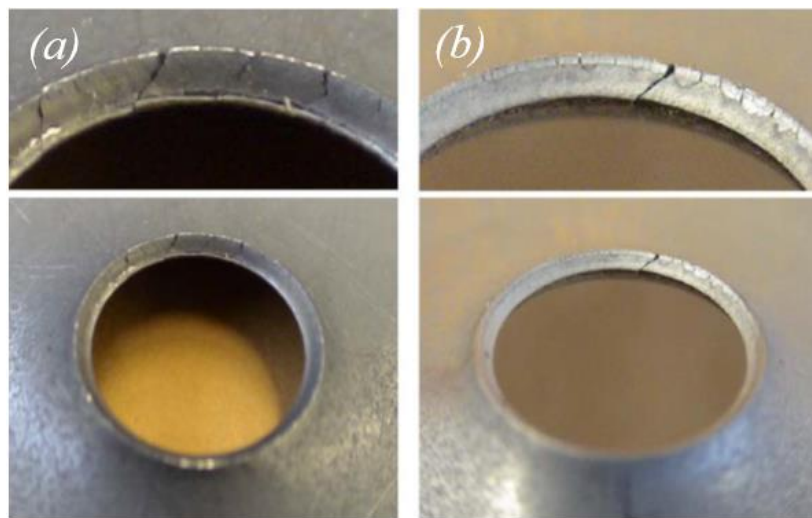


Figure 2. 52 Impact of burr direction on HET and fracture evolution in dual phase steel sheets (Zhang, et al., 2007)

(a) Burr up and (b) burr down conditions

According to Schneider et al., the damage induced via shear cutting of dual-phase and ferritic-bainitic steels results in a reduced edge formability of the steel sheets (Schneider, et al., 2016).

Gläsner et al., in their work on SZBS800 complex phase steel edge sensitivity indicated that adopting a two-stage shear machining as opposed to one-stage shear cutting has the tendency of enhancing the edge-forming limit of the material (Gläsner, et al., 2016).

Behrens et al., in their research examined the possibility of enhancing the HER of DP800 and DC06 steels during a fractional factorial design of experiments for HET for edges prepared via adjusted AWJ machining parameters. Their work found that utilising a reduced stand-off distance, high water pressure, slow transverse speed and machining the test-piece underwater have the tendency of delaying the failure initiation during HET (Behrens, et al., 2018).

2.11.4 Edge failure and limit strain evolution

Failure observed during HET are mostly attributable to either localised damage or necking (Krempaszky, et al., 2014). For failure due to localised damage, the limiting hole expansion ratio could be considered almost free of strain gradient but a function of the edge condition or material parameter representing the stretch flangeability. This is regarded during sheet metal forming process as the limiting criteria for numeral design (Krempaszky, et al., 2014). For failure controlled by necking however, the evolution of the hole expansion is a function of the original hole diameter. Hence, the strain gradient must also be accounted for when employed in numerical design of a forming process (Krempaszky, et al., 2014).

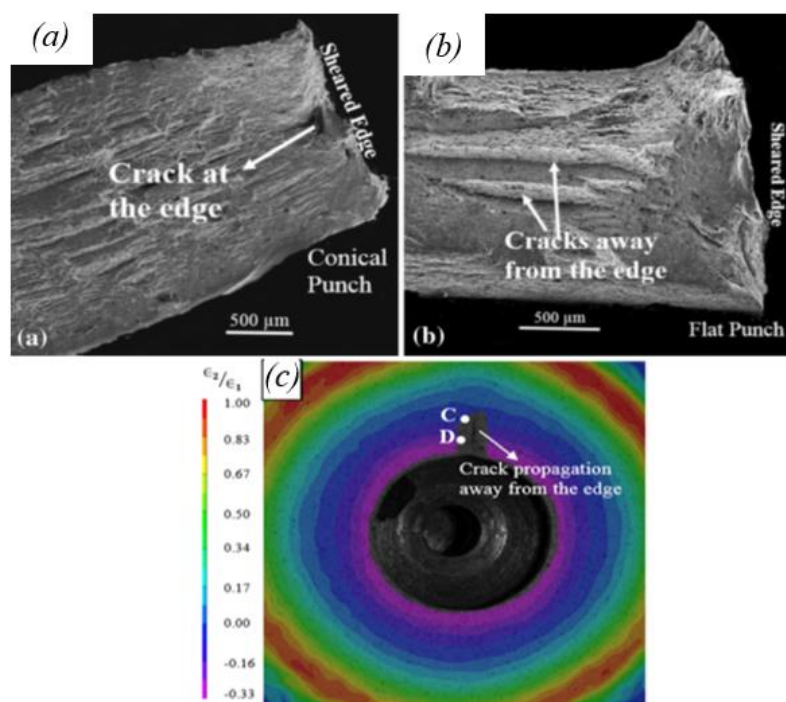


Figure 2. 53 Influence of punch geometry on the crack position in dual and complex phase steels (Pathak, et al., 2016)

Failure of complex phase steel with (a) conical punch, (b) flat punch, (c) strain ratio contour with crack away from dual phase steel sheet edge using flat punch

Pathak et al., in their research examined the impact of different punch geometries on the failure evolution in dual and complex phase steels during HET (Pathak, et al., 2016). Their work showed that flat punch is not adequate for examining sheet metal edge conditions since the onset of cracks occur away from the metal cut edge in contrast to conical punch, Figure 2.53. According to their work, failure initiated by flat punch is under plane-strain loading condition hence occurring away from the sheet edge whereas those generated by conical punch are under uniaxial tension near the edges hence their sensitivity to burr direction.

Furthermore, HET has been identified to be instrumental in ascertaining the edge limit formability in materials. Shi and Chen, in their work using HET to project the limit of stretch flangeability of advanced high strength steels showed that the HER can be utilised as a failure criteria, when adopted in simulations to evaluate edge cracks as well as limits of stretch flangeability (Shi & Chen, 2007). According to their work, the traditional FLD are not suitable for assessing the edge-cracking limit in the material due to the fracture strain values being lower than its forming limit, Figure 2.54.

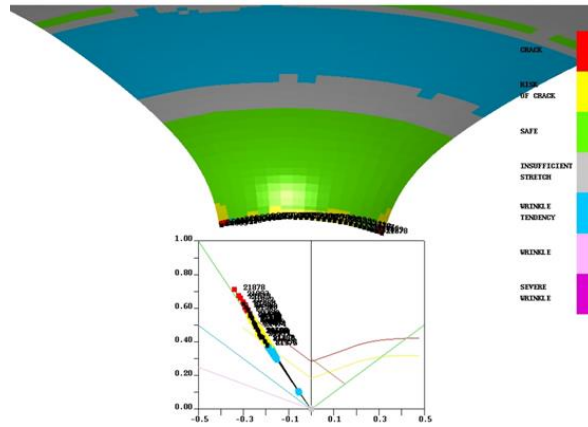


Figure 2. 54 Attained strain path after HET (Shi & Chen, 2007)

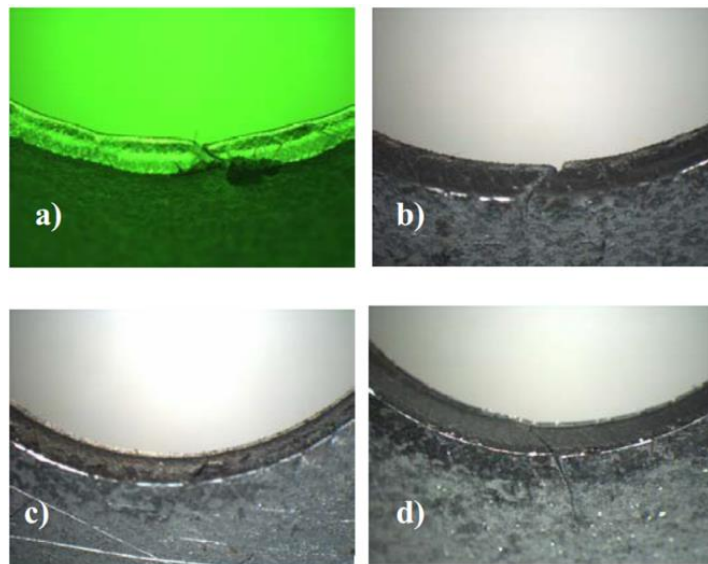


Figure 2. 55 Edge fracture types for various steels after HET (Konieczny & Henderson, 2007)

(a)50XX, (b)DP590, (c)DP780, (d)DP980

Konieczny and Henderson in their research observed differences in the fracture modes between conventional and AHSS steels with thicknesses of 1.4mm at die clearance of 6.4%. Their

findings on the various steel materials after HET showed that when the materials undergo ductile failure with prior inception of necking (Figure 2.55a), their failure could be estimated with the traditional FLD (Konieczny & Henderson, 2007). According to their work, other forms of failure observed after HET on the materials (Figure 2.55 b,c,d) occurred earlier than the values projected by the FLD thereby making their prediction cumbersome.

Chen et al., in their work also adopted the true strain value after HET as the failure criteria to ascertain the collar formability of high strength steels (Chen, et al., 2003).

Dykeman et al., in their work used the traditional, centre hole and side notched uniaxial tensile samples to study the nature of edge fracture present in different types of advanced high strength steels fabricated with different machining techniques (Dykeman, et al., 2011). Their work showed that fracture strains attained at the part edges are a function of the material, edge conditions and the stress state with respect to the loading geometries, Figure 2.56. According to their work, the notched test samples (multi-axial stress state) recorded reduced fracture strains compared to the traditional uniaxial tensile test samples (uniaxial stress state) due to the influence of the stress concentration attributes.

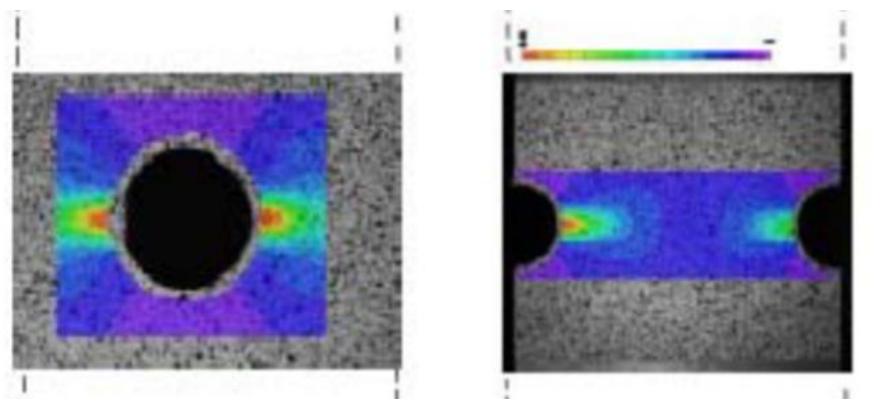


Figure 2. 56 Attained tensile fracture strain with varying stress state (Dykeman, et al., 2011)

Wang et al., upon using the centre hole tensile specimen to study the edge fracture limit in advanced high strength steels fabricated with different cutting methods showed that the drop in the load curve is attributable to the edge crack occurrence. According to their work, the drop in load curve could be considered as the benchmark for estimating fracture and the fracture limit could be considered as the displacement at fracture, Figure 2.57 (Wang, et al., 2014).

Generally, the conventional FLD provides information on the possibility of forming a sheet component. However, when considering the feasibility of forming sheet with peculiar edge conditions, the FLD does not provide enough information with respect to the failure prediction

of components. Hole expansion test with a Nakajima punch (NAK_HET) has been explored in this regard to account for the edge forming limit of parts (Schneider, et al., 2016).

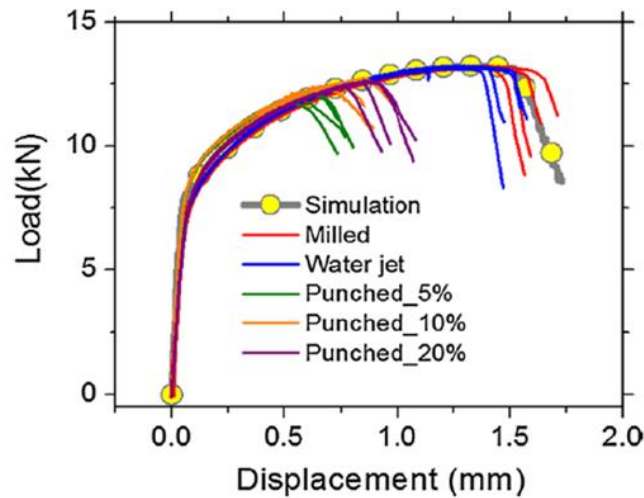


Figure 2. 57 Load curve drop considered as edge- stretch limit indicator (Wang, et al., 2014)

The set-up adopted during NAK_HET to account for the edge forming limit are the same tool set-up adopted during standard Nakajima test, consistent with EN ISO 12004-2. The critical strains obtained from the NAK_HET could also serve as failure criteria, which can be adopted on conventional FLD for projecting part edge surface failure limit (Schneider, et al., 2016); (Gläsner, et al., 2016). Major strains gotten from the experimental studies with the NAK_HET could provide useful data, which could be incorporated into forming simulations (Larour, et al., 2016).

2.11.5 Modelling and numerical predictions of sheet edge forming performance

Owing to the major successes accrued industrially from numerical simulations of sheet metal forming such as; time and cost reduction as well as enhanced product quality (Tekkaya, 2000), some researchers have explored different damage criteria and FEM techniques to predict HER. Butcher et al., in their work utilised FEM and the Gurson-Tvergaard-Needleman (GTN) damage criteria to predict the HER of dual phase steel (Butcher, et al., 2013). Park et al., utilised FEM based on different fracture criteria and a representative volume element, which accounts for microstructural effects to predict the HER of advanced high strength steels (Park, et al., 2018). Chung et al., in their work developed a triaxiality dependent fracture criterion with hardening behaviour and stiffness deterioration within an anisotropic criterion to predict the

HER and edge condition sensitivity of advanced high strength steel sheets (Chung, et al., 2011). According to their research, these criteria were used within an FEM package to predict the HER. Studies done by Leu, using an incremental elasto-plastic FEM to simulate the hole flanging capability of anisotropic materials showed that an increase in the material anisotropy in the direction normal to the sheet and the strain hardening index enhances the hole flanging ratio of the material. Their work was based on the assumption that the stress at the hole periphery in the flange was a state of circumferential uniaxial tension, in order to simplify the fracture mode as a simple tension test (Leu, 1996). However, Hu et al., in their work recognised the difficulty in adopting FEM to predict the hole edge forming performance after hole piercing such as; (1) the difficulty in accurately predicting the sheared edge geometry and damage, as well as (2) effectively and accurately incorporating the above-predicted shearing-induced edge geometry and damage into the subsequent formability simulations (Hu, et al., 2016).

Generally, the stress state observed at the hole edge after HET is the uniaxial tension (Paul, et al., 2014), which is similar to the stress state observed during a conventional uniaxial tensile test. This observation has prompted several researchers to correlate the HER to material uniaxial tensile properties. Kumar De et al., in their work on hot-rolled high-strength steels suggested that where strengthening mechanism of steels are the same, the ultimate tensile strength correlates well with the HER (Kumar De, et al., 2011). However, Chen et al., in their work on ultra-high strength steels observed that there is a strong inverse correlation between the HER and tensile strength with values below 640MPa and no change in HER for tensile strength above 840MPa (Chen, et al., 2014). Fang et al., in their study on C-Mn steels showed that higher values of the yield to tensile ratio correlates well with the HER (Fang, et al., 2003). Adamczyk and Michal utilised a multiple linear regression model for correlating the HER to the transverse total elongation and average plastic anisotropy of high-strength cold-rolled steels (Adamczyk & Michal, 1986). Some works have also recognised the difficulty in correlating material tensile properties to the HER. Kim et al., in their work using basic tensile properties to predict the HER of thin steel sheets with a machined hole recognised the difficulty in correlating the parameters (Kim, et al., 2018). Their work proposed evaluating the width strains from the measured normal anisotropy as well as considering the tensile elongation only along the sheet rolling direction. They also suggested that utilising the width strain in uniaxial tension to represent the planar anisotropy would improve the correlation with the HER.

2.12 Summary

- The increase in surface roughening with deformation in sheet metals are essential in examining the strain limit and the strain instability. Surface roughening during sheet metal forming is detrimental to the surface integrity of the final product and provides a nucleation site for strain localization. Surface defects produced during sheet forming affects the optimum formability of components.
- Optimisation techniques adopted during either sheet metal forming or manufacturing have the tendency of enhancing the surface integrity as well as the formability of finished parts.
- The difficulty in machining titanium is attributable to their high temperature strength, low elastic modulus (makes part prone to deflection and vibration) and low thermal conductivity (reduces their heat removal rate and increases the machining force required).
- Alloying constituents and mechanical properties of materials have a significant effect on their machinability.
- The quality of a machined surface in terms of the texture can be classified according to their roughness and waviness. However, the surface state of machined edges can be described by their geometrical, mechanical and metallurgical parameters.
- The quality of the edge surface finishes produced after either EDM, laser or AWJ machining are responsive the machining parameters adopted.
- Hole flanging operation is an integrated sheet metal forming process which involves the use of machining to fabricate a hole in sheet metals prior to the forming process. The extent of edge formability of sheet metals is a function of the type of machining method employed.
- The choice of tool geometry could have a significant impact on the edge formability of sheet metals. The standard conical punch and the Nakajima punch with their accompanying die set are suitable tool geometries for performing HET.
- Numerical models and FEM approaches offer a premise for ascertaining the edge forming performance of sheet metals.

Chapter 3

Experimental approaches and analysis methods

Overview

This chapter elucidates the major techniques and analysis methods utilised to address the research objectives identified in this EngD research. For the machining methods adopted, the quality of edge surfaces produced in terms of accuracy are governed by industry standards. However, the edges produced with different machining methods were compared on the basis of their impact on the edge surface micro-feature changes, the response of different titanium grades to machining and the nature of the attained surface finish quality according to industry standard. Mechanical testing and dimensioning of the test samples were consistent with international standards. For the DIC analysis performed, the natural texture of SEM images and the artificial speckle patterns produced from white paint background with sprinkled black dots were used as the grey intensity patterns in their role as the major conveyor of deformation information. The Matlab based Ncorr DIC software utilised for the localised strain evaluation allows for large strain computation by automatically updating the region of interest using a polygon fill algorithm. ANOVA analysis in Minitab was conducted to compare group means of sheet edges prepared with either AWJ or EDM as well as their corresponding mechanical deformation parameters to ascertain if there were any statistically significant difference between them. This chapter also discusses the proposed statistical numerical regression model formulated to predict the HER of titanium alloys. R codes were written with logarithmic and polynomial functions introduced to capture the non-linearity in the data fitting process. The main titanium grades examined in this EngD research includes; CP-Ti (Grade 2), Ti-35A, Ti-21S, Ti-6Al-4V and Ti-3Al-2.5V (UNS R56320).

3.1 Machining, mechanical testing and measurements

3.1.1 Approach adopted for machining samples for hole expansion test and tensile test

The approach adopted in this research was to EDM, AWJ and laser cut the studied materials with machining parameters capable of producing the sort of surfaces, which are optimum and known to be industrially and commercially acceptable machined surfaces. The edge surface qualities produced for the laser, AWJ and EDM test samples were outsourced from industry.

BS ISO 14137:2015 standard guides test conditions for EDM machining with respect to testing of accuracy industrially. Thus, in practice the sort of surface qualities produced for experimental examination in this research could be used in a potential hole flanging operation in the absence of a surface treatment process (e.g. deburring) or substitute machining technology. Comparison of the edge surfaces with similar roughness for laser, EDM and AWJ machined edges were not considered in this work due to the following reasons;

- i. The mechanical erosion attributes of AWJ translates into its bulk material removal tendencies, making it commercially (in terms of machining time) and industrially inapplicable to produce the sort of edge qualities obtained for either EDM or laser cutting
- ii. The thermal erosion attributes of EDM cutting makes it commercially (in terms of machining time) unattractive to replicate the sort of edge surface finishes obtained in either AWJ or laser cutting
- iii. The ISO 9013 international standard is employed to govern the choice of materials adequate for oxyfuel flame cutting, plasma cutting and laser cutting as well as geometrical product specifications. This makes it economically unattractive to adopt laser cutting technique to produce the sort of edge qualities attainable for either AWJ or EDM cut methods

However, the dissimilarities in the nature of the edge surface micro-features produced by virtue of machining provides an opportunity to study how they affect the edge forming performance of titanium alloys when employed in a given hole flanging operation.

Apart from the fact that the machining methods studied are widely adopted in industry, one common point of comparison will be the unique nature of edges produced by each method (machining induced defects), which could be interrogated for onward adoption in hole flanging operations. Another point of comparison could be the performance of the final edge surface qualities, which are known to be commercially applicable for each cutting method examined. Comparisons could also be made for instances where the same machining parameters are applied to different titanium alloys to ascertain their response to hole flanging operations. Another important point for comparison could be economic viability of the cutting processes adopted, although this is outside the remit of this work.

3.1.2 Dimensioning of tensile test sample

Traditional uniaxial tensile test are universally accepted testing technique for ascertaining the mechanical properties of materials. The dog-bone shaped test samples examined were fabricated using the format of AFRC flat tension test specimen (part number S0075_470_2), (Figure 3.1) with its accompanying design based on ASTM-E8/EM. All uniaxial tensile tests were conducted under standard room temperature conditions in accordance with ISO 6892-1:2016.

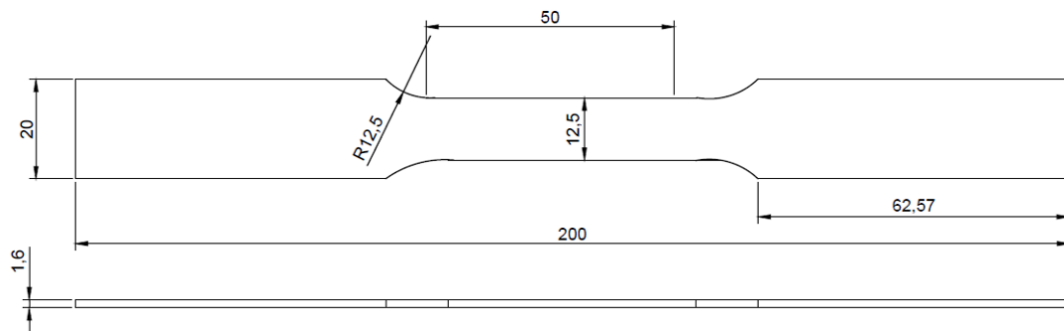


Figure 3. 1 Dimensioning of the tensile test specimen

The thickness of the tensile specimen was determined using Mitutoyo IP65 coolant proof calliper, the width with Mitutoyo IP67 coolant proof calliper and the length with Mitutoyo absolute digimatic calliper. The measured values were fed into a testXpert II software prior to the uniaxial tensile testing process.

3.1.3 Uniaxial tensile test

A Zwick/ Roell Z150 tensile testing machine furnished with a 150kN load cell was utilised to perform uniaxial tensile testing on the titanium alloys, Figure 3.2a. The load cell in the tensile testing machine evaluates the load exerted on the test samples at any given position. An extensometer was used to evaluate the changes in test sample gage length during the testing process. The load (force) with the corresponding extension (displacement) in sample length attained during the testing process were recorded using a testXpert II software for the onward computation of the stress-strain data. A constant strain rate of 0.001/s was adopted for this work and was controlled by the testXpert II software for a steadily varying cross-head speed. The test terminates when the material fractures and fails with an accompanying drop in the load.

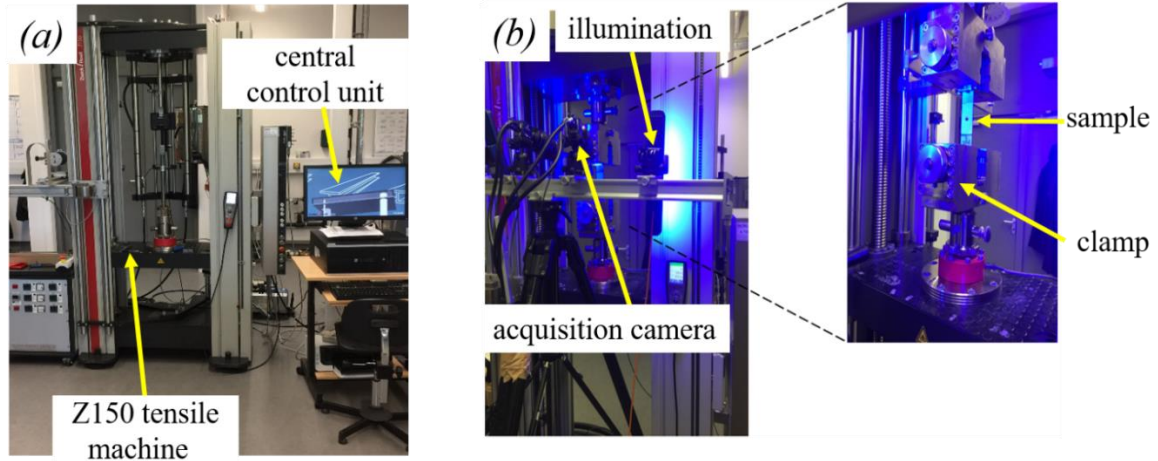


Figure 3. 2 Uniaxial tensile test experimental set up

(a) Z150 tensile machine, (b) DIC installation

The uniaxial tensile behaviour is accounted for by Hooke's law (Equation 3.1) as well as the Swift hardening equation (Equation 3.2) with both inculcated into the true stress-strain data obtained for each test specimen (Marciniak, et al., 2002);

$$\sigma_e = E \varepsilon_e \quad (3.1)$$

$$\sigma_y = K(\varepsilon_0 + \varepsilon_p)^n \quad (3.2)$$

Where;

K - Linear hardening parameter, n - strain hardening exponent, ε_0 - initial strain, ε_p - plastic strain, ε_e - elastic strain, σ_e - stress in the elastic zone, σ_y - yield strength, E - Elastic modulus.

In order to account for the surface strain evolution during the uniaxial tensile test trial, digital image correlation (DIC) was employed, Figure 3.2b. Randomly placed black dots sprayed over white paint was used as the speckle pattern with their displacement tracked with two digital cameras. The strain distribution after the tensile deformation was analysed using Davis 8.0 software supplied by LaVision.

3.1.4 Dimensioning of hole expansion test samples

Generally, dimensioning for hole expansion test sample preparation are governed by ISO 16630:2017. For the samples deformed with a Nakajima/hemispherical punch, a 200mm diameter disc with a 20mm inner diameter hole was employed, Figure 3.3a. This dimensioning was consistent with ISO 16630:2017 which states that; *'the test piece shall be flat and of such*

dimensions that the centre of any hole is not less than 45 mm from any edge of the test piece'. For the center hole test samples prepared for examination with standard conical punch, the inner hole diameter of 10mm employed was consistent with ISO 16630:2017, Figure 3.3b.

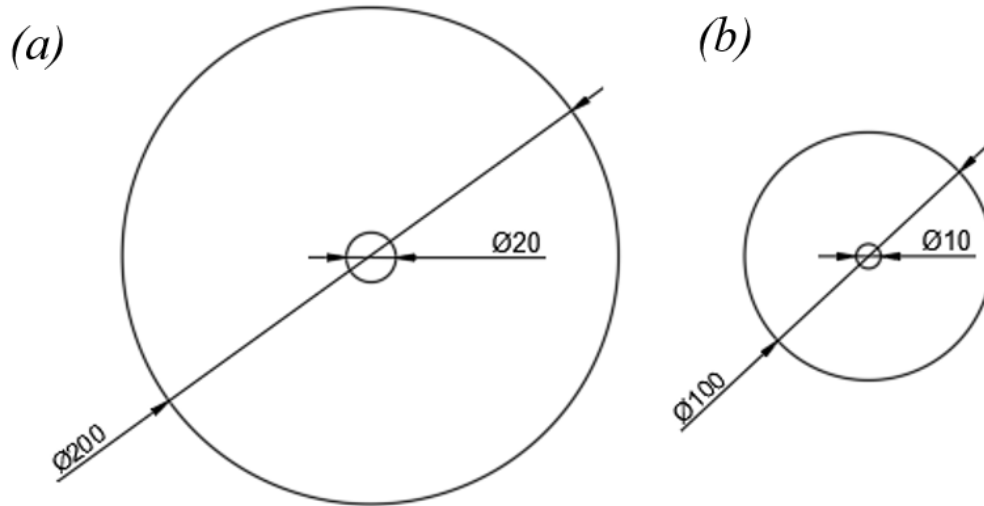


Figure 3. 3 Dimensioning of the hole expansion test specimen

Test samples deformed with (a) Nakajima and (b) conical punches

3.1.5 Hole expansion test and Erichsen cupping test

A Zwick/ Roell BUP 1000 sheet metal testing machine was utilised to ascertain the sheet metal formability. The fast and easy tool kit fixture substitution meant that different formability tests can be conducted on the BUP machine including; HET, forming limit test, earing test and Erichsen cupping test. A Zwick/ Roell BUP 1000 testing machine equipped with a maximum ram force of 1000kN was used in this project to perform the hole expansion tests and Erichsen cupping tests, Figure 3.4. The testXpert II software utilised permits for the test results to be evaluated and presented graphically. A GOM Aramis system with a 2448×2050 camera acquisition mode was used to capture the displacement of the speckle pattern during the deformation process. A GOM Aramis 5M (GigE) sensor type was used in this work. The cameras were calibrated in a snap mode using a CP20/90/D11557 standard calibration panel with calibration measuring volumes of $110\times 95\times 70\text{mm}^3$ and $90\times 72\times 77\text{mm}^3$ for the HET and the Erichsen cupping test samples respectively. For the HET, the cameras were inclined at an angle of 24.157° with scale and calibration deviations of 0.002mm and 0.023299 respectively at room temperature.

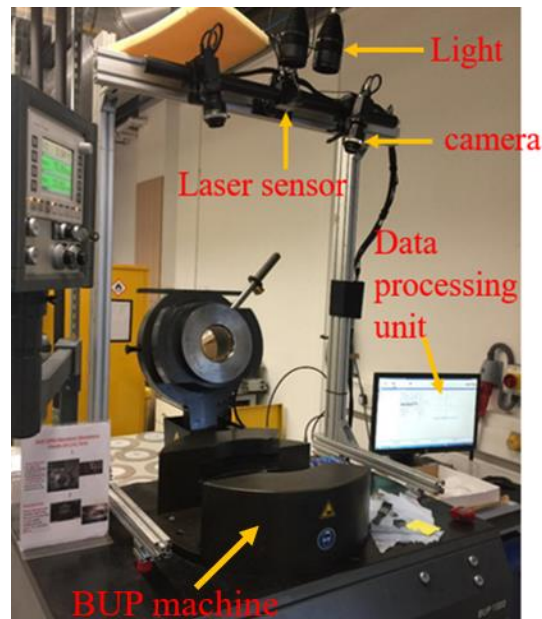


Figure 3. 4 BUP testing machining with an accompanying DIC installation

Two main types of tool geometry sets were utilised in this research to perform the HET on the titanium alloys. This allowed an investigation of the effect of the difference in sheet loading conditions offered by the varying tool geometries to be assessed in the light of the hole edge forming performance of the titanium alloys. Firstly, a traditional hemispherical punch with its accompanying die set used for Nakajima test to ascertain the forming limit of sheet metals was employed, Figure 3.5a. For subsequent test trials on the BUP machine, a conical punch fabricated with die set dimensions consistent with ISO 16630:2017 were also utilised to examine the hole edge formability of the titanium alloys, Figure 3.5b. Grease was used as a lubricant to minimise the effect of friction between the tool- blank interfaces.

The conical punch and its accompanying die set were manufactured from D2 tool steel after heat treatment to the required hardness (55HRC). The heat treatment regime adopted, the engineering drawings with their dimensioning as well as the GOM Atos optical non-contact measurements for assessing the tool integrity before and after the HET experimental trials are detailed in Appendix B. Mostly, wear analysis and the appraisal of structural deviations with respect to the reference geometry of the tools are representative assessment of the industrial quality assurance.

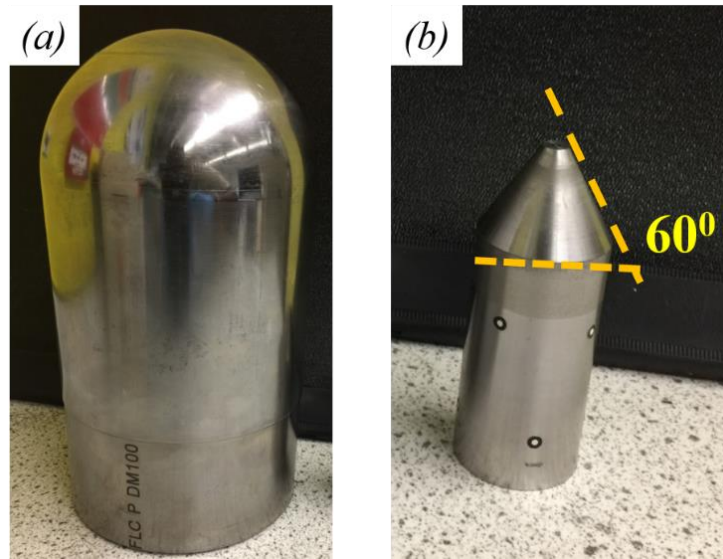


Figure 3. 5 Tool geometries utilised for HET of titanium alloys

(a) Nakajima punch, (b) conical punch

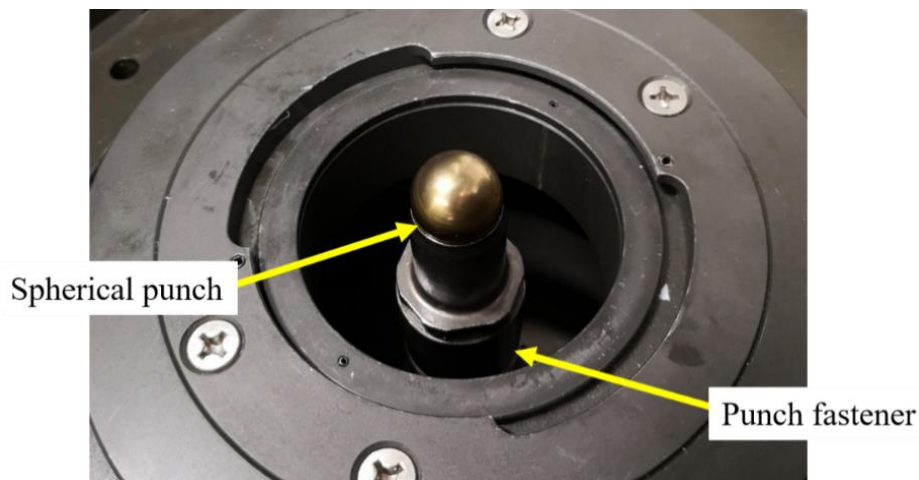


Figure 3. 6 Spherical punch for cupping test trial

An Erichsen cupping test consistent with ISO 20482 was performed on the fully constrained titanium sheets (maximum force of 250kN). During the cupping test trial, high blankholder force (1kN) was applied to prevent the sheet from slipping during the deformation process. A spherical punch (Figure 3.6) was used to deform the clamped sample until it fractured, Figure 3.7*b*. The HET was also performed in accordance with ISO 16630:2017. During the HET, the titanium sheet with pre-fabricated center hole was constrained with a blankholder force high enough (150kN) to prevent it from deep drawing. The constrained sheet was then deformed until an outer crack at the hole edge appears, Figure 3.7*d*.

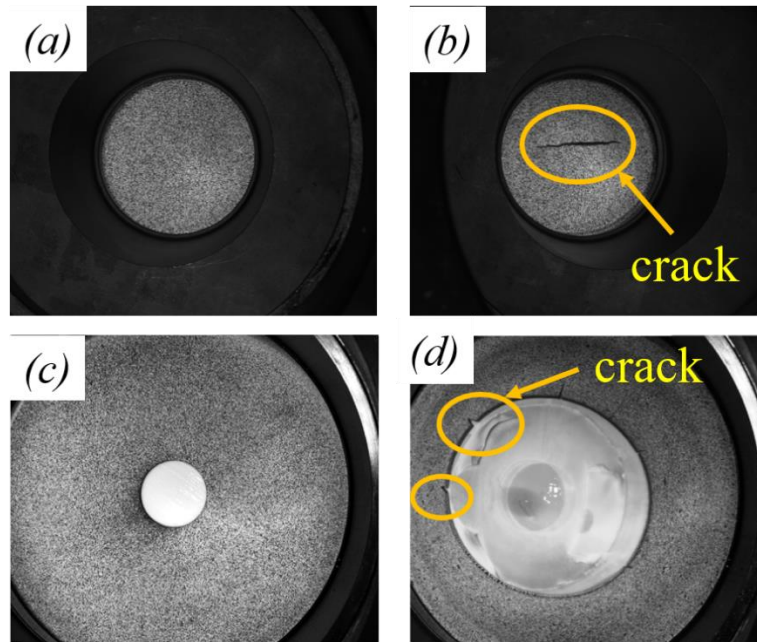


Figure 3. 7 Test termination criteria during HET and Erichsen cupping test

Erichsen test sample (a) before and after (b) test trial. HET test sample (c) before and (d) after test trials

3.1.6 GOM Atos metrology

GOM Atos optical non-contact measurement system was utilised to extrapolate the three dimensional visualisation of the deformed uniaxial tensile test samples as well as the hole expansion test samples. GOM Atos metrology was utilised to assess the thinning evolution after plastic deformation in this EngD research.

For the hole expansion test samples, an ATOS III Rev.02 sensor with an SO camera position and a CP40/MV320 standard calibration panel were utilised for the GOM Atos metrology scanning process. A measuring volume of $320 \times 240 \times 240 \text{mm}^3$ with a measuring point distance of 0.095mm was employed. A camera angle of 28° was adopted for a measuring distance of 490mm and a recommended reference point of 1.5mm . The focal length of the camera and projector lenses used were 24mm and 30mm respectively. Prior to the scanning process, the test samples were cleaned thoroughly in acetone and then sprayed with Ardrex 9D1B to minimise reflection of light on the test sample surface. The sprayed test samples were then clamped in position on a circular turning table for the onward scanning process. To ensure full scanning of the test samples, multiple reference markers were attached to the clamped sample prior to scanning. A GOM Tritop system was utilised to capture the location of the reference

markers. A GOM Atos system was then used to scan the surface areas of interest by using the reference marker file from the previous step to take multiple scans from either side of the test sample in order to capture the full surface. Polygonisation was then done by virtue of meshing the scans together using GOM Atos software. The GOM Atos software was then used to complete the analysis process.

0.8mm Reference marker

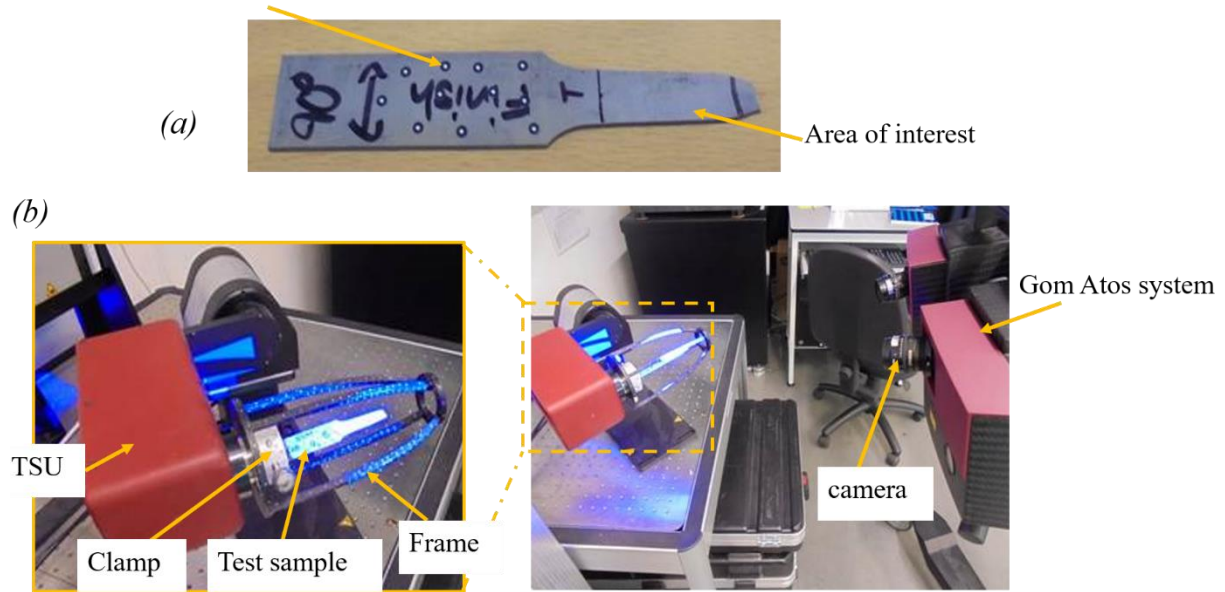


Figure 3. 8 GOM Atos set-up for tensile specimen measurement

(a)Tensile sample after spraying and marking, (b) TSU and GOM Atos scanning of part

For the tensile test samples, an ATOS III Rev.02 sensor with an SO camera position and a CP40/MV100 standard calibration panel were utilised for the GOM Atos metrology scanning process. A measuring volume of $100 \times 75 \times 70 \text{mm}^3$ with a measuring point distance of 0.031mm was employed. A camera angle of 28° was adopted for a measuring distance of 490mm and a recommended reference marker point of 0.8mm. The focal length of the camera and projector lenses used were 60mm and 90mm respectively. Prior to the scanning process, the test samples were cleaned thoroughly in acetone and then sprayed with Ardrex 9D1B to minimise reflection of light on the test sample surface. In attaching the reference markers to the test samples, it is imperative to avoid the areas of interest, Figure 3.8a. The test sample was then placed in a frame on the GOM Tilt Swivel Unit (TSU) while clamping on the grip section of the test sample. The test sample was then scanned using TSU and GOM Atos, Figure 3.8b. The test sample was then removed from the clamp and the area previously held in the clamp was also scanned. The scanned sample was then polygonised for the onward meshing of scans together.

Alignment and measurement of the scanned test sample was conducted using the GOM Atos software.

3.1.7 Speckle pattern fabrication

Speckle patterns in their role as the major conveyor of deformation information becomes a significant process during DIC computation. The quality characteristics of adopted speckle patterns are mainly based on intuition. However, a good speckle pattern must have high contrast, random/ isotropic appearance as well as strong stability on the surface (Dong & Pan, 2017). For a sample surface with varying intensity distribution and sufficient contrast, speckle fabrication could be omitted. Normally, surfaces with naturally good texture distribution can be employed to perform correlation computation (Sánchez-Arévalo & Pulos, 2008). Speckle patterns can be classified into two; natural texture and artificial speckle patterns (Dong & Pan, 2017). Natural texture on the test sample can be utilised to perform correlation computation. Natural textures are considered to be sample microstructure features including second phases, grain boundaries and inclusions (Dong & Pan, 2017).

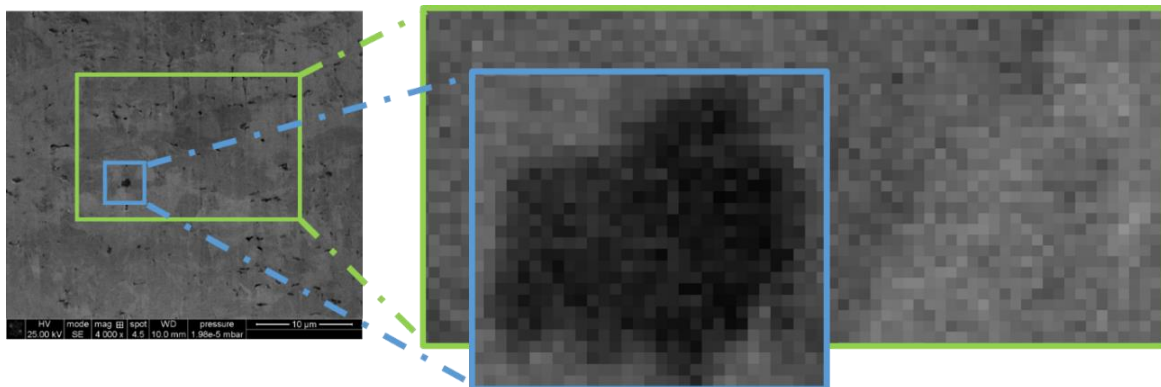


Figure 3. 9 SEM random grey intensity pattern of Ti-3Al-2.5V

These natural texture patterns are mostly adopted for analysis under SEM and optical microscopes with high magnification (Jin & Bruck, 2005). However, due to the difficulty in locating good pattern to promote accurate DIC matching with relatively small subsets, utilising microstructures as speckle particles have been reduced mostly to micro-scale measurements. Scanning electron microscope (SEM) image features were adopted in this thesis to compute the micro-scale localised strain evolution during an ex-situ tensile deformation of Ti-3Al-2.5V, Figure 3.9.

A white paint background sprayed with black dots on the test piece surface is one of the most adopted artificial speckle pattern fabrication methods (Pan, et al., 2009). For DIC computations on materials like ceramic matrix composites at high temperature, laser speckle patterns are employed (Meyer & Waas, 2015). Artificial speckle patterns depending on their fabrication type can be applied constructively or destructively. The constructive types have no impact on the surface integrity of the test samples during the fabrication process. They can be applied to mm-m scale level (e.g. Spraying and airbrushing) or with μm -nm scale level (e.g. Nanoparticle patterning, lithography and spin coating). Conversely, the destructive types have impact on the surface integrity of the test samples during the fabrication process. They are usually deployed in μm scale pattern fabrications (e.g. Chemical etching, abrading and scratching) (Dong & Pan, 2017).

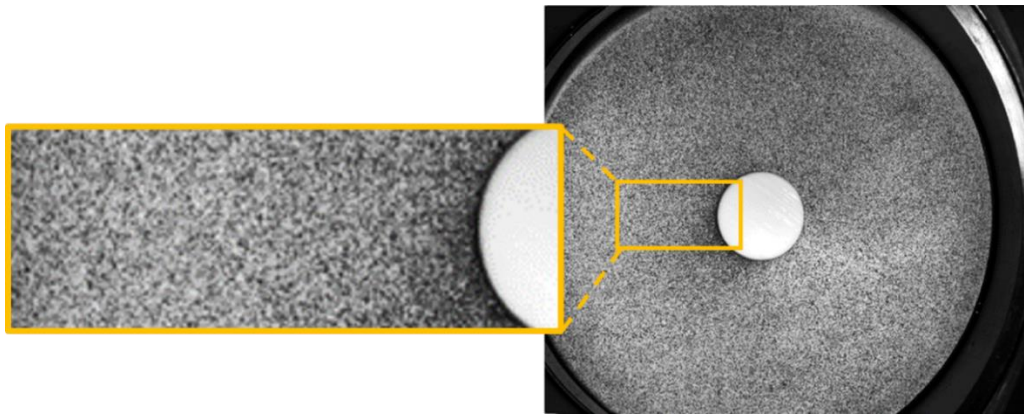


Figure 3. 10 Constructive speckle pattern of the HET sample

Constructive artificial speckle patterns were utilised in this work to prepare titanium sheet metals for HET, the Erichsen cupping test and uniaxial tensile tests. The white paint background with sprinkled black dot paint technique was adopted to produce random grey intensity pattern for the onward DIC computation, Figure 3.10.

3.2 Results characterisation and analysis methods

3.2.1 Image processing during ex-situ analysis of Ti-3Al-2.5V

The Ncorr version 2.1.1 software was developed on Matlab 2009 and applicable on version above it with image processing and statistics as additional toolbox requirements. The software also functions well with either Windows or Linux operating systems (Blaber, 2017). A Matlab R2018a version was employed in this EngD research to execute the Ncorr version 2.1.1 software for the onward DIC computation. A C++ compiler was installed to access the

multithreading capability of the software. The folder containing the Ncorr package was then uploaded into Matlab R2018a version. In the Matlab command window, ‘*handles_ncorr=ncorr*’ was typed and operationalised. Two logical cores were selected for the ‘*OpenMP*’ dialogue window in order to ensure that the computer operation was not compromised during the computation period. A successful compilation of the files opens the graphic user interface of Ncorr for onward DIC analysis. The ‘*reference image*’ was then loaded into the Ncorr graphic user interface with a resolution of 1024×943, Figure 3.11. The reference image is an undeformed image, which is used as a reference frame for correlating the subsequent deformed elements. For the ‘*current image*’ window, the images uploaded were arranged according to the order of deformation. Thus, the images were uploaded with ascending order of deformation strains. A current image window can be navigated to ensure that the uploaded images are arranged in the right order of deformation, Figure 3.11.

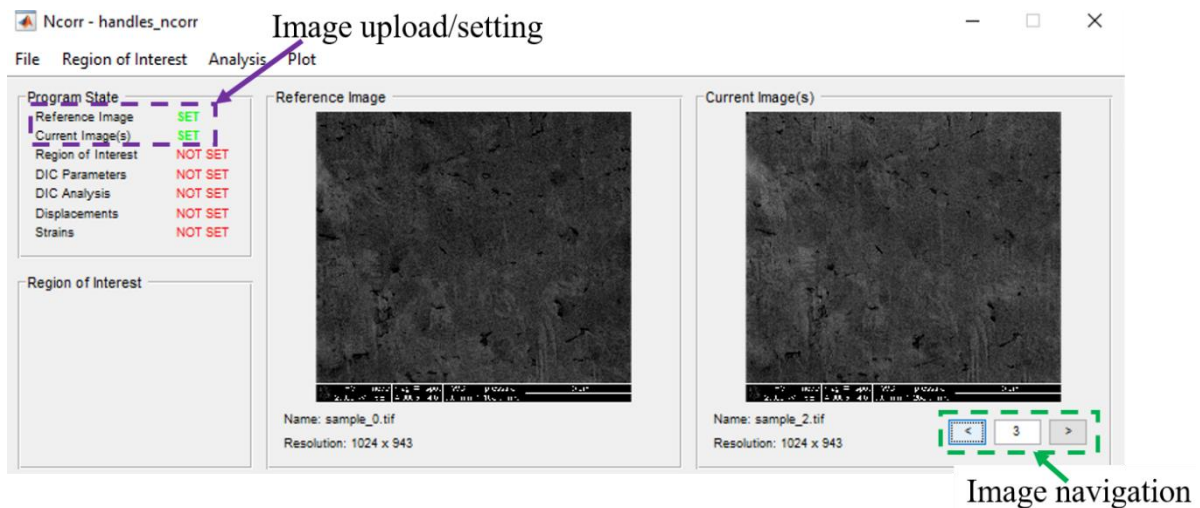


Figure 3. 11 Ncorr graphic user interface

The ‘*region of interest*’ was set with respect to the reference image by drawing it directly in Matlab. The ‘*DIC parameters*’ were then set with subset radius of 28 and subset spacing of 1, utilised to attain optimum resolution. The green *impoint* represents the center of the subset location, Figure 3.12a, which were amplified to provide details of the subset spacing, Figure 3.12b. ‘*DIC analysis*’ was performed by selecting a region for continuous processing. This was done by placing the *impoint* at the preferred region for onward processing. This was followed by seed placement, which provides initial guesses for the reliability-guided (RG) DIC analysis (Blaber, 2017). Seed placement during DIC analysis must satisfy the following criteria (Blaber, 2017); firstly, seed placement must be done in such a way that they are not displaced out of the field of view during deformation. Secondly, for a particular seed placement the region of

interest must be evenly partitioned. One seed set was placed within the region of interest for the onward DIC analysis. A seed preview was conducted in the Ncorr graphic user interface to check if the placed seeds were processed correctly. The criteria for assessing the correctness of the seed placement is the appropriate matching of the seed location in the reference image to those observed in the current images. In addition, similarities were observed between the reference and transformed subsets, Figure 3.12c.

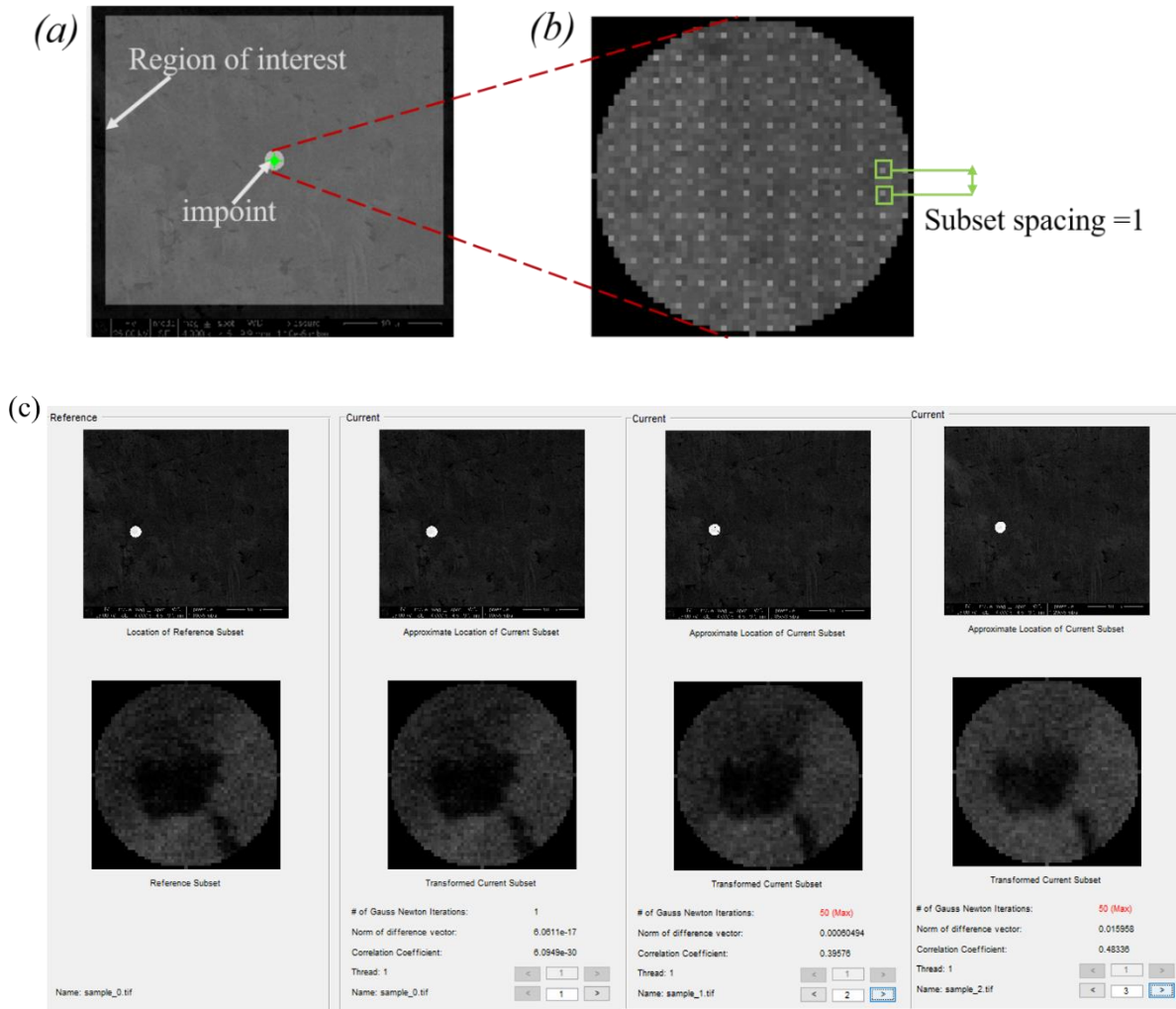


Figure 3. 12 DIC analysis

(a) DIC parameter setting, (b) subset spacing, (c) seed preview

The u and v displacement formatting was done in the main Ncorr graphic user interface. Unit conversion from pixels to real units was done by loading the reference image for onward calibration. A line set was drawn across the micrograph scale. For the 'unit option' tap, the unit was set to millimetres (mm) and the 'number of units' set to 6. Since the examined notched tensile sample has a gage width of 6mm, the appropriate conversion of displacements from pixels to mm is 0.022695mm/pixel, Figure 3.13.

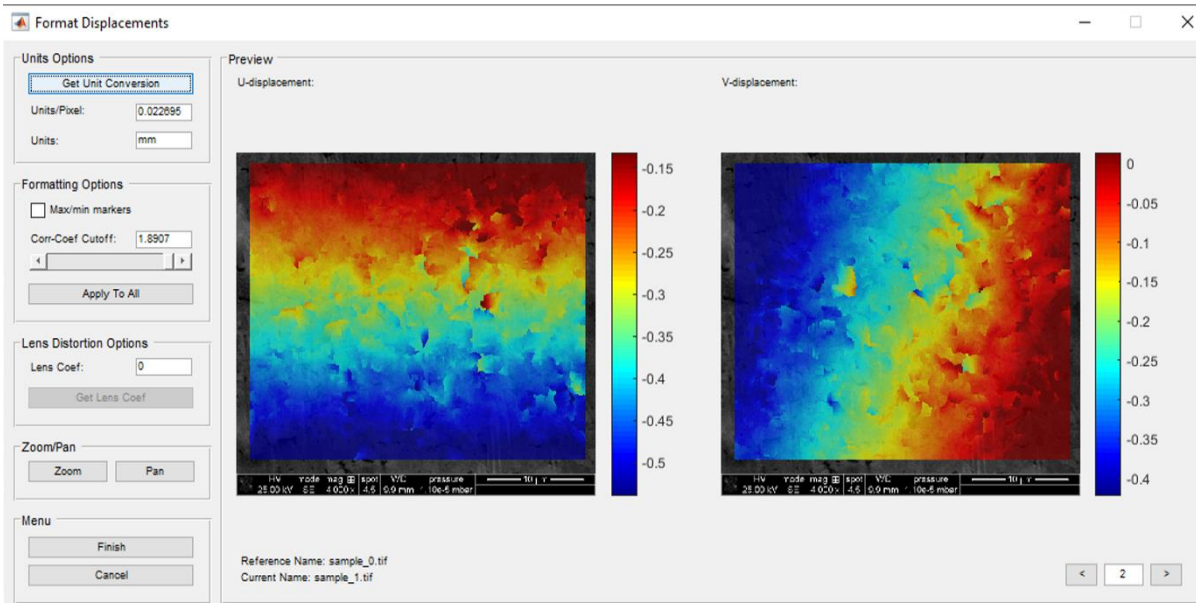


Figure 3. 13 Ncorr graphic user interface for unit conversion during displacement formatting

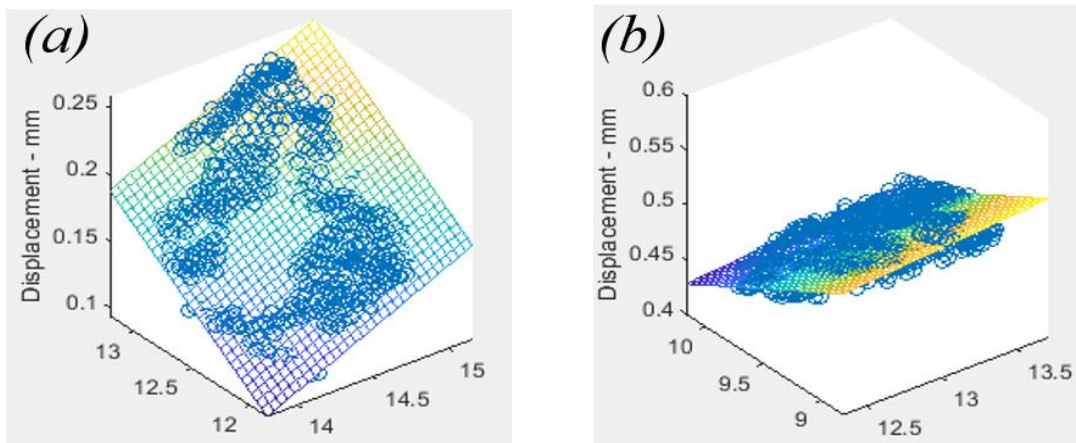


Figure 3. 14 Plane fitting for strain radius 15 with Lagrangian view option

(a) v -displacement, (b) u -displacement

Strain analysis was conducted in the Ncorr graphic user interface. The strains are computed from the displacement information by utilising the least squares plane fit to a local group of data points governed by Bing Pan's strain computation (Blaber, 2017). The displacement gradients are obtained from the plane parameters and are employed for computing the Green-Lagrangian and Eulerian-Almansi strains (Blaber, 2017). The strain radius elects a group of points, which are utilised for the plane fitting. Hence, the choice of strain radius capable of reducing noise in the strain data is critical. *Impoint* was placed on the displacement map with higher deformation (image with highest displacement gradient) to observe how the elected points fits the plane, Figure 3.14. Strain radius of 15 reduces noise in the strain data for the

analysed displacement maps. The strains were then plotted for the onward analysis of the deformation strain evolution.

3.2.2 Statistical evaluation: ANOVA analysis

Analysis of variance (ANOVA) are conducted to ascertain the difference in the means of three or more unknown populations by separating the variability subject to some factors of interest and error. One-way ANOVA deals with the comparison of variable means identified by only one other variable known as a *factor*. The number of possible values identified for a *factor* are referred to as *levels of factor* (Sally, 2019). In order to establish if the edge surface roughness Ra values attained after machining were linked to the nature of the machining qualities, one-way ANOVA was employed to compare the variability in group means. One *factor* (machining type) with three *levels of factor* (finished surface, unfinished surface and semi-finished surface) were identified with a *continuous response variable* (edge surface roughness, Ra). For all test cases, statistical significance when $p < 0.05$ was assumed. The data for each designation was put into separate columns in a new worksheet in Minitab software with the respective columns duly labelled.

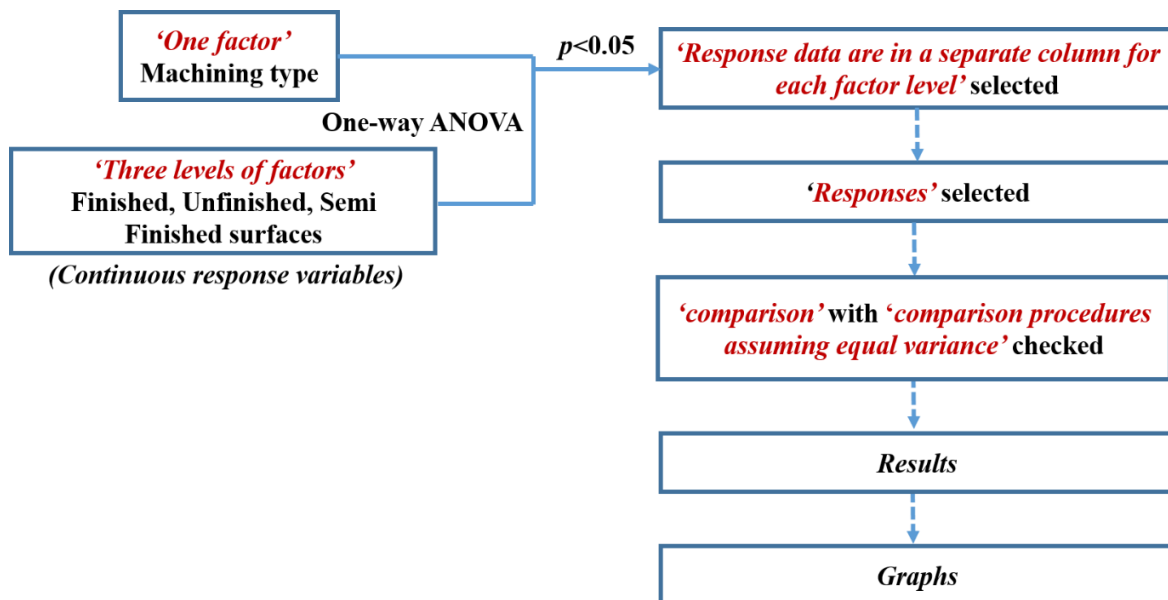


Figure 3. 15 Flowchart of the one-way ANOVA

The Minitab software was navigated and one-way ANOVA was selected. ‘*Response data are in a separate column for each factor level*’ in the Minitab graphic user interface was selected. For the ‘*Responses*’ tab, unfinished, semi-finished and finished data was selected. The ‘*comparison*’ tab was clicked and all boxes checked under ‘*comparison procedures assuming*

equal variance'. The *'Results'* tab was also checked for all checkboxes. For the *'graphs'* tab, all checkboxes were checked for *'data plots'* and *'three in one'* checked for *'residual plots'*. All dialogue boxes were clicked ok for the onward computation of the statistical parameters. The flowchart of the procedure followed during the one-way ANOVA analysis is shown in Figure 3.15.

For ANOVA analysis with post-hoc comparisons, Tukey's method was employed in this research. This method was created to conduct all pairwise comparison of means and at the same time preserving the error rate of the pre-determined significance level. This method is based on *q*-test statistics and is largely regarded as the most suitable test method in a wide array of situations. Even though it utilises a single critical value in all comparisons, it is rather conservative (Brown, 2005). The ANOVA test was conducted to compare the mechanical properties of CP-Ti (Grade 2) generated from EDM and AWJ machined tensile samples. The material property evolution was tested in three sheet-rolling directions (0°RD, 45°RD and 90°RD with respect to the sheet rolling direction). The data were arranged in three columns on a new worksheet in Minitab software and labelled.

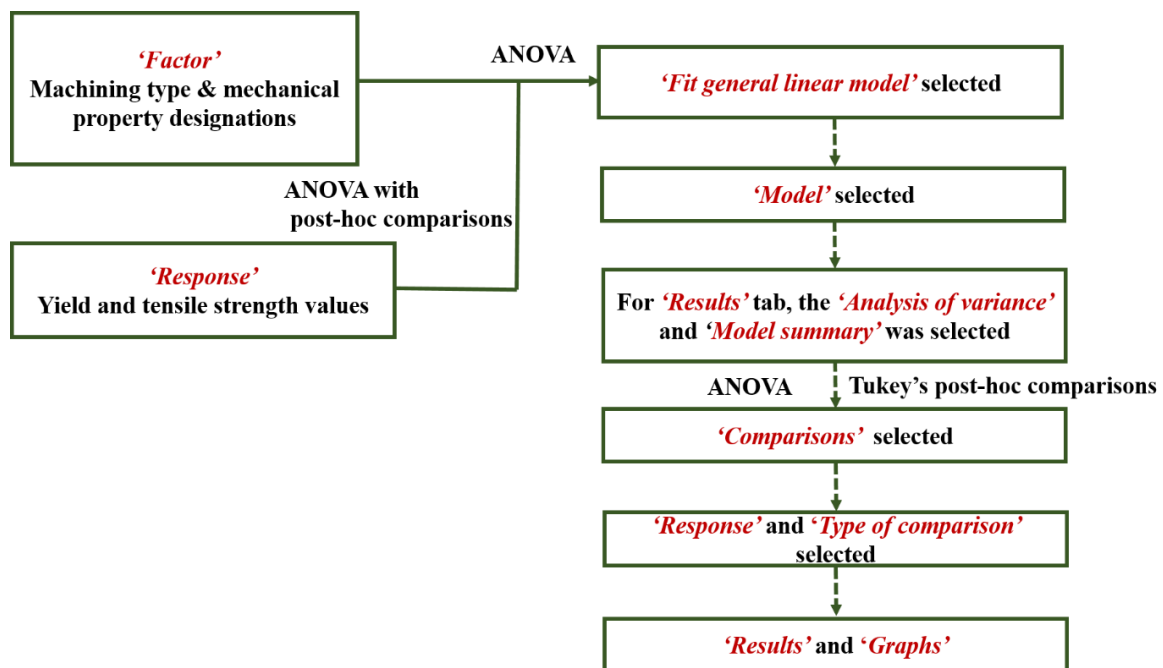


Figure 3. 16 Flowchart of ANOVA analysis with post-hoc comparisons

In the Minitab graphic user interface, ANOVA was navigated and *'Fit general linear model'* was selected. The tensile and yield strength values (put together in the same column) were selected in the *'Response'* tab and the machining type and mechanical property designations were selected in the *'Factors'* tab. The *'Model'* tab was clicked and the two factors were

highlighted. The chosen factors were added to the model. In the ‘*Results*’ tab, the ‘*Analysis of variance*’ and ‘*Model summary*’ was selected. For the post-hoc test, Tukey’s post-hoc comparisons method was employed. ANOVA was navigated and ‘*Comparisons*’ selected. The terms for comparison were selected and Tukey’s method also selected. The ‘*Response*’ tab was kept on the yield and tensile strength values and pairwise was chosen for the ‘*Type of comparison*’ tab. All dialogue boxes were clicked ok for the onward computation of the statistical parameters. The flowchart of the procedure followed during the ANOVA analysis with post-hoc comparisons is shown in Figure 3.16.

3.2.3 Regression model development in R programming

R programming language is a particular sub-language of the S programming language. The early development of the S programming language were originally executed as FORTRAN libraries. Advancement in technology saw S programming transition to C programming language in the late 1980s. Further improvement led to its development as S-Plus package. However, what is instructive is that the philosophical roots of S-Programming are derived from a data analysis background rather than programming language. A problem with the S-programming language is that it is only available as the S-Plus commercial package. R Programming on the other hand is an open source, freely available and are easily adapted to computer platforms and operating systems (Peng, 2018). One major virtue of R-programming is that when regression functions are called during run time, its object-oriented nature allows for the return of the results with all statistical parameters as opposed to other statistical packages (e.g. SAS or SPSS) where a large pile of results flood the screens. R-programming language is a block-structured language comparable to the algorithm language-progeny (C, C++, Python, etc.) with the blocks portrayed in braces. Statements written in R-programming are partitioned by newline characters and in some cases by semi-colon (Matloff, 2011).

3.2.4 Experimental data exploration and regression model expressions

Using plots or graphics to visualise data can be vital during the initial stages of data analysis in order to ascertain the fundamental data properties, establish simple data patterns and to propose a potential modelling strategy. Scatter plots are effective tools for data exploration with

enhanced capability of transforming variables (e.g. logarithmic scale) for successful visualisation (Peng, 2015).

HER is the standard metric used to assess the edge formability of materials. The Erichsen index number (*EI*), obtained after conducting Erichsen cupping tests on the titanium alloys and the material thickness (*t*) values were used in this research to propose a regression model expression capable of predicting the hole edge forming performance of the studied materials. In order to build the regression model expression, the predictor and response variables were explored in order to establish the relationship that exists between them. A scatter plot was utilised as the exploratory data analysis tool for interrogating the relationship between the response and predictor variables, Figure 3.17. The relationship observed between the HER and *EI* was largely linear with $R^2=0.7734$, whereas the relationship between HER and *t* was very cumbersome to discern with $R^2=0.427$, Figure 3.17. From the observation made after the exploratory data analysis, a linear regression model was utilised to develop the regression model expression, capable of capturing the relation between the predictor and the response variable for the onward generation of regression equations and the prediction of HER values of titanium alloys.

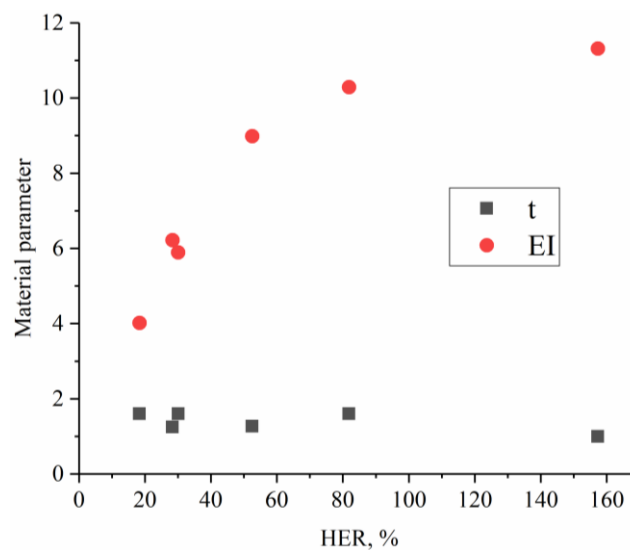


Figure 3. 17 Scatter plot for exploring the relationship between the response and predictor variables

Based on the discerned data trend, R codes were written to express the relationship between the response and the predictor variables. The object-oriented nature of the R programming means that the data dynamics can be well explained in order to attain the desired results. Figure 3.18 shows the graphic user interface of the R codes adopted for the initial linear regression

model expression proposed for the onward prediction of the HER values of titanium alloys. The statements written for the onward execution in R programming language were separated into four newline characters, Figure 3.18;

- 1) The upload data statement; where the experimental data source containing the HER, EI and t values are uploaded into the software.
- 2) Model fitting statement; a proposed linear regression model expression for fitting the data uploaded into the software in step (1). This regression model expression generates regression model equations based on the input variables.
- 3) Creating new data statement; a new data with known EI and t values are inserted for the onward execution of the unknown HER value of an alloy of interest.
- 4) Predicting with new data statement; this statement executes (based on generated regression equation) the HER values of the input parameters in step (3).

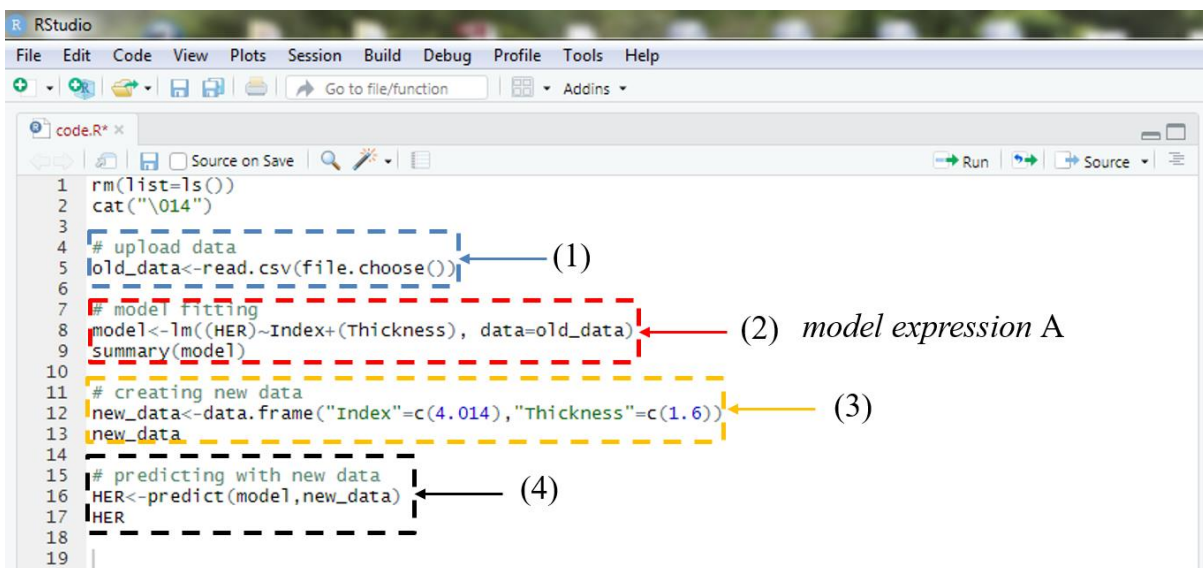


Figure 3. 18 Graphic user interface for model expression A

Figure 3.19 shows the statistical parameters generated after executing the proposed linear regression model for model expression A in R programming. It spells out the statistical indicators for assessing the model performance and reveals the coefficients of the formulated regression model equation. A significant test, based on the enumeration of p -value with statistical significance level accepted at $p < 0.05$ was employed in this work.

Response on console –Model expression A

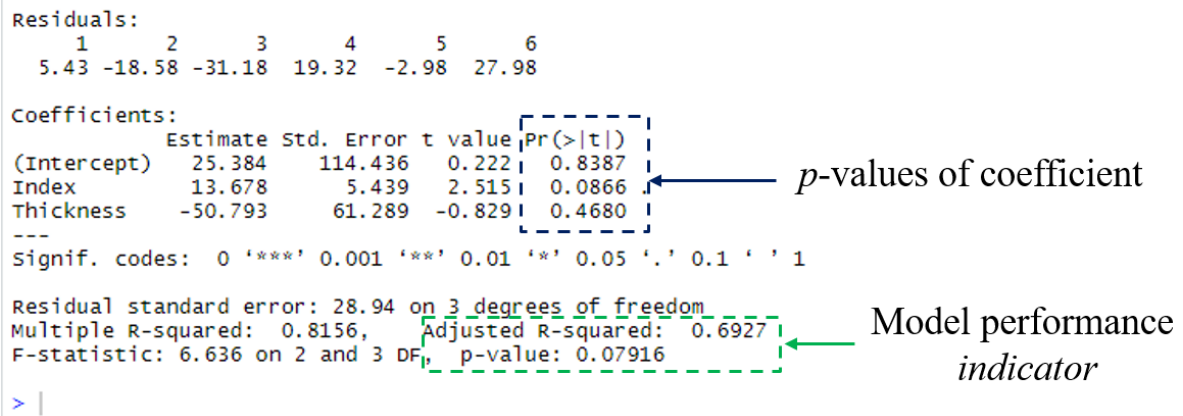


Figure 3. 19 Statistical parameters for model expression A

A statistical significance level implies how well the regression model fits the given data. According to Verzani, p -values ranging from 0.05-0.1 could be significant (Verzani, 2014). The overall p -value obtained for Model expression A, examined for the given experimental data was 0.0792 (greater than 0.05) showing the low ability of the proposed regression model expression to effectively fit the data. The p -values for the generated model coefficients were also greater than 0.05 with an overall R^2_{Adj} of 69.3%.

An improvement on model expression A was proposed by introducing functions capable of compensating for the non-linearity in the data fitting process. Figure 3.20 shows a revised model expression B, where logarithmic and polynomial functions were introduced to capture as well as account for the non-linearity that exist in fitting the experimental data. Same procedure was followed as stated for Figure 3.18 (model expression A) for the onward generation of regression model equations capable of predicting the HER values of titanium alloys based on the model expression B.

Figure 3.21 shows the statistical parameters indicating the model performance of the proposed linear regression model expression B. The overall p -value obtained for Model expression B examined for the given experimental data was 0.0007731 showing the high ability of the proposed regression model expression to effectively fit the data.

According to Verzani, p -values ranging from 0-0.001 are extremely significant (Verzani, 2014). The p -values recorded for the model coefficients were also less than 0.05 showing how well the coefficients described the data with an overall R^2_{Adj} of 99.9%.

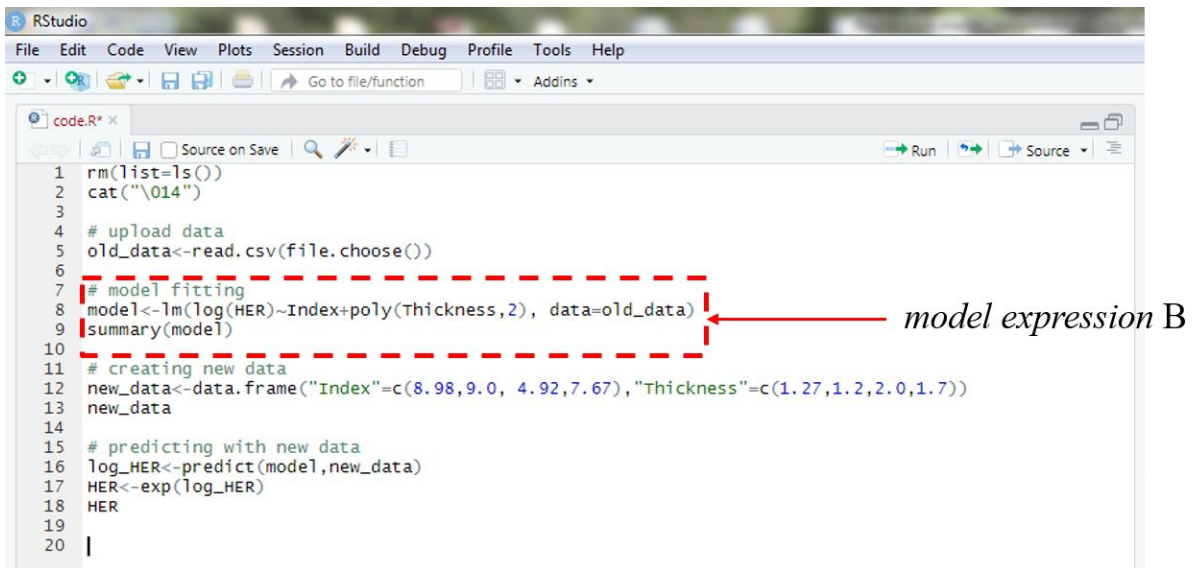


Figure 3. 20 Graphic user interface for model expression B

Response on console –Model expression B

```

Residuals:
    1      2      3      4      5      6
0.0297137 0.0070291 -0.0069029 -0.0240068 -0.0055293 -0.0003037

Coefficients:
              Estimate Std. Error t value Pr(>|t|)
(Intercept)  2.014525   0.045263  44.507 0.000504 ***
Index        0.235445   0.005624  41.864 0.000570 ***
poly(Thickness, 2)1 -0.223388   0.034304  -6.512 0.022779 *
poly(Thickness, 2)2  0.377374   0.029918  12.613 0.006227 **
---
signif. codes:  0 '***' 0.001 '**' 0.01 '*' 0.05 '.' 0.1 ' ' 1

```

Residual standard error: 0.02817 on 2 degrees of freedom
Multiple R-squared: 0.9995, Adjusted R-squared: 0.9987
F-statistic: 1310 on 3 and 2 DF, p-value: 0.0007631

Figure 3. 21 Statistical parameters for model expression B

3.2.5 Model predictive power assessment

Research by Cattin stated that the mean squared error of prediction and the cross-validated multiple correlation are the two commonly adopted methods for assessing the predictive powers of a regression model (Cattin, 1980). The cross-validation method was employed in this work to assess the predictive power of model expressions A and B. The six data sets were divided into two portions. One portion comprised data of the material of interest with known EI and t values. There was a deliberate omission of the HER value for onward comparison and validation. The other portion of the data was the other five data set with full values of HER, EI and t for calibration. The five data set were then uploaded as stage (1) as explained in Figure

3.18. The regression model expression was run to generate the regression model equations and statistical parameters. The data of the material of interest with known EI and t values were inserted at stage (3) as explained in Figure 3.18. Stage (4) was run in the software to generate the predicted HER value for comparison with the experimental HER and validation. This process was repeated for both model expressions A and B as well as all materials studied in this research and the results are displayed in Table 3.1.

Kotkunde et al., in their work employed the correlation coefficient, average absolute error and standard deviation statistical parameters as metrics for measuring the predictability of constitutive models (Kotkunde, et al., 2018). The correlation coefficient R, statistical parameter explains the strength of linearity that exists for the relationship between the predicted and experimental values.

Table 3. 1 Comparison of model predictability using cross-validation method

Material	Experimental HER,%	Predicted HER,%	
		Model expression A	Model expression B
CP-Ti ;Grade 2	81.87	98.96325	84.647
Ti-3Al-2.5V (1.6)*	30.096	22.09155	28.726
Ti-3Al-2.5V (1.25)*	28.357	60.98542	27.887
Ti-6Al-4V	18.344	-22.10734	19.574
Ti-21S	52.529	92.36625	53.4304
Ti-35A	157.317	69.15988	231.597

()*-Thickness in mm

However, a higher correlation coefficient does not necessarily indicate high model performance (Kotkunde, et al., 2014), since it has the tendency of being biased towards lower or higher values for a given data set. Hence, correlation coefficient statistical parameter is not a very strong statistical parameter (Kotkunde, et al., 2014). The average absolute error on the other hand is not data biased, and are calculated via comparing the relative error for each term (Kotkunde, et al., 2018). In order to understand how well the regression line fits the given data, the coefficient of determination R^2 is employed. According to Palmer and O'Connell, the main goal for selecting a good model is based on their ability to reduce the number of predictors, which produce high variance in the criterion. Thus, efficient models are those, which maximises the coefficient of determination R^2 . The higher the R^2 , the lower the error and the better the model predictability. In essence, the aim of model selection is to produce a model capable of realising the highest estimated value for R^2 (Palmer & O'Connell, 2009). However, R^2 is a data bias statistical parameter and could improve with increased data size. In order to

correct the flaws posed by R^2 and eliminate the tendency of increasing the predictor variables to obtain higher R^2 values, the adjusted R^2 (R^2_{Adj}) are adopted to avoid spurious relationships (Verzani, 2014). The multiple correlation coefficient R explains the relationship between the predicted and the experimental/observed values. If $R=1$, then no difference exists between the predicted value and the experimental/observed value. Thus the closer the R -values are to 1, the higher the accuracy of prediction (Palmer & O'Connell, 2009).

The statistical parameters adopted to assess the predictive capability of the two linear regression models proposed for the onward prediction of HER values of titanium alloys are shown in Table 3.2. Model expression B shows a higher level of accuracy of fit ($R=0.9884$) compared to model expression A ($R=0.5063$). In addition, the proximity of the R -values in model expression B to 1 compared to Model expression A shows that very little difference exists between the predicted and the experimental HER values. This proximity of R -values of Model expression B to 1 also indicates its higher accuracy of prediction compared to Model expression A. Model expression B also showed higher capability of the formulated regression model expression of fitting the data ($R^2_{Adj}=0.9987$) with reduced average absolute error (8.8%) compared to model expression A ($R^2_{Adj}=0.6927$ with average absolute error of 14.9%). Model expression B also showed very high overall p -values (0.0007631) signifying the high robustness of the model to fit the data and predict the HER values of titanium alloys compared to model expression A (overall $p=0.07916$).

Table 3. 2 Comparison of statistical parameters

Model type	Average absolute error, %	R^2_{Adj}	p-value	Correlation coefficient, R
Model expression A	14.912	0.6927	0.07916	0.5063
Model expression B	8.8	0.9987	0.0007631	0.9884

Considering the performance of both model expressions based on how their statistical parameters compared, Model expression B outperforms its competitor (Model expression A).

Therefore, Model expression B was presented as the proposed regression model expression suitable for predicting the HER of titanium alloys in this EngD research.

3.3 Summary

- The accuracy of the machining methods adopted to prepare the titanium sheets for mechanical testing are governed by industry standards (EDM- BS ISO 14137:2015 and laser- ISO 9013). Mechanical tests conducted were also consistent with international testing standards (HET- ISO 16630:2017, tensile test- ISO 6892-1:2016 and Erichsen cupping test- ISO 20482).
- GOM Atos metrology was utilised to extrapolate the 3D visualisation of the test samples after failure. Polygonisation was conducted to mesh the scanned samples for onward thinning evolution assessment.
- The natural texture of the SEM image was used to compute the local strains after ex-situ tensile test. Also, speckle patterns in the form of white paint background with sprinkled black dots were adopted during the HET and the Erichsen cupping test to compute the surface strains. Both grey level intensity patterns were used in the DIC analysis in their role as the major conveyors of deformation information.
- The Ncorr software utilises the Green-Lagrangian strains, which are obtained from the displacement gradients. Generally, the strains are cumbersome to resolve compared to the displacement field since they involve differentiation which is susceptible to noise. Therefore, plane parameters are obtained by applying a least square plane fit on the subset displacement data during which, the strain radius can be estimated for the onward computation of the strain.
- ANOVA analysis in Minitab was conducted to compare group means of sheet edges prepared with either AWJ or EDM as well as their corresponding mechanical deformation parameters to ascertain if there were any statistically significant difference between them.
- A linear regression model expression was formulated in R programming language to forecast the HER of titanium alloys. The choice of linear modelling was based on an initial data exploration using scatter plots to discern the relationship between the predictor and the response variables. Non- linearity in the data fitting process was captured by introducing polynomial and logarithmic functions.

Chapter 4

Effect of machining induced edge defects on the tensile deformation of CP-Ti sheet at room temperature

Overview

Non-conventional machining methods are adopted industrially due to their tendency to produce better surface finish and also eliminates the tool-part contact related issues associated with traditional machining. Dimensioning for uniaxial tensile test sample fabrication are well defined with standardised systems (eg. ASTM E8-04). However, there is no clarity on the ideal machining methods as well as the quality of edge surfaces, governing test sample preparation for tensile testing. This chapter assesses the nature of EDM and AWJ machining induced edge surface defects and their effect on the tensile properties of CP-Ti (Grade 2). Analysis of variance in Minitab was utilised to compare differences in group means for the machined edge qualities as well as the attained mechanical properties for both manufacturing methods. There was no statistically significant difference between the tensile deformations for the two machined edges. A DIC method analysis of the tensile deformation process found that the strains were majorly concentrated within the bulk material and away from the machined edges.

4.1 Experimental procedure

4.1.1 The material

The material studied in this section is a CP-Ti (Grade 2) with a sheet thickness of 1.6mm. CP-Ti (Grade 2) exhibits an excellent strength to weight ratio and has the tendency to retain its strength substantially during deformation. Notable among their use in the aerospace industry is their adoption in airframe skin application (Peters, et al., 2003).

4.1.2 Microstructure characterisation and chemical composition

EBSD technique was conducted on an electropolished as-received sample to ascertain the material grain morphology and structure. Results after the electron microscopy analysis revealed fine equiaxed alpha grained structure with an average grain size of $5.7 \pm 0.5 \mu\text{m}$ evaluated with misorientation angle below 2° not considered, Figure 4.1. This average grain

size value is consistent with the ASTM grain size number 12 governed by ASTM E112:2010. The band contrast discloses the quality between the Kikuchi bands and the background contrast quality utilised for the EBSD image acquisition, Figure 4.1. Band contrast is essentially the measure of the intensity of the Kikuchi bands (Claves & Deal, 2005). The chemical constituents of the researched material is shown in Table 4.1.

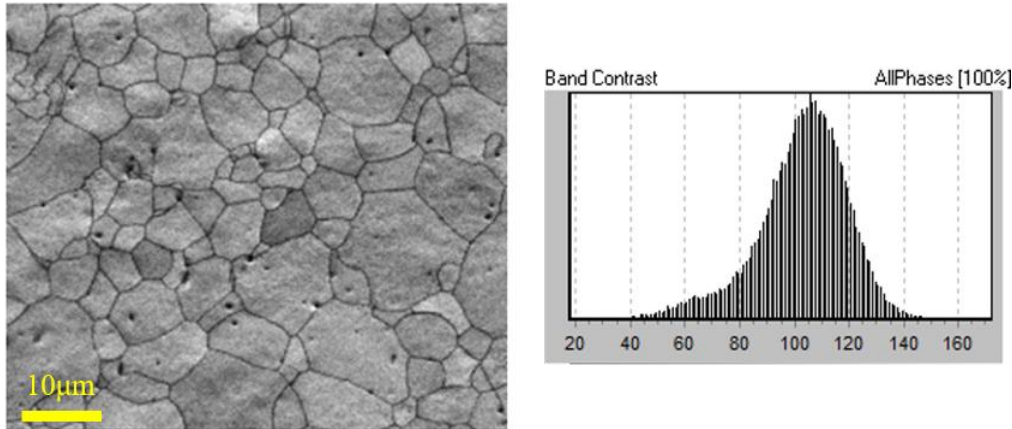


Figure 4. 1 EBSD micrograph of the as-received CP-Ti (Grade 2) sheet

Table 4. 1 Alloying constituents of CP-Ti (Grade 2)

Alloying elements	Ti	N	C	H	Fe	O
Composition, wt% (Max)	Balance	0.03	0.08	0.015	0.30	0.25

4.1.3 Edge preparation methods and characterisation

The extent of edge surface degradation after EDM and AWJ cuttings were characterised using an Alicona infinite focus microscope equipped with an Alicona measure suite 5.3.1 software. The AWJ machined tensile specimens were prepared using a Calypso water jet cutting machine furnished with a 70 Horse power pump and powered by an abrasive feed rate of 400g/min. The transverse cutting speeds (250, 400 and 600mmmin⁻¹ for finished, semi-finished and unfinished edges respectively) were varied to attain three distinct edge surface finishes (finished Ra~3.76µm, unfinished Ra~7.66µm and semi-finished Ra~5.42µm). The EDM machined test samples were prepared using a GF FI 440 CCS machine furnished with a 0.25mm diameter brass wire. Three different edge surface finishes (finished Ra~0.85µm, unfinished Ra~3.67µm and semi-finished Ra~1.89µm) were attained by varying the pulse off and on duration times (0.7, 0.1 and 0.05µs for unfinished, semi-finished and finished edges respectively) as well as

the wire tensions ($1.3 \times 10^1 \text{N}$, $2 \times 10^1 \text{N}$ and $2.8 \times 10^1 \text{N}$ for unfinished, semi-finished and finished edges respectively).

A 3D analysis of the image files imported from Alicona microscope was performed using OmniSurf 3D software. A bilinear fill was utilised with Gaussian short (0.0025mm) and long (0.8mm) filters as well as a transmission band of 300:1. This allows for the visualisation of the surface profile. The 3D surface morphology of both EDM and AWJ machined edges were majorly characterised by grooves and peaks, Figure 4.2 and 4.3. Hence, the maximum pit height (S_v) surface texture parameter was utilised to quantify the edge surface area roughness values.

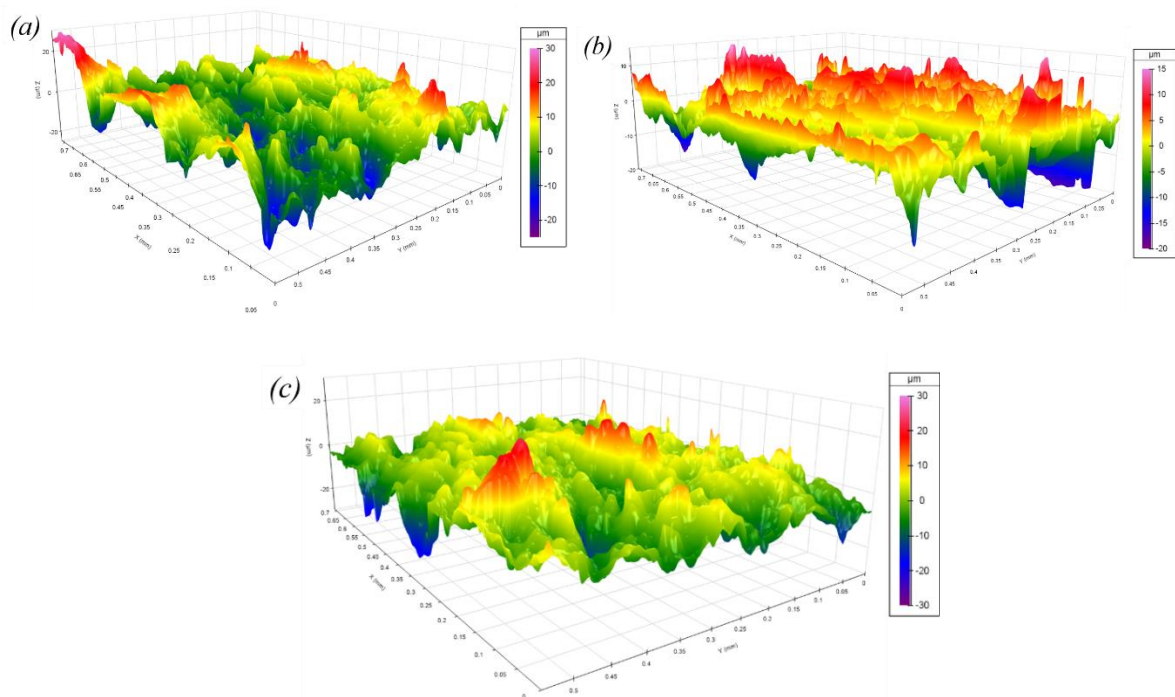


Figure 4. 2 3D surface morphology of the AWJ machined edges

(a) Unfinished edge (b) Semi-finished edge (c) Finished edge

For the measured surface texture parameters of the AWJ machined edges, the highest S_v value was recorded in the unfinished edge surface ($23.73 \mu\text{m}$) followed by the semi-finished ($20.78 \mu\text{m}$), with the finished edges ($18.60 \mu\text{m}$) producing the least maximum pit height, Figure 4.2 *a,b,c*.

For the measured surface texture parameters of the EDM machined edges, the highest S_v value was recorded in the unfinished edge surface ($13.58 \mu\text{m}$) followed by the semi-finished ($8.40 \mu\text{m}$), with the finished edges ($5.55 \mu\text{m}$) producing the least maximum pit height, Figure 4.3 *a,b,c*.

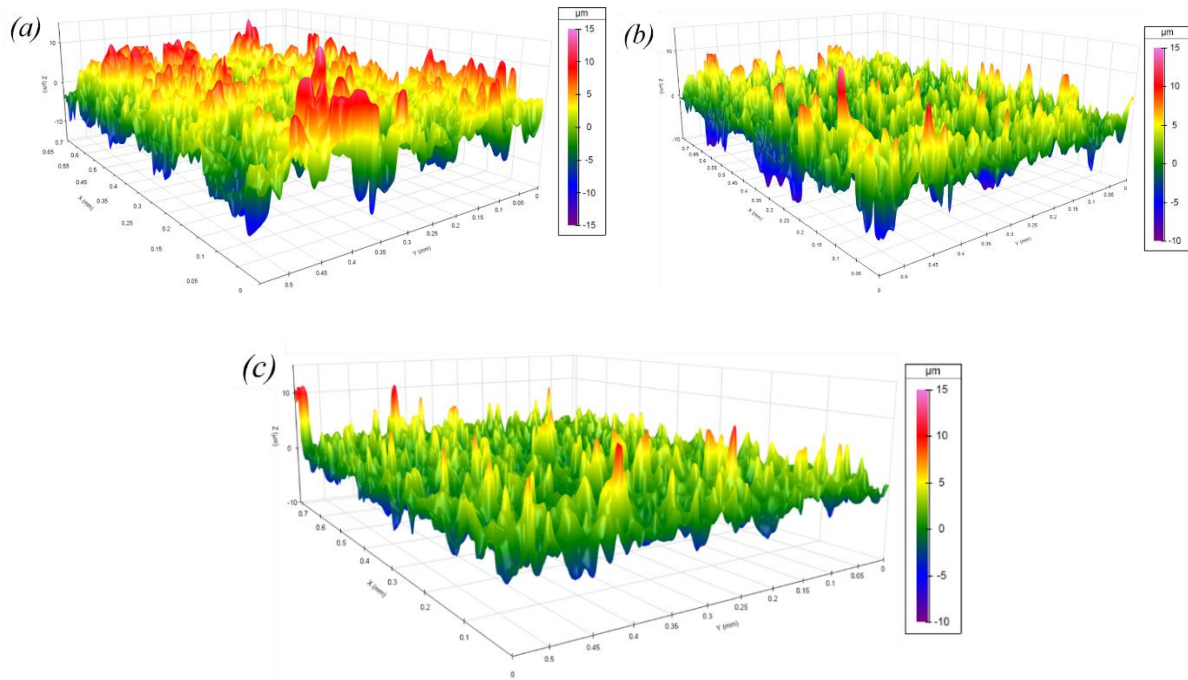


Figure 4. 3 3D surface morphology of the EDM machined edges
 (a) Unfinished edge (b) Semi-finished edge (c) Finished edge

4.1.4 GOM Atos measurement

GOM Atos optical non-contact measurements were carried out on the EDM and AWJ fabricated tensile samples after uniaxial tensile deformation to ascertain the thinning evolution along the gage sections. The region through the mid-section of the gage length over the reduced section of the tensile specimens were evaluated and the thickness measurement was conducted at 1mm interval, Figure 4.4, (see Appendix C).

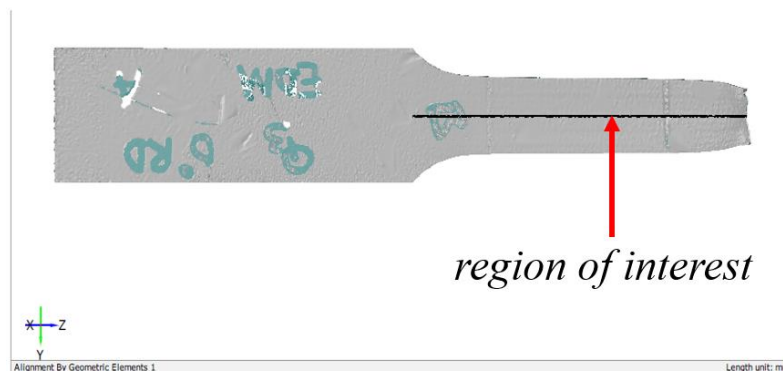


Figure 4. 4 GOM Atos measurement of thinning along gage section

4.1.5 ANOVA analysis

The measured edge roughness values and the uniaxial tensile property values were subjected to statistical analysis using ANOVA in Minitab 18 statistical software. One-way ANOVA was employed to evaluate the differences between group means in order to ascertain if there were any statistically significant difference between the attained values. A confidence interval (CI) of 95% was used in this work with a significant difference considered acceptable at $p < 0.05$.

4.1.6 Uniaxial tensile test

A 150kN Zwick/ Roell Z150 load cell tensile testing machine furnished with a programme service for the manoeuvre of its transverse motion was utilised to conduct a room temperature tensile test on the titanium test samples in accordance with ISO 6892-1:2016. A constant strain rate of 1×10^{-3} /s was used for the test and controlled by the testXpert II software for a steadily changing crosshead speed. An extensometer was also utilised to measure the changes in the gage length during the testing process. Three repeats of each edge surface quality for their respective machining methods were conducted for the onward determination of the tensile deformation response.

DIC was used to evaluate the strain distribution during the tensile deformation process. A speckle pattern comprising a white paint background with sprinkled dots of black paint were utilised. The displacement of the randomly placed speckle particles (size~50 μ m) were tracked during the deformation process with two digital cameras at 4 Frames/s. The strain distribution during the tensile deformation was analysed using Davis 8.0 software supplied by LAVision. A sum differential correlation mode was utilised with the subset and step sizes of 55 and 5 respectively. The outlier and smooth filter modes were also selected.

4.2 Results and Discussion

4.2.1 Machining induced edge defects

SEM images of the edge surface morphology after AWJ machining are typified by its mechanical erosion attributes. The surface draglines observed are mainly due to the path traversed by the abrasive particles during the cutting process, Figure 4.5a. The direction of the AWJ machining was with respect to the abrasive particle trajectory (surface draglines). SEM analysis of the EDM cut edge shows an edge surface characterised by their thermal erosion

attributes with pockmarks, micro-cracks and voids, (Figure 4.5b) as the main defect features. The edge surface integrity after EDM cutting is dependent on the extent to which the dielectric fluids are able to wash away the debris on the cut edge during the machining process.

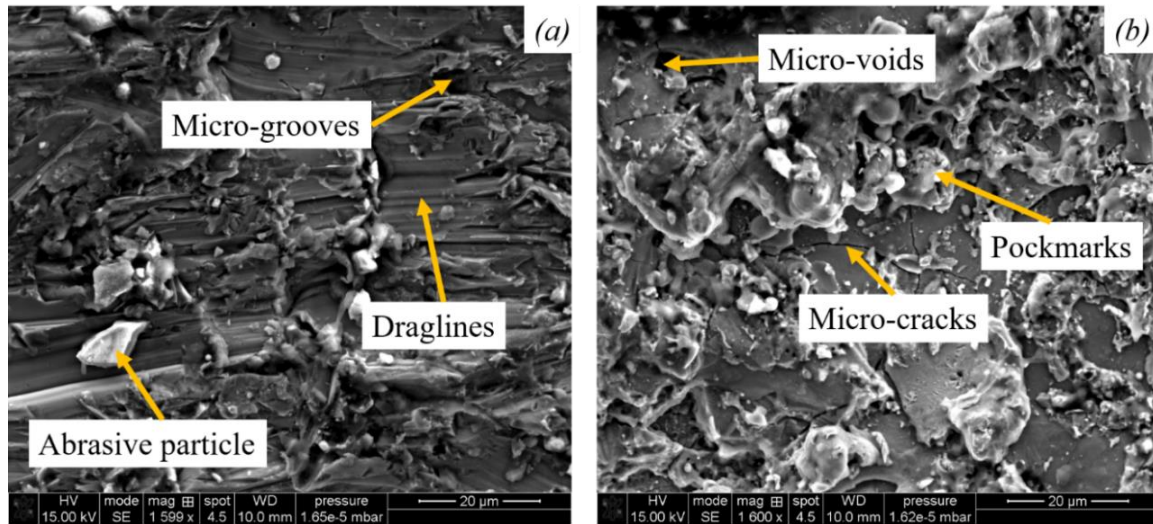


Figure 4. 5 SEM micrograph of machined edges

(a) AWJ and (b) EDM cut edges

4.2.2 One-way ANOVA analysis of edge roughness values

One-way ANOVA with a null hypothesis of equal means for roughness values was utilised to evaluate the difference in the attained cutting regimes. Equal variances were also assumed for this analysis with a significance level accepted at 0.05.

Figure 4.6 shows the various edge roughness values attained for each machining parameter after AWJ cutting of the test material. The finished edge surface possessed the lowest edge roughness value (mean~3.76µm) with a 95% CI that the attained surface quality lies between the intervals of $3.66 \leq Ra \leq 3.87 \mu\text{m}$. The unfinished edge surface possessed the highest edge roughness value (mean~7.66µm) with a 95% CI that the edge surface quality attained after AWJ cutting lies between $7.56 \leq Ra \leq 7.76 \mu\text{m}$. A comparison between the AWJ cutting regimes using the Tukey method also shows that a statistically significant difference exists between the measured roughness values for the respective machining parameters, Table 4.2.

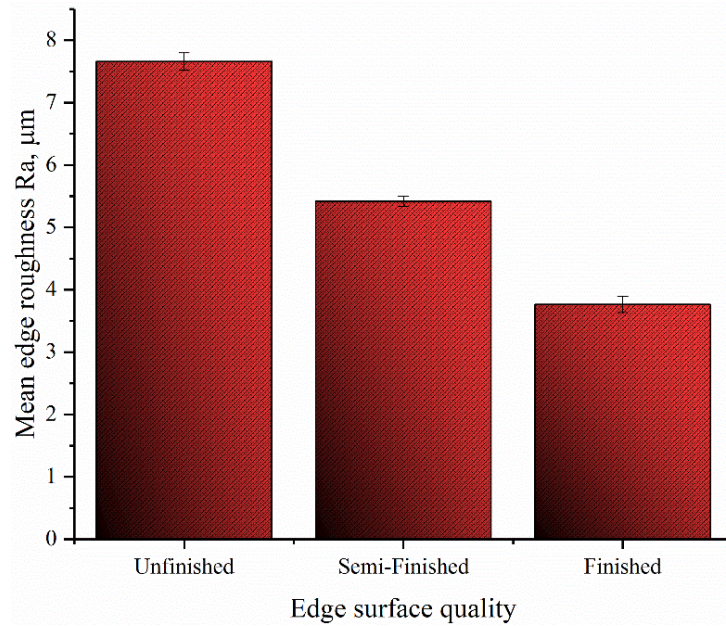


Figure 4. 6 Mean edge roughness after AWJ cutting

Table 4. 2 Grouping information using the Tukey method for AWJ cut quality

Factor	N	Mean	Grouping
UnFinished	6	7.6605	A
SemiFinished	6	5.4192	B
Finished	6	3.7626	C

Means that do not share a letter are significantly different.

Figure 4.7 shows the attained machining edge surface roughness value ranges after EDM cutting. The finished edge surface possessed the lowest edge roughness value (mean~0.85 μm) with a 95% CI that the measured values fall between $0.76 \leq Ra \leq 0.93\mu\text{m}$. The unfinished edge surface also recorded the highest edge roughness value (mean~3.67 μm) with a 95% CI that the measured values are within the ranges of $3.58 \leq Ra \leq 3.75\mu\text{m}$. A comparison between the various EDM cutting regimes using the Tukey method also shows that a statistically significant difference exists between the measured roughness values for the respective machining parameters, Table 4.3.

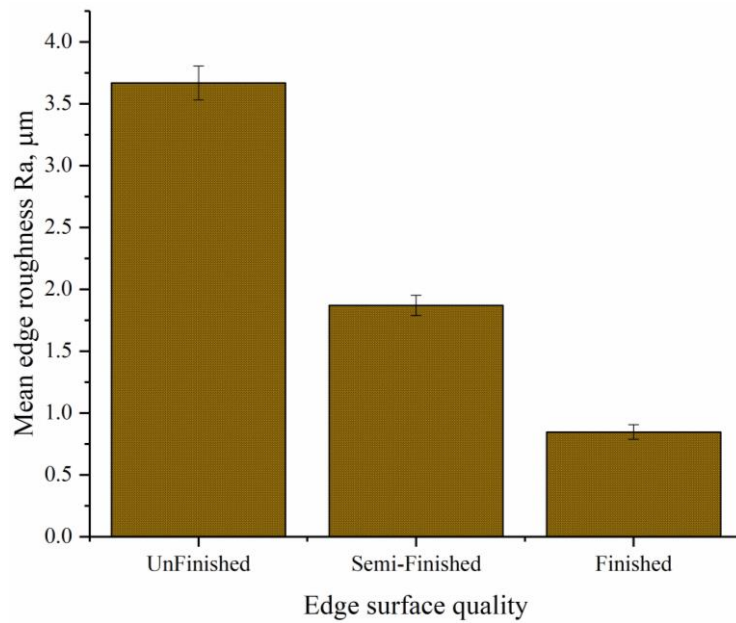


Figure 4. 7 Mean edge roughness after EDM cutting

Table 4. 3 Grouping information using the Tukey method for EDM cut quality

Factor	N	Mean	Grouping
UnFinished	6	3.6677	A
SemiFinished	6	1.8696	B
Finished	6	0.8464	C

Means that do not share a letter are significantly different.

4.2.3 Effect of machining parameters on tensile deformation behaviour

Uniaxial tensile tests were conducted on the AWJ and EDM fabricated tensile test samples in order to ascertain if the quality of the edge surface finishes have any impact on their tensile deformation behaviour. The material was investigated in three sheet-rolling directions; 0⁰RD, 45⁰RD and 90⁰RD orientations with respect to the sheet rolling direction. A visual inspection of the true stress- strain plot for both EDM and AWJ fabricated samples showed that the variation in machining parameters poses limited impact on the tensile deformation behaviour of the material, Figure 4.8 and 4.9.

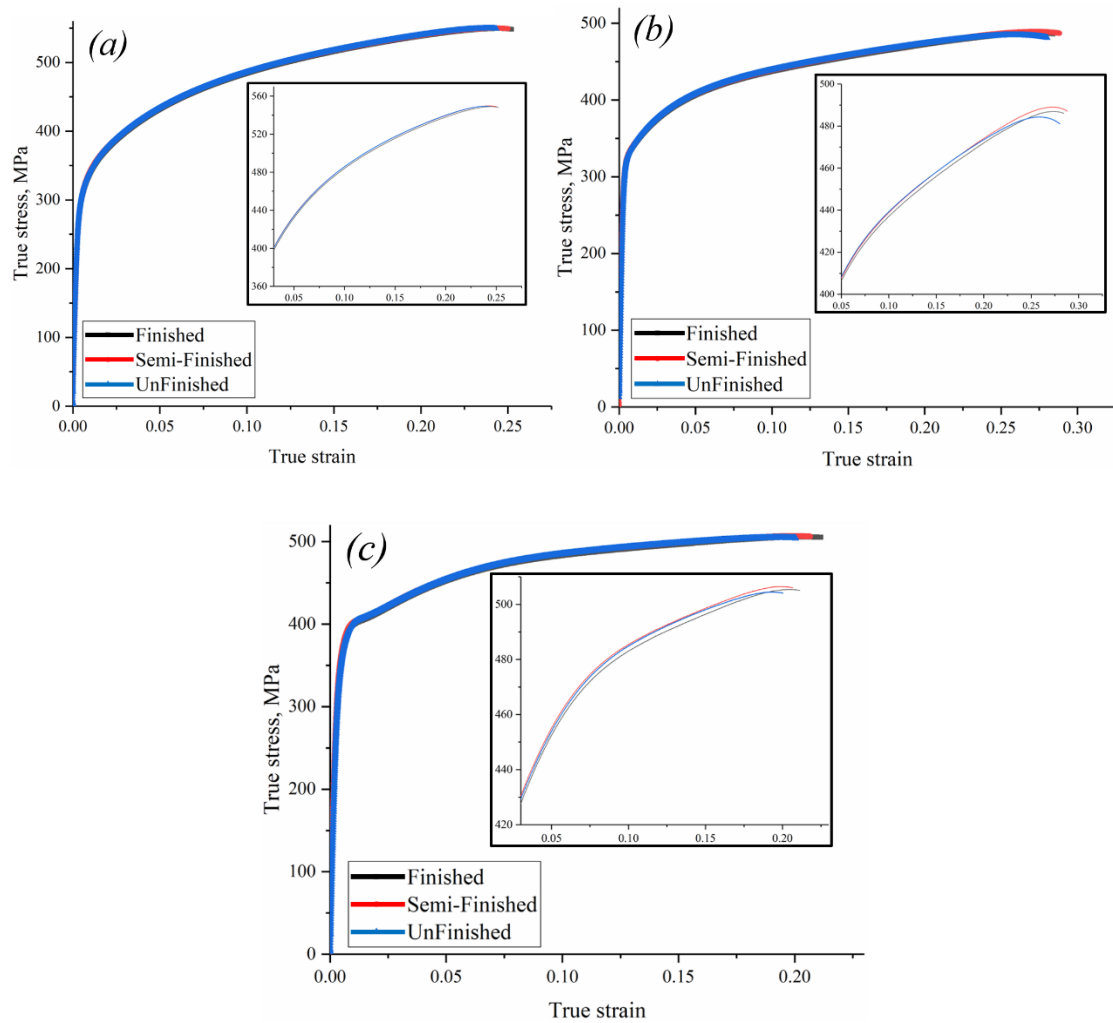


Figure 4. 8 Tensile response of AWJ machined edges with different cut edge quality

(a) 0° RD (b) 45° RD (c) 90° RD

The material exhibited high strain hardening tendencies along the 0° RD sheet direction, for both AWJ and EDM fabricated test samples. The variations in mechanical properties with sheet rolling directions observed in the material are consistent with the trends observed by some researchers (Chen & Chiu, 2005). According to Chen and Chiu, slip deformation is observed very early when working CP-Ti along 0° RD and 90° RD sheet directions. According to their work, further deformation however results in the formation of twinning deformation that prevents dislocation slip, resulting in their high values of elongation and strain hardening tendencies along 0° RD (Chen & Chiu, 2005). The material exhibits different tensile deformation behaviour when examined in different sheet-rolling directions.

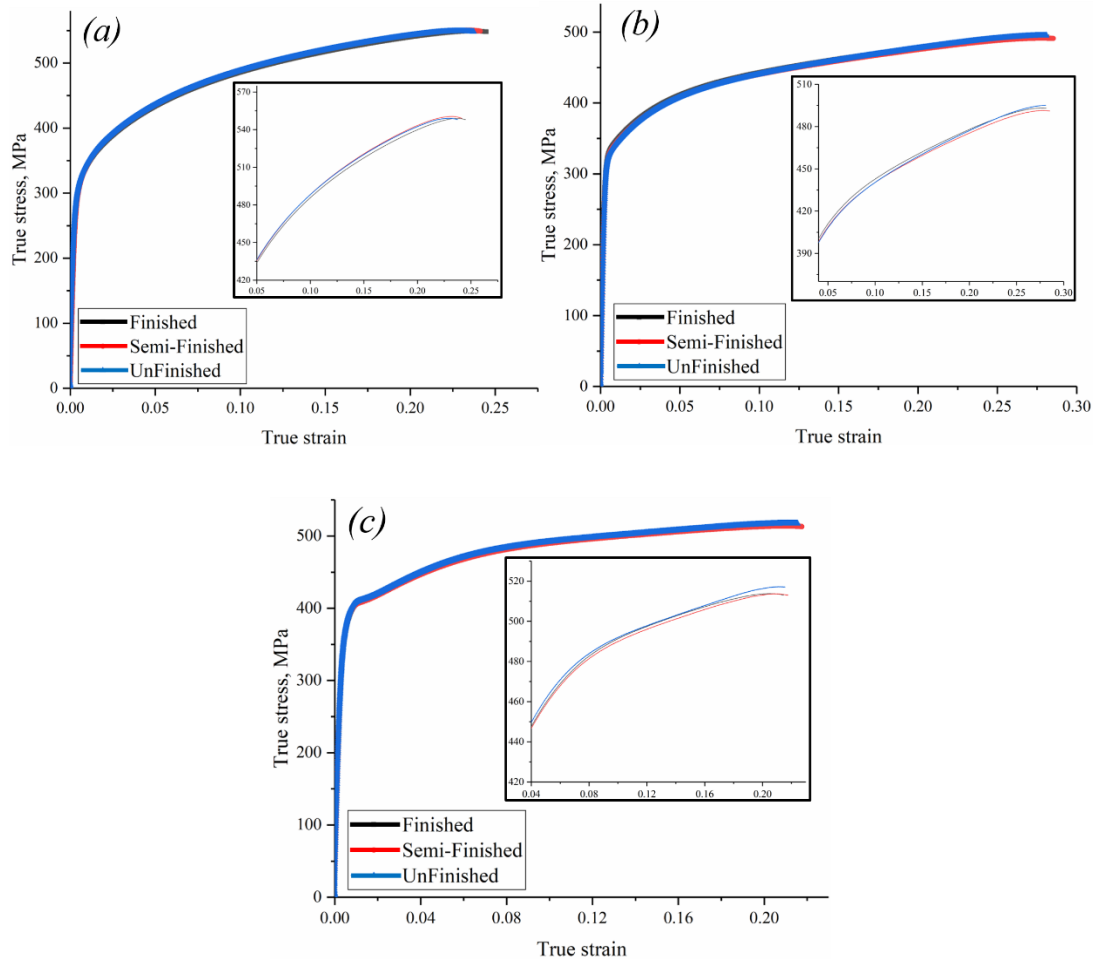


Figure 4. 9 Tensile response of EDM machined edges with different cut edge quality

(a) 0° RD, (b) 45° RD, (c) 90° RD

Figure 4.10 shows a plot of the width strain versus the thickness strain for the three sheet-rolling directions. The magenta lines on the curve are the linear portion of the curve used for evaluating the slope that represents the anisotropic coefficient (R_{Ani}) of the material. The variations observed in the strain path evolution for each sheet-rolling direction clarifies the high anisotropy of the material (R_{Ani} of 1.13, 2.86 and 3.20 for 0° RD, 45° RD and 90° RD sheet rolling directions respectively).

Figure 4.11 shows a combined plot of the true stress-strain curve explored in three sheet-rolling directions for the finished edges of tensile samples fabricated with either EDM or AWJ. The plot shows similar trends in tensile behaviour for both machining methods. These trends are consistent with the observed insensitivity of low carbon steel sheet edges machined with either wired EDM or AWJ to tensile deformation (Krahmer, et al., 2016). Krahmer et al., in their work attributed the insensitivity to the inability of both wired EDM and AWJ cutting

technologies to impose a work hardening effect on the test samples after machining (Krahmer, et al., 2016).

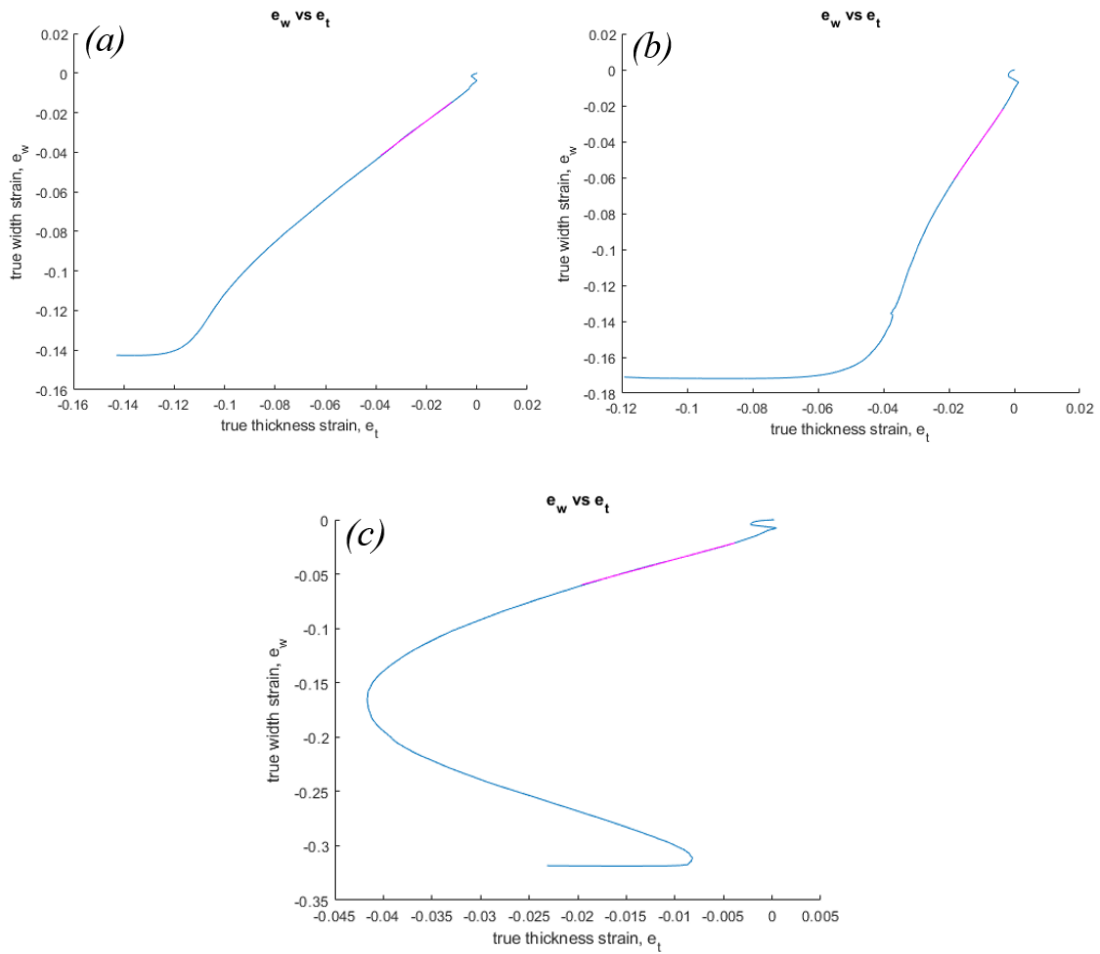


Figure 4. 10 Plot of width strain versus thickness strain
(a) 0° RD, (b) 45° RD, (c) 90° RD

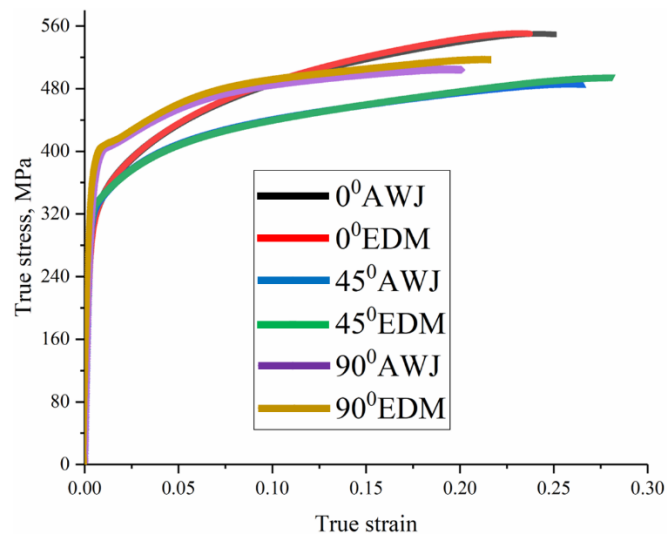


Figure 4. 11 EDM and AWJ fabricated edges deformed in three sheet directions

In order to statistically verify the proximity in tensile deformation behaviour observed for both EDM and AWJ fabricated samples in Figure 4.11, the attained ultimate tensile strength (UTS) and yield strength values for the respective machining methods were subjected to ANOVA test. Table 4.4 shows the grouping information using the Tukey method with 95% CI for the comparison of UTS and yield strength values of the EDM and AWJ fabricated tensile samples with finished edge surface quality. For the ANOVA test, three repeats for each sheet-processing direction were examined for the respective machining methods. The result reveals that there is no statistically significant difference in the UTS and yield strength values for the AWJ and EDM fabricated tensile test samples.

Table 4. 4 Tukey Pairwise Comparisons for UTS and yield strength values

Factor	N	Mean	Grouping
EDM_UTS	9	518.67	A
AWJ_UTS	9	511.8	A
EDM_Yield strength	9	392.06	B
AWJ_Yield strength	9	387.43	B

Means that do not share a letter are significantly different.

4.2.4 Thinning evolution analysis

The GOM Atos optical non-contact measurement system was utilised to assess sample-thinning evolution from the fracture zones towards the grip section for the EDM and AWJ deformed test samples. Table 4.5 shows the thinning evolution recorded for the test samples studied in three sheet-rolling directions after tensile deformation. Significant sheet thickness reduction was observed at the fracture tip of the tensile samples after failure. The sheet thickness however increased towards the grip section of the test specimens. The reduction in thickness is attributable to the occurrence of necking deformation prior to failure. The reduction in sheet cross sectional area at the fracture zone is a function of the sheet orientation. The stress concentration varies with the sheet orientation and relies on the nature of stresses acting during the tensile loading process. The thinning tendencies therefore provides significant information about the plastic workability of the sheet in a particular sheet-rolling direction in terms of their ability to delay thinning/ necking during the deformation process.

Table 4. 5 GOM Atos measurement of thinning evolution after tensile testing

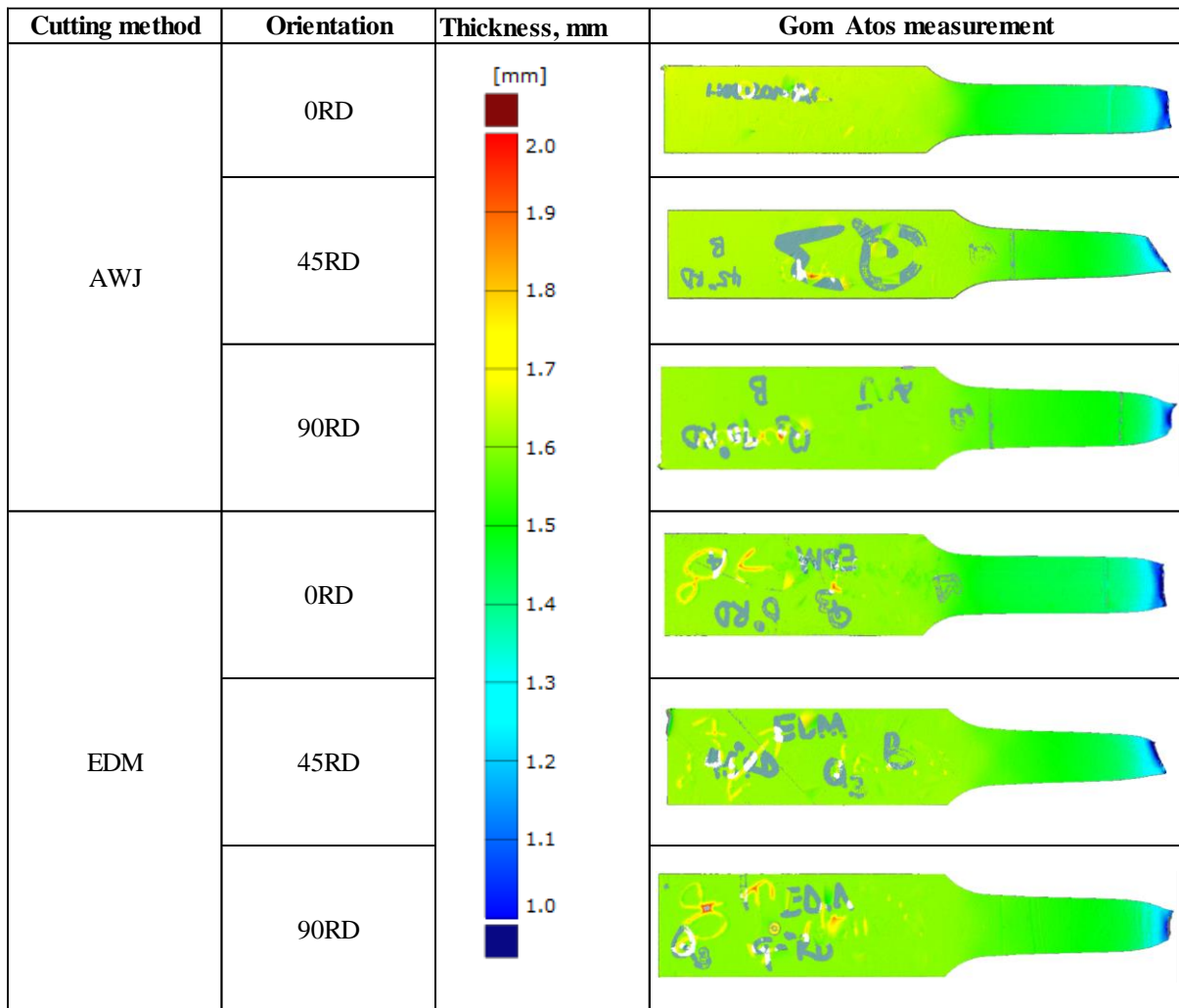


Figure 4.12 shows a comparative plot of the thickness evolution for distances measured from the fracture tip of the deformed tensile sample for the EDM and AWJ fabricated samples. Both EDM and AWJ fabricated tensile test samples exhibited similar thinning evolution in all three sheet-rolling directions. The samples exhibited the highest resistance to thinning along the 0⁰RD sheet rolling direction. This observation is consistent with the high strain hardening behaviour obtained in the same sheet rolling directions (Chen & Chiu, 2005). The shearing nature of the fracture tip for the 45⁰RD oriented test samples offered the least opposition to sheet thinning. Overall, the thinning evolution was approximately stable at a sheet thickness value of ~1.45mm along the gage section, Figure 4.12. The observed trend shows that the edge roughness and their accompanying defects as well as fabrication methods used for preparing CP-Ti (Grade 2) tensile test samples have no impact on their tensile deformation behaviour.

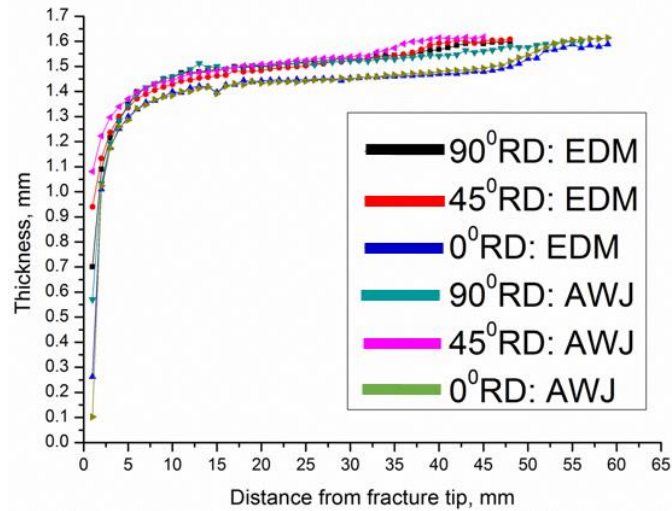


Figure 4. 12 Thickness variation for EDM and AWJ test samples

4.2.5 Failure Analysis

The general deformation mode observed after the uniaxial tensile testing of the samples is diffused necking followed by localised necking, reminiscent of ductile fracture, Figure 4.13. Inspection of both EDM and AWJ fabricated test samples after tensile deformation shows that both exhibited similar deformation traits. The extent of reduction in the gage section cross sectional area observed for the 45⁰RD oriented test samples is an intermediate between the deformation modes observed at 0⁰RD and 90⁰RD sheet orientations. The 45⁰RD oriented test samples have visibly undergone localised necking with ductile shear fracture after diffused necking. The acting stresses are mainly attributable to the shear stresses exerted during the deformation process, identical to the evolution of the triaxial stress state during necking (Ellis, 2007). The exerted shear stresses are optimum, when acting at 45⁰ to the applied load axis resulting in failure of the specimen at zones where those stresses are highest. This occurrence is the main reason for the visible 45⁰ angled fracture line observed with respect to the tensile axis for the 45⁰RD oriented test samples, Figure 4.13. Generally, plastic flow anisotropy governs shear fracture (Benzerga, et al., 2019). Thus, tensile orientation has a strong impact on the fracture behaviour of materials. The reduction in plastic instability reduces the triaxial character of the stress at the final ductile fracture. Normally, shear ductile fracture occurs at relatively low-stress triaxiality. For situations of higher stress triaxiality with severe plastic instability, coalescence of voids is by virtue of necking of the inter-void ligaments rather than shear linking up of voids (Lou, et al., 2014). This could account for the observed reduction in the shear fracture angle from ~89⁰ to ~45⁰ with sheet orientation.

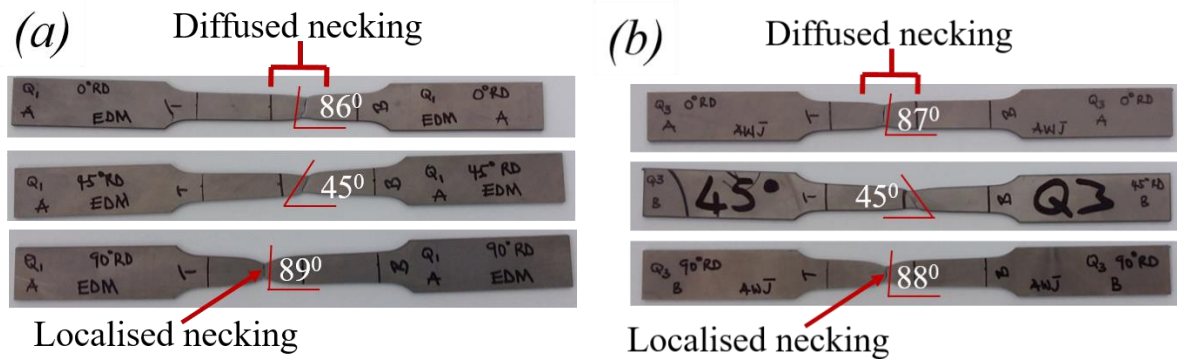
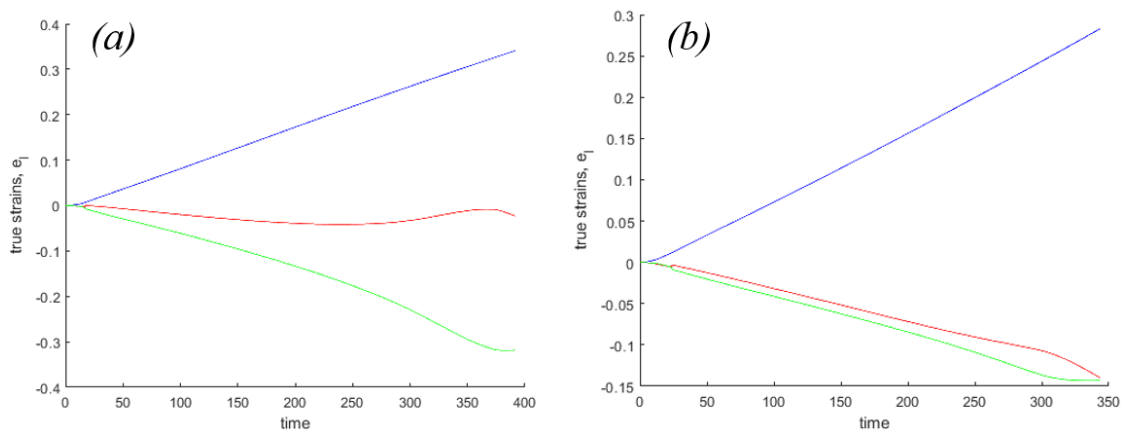


Figure 4.13 Deformation mode after plastic deformation

(a) EDM and (b) AWJ test samples after tensile deformation

Yu et al., in their work on ultrafine-grained AA6061 aluminium sheets also suggested that various damage criteria could be utilised to estimate shear fracture angle evolution during uniaxial tensile deformation (Yu, et al., 2014). According to their work, maximum shear stress estimated with Tresca criteria are observed to orient 45° to the tensile axis resulting in 45° angled fracture line at gage sections of samples during tensile testing. Their work also indicated that Cockcroft-Latham fracture criterion is suitable for forecasting 90° fracture angles with the Gurson-Tvergaard-Needleman (GTN) ductile fracture criterion also capable of forecasting fracture angles between 45° and 90° during tensile deformation.

Figure 4.14 shows the strain fields for the true strain evolution over the tensile deformation period for the tested material. An appreciable reduction in sheet width and thickness strains with an increase in length strain are observed over the deformation period. The high reduction in the width strains are synonymous with the reduction in cross-sectional area leading to diffused necking occurrence during the deformation process.



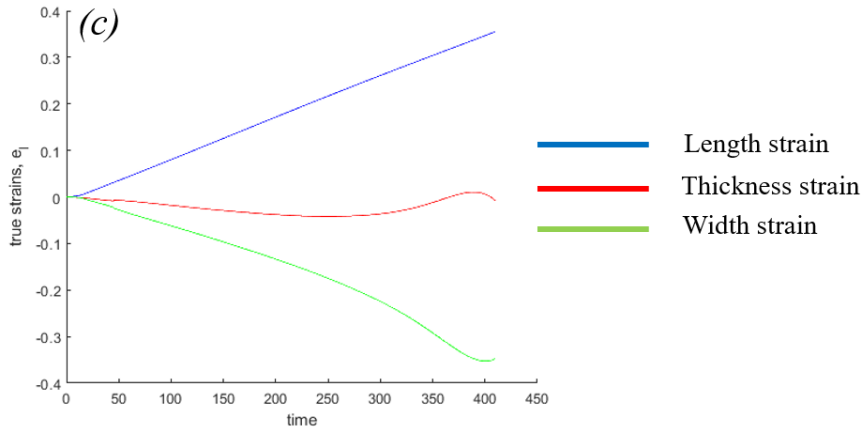


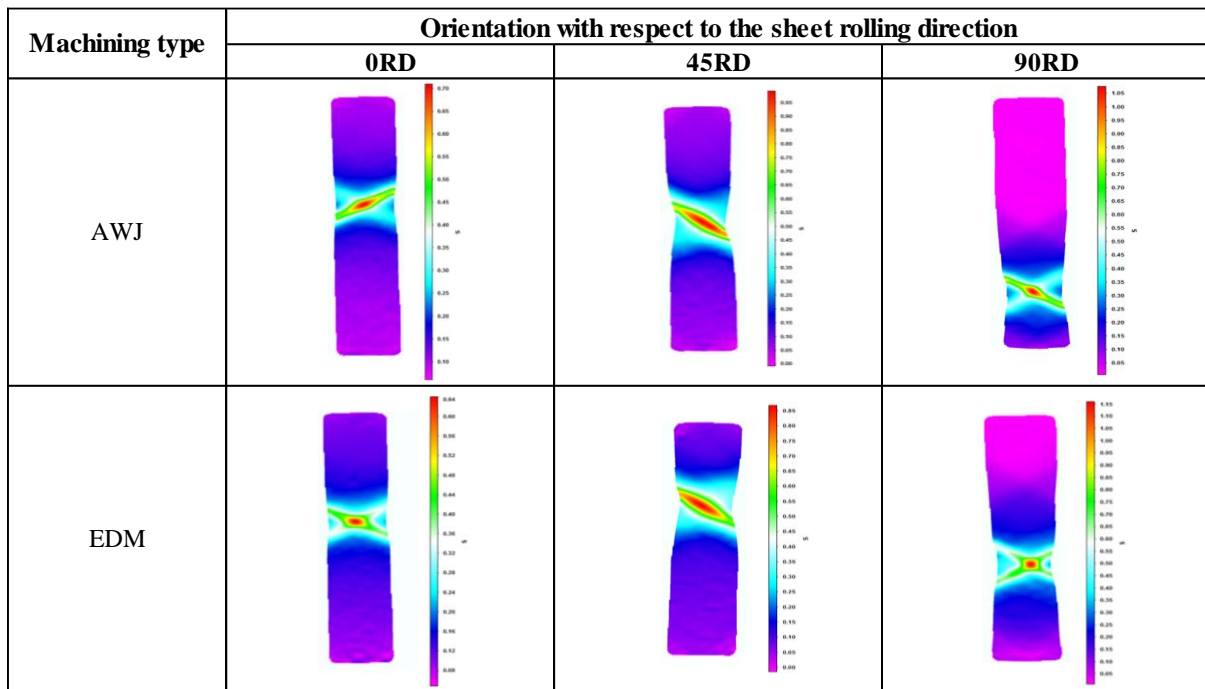
Figure 4. 14 True strain evolution with deformation period

(a) 0° RD, (b) 45° RD and (c) 90° RD sheet rolling directions

DIC technique was adopted to quantify the strain distribution during the uniaxial tensile deformation process. The DIC analysis showed that the strains are concentrated predominantly in the middle of the gage section, away from the machined edges for both EDM and AWJ fabricated tensile samples after 90% uniaxial tensile deformation, Table 4.6. Inspection of the analysed DIC images also shows that the fracture strains obtained are significantly higher and concentrated within the localised necking region compared to those observed at the diffused necking region. Thus, cracks produced are nucleated at the mid-gage section of the samples and travel towards the periphery until failure occurred. This observation explains the insensitivity of the machined edges to failure nucleation and tensile property alteration of the material. Similar observations were made after DIC analysis by Al-Shawk et al., on DP780 steel uniaxial test samples fabricated with either EDM or milling (Al-Shawk, et al., 2018). According to their work, for the samples assessed in the sheet rolling and transverse directions, the high fracture strain values obtained around the localised necking zone (within the sample centre) were probably due to the variation in the stress state from those occurring around the machined edge during the deformation process (Al-Shawk, et al., 2018).

Overall, failure observed during the tensile deformation of CP-Ti (Grade 2) test samples is attributable to static overload leading to fracture. Ductile fracture was observed in samples fabricated with either AWJ or EDM methods with a substantial level of diffused necking typified by the traditional reduction in the cross-sectional area at the fracture zone.

Table 4. 6 Global strain distribution prior to fracture (after 90% deformation)



Fractography analysis was conducted on the crack edges of both EDM and AWJ deformed test samples. The fractured surfaces were largely characterised by very fine dimples with varying size in addition to the presence of micro-voids typical of ductile fracture, Figure 4.15. The presence of a high volume fraction of dimples results in subsequent formation of a substantial amount of micro voids during the deformation process. The mechanism of ductile fracture involves the nucleation, growth and coalescence of the micro voids resulting in fracture. Coalescence of micro voids resulting in micro-cracks are seen in deep pockets besieged by a high volume fraction of dimples with distinct sizes, Figure 4.15*f*. The high volume fraction of these micro voids and the generation of these micro-cracks results in the reduction of the true strain-to-failure, which is synonymous with ductile fracture.

Overall, the SEM of the fractured surfaces of both EDM and AWJ samples showed a high volume fraction of fine dimple texture with accompanying long tearing ridges and the presence of micro voids, which are synonymous with ductile fracture mechanism during plastic deformation. Since the shear stresses acting are optimum in the 45⁰RD oriented samples, elongated dimples which are parabolic depressions that coalesce in the planes of optimum shear stress were observed on the fracture surfaces, Figure 4.15*b,e*. However, no significant differences were observed in the fractographs for the 0⁰RD and 90⁰RD oriented samples in terms of the microscopic fracture features. Bathini et al., in their work on the uniaxial tensile deformation of CP-Ti (Grade 2) examined in the longitudinal and transverse directions, also

reported that the material exhibited identical ductile fracture mechanism in terms of the macroscopic fracture mode and the microscopic fracture features in the two sheet rolling directions (Bathini, et al., 2010).

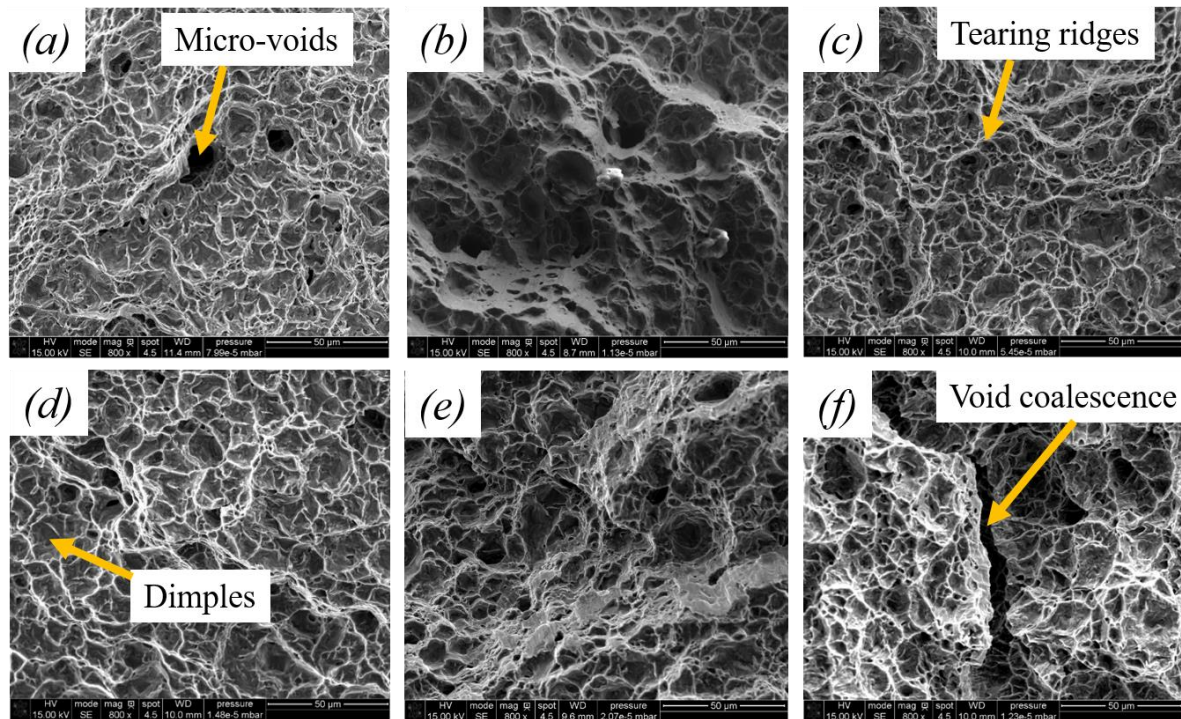


Figure 4. 15 Fractograph of crack edges after tensile testing

AWJ fracture edge (a) 0⁰RD, (b) 45⁰RD, (c) 90⁰RD and EDM fracture edge (d) 0⁰RD, (e) 45⁰RD, (f) 90⁰RD

4.3 Summary

Geometrical specifications for fabricating standard tensile test samples are well defined and documented in the literature (eg. ASTM E8-04). However, the type of machining method as well as the integrity of edge surface finishes suitable for examining the tensile properties of metallic materials have not been extensively examined. Considering the sensitivity of titanium and its alloys to notch and surface inhomogeneity, there is the need to understand the impact of different machining methods and their consequential edge surface qualities on tensile deformation performance. This chapter examines the impact of EDM and AWJ machining and the resultant edge surface defects on the tensile property evolution of CP-Ti (Grade 2) at room temperature. The research found that;

- The quality of the edge surface finishes for tensile samples prepared with either EDM or AWJ machining have no statistically significant effect on the tensile deformation behaviour of CP-Ti (Grade 2) at room temperature.
- The machining induced surface micro-feature alterations and defects produced after either EDM or AWJ machining have no statistically significant effect on the uniaxial tensile deformation behaviour of CP-Ti (Grade 2) at room temperature.
- The EDM and AWJ fabricated tensile samples exhibit similar thinning evolution trend in all three sheet-rolling directions during the uniaxial tensile deformation. The general deformation mode observed after the uniaxial tensile testing of the samples are diffused necking followed by localised necking. The extent of reduction in the gage section cross sectional area observed for the 45⁰RD oriented test samples is an intermediate between the deformation modes observed at 0⁰RD and 90⁰RD sheet orientations for both fabrication methods.
- The DIC analysis showed high fracture strain values at the zones of localised necking with lower fracture strains around the diffused necking region prior to fracture. Thus, cracks produced during the tensile test nucleated from the mid-gage section of the samples and travelled to the periphery until failure. This occurrence negates the influence of the machining induced edge defects and roughness on the tensile deformation behaviour of the material.

Chapter 5

Effect of machining on the edge formability of commercially pure titanium sheet

Overview

Different machining methods are used to prepare sheet metals for forming operations. The nature of the machining induced surface defects produced in the form of edge surface micro-feature alterations have significant impact not only on the part surface integrity but also on the sheet edge forming performance. In a typical industrial setting, different machining methods are utilised to machine titanium sheets. However, research directed at ascertaining the impact of machining methods on titanium sheet edge formability at room temperature has not been previously investigated. In this chapter, the impact of laser cutting, AWJ and EDM machining on the edge forming performance of CP-Ti (Grade 2) was examined using the hole expansion test. The deformation behaviour of the material after HET and uniaxial tensile deformation were also examined in this chapter.

Most aspects of the results presented in this chapter have been published in peer-reviewed journals and conference proceedings.

5.1 Experimental procedure

5.1.1 The material and material characterisation

The material researched in this work was CP-Ti (Grade 2) sheet with a thickness of 1.6mm. An EBSD analysis was performed on the electropolished as-received test samples, using a Quanta FEG 250 microscope. Figure 5.1 shows the EBSD orientation map with its accompanying distribution of the coloured inverse pole figure (IPF) map of the as-received material assessed in the sheet rolling direction. The standard stereographic triangle with colour codes; red (0001), blue (01 $\bar{1}$ 0) and green ($\bar{1}$ 2 $\bar{1}$ 0) are representative of the crystallographic orientation of the respective grains. The colour contrast within the grains qualitatively denote differences in the internal misorientations. The micrograph of the supplied sheet showed fine equiaxed alpha grained structure, Figure 5.1.

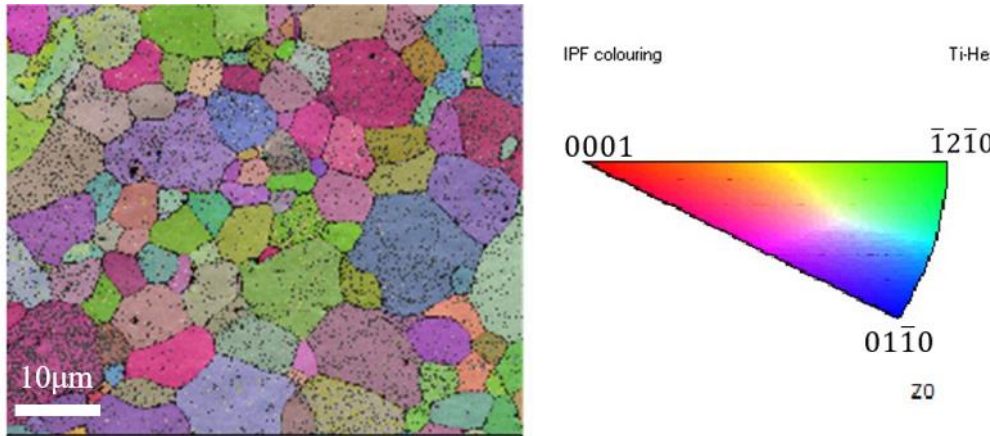


Figure 5. 1 Microstructure of supplied sheet; EBSD image

5.1.2 Mechanical properties

A 150kN load cell tensile testing machine; a Zwick/ Roell Z150, was used to perform uniaxial tensile tests on the material at room temperature in accordance with ISO 6892-1:2016. A dog-bone tensile test sample with gage section dimension of 50×12.5×1.6mm was used. The material was deformed at a constant strain rate of 0.001/s and the change in length captured with an extensometer. The mechanical properties were explored in three directions with respect to the sheet rolling direction and are presented in Table 5.1. The true stress-strain curve of the material explored in three directions showed the high anisotropy of the material, Figure 5.2. Such anisotropic tendencies observed in CP-Ti (grade 2) are attributable to the material texture (Nasiri-Abarbekoh, et al., 2012); (Nasiri-Abarbekoh, et al., 2013) and its effects on slip and twinning activity (Yi, et al., 2016).

Table 5. 1 Mechanical properties of CP-Ti (Grade 2) at room temperature

Sheet direction	Yield strength, MPa	Tensile strength, MPa	R_{Ani}
0°RD	197.99	550.31	1.131
45°RD	218.19	489.43	2.855
90°RD	250.05	513.25	3.200

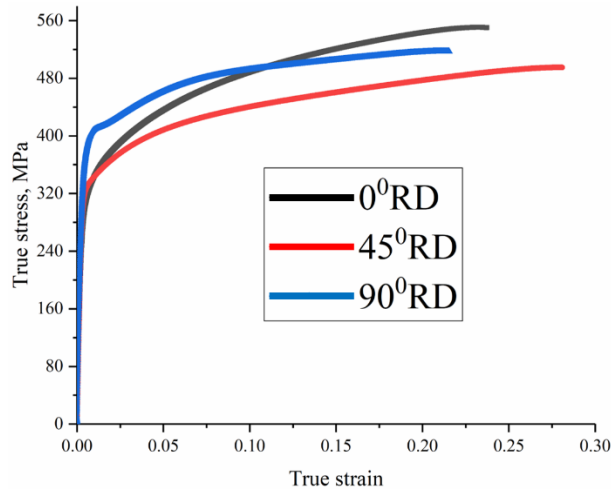


Figure 5. 2 True stress-strain curve

5.1.3 Hole expansion test

A standard hole expansion test consistent with BS ISO 16630:2017 was conducted on the test samples. The schematic set-up of the tools adopted to perform the HET are as shown in Figure 5.3. Two different punch geometries were adopted in order to ascertain the impact of different forms of sheet loading on the edge forming performance of CP-Ti (Grade 2). Similar test conditions and edge preparation processes were adopted and applied to both tests.

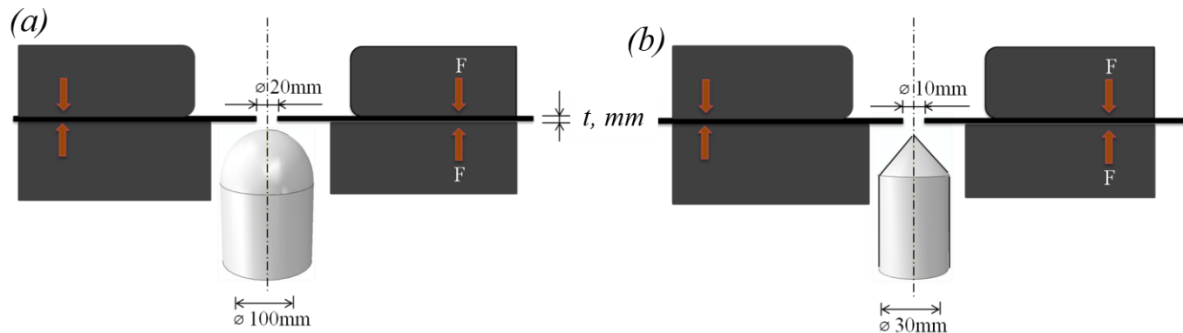


Figure 5. 3 Schematic of the HET set-up; (Not drawn to scale)
 (a) Nakajima punch tool and (b) conical tool set-up

5.1.4 Tool Geometry and sheet loading condition

The CP-Ti (Grade 2) sheets were deformed with two different tool geometries; a 100mm diameter Nakajima / hemispherical punch and a 30mm diameter conical punch with 60° cone head, Figure 5.4. The Nakajima punch exerts both horizontal and vertical load on the hole edge via in-plane stretching, Figure 5.4a. The conical punch on the other hand exerts vertical load

on the hole edge via out-of-plane loading, Figure 5.4b. The conical punch together with its die tool set were fabricated with dimensions consistent with BS ISO 16630:2017 (see Appendix B).

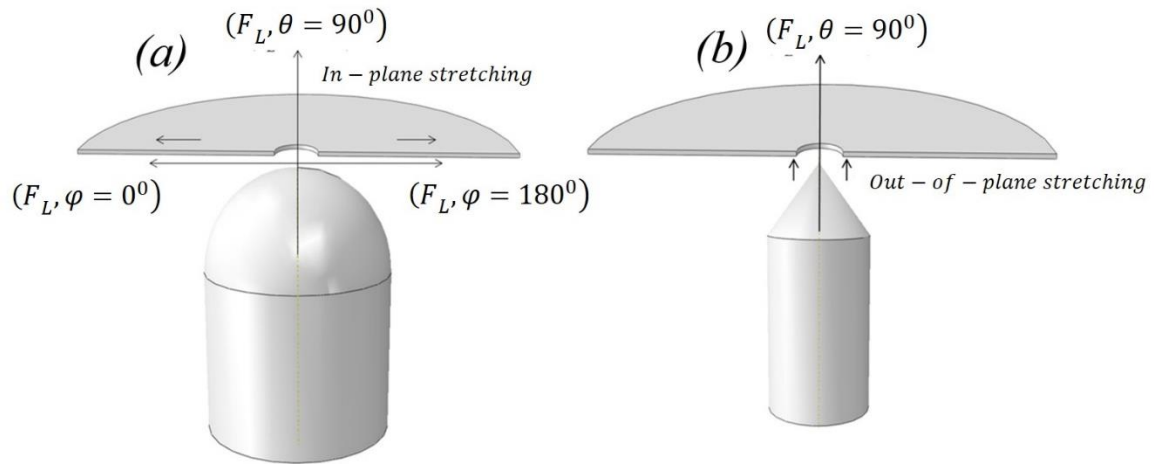


Figure 5. 4 Schematics of tool geometry and sheet loading condition
(a) hemispherical punch, (b) conical punch

5.1.5 Material edge preparation

Machining techniques known to be extensively adopted in industry for fabricating titanium sheets were analysed in this work. As such, the sort of edge surface finishes which are obtained under commercially viable machining conditions are examined in this research. The test samples were prepared by companies with specialisation in the respective machining technologies used. Thus, the edge surfaces examined for each machining method are surface quality ranges, which are commercially and industrially applicable for fabricating CP-Ti (Grade 2). The nature of the edge surface micro-feature alterations produced from the industry standard machining qualities were examined to ascertain their influence on the edge forming performance of CP-Ti (grade 2) for an onward adoption in hole flanging operations. The EDM samples were machined using a GF F1 440 CCS machine equipped with a 0.25mm brass wire with varying cutting parameters (pulse on duration time: 0.7, 0.1 and 0.05 μ s for unfinished, semi-finished and finished edges respectively). Test conditions for EDM with respect to machining accuracy are governed by BS ISO 14137:2015. An AMADA LCG-3015AJ laser-cutting machine furnished with a 4kW fibre laser and a 2mm beam diameter was used to machine the laser cut test samples. For the waterjet cutting, a Calypso waterjet machine with a 70HP KMT pump charged with an abrasive feed of 400gmin⁻¹ was employed with varying

machining parameters (transverse cutting speeds; 250, 400 and 600mmmin⁻¹ for finished, semi-finished and unfinished edges respectively) to achieve different surface finishes.

5.2 Results and discussion

5.2.1 Machining induced edge surface defects

Figure 5.5 shows the Alicona optical microscope micrographs of the three-cut edge finishes realized after AWJ cutting. The AWJ machined surfaces are marked by deep surface grooves, which are attributable to the path traversed by the abrasive particles during the cutting process. Intense surface grooves were observed on the unfinished cut surface, (Figure 5.5c) with the semi-finished and finished cut surface counterparts showing less severe surface grooves, (Figure 5.5 a, b). The direction of the AWJ cut was along the trajectory of the abrasive particles.

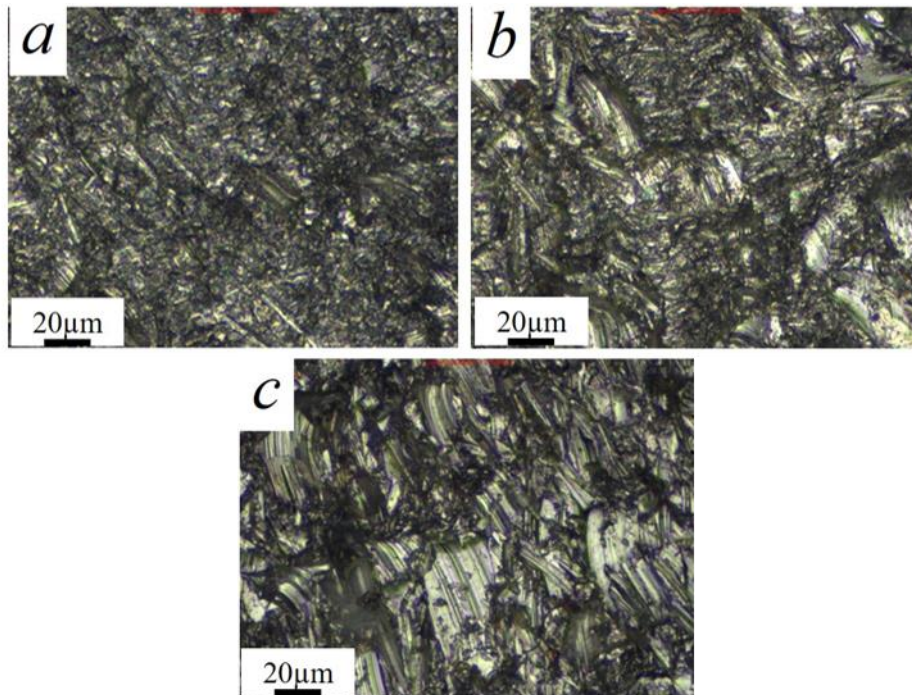


Figure 5. 5 Alicona micrograph of edge surface finishes after AWJ cutting

(a) Finished edge surface, (Ra~3.8µm), (b) Semi finished edge surface, (Ra~5.4µm), (c) Unfinished edge surface (Ra~7.7µm), with grooves from abrasive particle path

Figure 5.6 shows the various levels of edge surface finishes attained after EDM cutting. The observed surface morphology is typically marked with its thermal erosion characteristics. The severity of the post machining induced surface features is a function of the extent of material melt re-solidification as well as the quantity of molten material carried away by the dielectric

fluid during the cutting process. A 3D analysis of the edge surface micrograph revealed zones of high ridges, shallow craters, voids and terrain features, Figure 5.6*d*.

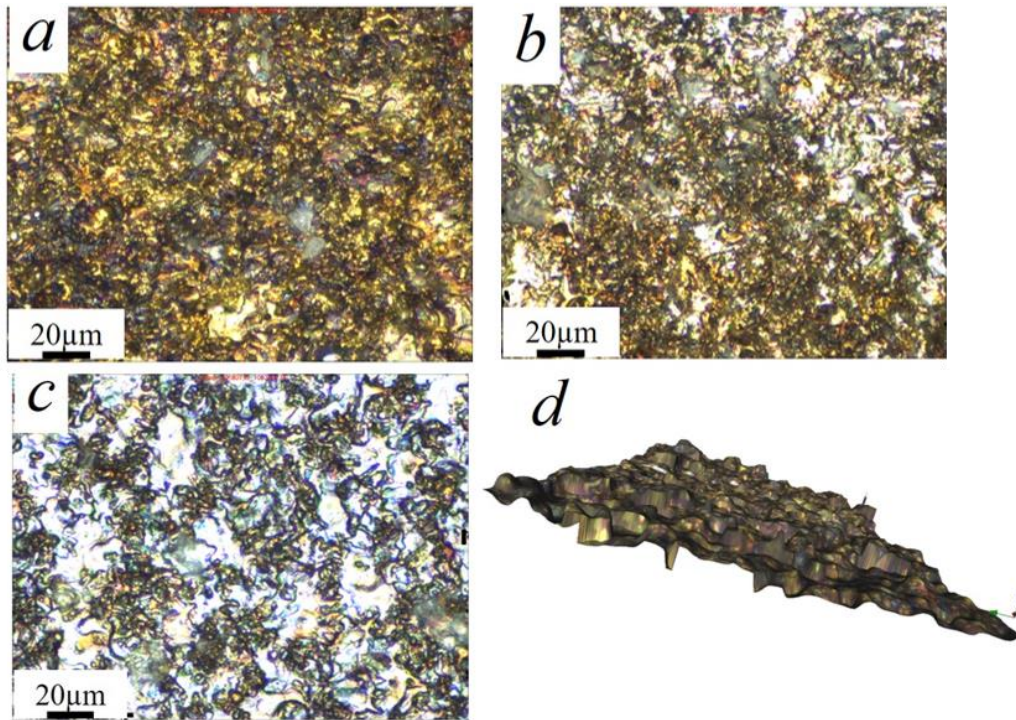


Figure 5. 6 Alicona micrograph of EDM cut edge surface

(a) Finished edge surface, ($R_a \sim 0.8 \mu\text{m}$), (b) semi-finished edge surface, ($R_a \sim 1.8 \mu\text{m}$), (c) Unfinished edge surface ($R_a \sim 3.7 \mu\text{m}$), (d) 3D surface roughness features

Low magnification micrographs taken from a Leica DM 12000M optical microscope of the finished edge surfaces prepared with either EDM, AWJ or laser machining are shown in Figure 5.7. The surface micrograph after AWJ cutting evidences its mechanical erosion attributes, Figure 5.7*a*.

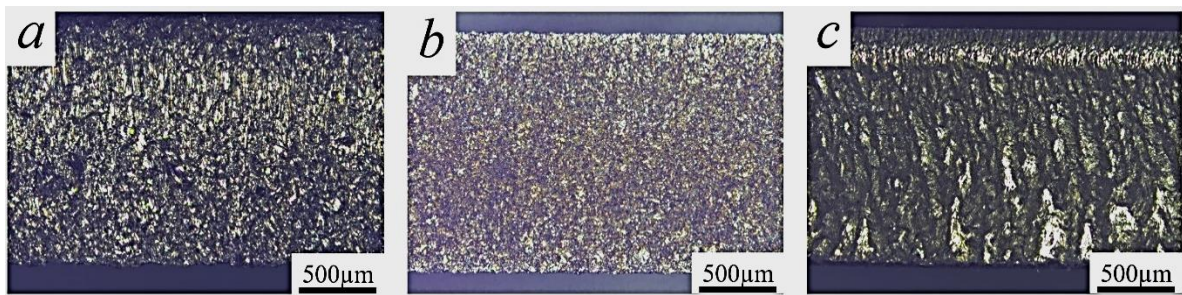


Figure 5. 7 Optical micrograph of CP-Ti (Grade 2) machined edges

(a) AWJ (b) EDM and (c) Laser cut surfaces

The edge surface after EDM cutting shows its heat erosion features produced due to melting of the part surface followed by quick cooling, Figure 5.7*b*. The laser cut edge micrograph also shows periodic kerf width and high depth of surface striations due to part remelting linked to the thermo-mechanical effect of the laser cutting process, with an attained edge surface finish of $Ra \sim 4.5\mu\text{m}$, Figure 5.7*c*.

A 3D analysis of the image files imported from the Alicona microscope was performed using an OmniSurf 3D software. A bilinear fill was utilised with Gaussian short (0.0025mm) and long (0.8mm) filters as well as a transmission band of 300:1. The 3D surface morphology of the laser, EDM and AWJ machined finished edges were characterised by grooves and peaks, Figure 5.8. Hence, a maximum pit height (S_v) surface texture parameter was utilised to quantify the edge surface area roughness parameter values.

For the measured surface texture parameters of the machined edges, the highest S_v value was recorded in the AWJ finished edge surface (18.60 μm), followed by the laser cut surface (10.60 μm), with the EDM finished edges (5.55 μm) producing the lowest maximum pit height, Figure 5.8 *a,b,c*.

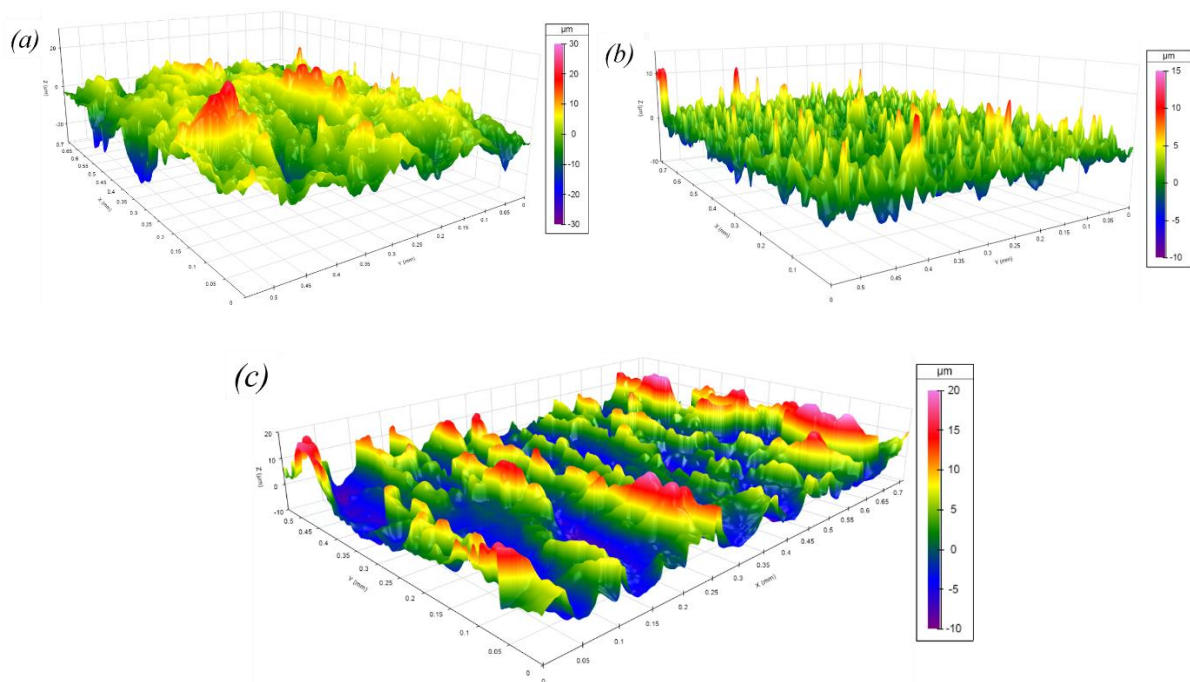


Figure 5. 8 3D surface morphology of machined edges
Finished (a) AWJ, (b) EDM and (c) laser edge surfaces

5.2.2 Impact of machining on HER: Hemispherical punch

Figure 5.9 shows the HER plotted for CP-Ti (Grade 2) fabricated with different cutting methods with finished edge surface qualities after HET with the hemispherical punch. The material exhibited the highest edge forming performance when fabricated with the EDM (194.55%) cutting method. The edge formability effect after EDM machining was more than twice that observed for the AWJ (81.87%) machined edges. The material also showed a very poor edge formability tendency for edges prepared with laser (47.78%) cutting method. Comparatively, improved edge forming performance was obtained with the AWJ fabricated edges juxtaposed to the laser prepared edges. These sensitivities of the material to the cut edge condition is due the surface micro-features alterations introduced during the machining process.

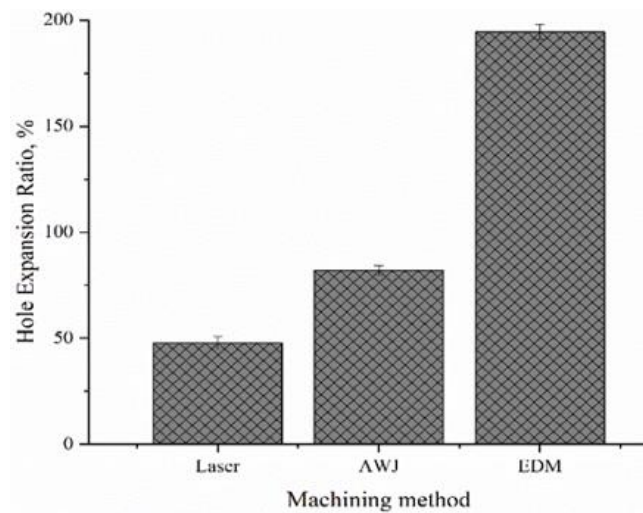


Figure 5. 9 HER of CP-Ti (Grade 2) fabricated with either laser, EDM or AWJ

Figure 5.10 shows the dome height evolution of samples for each machined edge type after HET. The EDM fabricated test sample exhibited the highest dome height (36.15 ± 0.66 mm), followed by AWJ cut test samples (31.78 ± 0.34 mm) with the laser-fabricated test sample edges producing the least dome height (26.20 ± 0.29 mm). The extent of dome height attained is a function of the degree of material flow. The higher the dome height, the higher the ease of plastic flow and the greater the material deformation. Since the stress concentrates around the hole edge during HET, the quality of the edge surface and the nature of the machining induced edge surface micro-feature changes produced thus plays a significant role in the dome height evolution of the material. Therefore, the dome height evolution is a significant indicator of material edge forming performance.

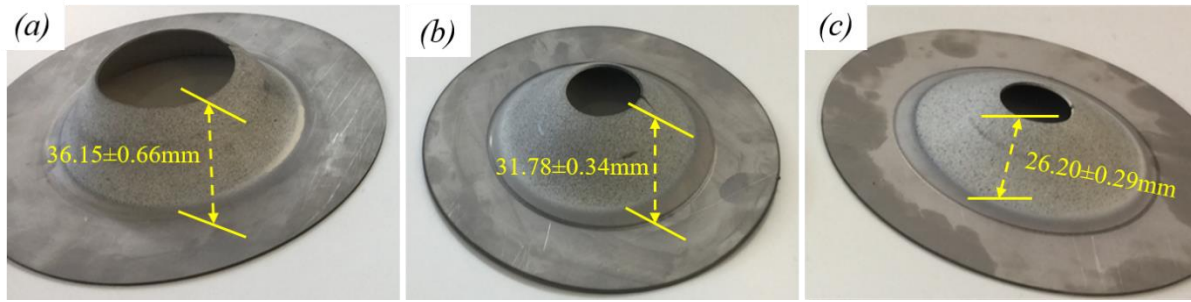


Figure 5. 10 Dome height evolution after HET

(a) EDM (b) AWJ and (c) Laser cut edges

5.2.3 Effect of different surface finishes on the HER: Hemispherical punch

HET with hemispherical punch was performed on the material fabricated with either AWJ or EDM examined for three different edge surface finishes (as explained in section 5.2.1). Three repeats were performed for each edge machining quality regime to ensure reproducibility of the results. Figure 5.11 shows the plot of the HER evaluated for all edge surface finishes studied.

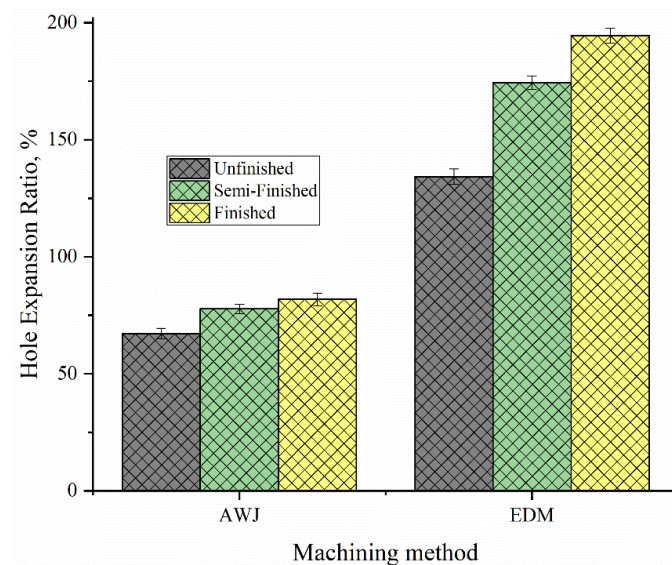


Figure 5. 11 HER for various edge surface finishes with hemispherical punch

The material showed a significant sensitivity to the quality of the edge surface finish with the HER values increasing as the edge surface texture decreased for both cutting methods. This trend could be attributed to the impact of the severity of the defects observed which varied with the quality of the surface finish. From the observed material behavior, it can be deduced that the more pronounced edge surface defects in terms of depth and size hindered the material

plastic flow more significantly compared to the subtler defect sizes seen in the more finely finished surfaces. The poorer the finish on the edge surface, the more severe its effect on the material formability. The quality of edge surface finishes in terms of the machining induced edge surface texture and their accompanying defects thus plays a major role in the edge formability of CP-Ti (Grade 2) at room temperature. Thus, the choice of machining parameters could have a detrimental effect on the edge forming performance of materials.

5.2.4 Edge forming limit evaluation

The pre-fabrication of hole in sheet metals prior to the forming process has the tendency of altering the stress state in the material. There has been lack of clarity on the appropriate approach for estimating the edge forming limits of sheet metals after HET. Previous works by Shi and Chen have indicated that the traditional FLD was not appropriate for estimating the edge limit strains of advanced high strength steels since the fracture strains obtained after HET are lower than the forming limit strain (Shi & Chen, 2007). However, recent research works have indicated that the critical strains obtained after HET with a Nakajima punch could serve as a failure criteria, which could then be adopted on conventional FLD for projecting sheet edge forming limit (Schneider, et al., 2016); (Gläsner, et al., 2016). An approach based on the traditional FLD is proposed in this EngD research to estimate the edge forming limit of CP-Ti (Grade 2) for edges prepared with either EDM, AWJ or laser machining.

A digital image correlation based on the GOM Aramis optical non-contact measurement technique was employed to measure the full-field strain values during the deformation process. A speckle pattern consisting of white paint sprayed with black dots was utilised. The speckle pattern application plays a significant role as the main conveyor of deformation information for the onward digital image correlation computation with the GOM software. The software tracks corresponding points of an image taken from a speckle-patterned surface to compute the local strain values (see Appendix A4). The major and minor strain evolution across the sheet surface from the hole edge measured during the HET trials with the hemispherical punch was analyzed for all finished cut edge conditions, Figure 5.12. The material showed a fracture strain value as high as ~0.83- 0.93 for the EDM cut samples, Figure 5.12*c*. The laser cut samples exhibited the lowest fracture strain of the three techniques (~0.28- 0.34), Figure 5.12*a* with AWJ showing an intermediate value between the other two (~0.53- 0.69), Figure 5.12*b*, when tested under the same conditions.

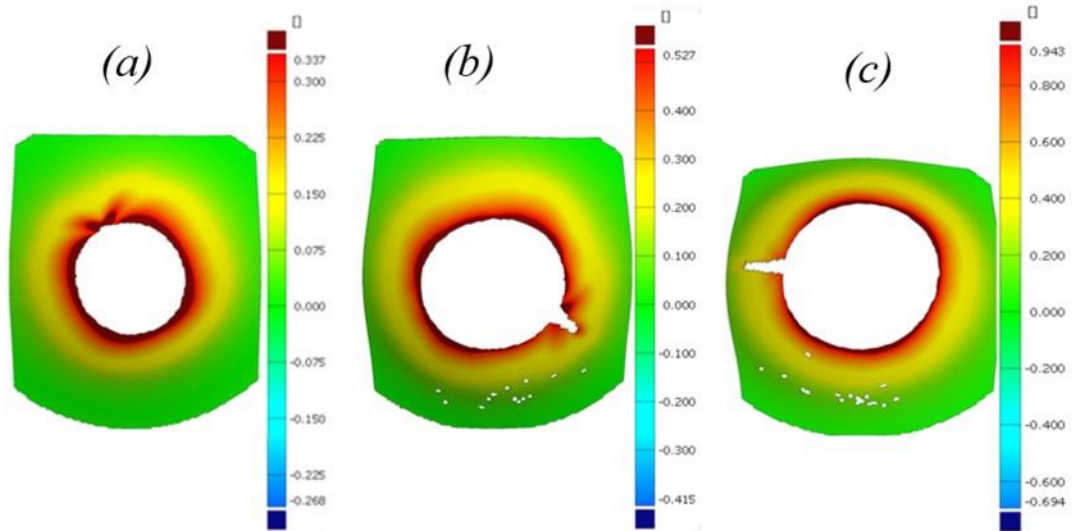


Figure 5. 12 Major and minor strain evolution during HET with hemispherical punch

Contour map for deformed (a) laser, (b) AWJ and (c) EDM finished edge surfaces

The reduced fracture strain values obtained under laser cutting are observed to be mainly due to the machining induced surface micro-feature changes produced on the edge surface during the machining process hindering the edge formability considerably. The deformation strains were concentrated around the hole edge area with reduced strains emerging away from the fabricated hole during the HET. In order to estimate the edge forming limit diagram, an analysis of the major and minor strains around the hole edge was also done for all finished edge conditions. The results showed that the strain path at the hole edge is reminiscent of pure uniaxial tension ($\epsilon_1 = -2\epsilon_2$) on the conventional forming limit diagram, Figure 5.13.

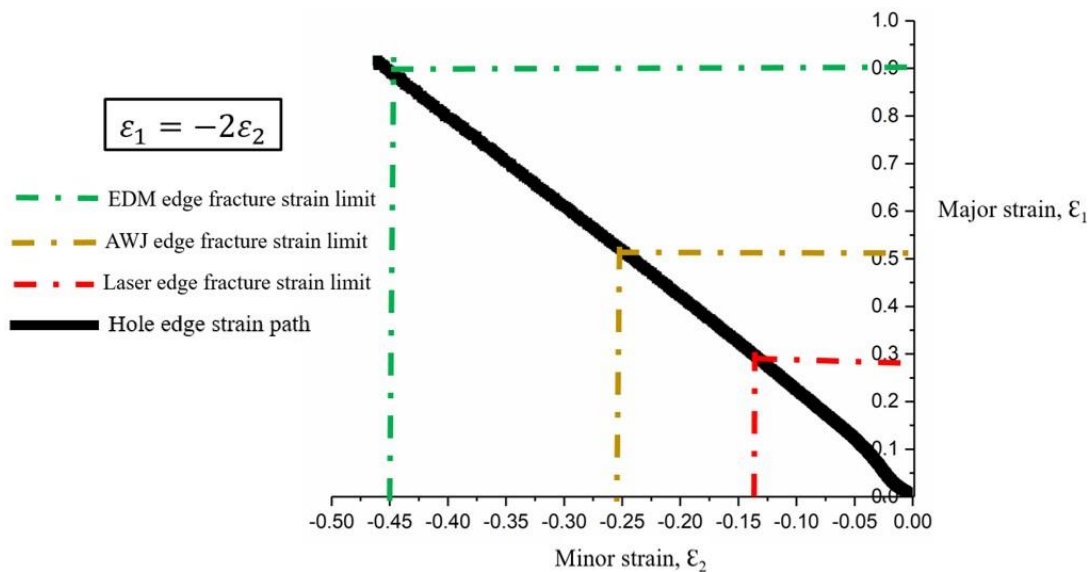


Figure 5. 13 Edge forming limit for the various machining methods

This represents the deformation path traversed during the edge stretching process. The fracture strains evaluated during the HET can therefore be used to predict the edge formability limit of CP-Ti (Grade 2) machined with the various cutting methods under investigation. Thus, the exact strains where the edge cracks begin to emerge could be predicted for each cutting method, Figure 5.13. The edge fracture limit strain values indicated on the graph are averages obtained for several repeated test results recorded for the results shown in Figure 5.9 for hemispherical punch. The laser cut edge of CP-Ti (Grade 2) showed a lesser edge forming limit compared to those observed in shear cut hot rolled steels (~0.43) (Gläsner, et al., 2016).

5.2.5 Effect of tool geometry on HER

Comparison of HER values determined with the hemispherical punch (NAK_HET) and standard conical punch (C_HET) on unfinished edge surfaces prepared with either laser, EDM or AWJ are shown in Figure 5.14. The conical punch showed higher edge formability tendencies for the machined edges compared to those obtained for the hemispherical punch. The HER values for finished edge qualities were not compared because the EDM prepared edges were not fractured for the conical punch deformed samples. The differences in forming performance of the tools are mainly due to the variation in the loading orientation instigated by the various punch geometries. These differences are also attributable to the varying strain gradients induced at the test piece hole edge during the experimental trial.

The conical punch produces the highest stretching at the workpiece hole edge due to the non-uniformity in the strains produced at various parts of the hole edge surface. Thus, when using the conical punch, strain localization is delayed since the hole edge is loaded out-of-plane. The hemispherical punch on the other hand loads the sheet in- plane with a concomitant higher tendency for a more uniform strain gradient at the hole edge with an accompanying potential for earlier strain localisation. Pathak et al., in their work on the edge formability of dual and complex phase steels also recorded higher HER values for conical as compared to flat punches (Pathak, et al., 2016). Their work showed that the flat punch initiates cracks away from the hole edge since it loads the sheet under a plain strain loading condition compared to the conical punch which exerts uniaxial tension at the hole edge (Pathak, et al., 2016).

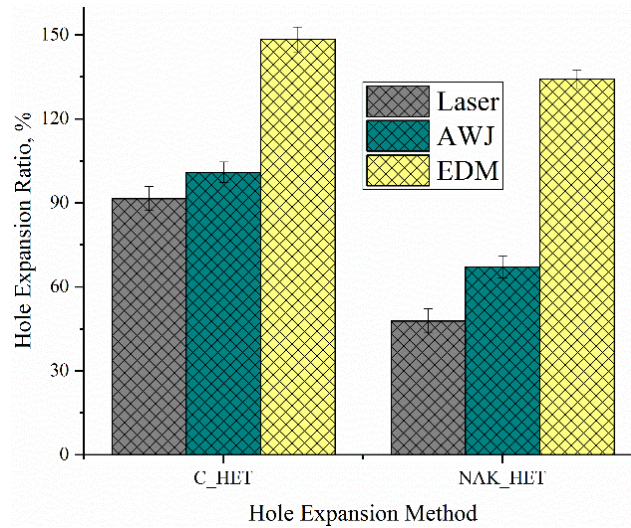


Figure 5. 14 Effect of tool geometry on HER of unfinished edge quality

For both tool geometries however, failure commenced under uniaxial tension near the hole edge. The similarities in the generated stress state near the hole edge and the occurrence of fracture at the hole edge makes both tool geometries desirable for edge formability determination of the material. Both the hemispherical and conical punches also exhibited the same trend of edge formability behavior in CP-Ti (Grade 2) sheet after laser, AWJ and EDM cutting. This trend confirms the suitability of both tool geometries for use in the assessment of the hole edge formability of the material. The tool geometry influence on the HER is telling mainly in terms of the loading conditions leading to varying HER. The nature of the edge structure produced after the edge fabrication method is therefore responsive to the nature of the tool geometry; hence the varying results for different machining methods. Thus, the ultimate edge formability performance lies in the integrity of the attained edge surface micro-features/defects produced during the material fabrication process. The results reflecting the edge formability response as illustrated in Figure 5.11 are as a consequence of the nature of the edge surface micro-features discussed at more length in section 5.2.1. The tool geometry plays a significant role in terms of the optimum ways of loading the hole edge surface with respect to the sheet material plane.

5.2.6 Assessment of edge formability using GOM Atos measurement

HER determination is key to the quantification of the edge formability of materials, but very difficult to characterize. Reliance on visual inspection (operator discretion) to determine the onset of cracks can also be difficult since it alters the HER values, leaving large variations

between repeated test results (Atzema, et al., 2012). The GOM Aramis system provides a better alternative by providing the option of tracking images frame by frame to determine the exact point of crack inception. However, there also exists the risk of data loss as a result of extreme deformation (Figure 5.15), the possibility of pixel point unavailability (due to poor speckle pattern application) at the hole edge and the uphill task of spotting the inner diameter of the hole edge (where the HER value evaluation is optimum).

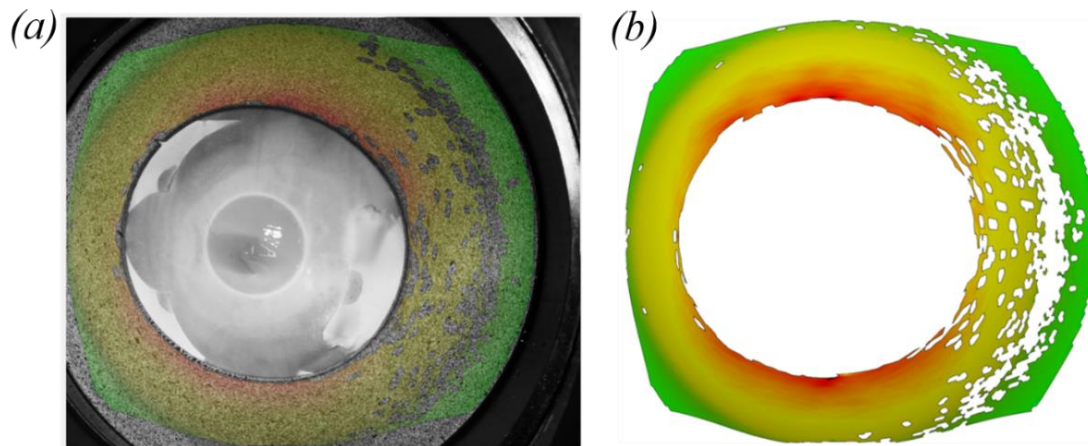


Figure 5. 15 Data loss due to extreme deformation of an EDM fabricated edge

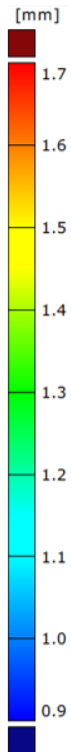
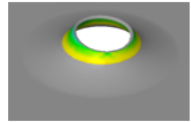
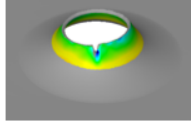
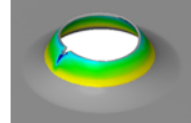
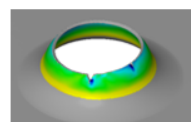
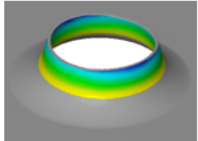
(a)Clamping position during HET, (b) GOM Aramis processed strain map

Some works have suggested equations to compensate for the crack width during HER determination (Larour, et al., 2016). Schneider et al., in their work also proposed various mechanisms that can be adopted for crack detection and correction during HET (Schneider, et al., 2016). However for fully flanged hole edges where no edge crack occurs, the approach of edge crack width correction to aid compute the edge forming performance will not apply. In addition, the edge formability assessment may be problematic for fully flanged edges since the standard equation for edge performance evaluation relies on the final hole diameter (see equation 2.2), which can only be determined upon the occurrence of edge cracks after the test termination. Therefore, there is the need to find an approach which could account not only for the edge forming performance of sheet metals but also for ones with fully flanged edges without edge cracks. This EngD research proposes the GOM Atos metrology technique as a more consistent and viable supplementary route to characterizing the edge formability of sheet materials.

5.2.6.1. GOM Atos measurement after HET with Conical punch

For the experimental test condition where the conical punch was used to deform the hole edges fabricated with either laser, AWJ or EDM cutting methods, the thinning evolution around the deformed hole edge zone and the extent of formability of each cutting technique during the test trial was assessed using the GOM Atos measurement. Table 5.2 shows the results of the thinning evolution assessment for the various edge surface finishes after HET.

Table 5. 2 Thinning evolution with HER and edge surface finish after HET with conical punch

Cutting Edge and finish quality	HER, %	Thickness, mm	Edge Flangeability	
			Passed	Failed
Laser	91.51			
Unfinished AWJ	100.9			
Finished AWJ	140.38			
Unfinished EDM	148.4			
Finished EDM	195.86 (Unfailed)			

For the AWJ finished edge surface, significant thinning was observed (~1.18mm) compared to their unfinished counterpart (~1.27mm). A similar trend was observed for the EDM fabricated edge after HET. The finished EDM fabricated edges also exhibited significant thinning (~0.90mm) at the hole edge after HET compared to their unfinished edge counterpart (~1.10mm). The linear relationship between the HER and surface finish quality was matched with a corresponding reduction in edge thickness. The thinning evolution around the hole edge is a function of the type and quality of the cut edge finish. The finished edge after EDM (Ra~0.8µm) cutting also showed higher HER compared to the unfinished EDM edge (Ra~3.7µm) with a corresponding reduction in edge thickness. With an improved edge finish

after EDM cutting however, the hole edge was successfully flanged with the 30mm diameter conical punch, Figure 5.16a. The EDM cut edge recorded the lowest thickness zones around the flanged region (~0.9mm) followed by AWJ cut edge (~1.18mm) and laser machined edge (~1.4mm), Figure 5.16.

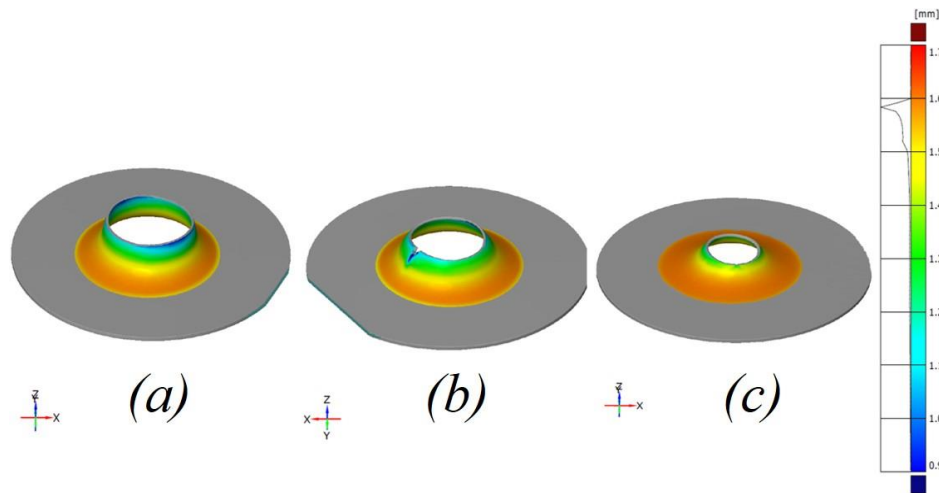


Figure 5. 16 Thinning evolution analysis after HET with conical punch
 (a) Finished EDM edge, (b) Finished AWJ cut edge, (c) Laser cut edge

The nature of the edge surface micro features after machining is therefore a major factor which influence the thinning evolution tendency at the hole edge of the material. Since the stress during the deformation process concentrates around the hole edge, the machining induced surface features become a critical feature during HET in their role as stress raisers. The GOM Atos metrology characterisation of the hole edge thinning evolution observed in the studied fabrication methods are consistent with the HER trends. Compared with GOM Aramis which focuses on the strain evolution during the HET, the GOM Atos technique is directed at ascertaining the thickness evolution after the test trials, which is indicative of the material flow and could therefore provide a viable route for assessing the edge forming performance of materials. The GOM Atos measurements are also more reliable for assessing samples, which have undergone high plastic deformation with no worries about speckle pattern integrity or pixel point loss.

5.2.6.2. GOM Atos measurement after HET with Hemispherical punch

GOM Atos metrology analysis was also carried out to evaluate the thinning tendencies of the material after HET with a hemispherical punch. The finished edge surfaces for laser, EDM and AWJ as well as the unfinished edge surfaces of AJW and EDM were evaluated. In order to

quantify the thinning evolution, the dome area of the test samples after HET were optically scanned and processed using GOM Atos metrology.

Table 5. 3 GOM Atos metrology measurement of samples deformed with hemispherical punch

Machining type and finish quality	HER, %	Thickness, mm	Edge formability after Gom Atos scanning
Laser	47.78		
Unfinished AWJ	67.15		
Finished AWJ	81.87		
Unfinished EDM	134.18		
Finished EDM	194.55		

Table 5.3 shows the thinning evolution distribution for both unfinished and finished edge surfaces of AWJ and EDM prepared samples as well as the laser fabricated edge surface after HET. The AWJ finished edge surface showed higher thinning distribution tendencies (~1.20mm) compared to the unfinished edge surface (~1.25mm). For the EDM fabricated test samples, the finished edge surface showed higher thinning distribution tendencies (~0.95mm)

compared to the unfinished edge surface (~1.11mm). The thinning trends are indicative of the edge forming capability of the material.

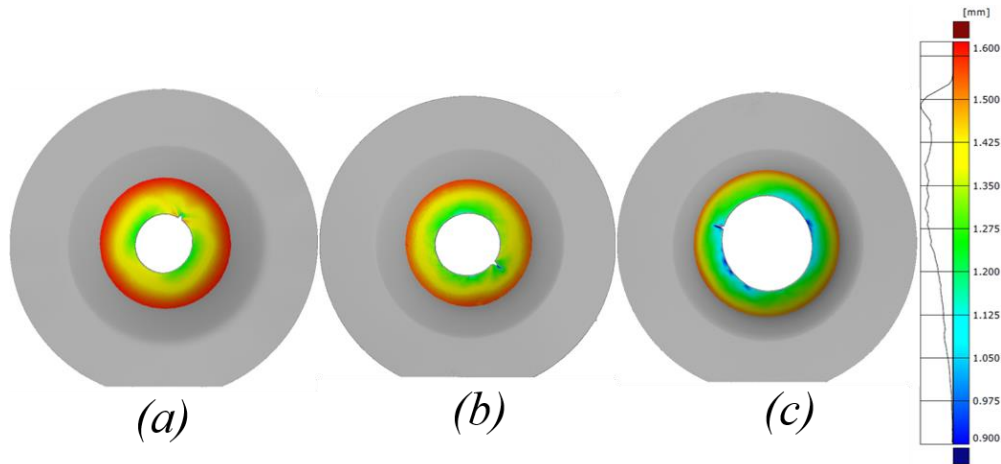


Figure 5. 17 Thinning evolution analysis after HET with hemispherical punch
 (a) Laser (b) Finished AWJ (c) Finished EDM cut edges

Figure 5.17 shows the comparison of thinning evolution observed for the finished edge surfaces of samples fabricated with either laser, AWJ or EDM after HET. The finished edge surface after EDM showed the highest thinning distribution tendency (~0.95mm), followed by AWJ (~1.20mm) and laser cutting (~1.35mm) showing the least thinning tendency. These observations are consistent with the HER trends, (see Figure 5.9) observed for this material in terms of their implications on edge formability. In general, the material exhibited thinning towards the hole edge along the dome region. This is due to the stresses moving towards and concentrating around the hole area during the deformation process. The response of the sheet edge to thinning therefore provides an important route to characterizing the edge forming capability of the material.

5.2.7 Failure behaviour of CP-Ti (Grade 2) during uniaxial tensile deformation and HET

An analysis of the strain path at the hole edges of CP-Ti (Grade 2) prepared with either laser, EDM or AWJ machining has been discussed extensively in section 5.2.4. The stress state observed at the hole edge during HET after GOM Aramis evaluation of the surface strains is uniaxial tension. Chapter 4 also examined the effect of machining on the uniaxial tensile properties of CP-Ti (Grade 2) with no impact observed for AWJ and EDM fabricated tensile

specimens. This section clarifies the disparities in deformation behaviour of both forming methods.

Digital image correlation technique was adopted to evaluate the surface strain evolution during the uniaxial tensile deformation of CP-Ti (Grade 2). Figure 5.18 shows the digital image correlation analysis of the global strain displacement in the plastic region during the uniaxial tensile deformation process. The global strain displacement appears to be mostly concentrated within the bulk material rather than the machined edges as the deformation progressed into the plastic region. Also, the strain distributions during uniaxial tensile deformation are likely to be governed by the material texture (see Table 4.6). The strains displaced and concentrated at high shear stress zones during localised necking with increasing deformation load for the 45°RD oriented sample, Figure 5.18d.

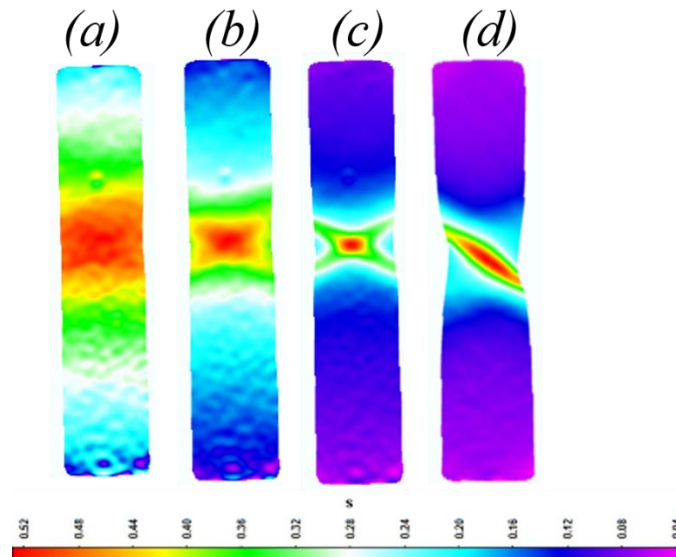


Figure 5. 18 Strain displacement in the plastic region for a 45° oriented sample

$$(a) \varepsilon_p = 0.19, (b) \varepsilon_p = 0.26, (c) \varepsilon_p = 0.53, (d) \varepsilon_p = 1.15$$

Where; $\varepsilon_p = \text{plastic strain}$

Figure 5.19 shows the surface strain distribution of the samples after HET (for sheet edge prepared with EDM) and uniaxial tensile test. For the tensile test sample, diffused necking occurred followed by localised necking with an accompanying decrease in the gage width cross sectional area at the fracture zone prior to failure, Figure 5.19a. Shear stresses acting are optimum when acting at 45° to the loading axis, and are concentrated in the localised necking region prior to failure. GOM Aramis analysis revealed that the stresses acting are highest around the hole edge after HET, Figure 5.19b. Localised necking was observed at the crack

edge with no visible reduction in the local cross-sectional area at the crack site, Figure 5.19*b* (inset). The exerted shear stresses are highest, when acting 45° to the applied load resulting in failure at edges where those stresses exist. This occurrence was the main reason for the visible 45° angled fracture line after HET with an EDM prepared hole edge (red arrow in Figure 5.19*b* inset), similar to the shear angle observed during the tensile deformation. Concisely, the main differences observed between the deformation processes lies in the necking morphology. Diffused necking followed by localised necking are observed during the tensile deformation process. However, failure observed after HET is characterised by localised necking with no visible diffused necking prior to fracture. The similarity in both deformation processes lies in the action of the acting shear stresses resulting in failure behaviour reminiscent of ductile shear fracture deformation mechanism.

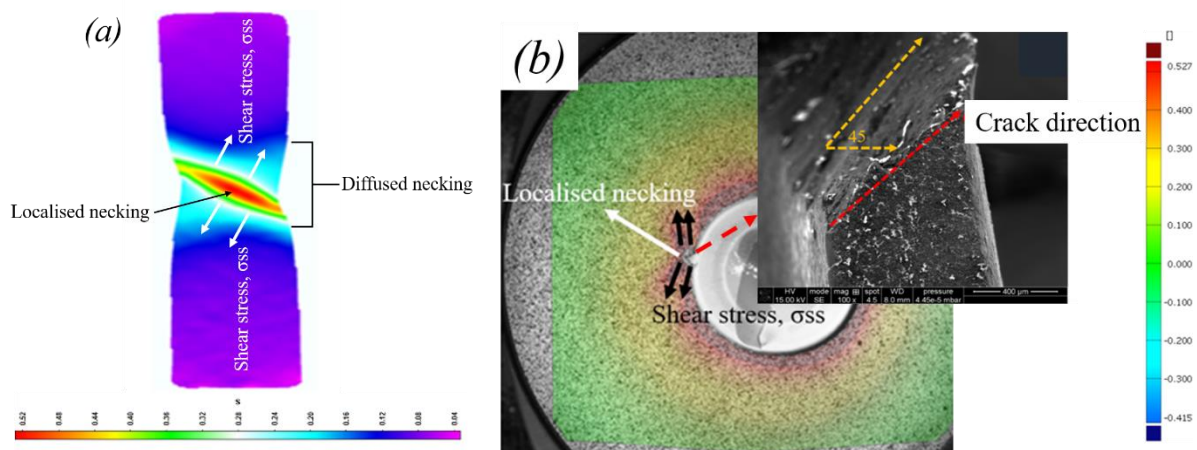


Figure 5. 19 Deformation mode analysis

(a)Tensile strain evolution, (b) Strain evolution during HET (inset: SEM of the hole edge)

Another striking difference observed between the conventional uniaxial tensile deformation behaviour and HET of CP-Ti (Grade 2) is the number of localised necking sites detected. There exist the tendency for the occurrence of numerous localised necking sites during HET (Figure 5.20), compared to the single localised necking site observed during conventional uniaxial tensile test. This could be attributable to the nature of the sheet loading (uniaxial tension verses biaxial stretching) and the role of sheet metal anisotropy. Karelova et al., in their work on CP800 steels also indicated that the occurrence of multiple crack sites at the hole edge after HET are governed by the sheet planar anisotropy (Karelova, et al., 2009). These multiple localised necking sites serve as zones of high strain gradient, making the prediction of the HER based solely on tensile deformation parameters (where generally only one form of localised necking occurs) very cumbersome.

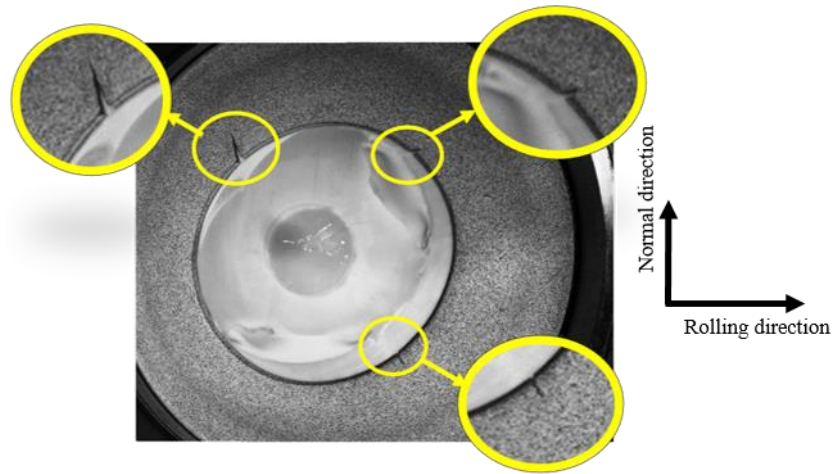


Figure 5. 20 Multiple localised necking sites during HET

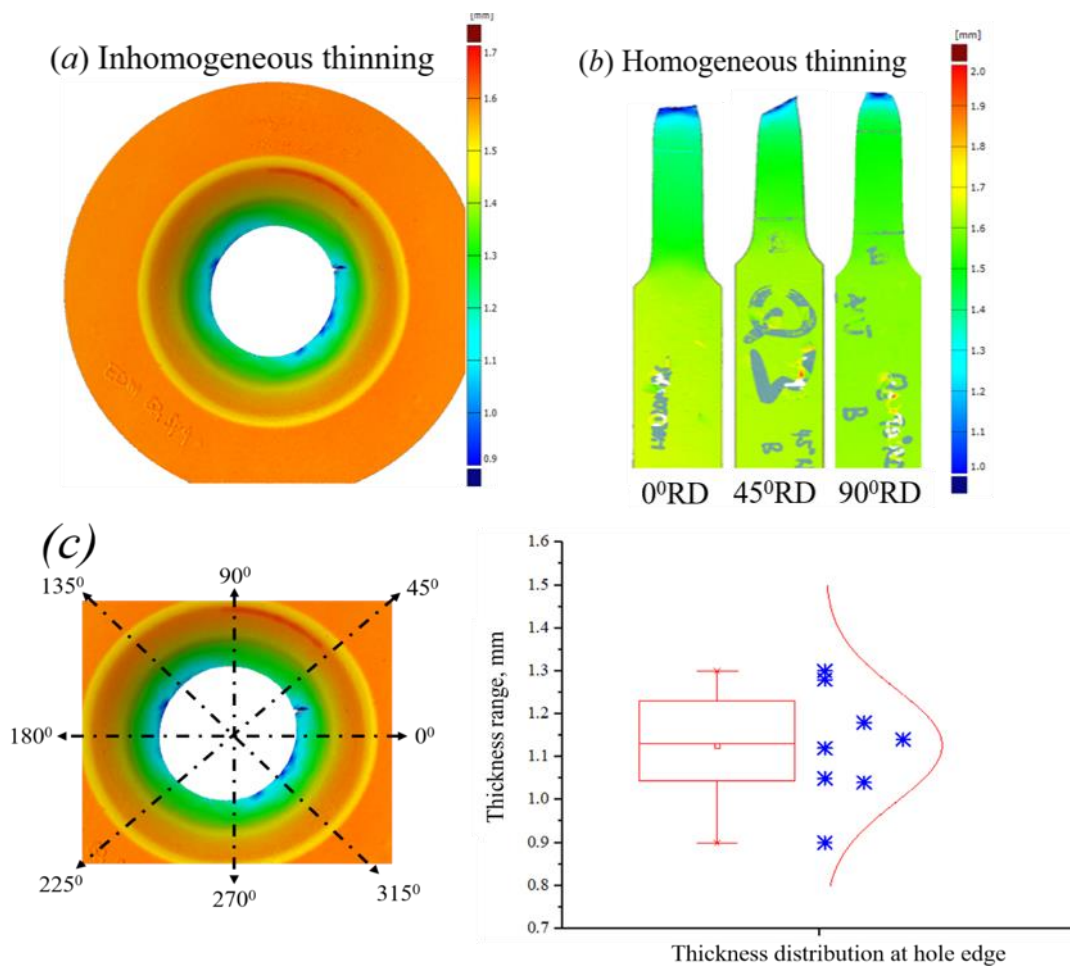


Figure 5. 21 Nature of thinning distribution at failure for CP-Ti (Grade 2)

(a) HET at fracture, (b) uniaxial tensile test at fracture, (c) thickness distribution at the hole edge after HET

Figure 5.21 shows the GOM Atos measurement analysis after fracture of the CP-Ti (Grade 2) samples after HET and uniaxial tensile test. Uniform sheet thinning (homogenous) are observed

for the tensile test samples at localised necking zones for samples tested in three sheet-rolling directions, Figure 5.21*b*. The changes in morphology of the localised necking with sheet-rolling direction confirms the responsiveness of the strain displacement to the material texture, (also see section 4.2.5). The CP-Ti (Grade 2) sample after HET also showed homogenous thinning at the zones of localised necking (edge crack sites). However, the higher number of localised necking sites seen after HET resulted in non-uniform thinning (inhomogeneous) at the hole edge region leading to higher deformation gradients, Figure 5.21*a*. The thickness distribution at the hole edge after HET was fairly Gaussian, Figure 5.21*c*.

GOM Atos optical metrology was preferred to micrometer gauge measurement in this research. The rounded nature of the HET samples permitted for a quicker scan of the detailed thickness distribution offered by the optical measurement. The manual nature of the micrometer gauge measurement meant that the detailed evaluation of the thickness values at the intricate edges will be cumbersome which could make the process prone to operator errors. The accuracy of measurement for the GOM Atos system was ensured by executing repeated calibration between scans and by making certain that sufficient-uniform Ardrox 9D1B was applied to reduce noise and error in the inspected elements. Mendricky in a research evaluated the accuracy of measurement of the GOM Atos non-contact 3D scanner by adopting the acceptance test in compliance with the VDI/VDE 2634:2008- part 3 standards. The work found that the GOM Atos passed and performed within the measuring accuracy when probed under the governing parameters (Mendricky, 2016).

5.2.8 Hole edge fracture initiation

Figure 5.22 shows SEM images of the laser cut edges before and after HET. The surface of the undeformed edge after laser cutting was characterised by surface defects in the form of periodic striation formations produced by virtue of material remelt on the part surface followed by rapid cooling, Figure 5.22*a*. During HET, the uneven nature of the striations act as stress concentration sites due to the presence of zones with deep striation features. Thus, the onset of crack initiation was observed in the trough of the striation formations, Figure 5.22*b*. Analysis of the deformed edge region of the laser crack surface after HET revealed the brittle intergranular nature of the cracks (yellow dash lines and inset) and the surface cracks rapidly propagated across the laser cut edge due to the brittle nature of the surface recast layer, Figure 5.22*c*. The poor thermal conductivity of the material meant that only surface recast layers were

formed. The cracks were initiated at the surface defect sites and the direction of crack propagation was influenced by the laser machining induced micro-feature changes on the surface. The cracks generated after the HET were traced in order to estimate the angle with respect to the loading axis. High angled localised necking was observed at the laser cut edge after failure during HET due to the typical brittle nature of the surface recast region; hence the poor edge formability, Figure 5.22*d*.

Figure 5.23 shows the SEM micrographs for the AWJ cut edge before and after HET. The micrograph of the AWJ machined edge shows surface defects in the form of surface draglines produced by the path traversed by the abrasive particles as well as micro-voids occupied or vacated by these abrasive particles, Figure 5.23*a*. During HET, these micro-voids act as stress raisers, thereby serving as crack initiation sites, Figure 5.23*b*. A zig-zag crack trajectory on the failed edge surface was also observed (yellow dotted arrows), Figure 5.23*c*. This could also be attributed to the more random distribution of the surface dragline features which obstructed quick crack growth. The failed sample edge after HET also exhibited localised necking representative of a more ductile fracture since no heat affected zones are associated with the AWJ cutting method, Figure 5.23*d*.

Figure 5.24 also shows the SEM micrograph of the examined EDM cut test sample. The micrograph of the EDM cut surface is characterised by surface defects in the form of craters, micro voids as well as re-solidified molten materials left behind during the machining process, Figure 5.24*a*. Strain gradients produced during the machining process by thermal stresses during cooling and/or plastic deformation would appear to have created an environment for fine surface micro-cracks to be produced on the workpiece edge surface, Figure 5.24*b*. These surface micro-cracks spread the applied stress during HET uniformly around the hole edge and resist crack propagation towards the sheet thickness direction, thereby delaying premature fracture. The integrity of the EDM induced micro- crack width (yellow arrows) was largely maintained after the HET, Figure 5.24*c*. Similar roles of strain induced surface micro-cracks generated after punching of martensite single phase steels inhibiting crack growth in the sheet thickness direction and consequently enhancing the material's HER has been reported in literature (Hasegawa, et al., 2004). These attributes of EDM cut edges are responsible for their superior edge formability compared to the other manufacturing methods. Inspection of the failed edge after HET also revealed that the EDM cut edge samples exhibited localised necking coupled with ductile shear fracture, Figure 5.24*d*. This could be attributed to the shear stresses exerted at the hole edge during HET being transformed to a uniaxial stress state during the

necking period. The shear stresses are optimum when acting at 45° to the applied load axis thereby producing failure at zones where the shear stresses are highest.

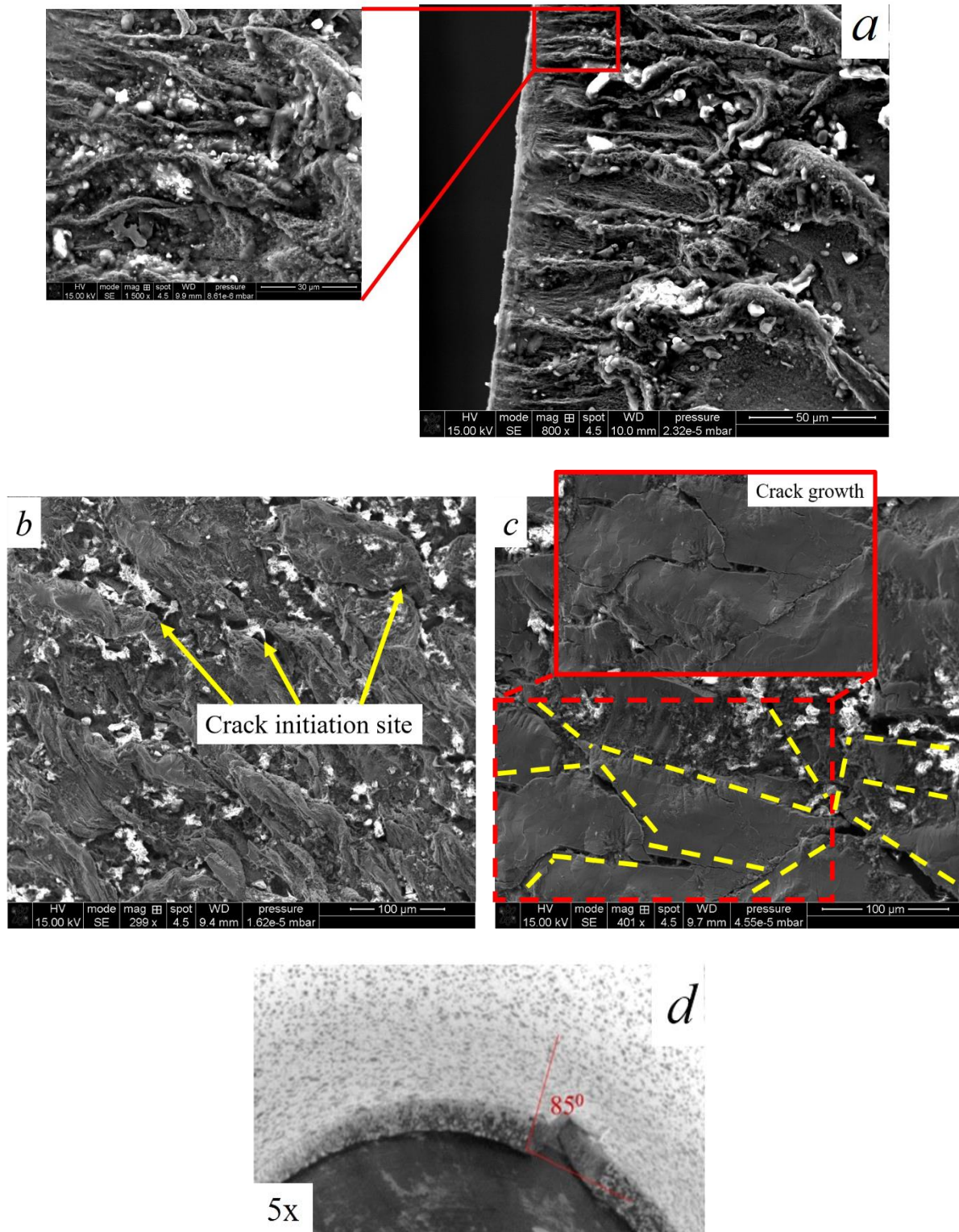


Figure 5. 22 SEM analysis of the failure process of the laser cut surface

(a) Laser cut surface, (b) failure initiation zone (yellow arrows), (c) inter-granular crack growth (yellow dash lines and inset), (d) brittle crack edge

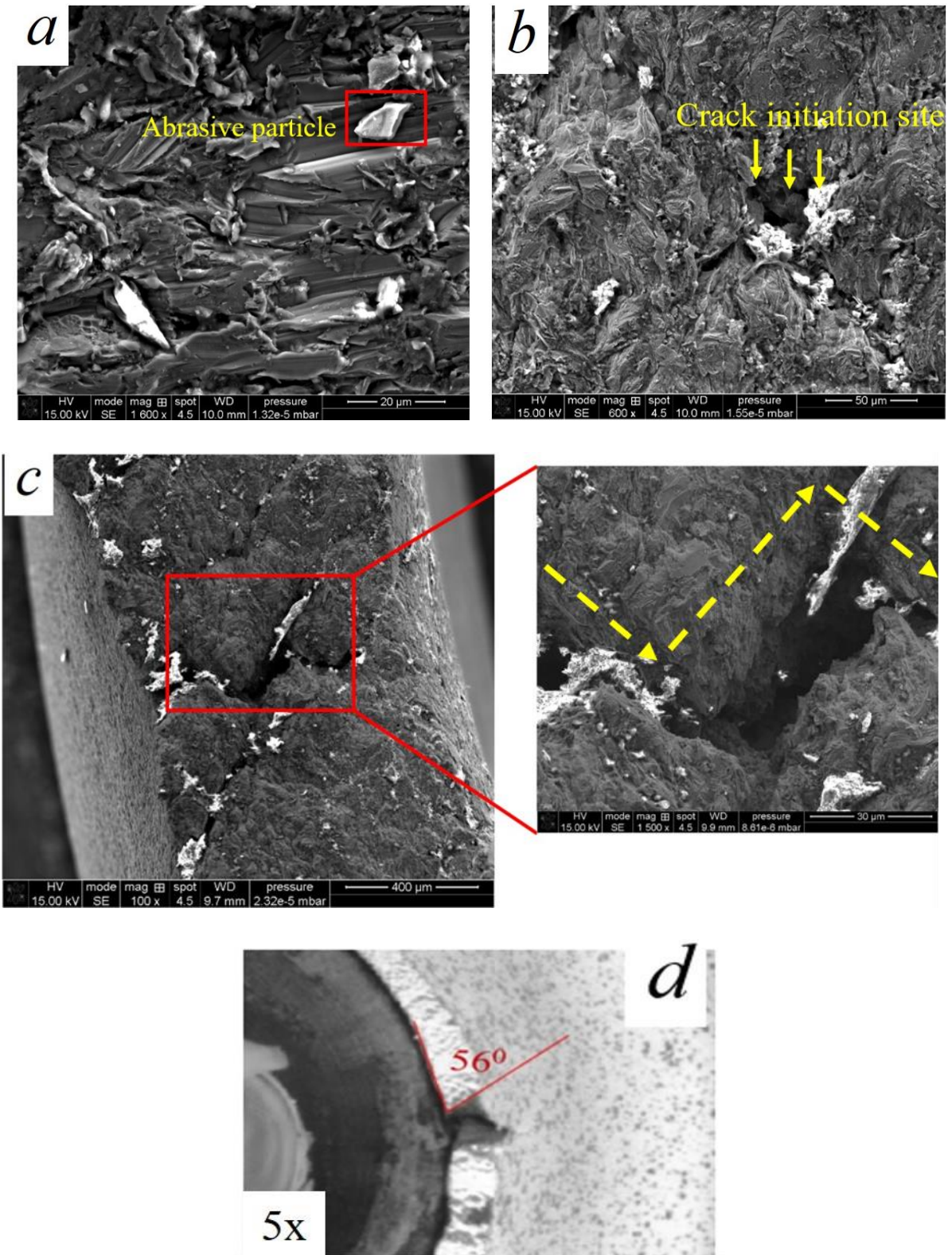


Figure 5. 23 SEM analysis of the failure process of the AWJ cut surface
 (a) Cut AWJ surface, (b) crack initiation site (yellow arrows), (c) crack path, (d)
 AWJ crack edge

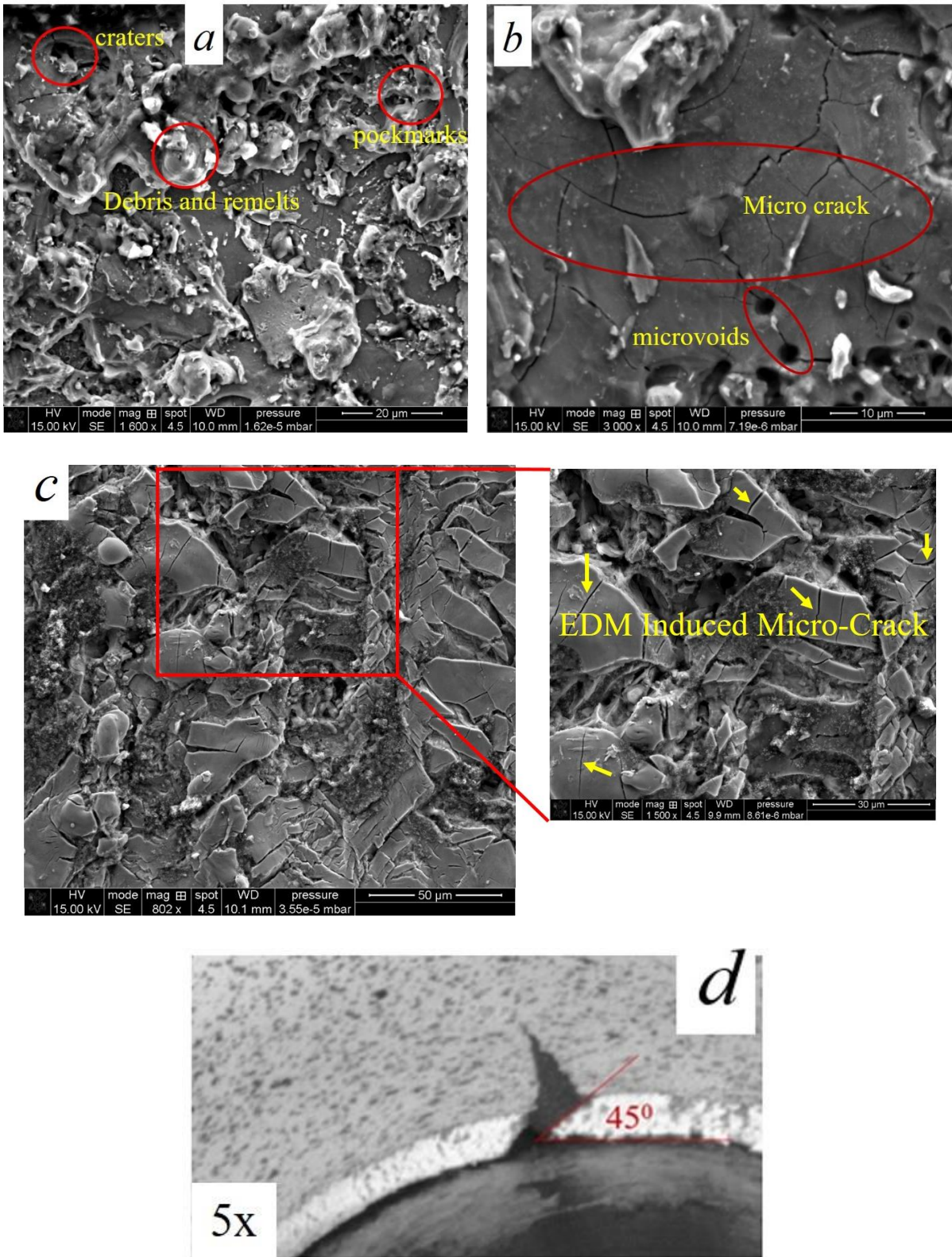


Figure 5. 24 SEM analysis of the failure process of the EDM cut surface

(a),(b) Cut EDM cut surface, (c) fractured EDM surface after HET with no significant growth in initial EDM induced micro-crack width (yellow arrows), (d) EDM crack edge

5.3 Summary

This chapter focused on the influence of machining induced defects on the edge forming performance of CP-Ti (Grade 2) fabricated with either laser, EDM or AWJ cutting. A HET was conducted using a standard conical punch and a hemispherical punch. The work also introduced the GOM Atos measurement technique as a supplementary method of characterising the edge formability of materials.

A uniaxial tension stress state is observed at the hole edge after HET which is synonymous with the stress state observed during traditional uniaxial tensile testing. However, conventional tensile testing methods are not suitable for determining the HER of sheet materials. This chapter employed optical non-contact measurement techniques to examine the failure processes of CP-Ti (Grade 2) during a uniaxial tensile test and HET. The chapter established that;

- The variability of edge surface finish attained after EDM and AWJ machining have a significant effect on the edge formability of CP-Ti (Grade 2). The machining induced surface defects play a vital role in the edge forming performance in their role as stress raisers.
- The EDM machined edges showed higher edge formability tendencies compared to AWJ and laser cut edges. The material also showed higher edge fracture limit strain for EDM cut edges (~0.93) compared to the other machining methods (laser~0.34 and AWJ~0.53). The proposed edge FLD helps to visualise the optimum machining choice adequate for use in a hole flanging operation.
- Both the hemispherical and conical punch tool geometries produced the same trend of sheet edge formability. This is due to the fact that both tools load the sheet by exerting a uniaxial tension stress state at the hole edge. The standard conical punch however produced higher HER due to the peculiar nature of the tool loading orientation.
- The GOM Atos metrology offers a viable supplementary approach for characterising the edge formability of materials. The thinning evolution trends observed after GOM Atos measurement are consistent with the material edge forming performance trends observed after HET.
- The dome height evolution is a function of the edge surface integrity response to edge loading and an indicator of sheet edge formability.

- For uniaxial tensile deformation, fracture is generally characterised by diffused necking followed by localised necking. However, only localised necking is spotted after HET. Shear stresses are noted to act for both forming techniques and are aligned 45° to the loading axes at optimum values. The occurrence of high number of localised necking sites after HET results in non-uniform thinning around the hole edge, leading to the formation of high deformation gradients.

Chapter 6

Effect of machining on the edge formability of an alloyed and unalloyed titanium grade

Overview

The variations in the response of different titanium alloys to machining are attributable to the fundamental differences in their metallurgical structures. The consequences of such differences are the varied response of their edge surface micro-feature evolution to machining type and machining parameters. However, the response of different grades of titanium to machining and their ultimate impact on their edge forming capability has not been previously studied. This chapter compares the edge forming capabilities of unalloyed titanium (CP-Ti Grade 2) to those of an alloyed titanium grade (Ti-3Al-2.5V) for sheet edges prepared with either AWJ or EDM machining methods.

Most aspects of the results discussed in this chapter has been presented and published in a journal/ conference proceedings.

6.1 Experimental procedure

6.1.1 The materials

The materials studied in this chapter were CP-Ti (Grade 2) and Ti-3Al-2.5V alloys. Ti-3Al-2.5V, sometimes referred to as ‘half Ti-64’, is a near α titanium alloy with an intermediate strength and good cold workability.

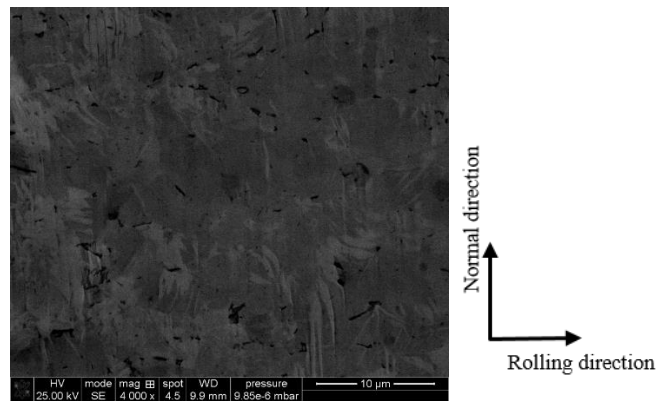


Figure 6. 1 Micrograph of as-received Ti-3Al-2.5V sheet

It is usually employed in aerospace applications such as hydraulic tubing systems and lightweight honeycomb structures. The SEM micrograph of the as-received Ti-3Al-2.5V sheet is shown in Figure 6.1. Near α titanium alloys are mostly highly α stabilised with a limited amount of β phase. CP-Ti (Grade 2) possesses a good strength to weight ratio and has the ability to maintain its strength appreciably during deformation. CP-Ti (Grade 2) is a predominantly single-phased structure of fine α grains (see Figure 4.1).

6.1.2 Material edge surface preparation

AWJ and EDM machining methods were utilised to prepared the materials for hole expansion test and uniaxial tensile test. The sheet fabrication process and machining parameters adopted for preparing the edge surfaces as explained in section 5.1.5 were applied to the two materials under investigation. For this section, finished and unfinished edge surface qualities for edges prepared with either AWJ or EDM were examined. Alicona optical microscope was utilised to assess the machined edge surface morphology of both materials after AWJ and EDM cutting.

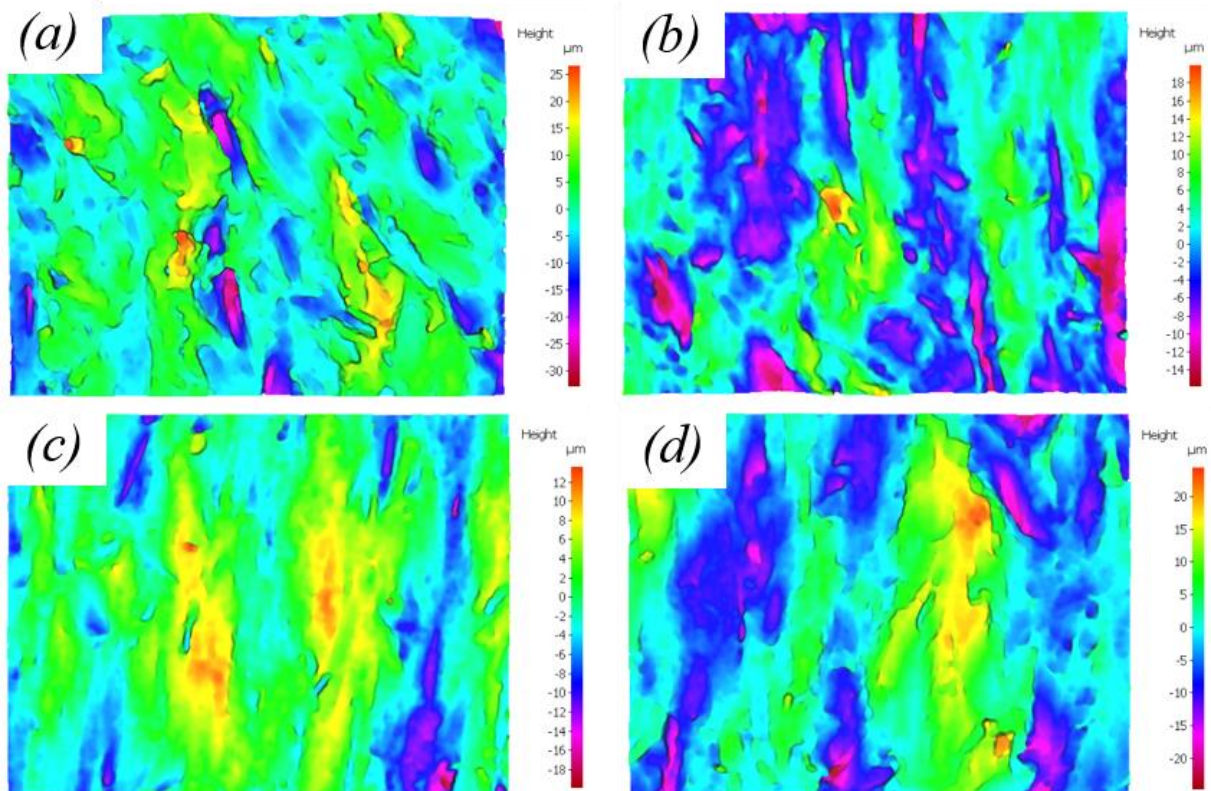


Figure 6. 2 AWJ machined edge surface morphologies

(a) Unfinished AWJ, CP-Ti (Grade 2) (b) Finished AWJ, CP-Ti (Grade 2) (c) Unfinished AWJ, Ti-3Al-2.5V, (d) Finished AWJ, Ti-3Al-2.5V

The Alicona optical 3D measurements of both materials exhibited higher edge surface micro-ridge and micro-groove distribution for the unfinished AWJ edges compared to the finished parts. The ratio of the edge surface micro-grooves to micro-ridges were also fairly even for the finished AWJ cut edges compared to the unfinished parts for both materials, Figure 6.2 *a,b,c,d*. The variations in the edge surface morphology response of both materials after machining with the same machining parameters are attributable to the inherent material metallurgical structure response to machining. The CP-Ti (Grade 2) performed better in terms of finer edge defect distribution indicating the ease of their machinability compared to Ti-3Al-2.5V alloy. This observation of pure titanium being relatively easier to machine compared to their alloyed counterparts have been highlighted in some works (Yang & Liu, 1999).

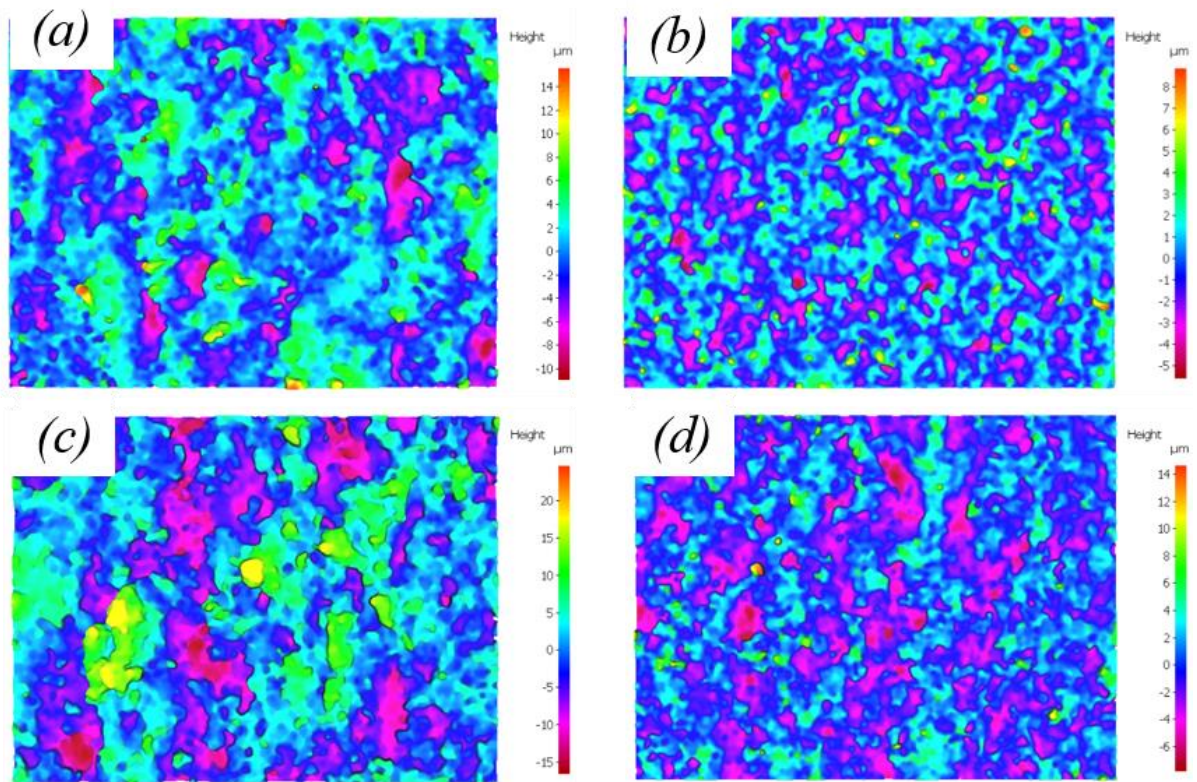


Figure 6. 3 EDM machined edge surface morphologies

(a) Unfinished EDM, CP-Ti (Grade 2) (b) Finished EDM, CP-Ti (Grade 2) (c) Unfinished EDM, Ti-3Al-2.5V (d) Finished EDM, Ti-3Al-2.5V

The Alicona optical 3D measurements of both materials showed a finer distribution of surface micro-grooves for the finished EDM edges compared to the unfinished edges for both materials, Figure 6.3*a,b,c,d*. The attained surface micro-groove size and distribution for the finished EDM edges for CP-Ti (Grade 2) are finer compared to those observed for Ti-3Al-2.5V, Figure 6.3*b, d*. Again, the variations observed for the edge surface morphology response

of both materials after machining with the same machining parameters are attributable to the inherent material metallurgical structure response to machining.

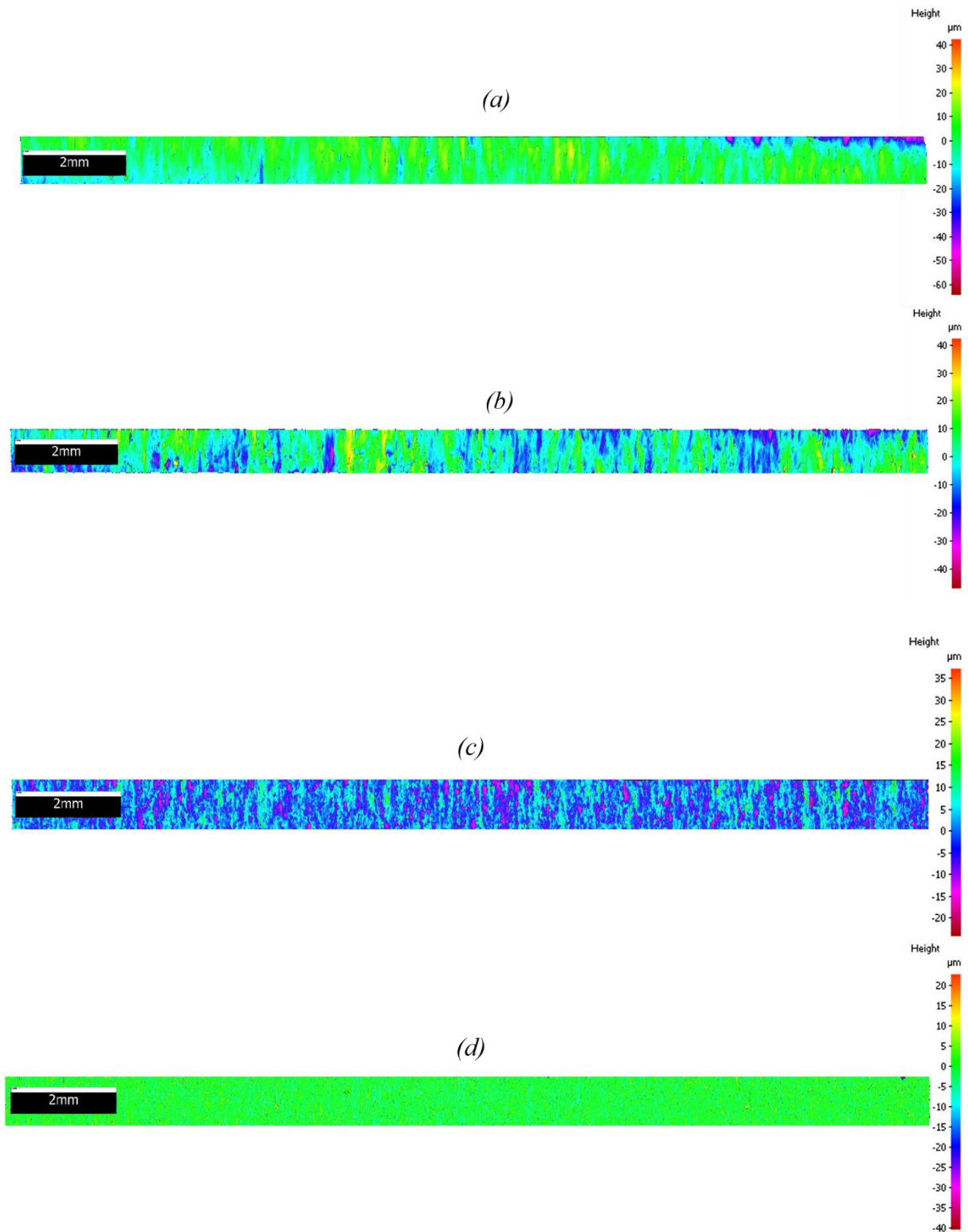


Figure 6. 4 Edge surface integrity of Ti-3Al-2.5V examined over 1.6cm distance

(a) Finished AWJ cut (b)Unfinished AWJ cut, (c) Unfinished EDM cut, (d) Finished EDM cut

In general, CP-Ti (Grade 2) exhibited better edge surface finishes with finer defect distribution for both edge surface qualities compared to Ti-3Al-2.5V signifying their better reception to machining.

EDM and AWJ machined edge micrographs of Ti-3Al-2.5V test samples for finished and unfinished edge qualities over wider surface areas were also studied using an Alicona optical 3D measurement system. Measurements were taken over a full-length distance (1.6cm) in order to visualise the edge surface defect distribution, Figure 6.4. The nature of the edge surface defects (micro grooves and peaks) distribution were significantly lower in the finished edge surfaces compared to the unfinished edges for both machining techniques.

6.1.3 Hole expansion test

A standard hole expansion test governed by ISO 16630:2017 was conducted on both materials to assess their edge forming capabilities. The same conditions for material preparation and test parameters described in this EngD research were adopted and applied to both materials. The HER values obtained were computed by applying equation (2.2).

6.1.4 Uniaxial tensile test and Mechanical properties

A Zwick/ Roell Z150 tensile testing machine was used to perform a standard room temperature uniaxial tensile test consistent with ISO 6892-1:2016. The tests were conducted at a constant strain rate of 0.001/s.

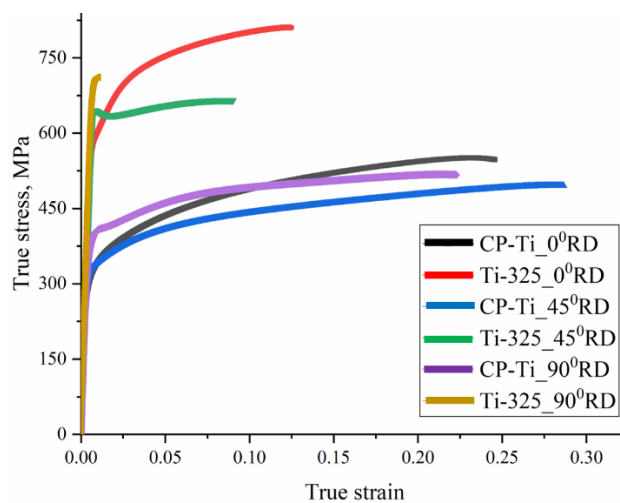


Figure 6. 5 Tensile properties of CP-Ti (Grade 2) and Ti-3Al-2.5V

Both materials exhibited highly anisotropic behaviour when examined in three sheet-rolling directions, Figure 6.5. Ti-3Al-2.5V exhibited higher strength and lower ductility in all three sheet-rolling directions compared to CP-Ti (Grade 2).

6.2 Results and Discussion

6.2.1 Machining induced edge surface defects

SEM analysis was conducted in order ascertain the nature of the edge surface morphology and defects obtained after EDM and AWJ machining of Ti-3Al-2.5V, Figure 6.6. The edge surfaces after AWJ machining were characterised by its surface mechanical erosion features. The surface tracks were produced by virtue of the routes taken by the abrasive particles during the cutting process. The micro-grooves and dents observed are also due to the areas occupied and/or vacated by the abrasive particles during the machining process. The direction of AWJ cut was along the trajectory of the surface draglines produced by the abrasive particles, Figure 6.6a. The edge surface micro-features observed were similar to those noted in CP-Ti (Grade 2) after AWJ machining (See Figure 4.5a).

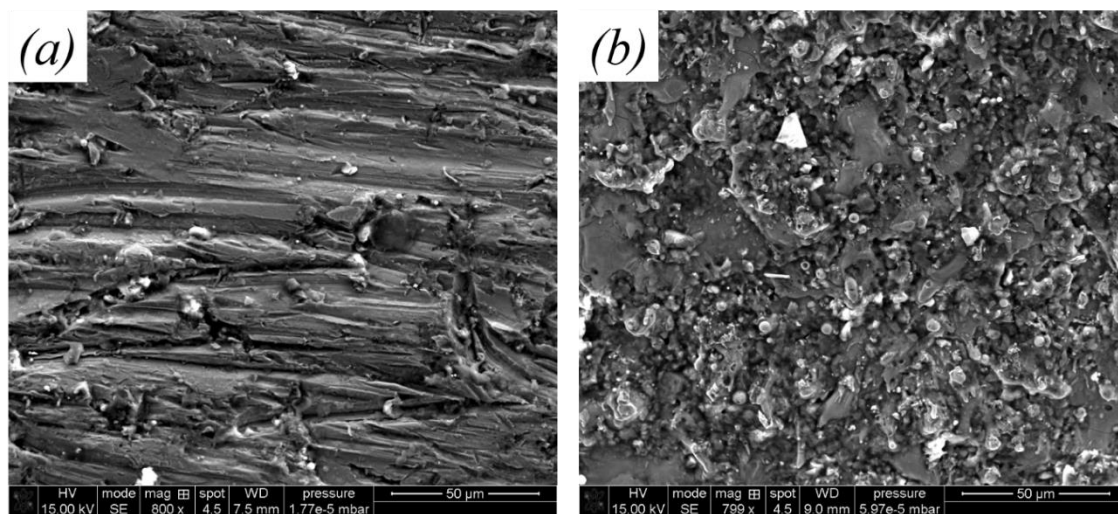


Figure 6. 6 Surface morphology of the machined edges of Ti-3Al-2.5V

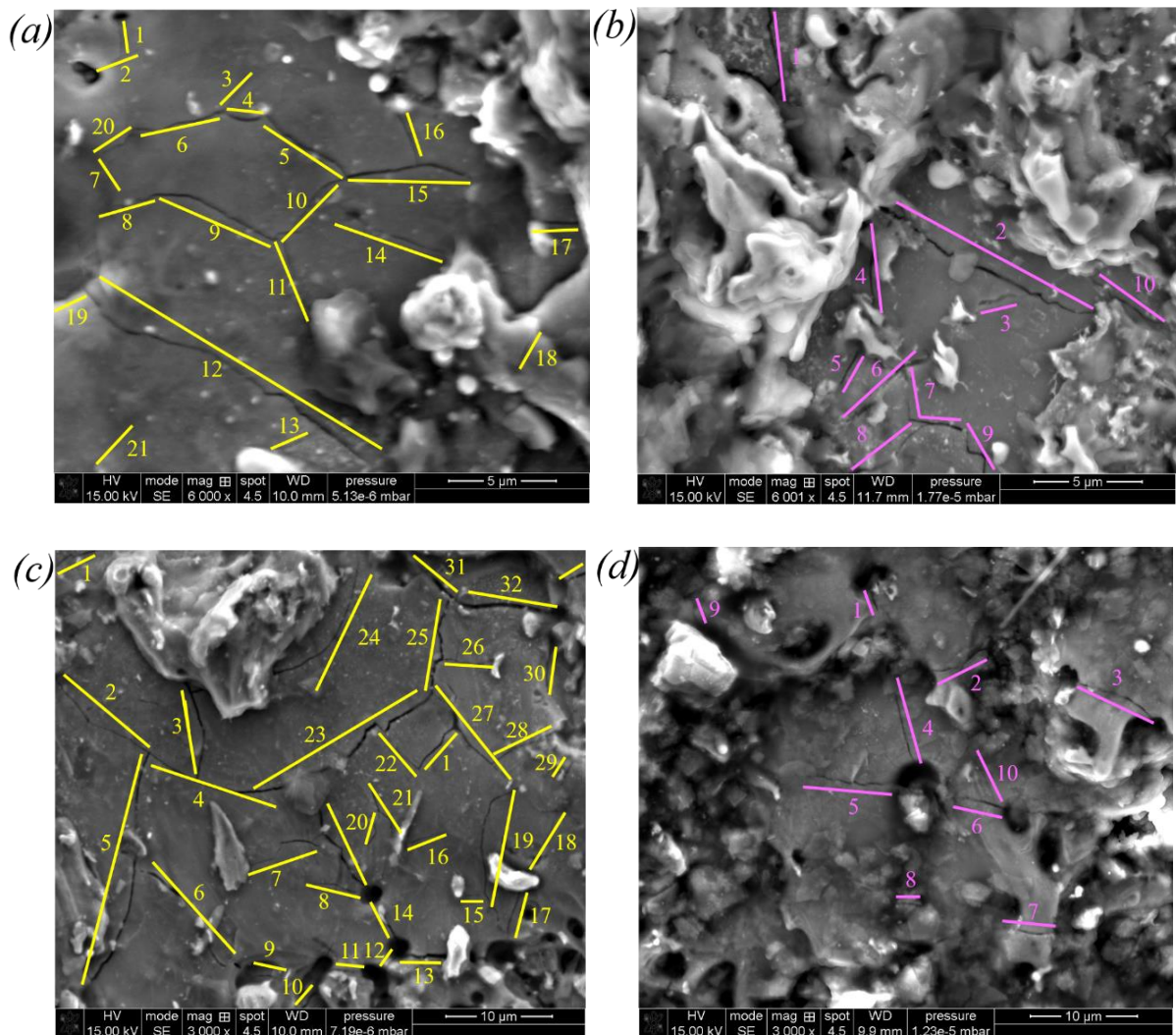
(a)AWJ cut edge surface, (b) EDM cut edge surface

An SEM analysis of the edge surface after EDM cutting of Ti-3Al-2.5V revealed features synonymous with its heat erosion characteristics (pockmarks, debris, micro voids and micro cracks). The EDM edge surfaces spotted micro voids, micro cracks, craters, ridges and pockmarks as the main edge defects, Figure 6.6b. The level of surface pockmarks produced is a function of the capability of the dielectric fluid to wash away debris during the machining

process in the pursuit to reduce melt solidification. The edge surface micro-features observed were similar to those observed in CP-Ti (Grade 2) after EDM machining (See Figure 4.5b).

6.2.2 Comparison of critical surface features and parameters after machining

One of the noticeable differences between the EDM machined edge features of both materials after SEM analysis was the variations in the amount of emergent surface micro-cracks. Since EDM machining parameters have a significant effect on the amount of surface micro crack density evolution (Kumar, et al., 2013), the compared SEM images analysed for CP-Ti (Grade 2) and Ti-3Al-2.5V were for those obtained with the same machining parameters. The finished EDM edge surface qualities are analysed in this section.



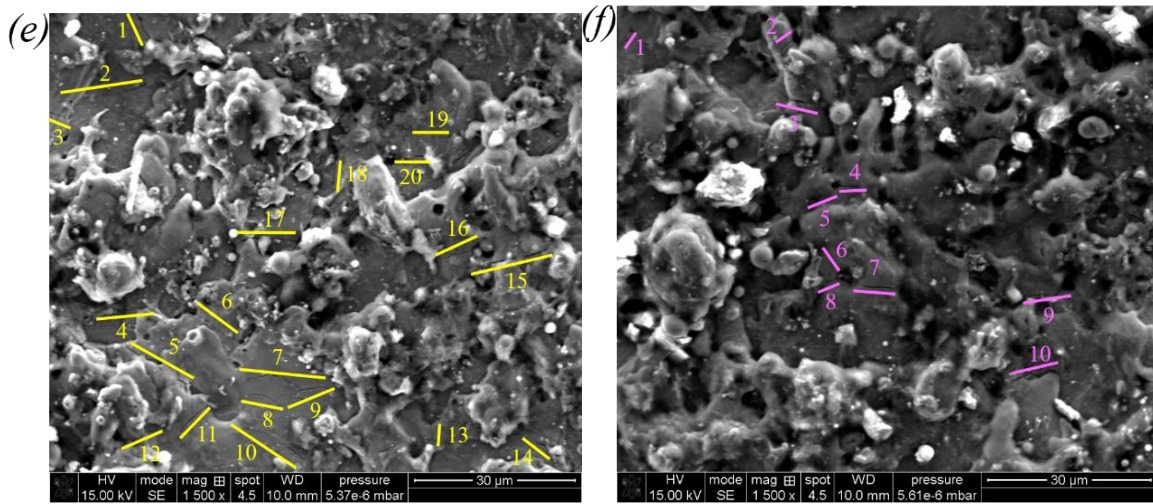


Figure 6. 7 SEM images for EDM surface crack density estimation

Analysis for areas (a, b) $15 \times 15 \mu\text{m}^2$, (c, d) $30 \times 30 \mu\text{m}^2$ and (e, f) $90 \times 90 \mu\text{m}^2$. The yellow and magenta micro crack length markings are for CP-Ti (Grade 2) and Ti-3Al-2.5V respectively. According to Lee and Tai, the severity of surface micro cracks after EDM machining can be estimated by using the so called surface crack density (Lee & Tai, 2003). According to the authors, this could be attained by evaluating the total length of crack per unit area. Kumar et al., in their work on the determination of pure titanium susceptibility to micro crack generation during wire EDM fabrication process found that micro crack formation was best estimated in terms of the average crack length (Kumar, et al., 2016). Figure 6.7 shows the identified average micro crack length and distribution for various unit areas identified for both materials after EDM machining. The analysis was done for repeated test samples over varied surface areas. The surface crack density for the CP-Ti (Grade 2) sample was almost twice that of Ti-3Al-2.5V for all areas investigated.

Table 6. 1 Surface texture measurement of AWJ machined edges

Materials	Highest maximum pit height Sv, μm	
	Finished edge	Unfinished edge
CP-Ti (Grade 2)	18.40-19.20	22.74-23.90
Ti-3Al-2.5V	22.45-24.79	26.70-28.04

For the AWJ machined edges, surface texture measurement was done for both materials using the Alicona system. Table 6.1 shows the results of the range of highest maximum pit height parameters measured for both materials. The measurement was done for five surface duplicates of each material. The CP-Ti (Grade 2) test samples exhibited lower forms of surface defects in terms of the surface texture compared to Ti-3Al-2.5V after AWJ machining, for both finished

and unfinished edge surface finish qualities. The differences in surface texture evolution could be attributed to the differences in the inherent material properties and their response to the AWJ machining process.

6.2.3 Edge forming performance: Conical punch

Figure 6.8 shows the edge forming performance of Ti-3Al-2.5V and CP-Ti (Grade 2) tested for two different edge-cutting methods and edge surface finish qualities deformed with a standard conical punch. Comparison between the edge forming performances were made on the basis that there are no direct linear correlation between the HER and titanium sheet thickness values. In general, the EDM machined edges showed the highest edge forming performance (CP-Ti Grade 2: ~195.86% and Ti-3Al-2.5V: ~78.16%) compared to the AWJ machined edges (CP-Ti Grade 2: ~140.38% and Ti-3Al-2.5V: ~49.84%) for both materials. Both materials exhibited better edge forming performance for the finished machined edge qualities (CP-Ti Grade 2: EDM ~195.86%, AWJ ~140.38% and Ti-3Al-2.5V: EDM ~78.16%, AWJ ~49.84%) compared to the unfinished edge qualities (CP-Ti Grade 2: EDM ~148.4%, AWJ ~100.9% and Ti-3Al-2.5V: EDM ~69.73%, AWJ ~42.48%) for both cutting techniques. Overall, CP-Ti (Grade 2) showed better edge forming performance compared to Ti-3Al-2.5V alloy. These trends are attributable to the nature of the edge surface micro-feature alterations and defects produced during the machining process, which proved to be a function of the metallurgical structure of both materials. Pure titanium is predominantly alpha phased alloys, relatively soft and easier to machine compared to alloyed titanium (Yang & Liu, 1999). Generally, the edge micro features attained for both materials are varied after EDM and AWJ machining. CP-Ti (Grade 2) after AWJ cutting showed lower levels of edge surface micro-grooves and defects compared to Ti-3Al-2.5V, Figure 6.9*a,b*. The EDM microstructure also showed a high volume fraction of machining induced micro-cracks in CP-Ti (Grade 2) compared to Ti-3Al-2.5V, Figure 6.9*c,d* (also see Figure 6.7). The impact of EDM induced micro-cracks and their role in the edge forming performance of materials are explained in subsequent subsections. The severity of defects produced during machining is a function of the ease of machinability of the materials. The general mechanical properties of the materials could also influence their edge forming behaviour. CP-Ti (Grade 2) exhibits higher ductility and lower strength resulting in their better formability compared to Ti-3Al-2.5V at room temperature.

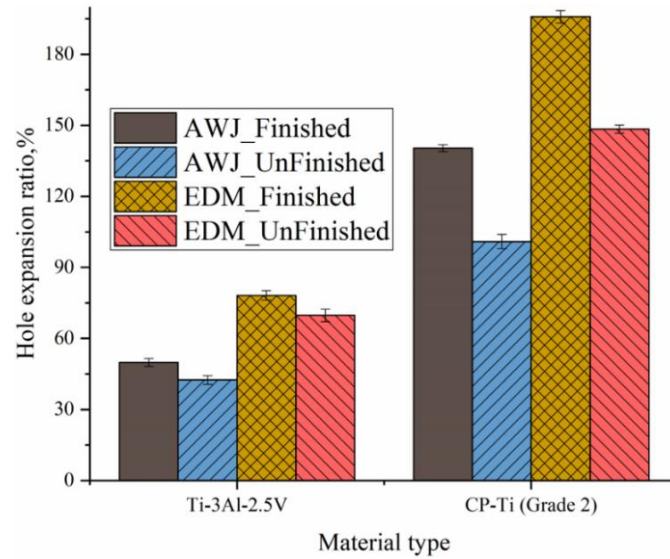


Figure 6. 8 Edge formability of CP-Ti (Grade 2) and Ti-3Al-2.5V alloys assessed with conical punch

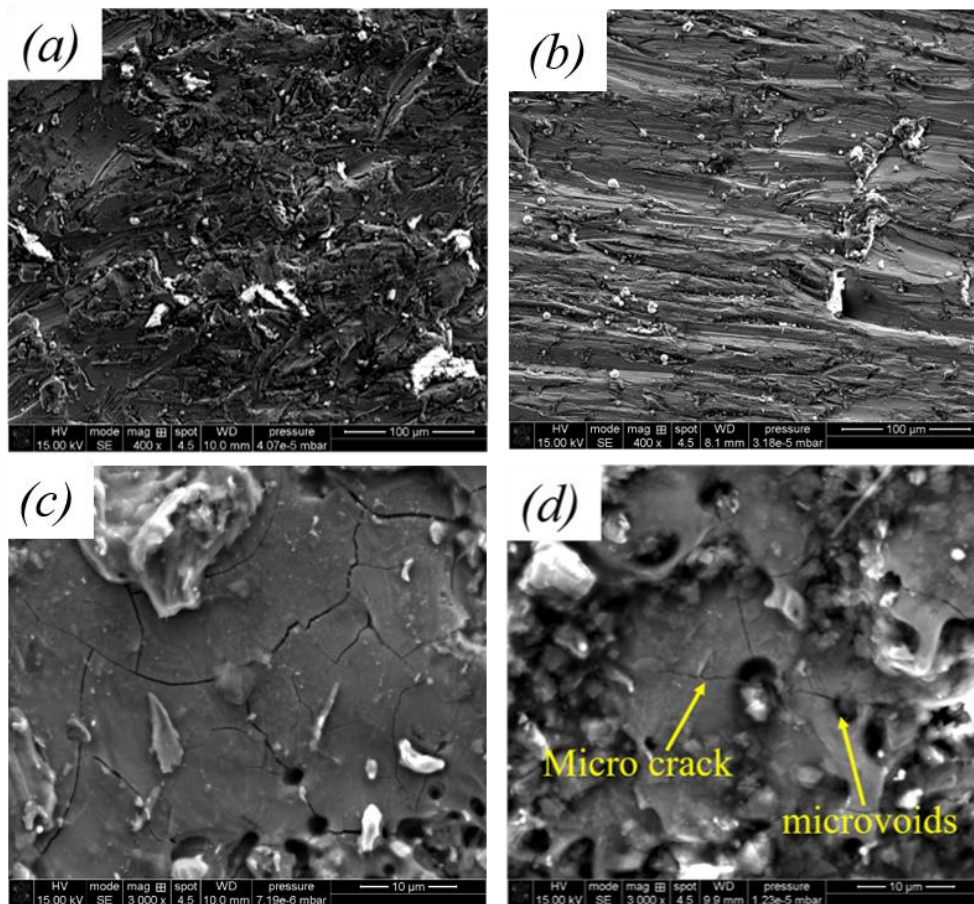


Figure 6. 9 Machining induced surface microstructure changes


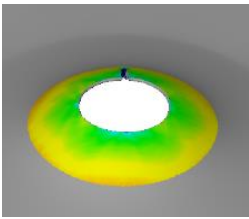
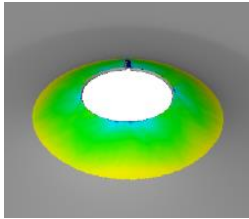
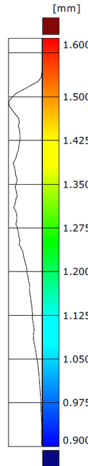
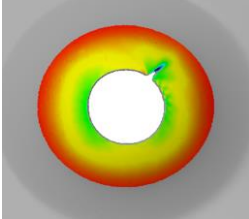
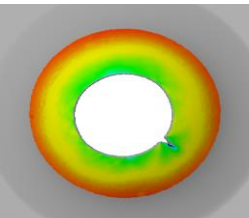
(a) CP-Ti (Grade 2) AWJ cut edge (b) Ti-3Al-2.5V AWJ cut edge, (c) CP-Ti (Grade 2) EDM cut edge, (d) Ti-3Al-2.5V EDM cut edge

6.2.4 Thinning evolution after HET: Hemispherical punch

The GOM Atos measurement technique was utilised to assess the thinning tendencies of the materials with machined edges prepared with either AWJ or EDM after HET.

Table 6.2 shows the thinning evolution of the test samples with AWJ fabricated edges deformed with a hemispherical punch. Overall, significant sheet thinning around the hole edges were observed in the finished edge qualities compared to the unfinished edges for both materials.

Table 6. 2 Comparison of thinning evolution of AWJ fabricated edges after HET with hemispherical punch

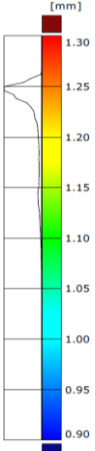
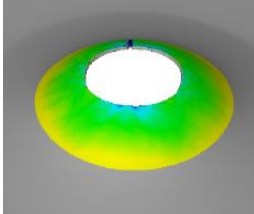
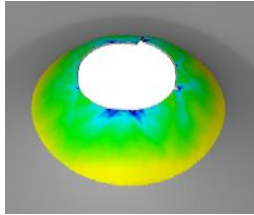
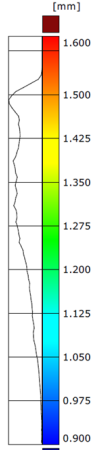
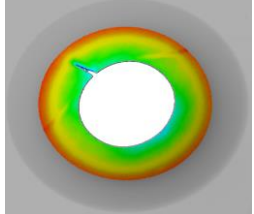
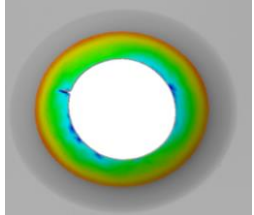
Material (Cutting regime)	Thickness, mm	GOM Atos metrology
Ti-3Al-2.5V (UnFinished AWJ)		
Ti-3Al-2.5V (Finished AWJ)		
CP-Ti Grade 2 (UnFinished AWJ)		
CP-Ti Grade 2 (Finished AWJ)		

For each cut edge quality however, CP-Ti (Grade 2) exhibited the highest thinning at the hole edge as compared to Ti-3Al-2.5V with respect to their reference thicknesses. For the finished AWJ cut edge surfaces of both materials, the high distribution of thinning observed is attributable to the plastic instability caused under tension load, which are distributed almost uniformly around the hole edges. These thinning zones occurred through the sheet thickness

during the HET. Generally, thinning at the hole edge is indicative of the tendency of crack occurrence at the hole edge rather than other regions of the test sample during the test trial. This observation reaffirms the suitability of the hemispherical punch for assessing the edge forming performance of sheet metals. The thinning behaviour observed was consistent with the edge forming performance trends of the materials and the machined edge surface quality responses examined in this work.

Table 6.3 shows the thinning evolution of the test samples with EDM machined edges deformed with a hemispherical punch. Again, an appreciable amount of sheet thinning around the hole edges were observed in the finished edge qualities compared to the unfinished edges for all machining methods and materials.

Table 6. 3 Comparison of thinning evolution of EDM fabricated edges after HET with hemispherical punch

Material (Cutting regime)	Thickness, mm	GOM Atos metrology
Ti-3Al-2.5V (UnFinished EDM)		
Ti-3Al-2.5V (Finished EDM)		
CP-Ti Grade 2 (UnFinished EDM)		
CP-Ti Grade 2 (Finished EDM)		

For each machined edge quality, CP-Ti (Grade 2) showed the highest sheet thinning at the hole edge relative to Ti-3Al-2.5V when assessed against their respective initial sheet thicknesses. For the finished EDM edge surfaces of both materials, the high distribution of thinning observed was attributable to the plastic instability caused under tension load, which was distributed almost uniformly around the hole edges. These thinning zones around the hole edge are observed to occur through the sheet thickness during the HET. Generally, thinning at the hole edge is indicative of the tendency of crack occurrence at the hole edge rather than other regions of the test sample during the test trial. The thinning behaviour observed are consistent with the edge forming performance trends of both materials and the edge fabrication qualities explored in this research. These observations reaffirm the suitability of the GOM Atos metrology approach as a viable supplementary route for assessing the edge formability of sheet metals.

6.2.5 Failure nucleation during HET

SEM analysis was performed to ascertain the failure nucleation process observed for the EDM and AWJ fabricated edges and their impact of the material edge forming performance during HET. The failure initiation processes are discussed with particular emphasis placed on the machining techniques employed and their impact on the edge forming performance. This was done because the influence of the machining technologies on the examined materials was similar in terms of the SEM features even though CP-Ti (Grade 2) outperformed Ti-3Al-2.5V in terms of edge performance output. The differences in edge forming performance have been clarified in subsections 6.2.3.

The edge surface defects observed after AWJ machining are mainly due to the action of the abrasive particles. The severity of the edge defects is a function of the machining parameters and the material's machinability. The surface defects produced on the material surface after AWJ machining act as stress concentration sites (yellow arrow) during HET, Figure 6.10*a*. These defect sites serve as areas of high-energy concentration where the cracks begin to grow (red dotted arrow), Figure 6.10*a*. The rate of the crack growth is dependent on the defect depth, distribution and size. The AWJ fracture surface is characterised by micro-void nucleation sites with equiaxed dimples on the surface at spherical inclusions, Figure 6.10*b*. The growth of these micro-voids around the spherical inclusions (by virtue of interface decohesion) are mainly due to the action of plastic strain and hydrostatic stress, which results in subsequent failure upon

coalescence of these micro-voids. Generally, the trajectory of the crack is a function of the stress state at the hole edge. The stress state around the hole edge during HET is pure uniaxial tension (Yoon, et al., 2016).

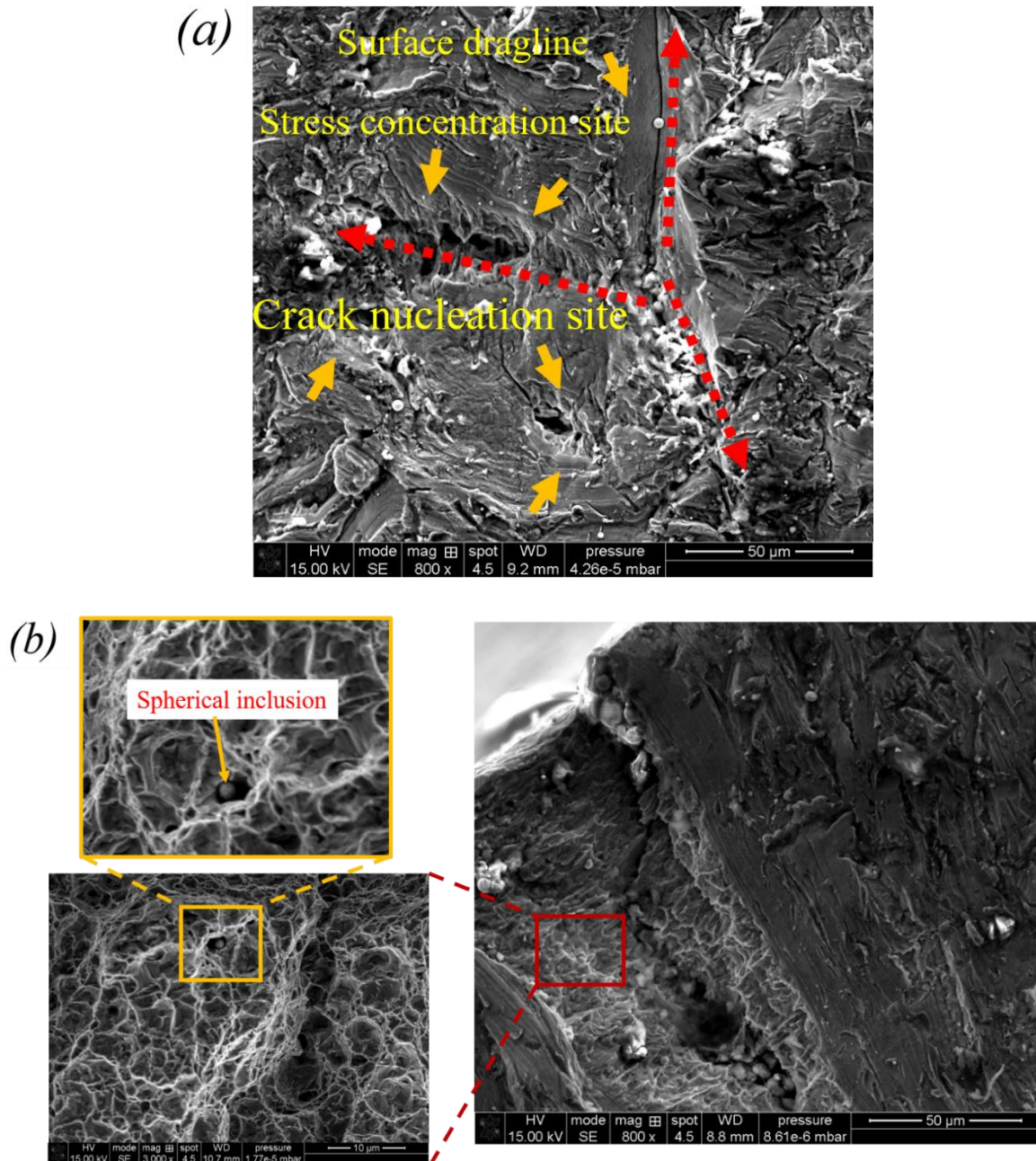


Figure 6. 10 Failure mode during HET of AWJ cut edge of Ti-3Al-2.5V

(a) Crack nucleation site at defect zones, (b) dimpled crack surface of AWJ cut edge

Since the AWJ edge surface is subjected to plane strain mode I loading (Figure 6.11a) during the deformation process, the optimum plastic strain is obtained at an angle of 45° to the crack axis. From a localised point of view, this angle becomes the favoured trajectory for micro-void growth and coalescence. However, global constraints like edge defects (surface micro-voids

and draglines) have the tendency of redirecting the crack plane path. The zigzag patterns seen at the AWJ cut edge fracture tip is as a result of the corrections made to the deviation by global constraints, reverting to the optimum plastic strain angle, Figure 6.11*b*.

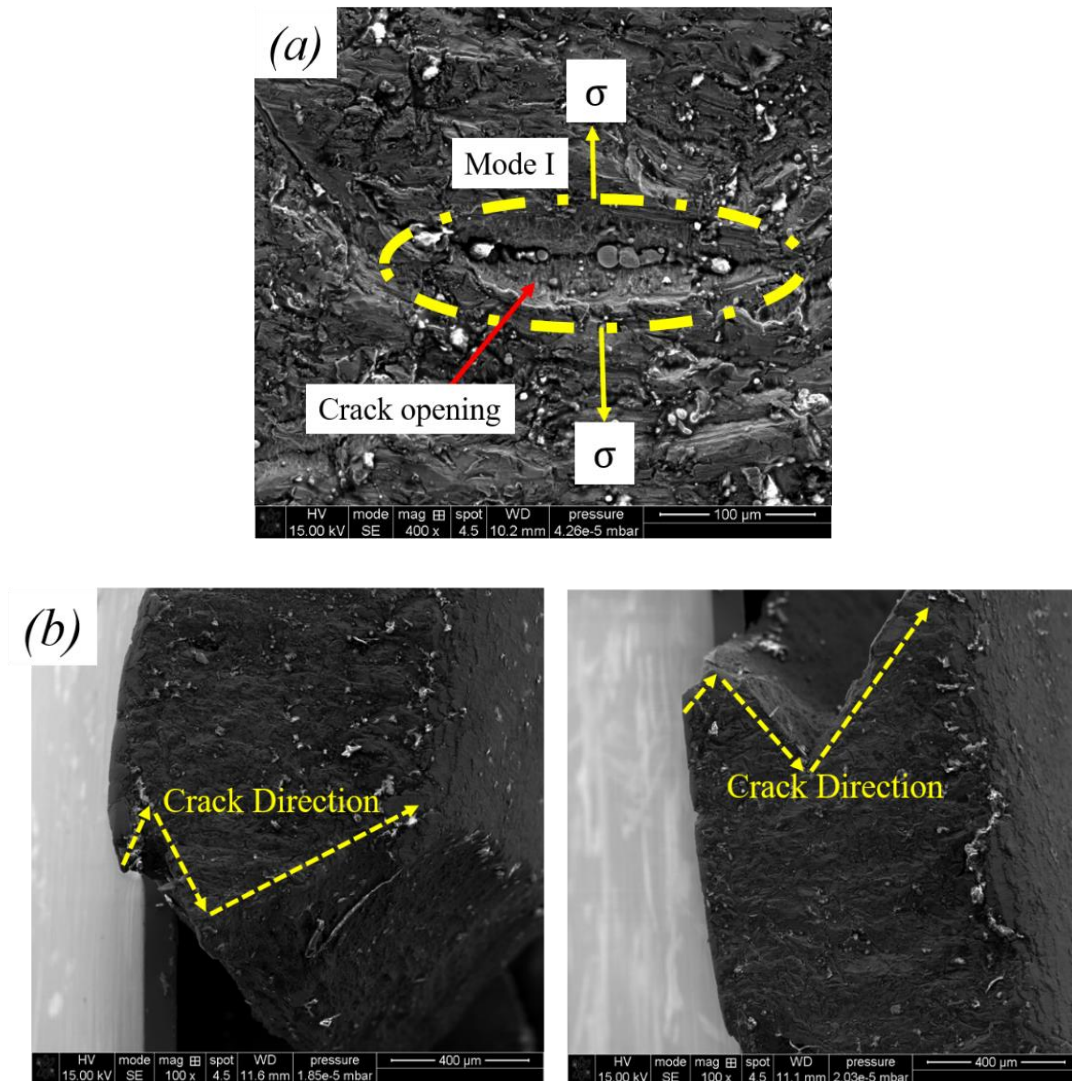


Figure 6. 11 AWJ edge crack behaviour of Ti-3Al-2.5V

(a) Fracture mode I opening (σ – tensile stress), (b) edge crack orientation

Similar trends were observed in the CP-Ti (Grade 2) test samples machined with AWJ after HET. The initial microstructure featured predominantly micro-groove surface defects produced by the abrasive particles during the machining process, Figure 6.12*a*. The abrasive particles create micro-voids in their final destination zones, which then become high stress concentration sites for crack initiation, propagation and growth, Figure 6.12*b*. Due to the actions of the surface defects produced during the AWJ machining process, the crack trajectory observed in the CP-Ti (Grade 2) test samples after HET were predominantly zig-zag patterned, Figure 6.12*c*.

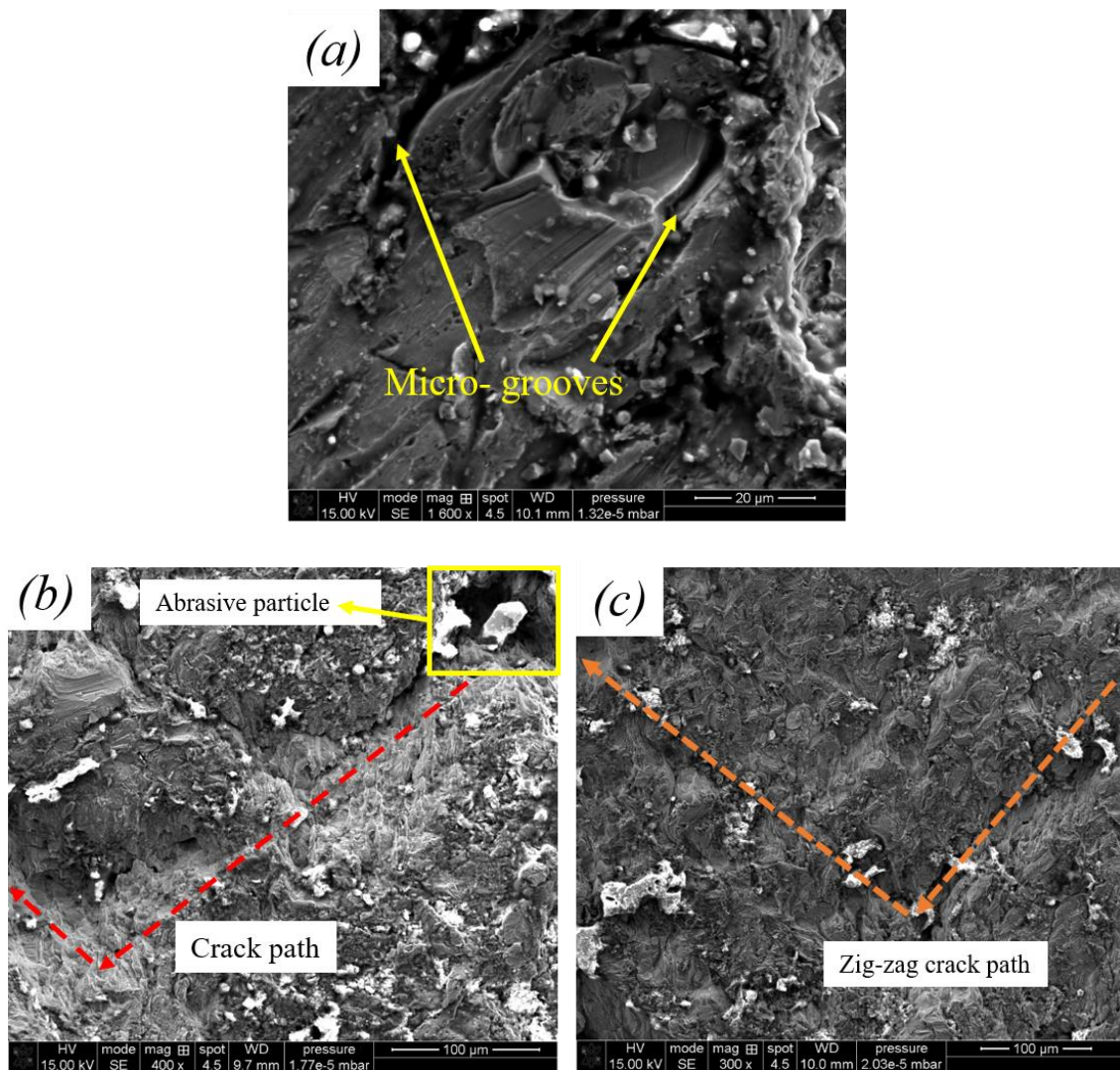


Figure 6.12 Failure behaviour in AWJ machined edge of CP-Ti (grade 2)

(a) Surface defects, (b) crack nucleation site, (c) crack trajectory

On the other hand, the thermal stresses produced during EDM machining due to plastic deformation or during the cooling process are manifested on the machined surface as micro-cracks (see Figures 6.7 and 6.9*c,d*). These surface micro-cracks are responsible for distributing the imposed stresses homogenously around the hole edge during HET (green arrows in Figure 6.13*a*). This phenomenon delays early failure of the material by preventing the cracks from developing towards the thickness direction (red arrows in Figure 6.13*a*) of the sheet during the HET of Ti-3Al-2.5V, Figure 6.13*a*.

Similar deformation behaviour was observed for the EDM fabricated edges of CP-Ti (Grade 2) sheet (see section 5.2.8). However, CP-Ti (Grade 2) exhibited a higher volume fraction of EDM machining induced surface micro-cracks compared to Ti-3Al-2.5V cut edges, (also see Figure 6.7); hence the higher edge forming performance of CP-Ti (Grade 2).

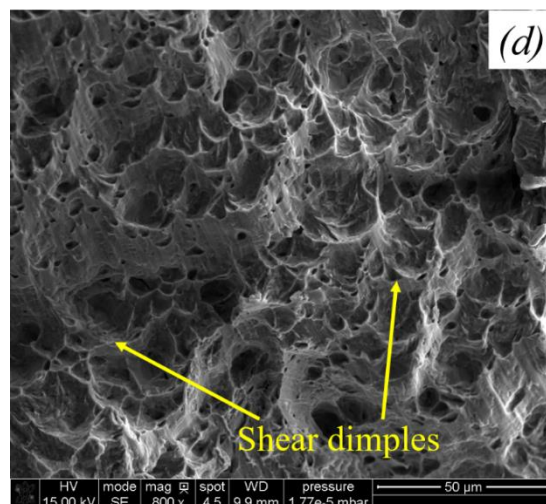
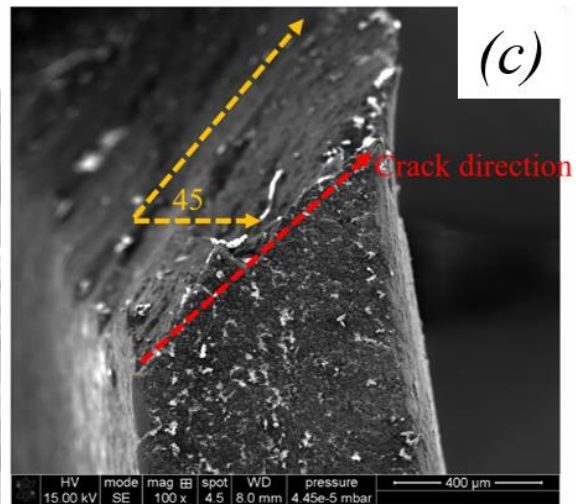
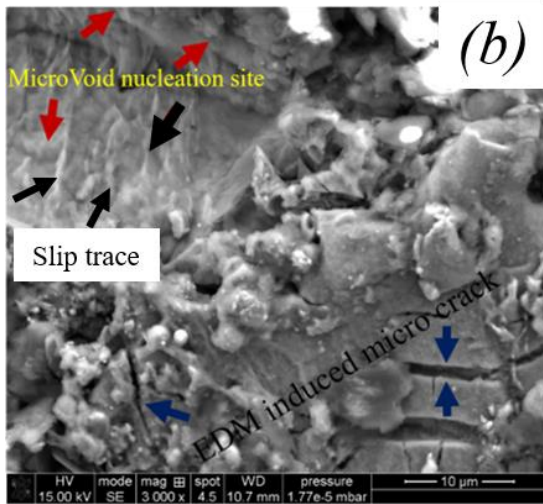
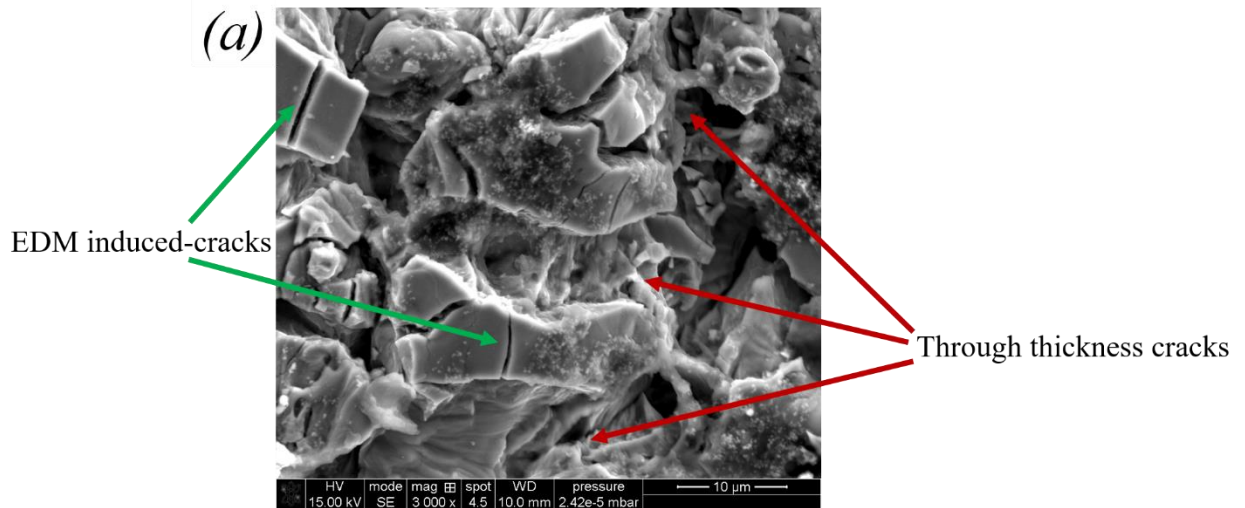


Figure 6. 13 EDM cut edge failure initiation process during HET of Ti-3Al-2.5V

(a) Resistance to through-thickness cracking by EDM induced surface micro cracks, (b) free surface formation (red arrow), (c) edge crack orientation, (d) shear dimple fracture surface

The higher the volume fraction of EDM induced surface micro-cracks, the higher the tendency of resisting crack growth towards the sheet thickness direction and the higher the edge forming performance of the material. The differences in the attained EDM edge performance observed for CP-Ti (Grade 2) and Ti-3Al-2.5V alloys could also be attributed to the variation in EDM induced residual stress. Normally, metallurgical alterations and thermal gradients produced during EDM machining induces residual stresses. EDM induced residual stress are tensile at the surface, which increases to an optimum value just below the heat affected zones (the optimum depth is a function of the spark energy), before reducing to low compressive residual stresses (Ekmekci, et al., 2005). Consequently, the attained strain results in the inception of tensile residual stresses, which are deleterious in terms of shortened fatigue life and enhanced fatigue crack growth. Fatigue generally emanates from the surface, hence the integrity of component surface is of significant essence. The residual stress values attained after EDM cutting are linked to the attained surface topography and the material yield strength (Cao, et al., 2014).

The crack tip of the EDM samples after HET showed localised necking with ductile shear failure, Figure 6.13c. The crack occurred just after the formation of micro-voids on the free surface, Figure 6.13b. Plastic deformation was observed to occur at the void nucleation site due to slip occurrence. The slip trace extension to the free surface of the void nucleation site are shown as black arrows in Figure 6.13b. The shear stresses acting during plastic deformation become highest for a plane of maximum plastic shear strain at 45° , Figure 6.13c. Through-thickness disparity in triaxiality could also be responsible for the shear deformation governed by the fracture trajectory at the crack tip orienting at 45° to the optimum principal stress. In such cases, the triaxiality at the crack tip offers an adequate upgrade for micro-void nucleation reminiscent of ductile fracture (Anderson, 2005). The acting shear stresses during the HET produced elongated dimples that are normally parabolic depressions, which coalesce in planes of maximum shear stress by virtue of ductile fracture via void coalescence. The depression acting towards the crack initiation point acts in the opposite direction to the failure produced by shear on the opposing fracture surfaces, Figure 6.13d.

6.3 Summary

Different machining methods are used to cut titanium alloys and these introduce edge surface defects onto the cut surface. Depending on the metallurgical structure of the titanium grade

employed, the edge surface finish response to machining may be varied. Considering the difficulty in machining titanium, there is the need to examine how different machining methods and parameters influence the edge surface micro-features and the edge forming performance of titanium alloys. This chapter examined the impact of AWJ and EDM induced micro-feature changes produced from varying machining parameters on the edge forming performance of an unalloyed (CP-Ti Grade 2) and an alloyed (Ti-3Al-2.5V) titanium grades. The chapter also examined the nature of the edge surface related failure modes and failure nucleation processes linked to these cutting methods. The chapter established that;

- Overall, the EDM machined test samples showed higher edge forming performance compared to the AWJ cut edges for both materials.
- The quality of the edge surface finishes is a function of the machining parameters and had a significant impact on the edge forming performance of the materials.
- The high edge formability of the EDM machined edges for CP-Ti (Grade 2) was due to the high volume fraction of the machining induced surface micro cracks compared to those observed in Ti-3Al-2.5V. CP-Ti (Grade 2) also showed lower surface texture feature evolution after AWJ cutting compared to Ti-3Al-2.5V. The response of the materials to machining are attributable to their inherent metallurgical structure. The machining induced defects influenced the edge forming performance of the materials in their role as stress raisers.
- The nature of the machining induced surface defects influenced the failure nucleation processes and failure mode of the materials. The fracture tips of the EDM machined edges were oriented 45° to the loading axis (shear deformation), whereas the fracture tips of the AWJ machined edges were zig-zag shaped.
- The GOM Atos optical non-contact metrology analysis of both materials showed edge thinning performance trends consistent with the HER values. The GOM Atos results obtained indicate the suitability of the technique for assessing the edge forming performance of materials.

Chapter 7

Statistical numerical prediction of the edge forming performance of titanium alloys

Overview

The stress state observed at the hole edge after HET is pure uniaxial tension. This observation has provoked several research interests directed at correlating the HER of materials to their uniaxial tensile properties. However, for highly textured materials like titanium, the attempt to link the tensile properties to the HER may be cumbersome and not necessarily representative of the optimum response of the material. Therefore, there is the need to consider material properties that encompasses the material response in all sheet-rolling directions. This chapter examined the edge forming performance of different grades of titanium alloys for edges prepared with AWJ machining and deformed with a Nakajima punch. The response of different titanium grades to AWJ machining with the same cutting parameters and their consequential effect on their edge forming performances was assessed. The idea of adopting the Erichsen index number and the sheet thickness values as opposed to conventional uniaxial tensile property parameters for forecasting the edge forming behaviour of titanium alloys was also examined. This chapter detailed a proposed regression model expression, capable of generating equations for the onward prediction of the HER of titanium alloys machined with AWJ and deformed with a Nakajima punch.

Most of the results presented in this chapter have been published in a peer-reviewed journal.

7.1 Experimental procedure

7.1.1 Edge preparation method and model limitation

AWJ machining method was employed to prepare the samples for the hole expansion test and a guillotine metal cutter was used to prepare the samples for Erichsen cupping test. A guillotine metal cutter was used to fabricate the Erichsen cupping test samples because the edge surface finish quality does not influence the forming behaviour of the materials during the test (due to the edges being fully constrained). For the AWJ fabricated samples, a Calypso waterjet machine with a 70HP KMT pump charged with an abrasive feed of 400g/min was employed with a transverse cutting speed of 250mm/min.

Previous chapters of this EngD research have highlighted the impact of machining parameters, tool geometry, material metallurgical structure and machining methods on the edge forming performance of titanium alloys. Therefore, the regression model expression proposed in this chapter was tailored and limited to the edges prepared with AWJ and deformed with Nakajima punch. All titanium grades investigated in this chapter were machined with the same machining parameters. However, the robustness of the proposed regression model expression suggests that it could be adopted for titanium alloys and other materials prepared with other machining methods. This could be achieved provided the experimental protocols followed to obtain the model calibration (thus, the same machining method, tool geometry and machining parameters) are consistent for all materials included in the regression model equation generation process.

7.1.2 The materials and mechanical properties

Different titanium alloy sheets with varied thicknesses were examined in this work. The materials with their corresponding chemical compositions are shown in Table 7.1.

Table 7. 1 Chemical composition of titanium alloys

Material	Chemical constituent, wt% (Max)									
	Mo	Al	V	Fe	O	C	N	H	Nb	Residual
Ti-6Al-4V	0	6.75	4.5	0.3	0.2	0.08	0.05	0.015	0	0.4
Ti-21S	16	3.5	0	0.4	0.17	0.05	0.05	0.015	3.2	0.4
CP-Ti (Grade 2)	0	0	0	0.3	0.25	0.08	0.03	0.015	0	0.4
Ti-3Al-2.5V	0	3.5	3	0.25	0.12	0.05	0.02	0.015	0	0.4
Ti-35A	0	0	0	0.2	0.18	0.08	0.03	0.015	0	0.4

In order to capture the full range of material property responses in the predictive regression model, a commercially pure titanium alloy (Ti-35A) and one with higher strength (Ti-6Al-4V) were included in addition to titanium alloys with intermediate properties. Ti-35A has the highest purity of the four pure titanium grades and has the lowest strength with good room temperature formability and ductility. Ti-6Al-4V is the most utilised titanium alloy and represents about 60% of the entire titanium production, with the commercially pure alloys accounting for 20% and all other alloy forms of titanium constituting the remaining 20% of total titanium production (Beal, et al., 2006). Standard room temperature uniaxial tensile testing was also conducted on the test samples at a constant strain rate of 0.001/s. The materials

exhibited highly anisotropic behaviour when examined in three sheet-processing orientations, (0° RD, 45° RD and 90° RD with respect to the sheet rolling direction), Figure 7.1.

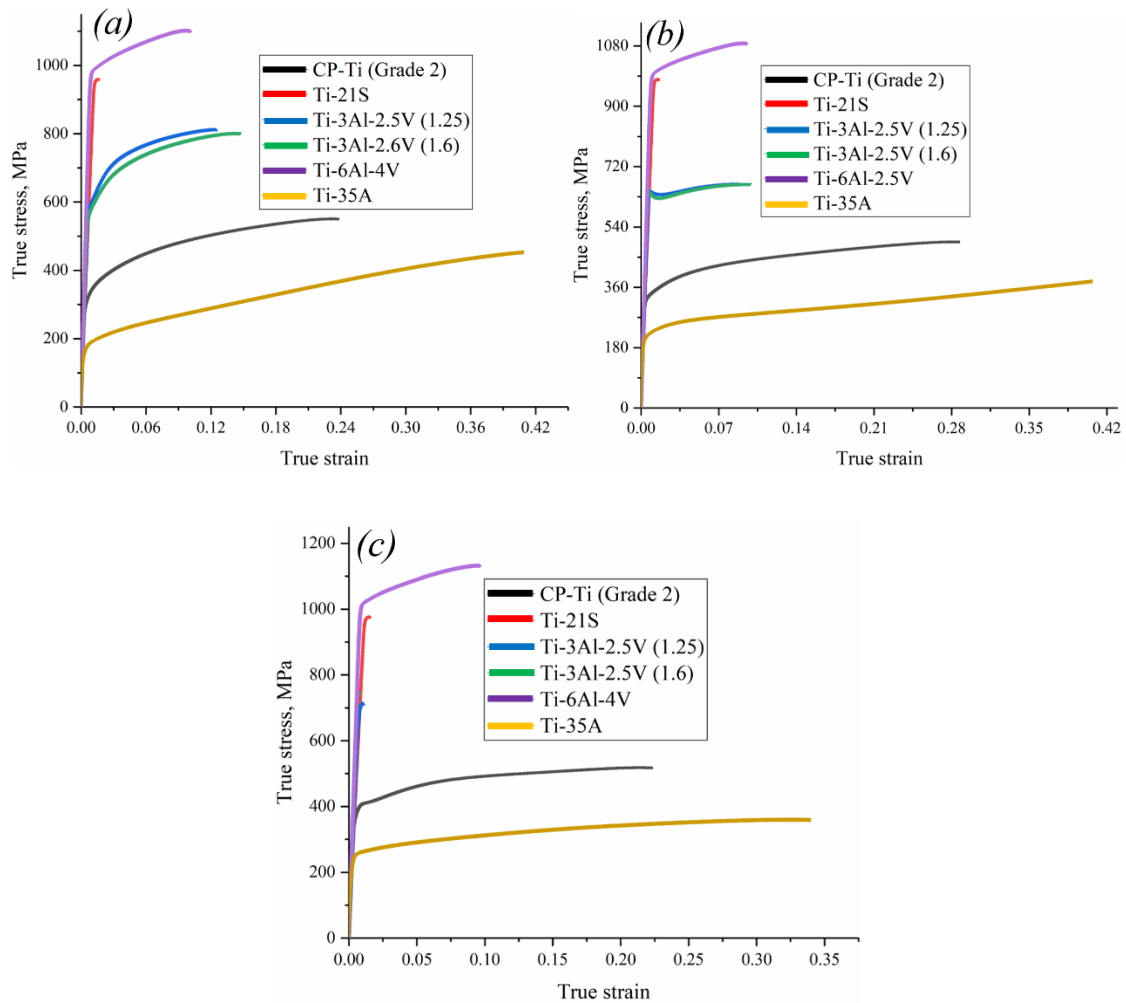


Figure 7. 1 Stress-strain curves for the titanium alloys examined

(a) 0° RD, (b) 45° RD and (c) 90° RD with respect to the sheet rolling direction

The pure titanium grades (CP-Ti Grade 2 and Ti35A) showed higher elongation with lower tensile strength in all three sheet-rolling directions examined when compared to their alloyed counterparts. On the other hand, Ti-6Al-4V also exhibited the highest strength with the lowest elongation when studied in all three sheet-rolling directions compared to the other titanium grades examined in this work.

It is worth mentioning however, that due to the enormous ductility of Ti-35A, they were not completely deformed to failure for the stress-strain values plotted in the 0° RD and 45° RD directions during the tensile deformation process. The tensile test trials were terminated for 0° RD and 45° RD oriented test samples during the tensile test due to the inability of the

extensometer to fully capture the extent of deformation (entire length change of Ti-35A) observed in Ti-35A examined in this work. The tensile tests were terminated prematurely as a precautionary measure to prevent damage to the extensometer used.

7.1.3 Hole expansion test and Erichsen cupping test

The HET was conducted on a Zwick/ Roell BUP 1000 machine with the test parameters controlled by the Zwick testXpert software. Circular disc test samples with an outer diameter of 200mm and an inner hole diameter of 20mm was employed. A Nakajima punch with a diameter of 100mm was used to deform the samples at a speed of 1mm/s until a crack through the entire sheet thickness at the hole edge was observed. A blankholder force of 150kN was used to ensure that the sheet is prevented from drawing-in during the deformation process. Three replicates of the AWJ machined hole edges were tested for each titanium alloy.

An Erichsen cupping test with a tool set consistent with ISO 20482:2013, was also conducted on the titanium alloys. A punch with a 20mm spherical head was used to deform blanks with a dimension of 75mm×75mm, until fracture occurred. Grease was used as a lubricant to minimise friction between the punch and the sheet metal sample. The extent of formability was assessed by measuring the distance from the initial punch contact to the point of fracture. This height represents the Erichsen index number. Three replicates of the Erichsen cupping test was conducted for each titanium grade.

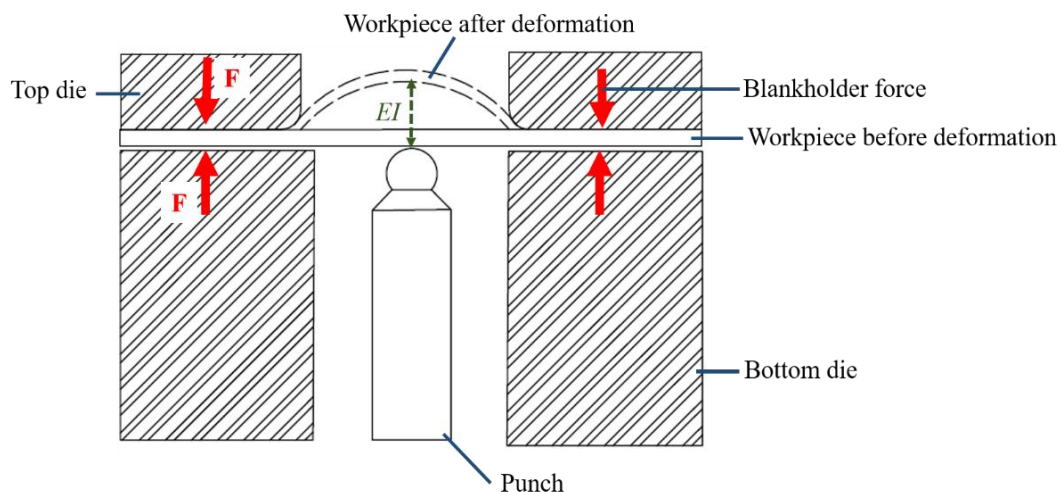


Figure 7. 2 Schematic of the Erichsen cupping test

A random speckle pattern consisting of splashed black dots on a white paint background were utilised for mapping the surface strains with a GOM Aramis optical non-contact measurement

system. This tracks the full-field displacement during the deformation process. A schematic set-up of the Erichsen cupping test is shown in Figure 7.2.

7.1.4 Model development in R programming

The R programming language is an open-source execution of the S functional programming language. R is an object oriented functional programming language, convenient for high-level scientific programming, data analysis, as well as modelling. For computationally cumbersome tasks, languages like C, C++, Python and FORTRAN could be linked and called up as required (Jones, et al., 2014).

For a model formula, fundamental forms are expressed as (Verzani, 2014);

response ~ predictor

The `lm ()` function for data fitting in R is utilised to perform analysis for linear modelling. For a simple linear model with a response variable y and a given predictor variable x , the data can be fitted to a linear model for which the result can be called as (Bloomfield, 2014);

```
> yfit = lm (y ~ x)
```

```
> yfit
```

Call:

```
lm (formula = y ~ x)
```

```
lm (formula, data = ..., subset=...)
```

Due to the linear dependence of the response variable on polynomial coefficients, linear models can also be adopted for polynomial fittings with the `lm ()` function. Data can be fitted to a linear model and the results called as;

```
> y2fit = lm (y ~ 1 + x + I(x^2)), or
```

```
y2fit = lm (y ~ poly (x, 2, raw = TRUE))
```

`I ()` function ensures the formula identity so that the function is uninterrupted. `TRUE` is used for cases where orthogonal polynomials are not required. The result can be called as;

Call:

$\text{lm}(\text{formula} = y \sim 1 + x + I(x^2))$

The fitting is plotted by adopting; $> \text{points} = (x, \text{predict}(y2\text{fit}), \text{type} = "l")$; for which, $\text{predict}()$ accounts for the vector of the predicted y values with their corresponding x vector values.

For this EngD research work, R scripts were coded and implemented in R studio programming software to predict the HER of titanium alloys based on their Erichsen index number (EI) and sheet thickness (t) values. The underlining model fitting expression executed to predict the HER of titanium alloys as well as generate the regression model equations is given by;

$$\text{lm}(\log(\text{HER}) \sim \text{Erichsen Index} + \text{poly}(\text{thickness}, 2), \text{data} = \text{experimental data}) \quad (7.1)$$

A logarithmic transform and polynomial functions were employed in the proposed regression model expression in order to capture the non-linearity in the data fitting process.

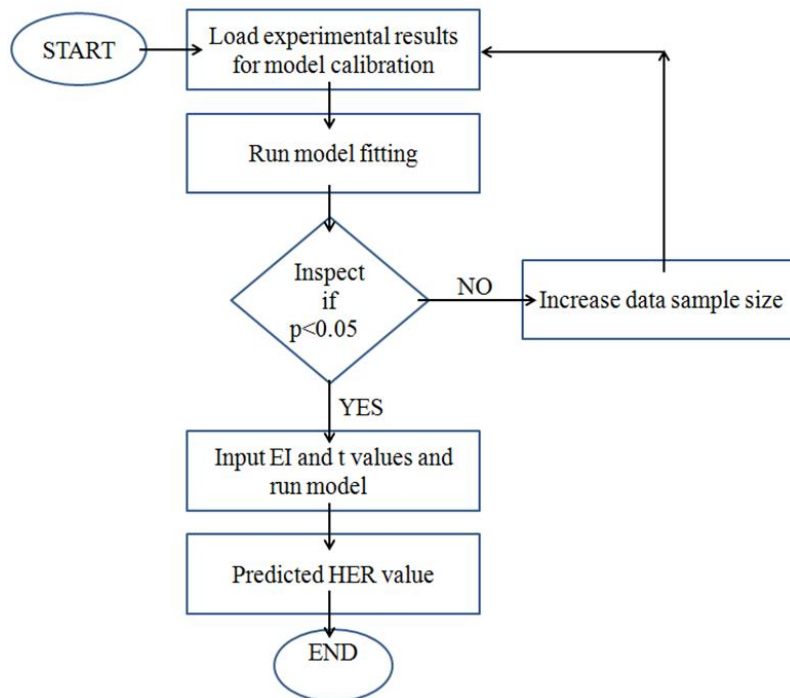


Figure 7. 3 HER prediction flowchart

Figure 7.3 shows the flowchart of the sequence logic followed to execute the model fitting expression governed by the R codes, for the accurate prediction of HER values for titanium alloys. An excel sheet location containing the experimental data with HER, EI and t values were loaded into the R-studio software, guided by the R codes. The model fitting expression according to equation (7.1), was then run to calibrate the resulting regression model. Based on the obtained p -value and the adjusted R squared (R^2_{Adj}) values, the generated regression model equation could be accepted or rejected. A statistically significant model (overall $p < 0.05$) with

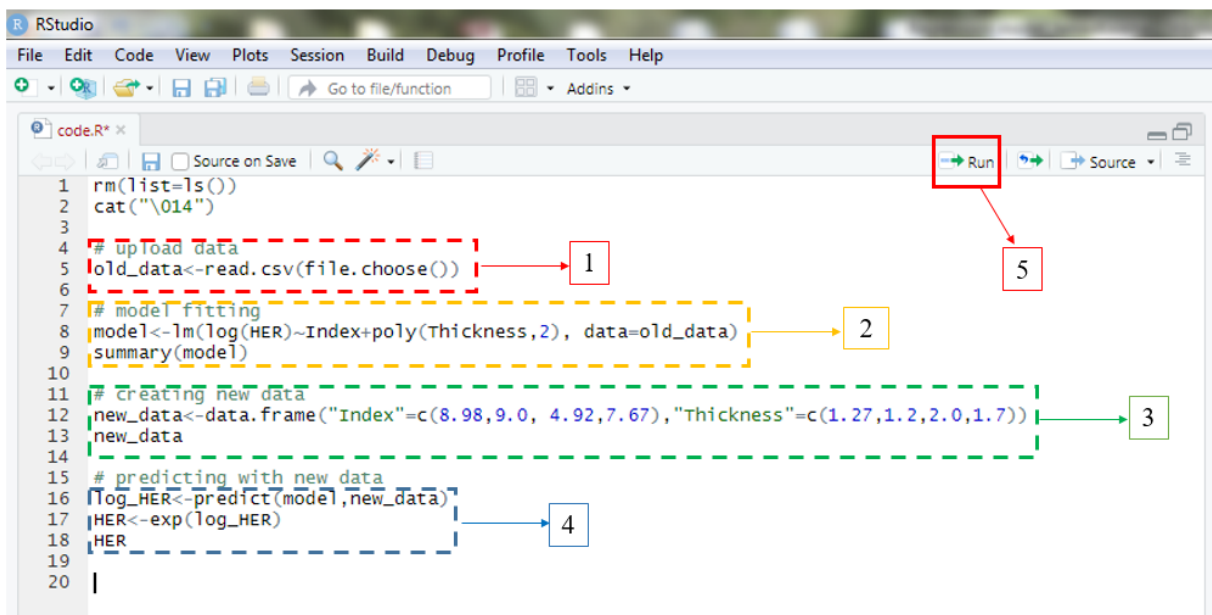
high correlation (R^2_{Adj} close to 1) translates to a very robust regression model equation capable of predicting the HER values. Depending on the statistical strength of the generated regression model equation, the HER of an unknown titanium alloy could then be predicted based on known EI and t input values.

7.1.5 Model description

Figure 7.4 shows the R code user interface with the scripts executed in R studio for the onward prediction of the HER values of the titanium alloys. These R-codes were carefully scripted upon an initial data exploration to ascertain the relationship between the response and the predictor variables. The R-scripts were then called into the software for the calibration, regression model equation generation and prediction process. The various facets of the R-code user interface called into the R-studio software as shown in Figure 7.4 are explained below;

1. This expression was utilised to upload the excel sheet location containing the experimental data (HER, EI and t) into the R-studio software.
2. Entails the proposed regression model expression. The model fitting expression was then run based on the uploaded experimental data set in step 1, to generate a regression model equation, capable of predicting the HER. The predictive power of the generated regression model equation was assessed based on the evaluated statistical indicators (see Figure 7.8).
3. This expression involves creating a new data set of different titanium alloys of interest, which have not been previously included in the calibration in step 1. This new titanium data must have known experimental EI and t values which can be inserted into step 3 for the onward evaluation process. This expression is capable of admitting as many EI and t values as possible for a single evaluation round. The EI values are listed in a row to correspond with their respective t values for each titanium alloy of interest.
4. This expression computes the HER of the titanium alloys of interest based on the inserted EI and t values in step 3 to predict their respective HER values.
5. Contains the 'Run' tab for executing the model commands.

6. On the response console of the user interface, the *EI* and *t* values input in step 3 are arranged in a column for onward inspection. These values can be cross-checked for accuracy prior to the HER computation in step 4.
7. On the response console of the user interface, this column represents the predicted HER upon calling and running the model computation expression in step 4, for the inserted *EI* and *t* values of interest in step 3. The rows for each predicted HER in step 7 corresponds to the column for each *EI* and *t* of interest in step 6.



Response on console

```

> # creating new data
> new_data<-data.frame("Index"=c(8.98,9.0, 4.92,7.67),"Thickness"=c(1.27,1.2,2.0,1.7))
> new_data
  Index Thickness
1  8.98      1.27
2  9.00      1.20
3  4.92      2.00
4  7.67      1.70
> log_HER<-predict(model,new_data)
> HER<-exp(log_HER)
> HER
  1      2      3      4
1 53.43040 58.29237 84.45545 54.64593
|>
  
```

Figure 7. 4 R code user interface in R studio window

7.1.6 Model performance assessment criteria

A significant test, based on the enumeration of the p -value is used in this work. The p -value helps to ascertain if differences seen between the test results and the null hypothesis are because of the null hypothesis failure or due to sampling variation. Generally, low p -values depict that there is a low probability of the null hypothesis to produce higher values than those obtained. The levels of significance for different limits of p -values are shown in Table 7.2. Statistical significance level was considered at $p < 0.05$ in this work.

Table 7. 2 p -value span for levels of significance (Verzani, 2014)

<i>p-value Span</i>	<i>Description</i>
0-0.001	Extremely significant
0.001-0.01	Highly significant
0.01-0.05	Statistically significant
0.05-0.1	Could be significant
0.1-1	Not significant

For the model to be robust, it should be able to capture variations observed in the response variable by adopting some predictor variables. The total variation in the response variable, the y values, about a mean point is defined by the total sum of squares, SST (Verzani, 2014);

$$SST = \sum (y_i - \bar{y})^2 \quad (7.2)$$

Equation (7.2) can be expressed algebraically as;

$$\sum (y_i - \bar{y})^2 = \sum (y_i - \hat{y}_i)^2 + \sum (\hat{y}_i - \bar{y})^2 \quad (7.3)$$

Where; $\sum (y_i - \hat{y}_i)^2$ is the residual sum of squares (RSS) and

$\sum (\hat{y}_i - \bar{y})^2$ is the regression sum of squares (SSReg), defined as the total variation in the fitted model about the mean.

The SST, RSS and SSReg thus enables for a proper definition of an appropriate regression line that fits the data. In order to ascertain how well the regression line fits the given data, the coefficient of determination R^2 , is adopted;

$$R^2 = 1 - \frac{RSS}{SST} = 1 - \frac{\sum(y_i - \hat{y}_i)^2}{\sum(y_i - \bar{y}_i)^2} \quad (7.4)$$

Putting SST in equation (7.2) back into equation (7.4)

$$R^2 = \frac{\sum(y_i - \bar{y})^2 - \sum(y_i - \hat{y}_i)^2}{\sum(y_i - \bar{y})^2} \quad (7.5)$$

But, from equation (7.3); $\sum(y_i - \bar{y})^2 = \sum(y_i - \hat{y}_i)^2 + \sum(\hat{y}_i - \bar{y})^2$

Substituting equation (7.3) into equation (7.5);

$$R^2 = \frac{\sum(y_i - \hat{y}_i)^2 + \sum(\hat{y}_i - \bar{y})^2 - \sum(y_i - \hat{y}_i)^2}{\sum(y_i - \bar{y})^2}$$

$$R^2 = \frac{\sum(\hat{y}_i - \bar{y})^2}{\sum(y_i - \bar{y})^2} \quad (7.6)$$

Equation (7.6) can be simplified as; $R^2 = \frac{SSReg}{SST}$ (7.7)

Thus, for values ranging between 0-1, the regression line captures most of the variations in the data when R^2 is close to one.

Generally, R^2 represents the sample approximate of the proportion of variance, which are captured in the outcome variables, and are favoured upwards with respect to the explained population proportion of variance. In order to attenuate the limitations of R^2 and discourage the use of more predictor variables to get higher R^2 values, the adjusted R^2 (R^2_{Adj}) are adopted to guard against spurious relationships. Thus, the R^2_{Adj} only increases when factors are highly correlated, for situations where more independent variables are added to the model. The sum of squares is divided by the degrees of freedom to account for the R^2_{Adj} . Generally, when considering simple regression models, $N-2$ are utilised for RSS and $N-1$ for SST (Verzani, 2014).

For a given number of predictor variable k and sample size N , the R^2_{Adj} can be expressed as (Harel, 2009);

$$R^2_{Adj} = 1 - \left[(1 - R^2) \left(\frac{N - 1}{N - k - 1} \right) \right] \quad (7.8)$$

Putting equation (7.4) into equation (7.8), R^2_{Adj} can also be written as;

$$R_{Adj}^2 = 1 - \left[\frac{RSS}{SST} \times \left(\frac{N - 1}{N - k - 1} \right) \right] \quad (7.9)$$

The adjusted R^2 is used in this EngD research to assess how well the regression line fits the data for accurate prediction of the HER of titanium alloys.

7.2 Results and Discussion

7.2.1. Formability of titanium alloys

Table 7.3 shows the HER and the EI values of the studied titanium grades after the experimental trials. The varied formability performance of the titanium grades suggests that apart from the influence of machining induced edge surface defects on the HER, the material inherent metallurgical structures played an important role in the edge formability of the titanium alloys.

Table 7. 3 Formability assessment at room temperature

Material	t , mm	EI , mm	HER, %
Ti-3Al-2.5V	1.60	5.889	30.096
Ti-3Al-2.5V	1.25	6.218	28.357
Ti-21S	1.27	8.980	52.529
Ti-6Al-4V	1.60	4.014	18.344
CP-Ti (Grade 2)	1.60	10.289	81.870
Ti-35A	1.00	11.313	157.317

The EI values are representative of the material ductility in all sheet-processing directions and reveal the extent of the material formability dependence on microstructure at room temperature. The unalloyed titanium sheets (Ti-35A and CP-Ti Grade 2) showed high edge formability compared to their alloyed counterparts due to their superior room temperature ductility and lower strength.

Ti-6Al-4V showed the lowest formability compared to the other titanium grades due to its high strength at room temperature. Similar limited room temperature formability as a result of low material hardening was recorded in Ti-6Al-4V during stretch forming (Badr, et al., 2015).

A graphical representation of the performance relationship observed in the material formability assessment after HET and Erichsen cupping test is shown in Figure 7.5. The materials exhibited a somewhat linear trend of formability response for both experimental methods, thus showing the possibility of correlating test results from both forming techniques.

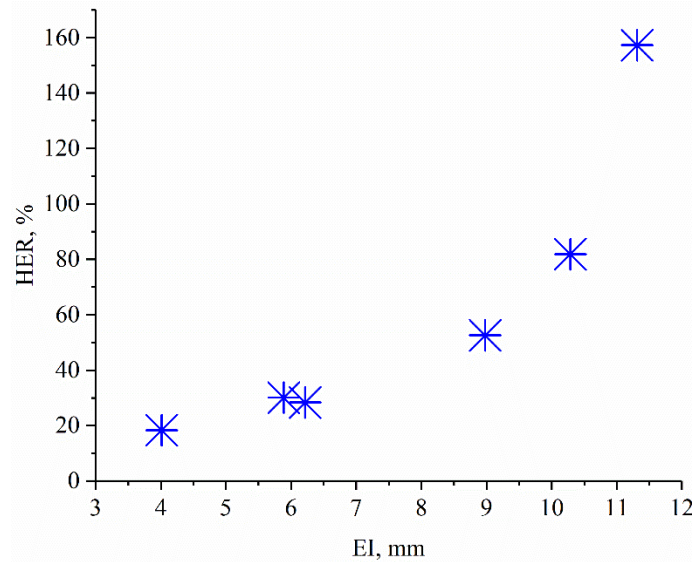


Figure 7. 5 HER and EI assessment of titanium alloys

7.2.2 Forming strains after the Erichsen cupping test

Figure 7.6 shows the forming strain evolution at the onset of localised necking prior to fracture during the testing process. Overall, high strain concentration sites were observed at the summit of the dome region indicating minimal friction between the spherical punch head and the test samples prior to the material yielding.

Failure in Ti-6Al-4V was sudden with limited strain localisation (15.9%) and no distinct necking prior to failure, Figure 7.6c. Similar trends were recorded in Ti-6Al-4V after stretch forming with a plane strain forming limit minimum under 10% (Badr, et al., 2015). In the present experiments, Ti-35A and CP-Ti (Grade 2) pure grades showed the highest resistance to fracture (76.26% and 64.46% respectively, Figure 7.6a, b), mainly due to their superior room temperature formability. Localised necking prior to fracture was observed in CP-Ti (Grade 2) and Ti-35A, resulting in delayed fracture. The response of CP-Ti (Grade 2) and Ti-6Al-4V to stretch forming are consistent with those observed in other works (Lin Prakash, et al., 2017).

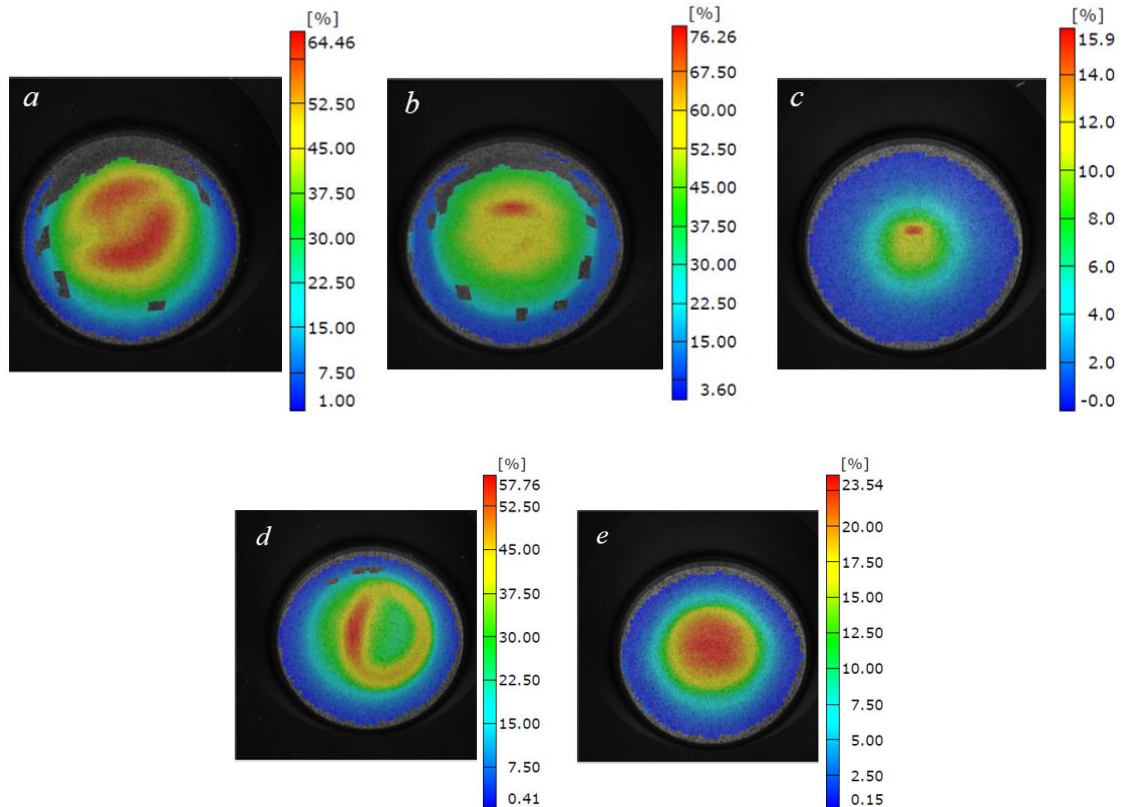


Figure 7. 6 Major strain evolution during Erichsen cupping test
 (a)CP-Ti (Grade 2), (b)Ti-35A, (c)Ti-6Al-4V, (d)Ti-21S, (e)Ti-3Al-2.5V

7.2.3 Thinning evolution after Erichsen cupping test

Figure 7.7 shows the material thinning evolution along the chosen section lengths of interest, at localised necking prior to fracture. Generally, optimum sheet thinning was observed around the dome summit prior to fracture during the biaxial stretching process. Reduced cupping height observed in Ti-6Al-4V reflected as poor thinning tendencies (21.6%) prior to failure, Figure 7.7c. The limited thinning noticed in Ti-6Al-4V is evidence of the abrupt fracture of the part observed during the forming process.

Ti-35Al and CP-Ti (Grade 2) pure grades exhibited the highest cupping height with an accompanying high formability, which reflected in their high resistance to localised thinning (64% and 60.3% respectively) prior to fracture, Figure 7.7a, b. Overall, the thinning tendencies exhibited by the titanium alloys are consistent with the forming performance observed after HET. The higher the thinning capability, the higher the formability of the material. For sheet metal forming processes like incremental sheet forming, the maximum allowable thinning is an indicator of sheet metal formability (Kurra & Regalla, 2014).

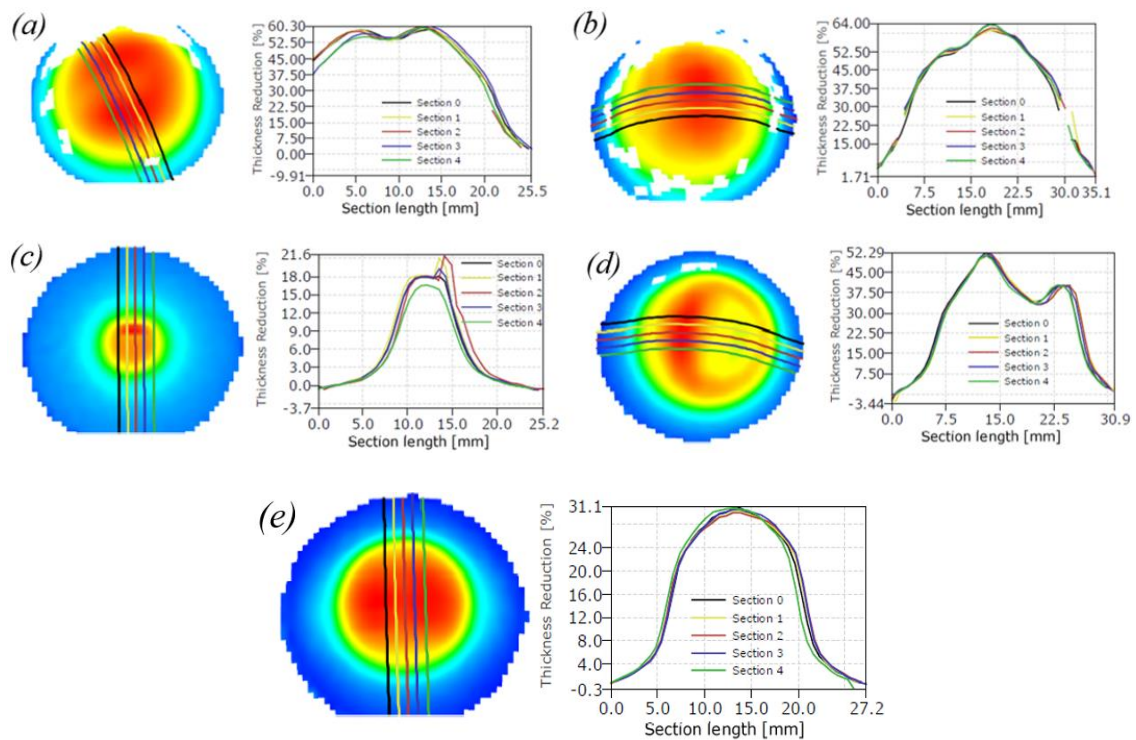


Figure 7. 7 Thinning evolution during Erichsen test

(a) CP-Ti (Grade 2), (b)Ti-35Al, (c)Ti-6Al-4V, (d)Ti-21S, (e)Ti-3Al-2.5V

7.2.4 Model predictability assessment and regression model equations

Figure 7.8 shows the results of the generated regression equation coefficients and their respective statistical parameters, based on the experimental results run by the model fitting expression stated in equation (7.1) using R programming. The asterisk codes observed after the associated p -values shows the strength of how well the generated coefficients describe the HER value (fits the data). The higher the asterisk code, the higher the statistical significance strength and the closer the coefficient are to fitting the data.

Inspection of the p -values generated for the regression model equation coefficients revealed that all the coefficients have $p < 0.05$. This shows that all the regression model equation coefficients appropriately fitted the data during the model calibration process. The overall regression model equation p -value (0.00076) also shows extreme statistical significance (see table 7.2), indicating the robustness of the model to predict the HER values of titanium alloys. An R^2_{Adj} value of 0.9987 for the generated regression model equation also shows how well the regression line fits the data for accurate prediction of the HER values of titanium alloys.

```

Residuals:
    1      2      3      4      5      6
0.0297137  0.0070291 -0.0069029 -0.0240068 -0.0055293 -0.0003037

Coefficients:
              Estimate Std. Error t value Pr(>|t|)
(Intercept)    2.014525   0.045263  44.507 0.000504 ***
Index          0.235445   0.005624  41.864 0.000570 ***
poly(Thickness, 2)1 -0.223388  0.034304  -6.512 0.022779 *
poly(Thickness, 2)2  0.377374  0.029918  12.613 0.006227 **
---
signif. codes:  0 '***' 0.001 '**' 0.01 '*' 0.05 '.' 0.1 ' ' 1

Residual standard error: 0.02817 on 2 degrees of freedom
Multiple R-squared:  0.9995,    Adjusted R-squared:  0.9987
F-statistic: 1310 on 3 and 2 DF,  p-value: 0.0007631

```

Figure 7. 8 Generated regression model equation coefficients for all six tested samples

Therefore, for edges prepared with AWJ machining and deformed with a Nakajima punch, the proposed regression model equation for predicting the HER of titanium alloys, based on the EI and t values is given by;

$$HER = e^{2.015+0.235EI-0.223t+0.377t^2} \quad (7.10)$$

Equation (7.10) generally takes the form of;

$$HER = e^{\beta_{\S}+\beta_{\S}EI+\beta_{\S}t+\beta_{\S}t^2}$$

$$HER = e^{\beta_0+\beta_1EI+\beta_2t+\beta_3t^2} \quad (7.11)$$

Where β_{\S} is regression coefficient, \S is an integer

In order to validate the predictability of the model fitting expression, a cross-validation process was adopted where the model was re-run with a deliberate omission of one experimental data point for all test values. For each validation round, the omitted experimental HER is compared to the predicted HER for each tested EI and t value, generated from the remaining five-data model fitting by the expression in equation 7.1 (model calibration data).

7.2.5. Cross-validation trial for predicting HER of Ti-21S

Figure 7.9 shows the results when the model expression in equation (7.1) was called and run using five experimental data sets of all the titanium alloys tested with the exception of Ti-21S. The generated p -values for the regression model equation coefficients generally showed high statistical significance ($p<0.05$) with an exception of the polynomial terms. However, an

overall p -value of 0.0277 (less than 0.05) suggested a strong suitability of the generated regression model equation for predicting the HER of Ti-21S.



Generated regression model equation coefficients

```

Call:
lm(formula = log(HER) ~ Index + poly(Thickness, 2), data = old_data)

Residuals:
    1      2      3      4      5
3.049e-02 -1.561e-17 -2.138e-02 -9.108e-03  5.204e-18

Coefficients:
            Estimate Std. Error t value Pr(>|t|)
(Intercept)  2.040553  0.065766  31.027  0.0205 *
Index        0.236434  0.008415  28.095  0.0226 *
poly(Thickness, 2)1 -0.268776  0.047185  -5.696  0.1106
poly(Thickness, 2)2  0.288485  0.044540   6.477  0.0975 .
---
Signif. codes:  0 '***' 0.001 '**' 0.01 '*' 0.05 '.' 0.1 ' ' 1

Residual standard error: 0.03833 on 1 degrees of freedom
Multiple R-squared:  0.9995, Adjusted R-squared:  0.9981
F-statistic: 703.6 on 3 and 1 DF, p-value: 0.0277

```

Figure 7. 9 Generated regression model equation coefficients based on 5 experimental data sets minus Ti-21S

An R^2_{Adj} value of 0.9981 also showed how well the generated regression model equation fits the data for the onward accurate prediction of the HER values of Ti-21S.

The generated regression model equation for predicting the HER of Ti-21S, based on the calibrated experimental data of the other five titanium grades tested, can be expressed as;

$$HER = e^{2.041+0.236EI-0.269t+0.288t^2} \quad (7.12)$$

Figure 7.10 shows the R-studio user interface for the computation and the prediction of the HER values of Ti-21S. After fitting the experimental data (model calibration) to the model expression (equation 7.1) and generating the regression model equation (equation 7.12), the known EI experimental data and the t value of Ti-21S were then inserted into the model for onward prediction of the HER value (red dotted rectangle; Figure 7.10).

```

1 rm(list=ls())
2 cat("\014")
3
4 # upload data
5 old_data<-read.csv(file.choose())
6
7 # model fitting
8 model<-lm(log(HER)~Index+poly(Thickness,2), data=old_data)
9 summary(model)
10
11 # creating new data
12 new_data<-data.frame("Index"=c(8.98),"Thickness"=c(1.27))
13 new_data
14
15 # predicting with new data
16 log_HER<-predict(model,new_data)
17 HER<-exp(log_HER)
18 HER
19
20 |

```

Response on console

```

> new_data<-data.frame("Index"=c(8.98),"Thickness"=c(1.27))
> new_data
  Index Thickness
1  8.98      1.27
> log_HER<-predict(model,new_data)
> HER<-exp(log_HER)
> HER
      1
53.4304
>

```

Figure 7. 10 R code window interface for predicting HER of Ti-21S

The input *EI* and *t* values are shown in a row as a confirmation of the input variables on the response console of the software (yellow dotted rectangle, Figure 7.10). Upon calling and running the model expression for the new data prediction (black dotted rectangle, Figure 7.10), the predicted HER of Ti-21S is then generated (green dotted rectangle, Figure 7.10) in the response console. The predicted HER value of 53.4304 obtained for Ti-21S showed close proximity to the experimental value of 52.5289, indicating the high predictability of the generated regression model equation. This proximity of the predicted HER to the experimental HER values of Ti-21S also vindicates the confidence level of the strength of the initial statistical indicators shown for the generated regression model equation (7.12) adopted for the prediction.

The cross-validation process was repeated for all titanium grades examined in this EngD research (see Appendix D) in order to ascertain the predictive power of the proposed regression model expression stated in equation 7.1.

7.2.6 Summary of generated regression model equations and model coefficient suitability

Table 7.4 shows the p -values obtained for the regression model equation coefficients of each titanium alloy used for predicting their HER values and those generated for the overall regression model equation as well as their corresponding R^2_{Adj} values.

Table 7. 4 p -value and R^2_{Adj} of generated regression model coefficients

Material	β_0	β_1	β_2	β_3	Overall p	R^2_{Adj}
Ti-3Al-2.5V (1.6)*	0.00781	0.0078	0.04324	0.02699	0.01066	0.9997
Ti-3Al-2.5V (1.25)*	0.022	0.0226	0.1208	0.0781	0.02908	0.9979
Ti-21S	0.0205	0.0226	0.1106	0.0975	0.0277	0.9981
Ti-6Al-4V	0.00381	0.00399	0.0164	0.01027	0.00474	0.9999
CP-Ti ;Grade 2	0.0354	0.0397	0.2492	0.0692	0.02877	0.998
Ti-35A	0.0204	0.0226	0.1781	0.593	0.04186	0.9957
All six	0.000504	0.00057	0.022779	0.006227	0.0007631	0.9987

(*)-Thickness in mm

Generally, the obtained p -values suggest that the generated regression model equation coefficients appropriately fitted the data during the model calibration process for onward HER prediction for all the titanium alloys examined. The overall p -values of the regression model equations generated also showed high statistical significance with their corresponding R^2_{Adj} values indicating a strong data fitting to the regression line, signifying the high statistical accuracy of the model. However, it is worth nothing that the robustness of the generated regression model equation coefficients are significantly improved when all six data sets are fitted by the model expression. This shows that the model could be improved with further data sets, even though the statistical indicators are strong enough to predict HER values for titanium alloys in this work.

Table 7.5 shows the generated regression model equations used to predict the HER of each titanium grade and those generated for all tested alloys, after calling and running the model fitting expression in R studio. The generated regression model equation provides a route to predict the HER for the titanium alloy of interest, based on the known EI and t experimental result of the alloy. The regression model equations for each alloy were generated from the

calibration of five other titanium alloy experimental test data excluding the alloy of interest via a cross-validation process, for the onward prediction their HER values.

Table 7. 5 Generated regression model equations

Material	Generated regression model equation for HER prediction
<i>All six</i>	$HER = e^{2.015+0.235EI-0.223t+0.377t^2}$
Ti-3Al-2.5V (1.6)*	$HER = e^{2.001+0.237EI-0.243t+0.361t^2}$
Ti-3Al-2.5V (1.25)*	$HER = e^{2.033+0.236EI-0.268t+0.311t^2}$
Ti-21S	$HER = e^{2.041+0.236EI-0.269t+0.288t^2}$
Ti-6Al-4V	$HER = e^{2.085+0.228EI-0.234t+0.393t^2}$
CP-Ti ;Grade 2	$HER = e^{1.987+0.240EI-0.206t+0.368t^2}$
Ti-35A	$HER = e^{1.932+0.236EI+0.136t+0.031t^2}$

()*-Thickness in mm

7.2.7 Model predictability analysis

Table 7.6 shows the experimental and the predicted HERs of the titanium alloys, based on the proposed model fitting expression in equation (7.1). The results show very high proximity of the predicted HER values to the experimental HER values. This strength in proximity are consistent with the strong statistical indicators observed for the generated regression model equations, obtained for each validation trial. However, the predicted HER of Ti-35A deviated significantly from the experimental HER, which was registered as high p -values in the β_2 and β_3 coefficients (Table 7.4). The high p -values recorded represents a high drift in capturing variation in the data and a low correlation between factors. This could be attributed to the fact that Ti-35A was set as the optimum threshold for material performance in this work due to its superior ductility. Therefore utilising CP-Ti (Grade 2) as the predictor- model –calibration-threshold value to capture Ti-35A was insufficient, because it has a lower HER value (81.9%) compared to Ti-35A (157.3%). Thus, the omission of Ti-35A during cross-validation produces a performance variability in their prediction response with the data set available, hence the deviation.

A plot of the predicted and the experimental HERs of the titanium alloys is shown in Figure 7.11. The plot shows a strong linear relationship between the predicted and the experimental HERs. These results confirm the high robustness of the model fitting expression and the high predictability of the regression model equations generated.

Table 7. 6 Comparison of experimental and predicted HER

Material	t , mm	Experimental HER, %	Predicted HER, %
Ti-3Al-2.5V	1.60	30.096	28.726
Ti-3Al-2.5V	1.25	28.357	27.887
Ti-21S	1.27	52.529	53.4304
Ti-6Al-4V	1.60	18.344	19.574
CP-Ti (Grade 2)	1.60	81.870	84.647
Ti-35A	1.00	157.317	231.597

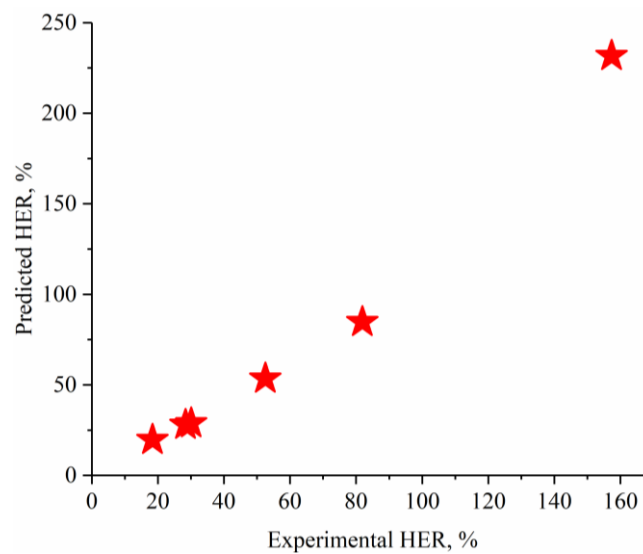


Figure 7. 11 Plot of the experimental and predicted HER

Standard statistical constraint optimization parameter equations (Kotkunde, et al., 2018), are adopted to examine the results obtained in this work. The average absolute error (δ_{abs}) obtained between the experimental HER (HER_{Exp}) and the predicted HER (HER_{Pre}) is given by;

$$\delta_{abs} = \frac{1}{N} \sum_{i=1}^N \frac{HER_{exp}^i - HER_{pre}^i}{HER_{exp}^i} \quad (7.13)$$

Where N is the number of data points considered

Putting values from Table 7.6 into equation (7.13), the average absolute error obtained between the predicted and experimental HER in the studied titanium alloys based on the proposed generated regression model equations is 8.8%.

In order to ascertain numerically, the strength of the linear relationship between the experimental and predicted HERs obtained from the generated regression model equations, the correlation coefficient R is evaluated according to the equation;

$$R = \frac{\sum_{i=1}^N (HER_{exp}^i - \overline{HER}_{exp}) (HER_{pre}^i - \overline{HER}_{pre})}{\sqrt{\sum_{i=1}^N (HER_{exp}^i - \overline{HER}_{exp})^2 \sum_{i=1}^N (HER_{pre}^i - \overline{HER}_{pre})^2}} \quad (7.14)$$

Where, \overline{HER}_{exp} is the average experimental HER and \overline{HER}_{pre} is the average predicted HER

Putting values from Table 7.6 into equation (7.14), the correlation coefficient for the titanium alloys, based on the proposed generated regression model equations is given by;

$$R = \frac{20800.95198}{\sqrt{442910563.4}} = 0.9884$$

The correlation coefficient of 0.9884 shows a strong linear relationship between the experimental and the predicted HER values obtained for the titanium alloys. This result confirms the high robustness of the proposed model fitting expression for predicting the HER values of titanium and its alloys.

7.3 Summary

The stress state observed at the hole edge of sheet metals after HET is synonymous to that observed during conventional uniaxial tensile testing. However, conventional tensile test methods are not adequate for evaluating the edge forming performance of sheet metals. This similarity in stress state has led some researchers to correlate the tensile properties of sheet metals to their HERs. However, for highly anisotropic materials like titanium and its alloys, predicting the HER based solely on the tensile mechanical properties may not be representative of the material response. This work proposed a model fitting expression, which can be called in the R programming language to generate regression model equations as well as predict the HER of titanium alloys based on known EI and t values. The work found that;

- The Erichsen cupping test based on biaxial stretching provides a route to assessing the ductile behaviour of materials in all sheet-rolling directions. This approach offers a better means of assessing the material forming performance as opposed to the limited routes offered by uniaxial tensile properties. The somewhat linear relationship between the EI and HER forming parameters makes a good case for correlating them.

- Apart from the major role machining induced defects play in sheet edge formability, the material inherent metallurgical structure response also have a significant impact on the edge formability performance of titanium alloys.
- The HER of titanium alloys can be predicted based on known EI and t values after initial data calibration in R programming, using the model fitting expression;

$\text{lm}(\log(\text{HER}) \sim \text{Erichsen Index} + \text{poly}(\text{thickness}, 2), \text{data} = \text{experimental data})$

- The proposed general regression model equation form, for predicting the HER of titanium alloys based on known EI and t values for edges prepared with AWJ and deformed with a Nakajima punch can be expressed as;

$$HER = e^{\beta_s + \beta_s EI + \beta_s t + \beta_s t^2}$$

- For the experimental data utilised for calibrating the model, the proposed regression model equation has an overall p -value of 0.00076 indicating an extreme statistical significance and signifying the robustness of the model to predict the HER values of titanium alloys. An R^2_{Adj} value of 0.9987 for the generated regression model equation also shows how well the regression line fits the data for the accurate prediction of the HER of titanium alloys.
- A correlation coefficient of 0.9884 was obtained between the experimental and the predicted HER values showing a strong linear relationship and a high goodness of fit with an average absolute error of 8.8%.

Chapter 8

Supplied sheet surface conditions and the impact of surface defects on the formability of Ti-3Al-2.5V

Overview

This chapter addresses the second aspect of this EngD research, which focused on the impact of sheet metal surface conditions on the room temperature forming capability of Ti-3Al-2.5V. In literature reports, most industrial responses linked to sheets with defective surfaces are dedicated towards the investment in technologies capable of detecting such defects during production. Nevertheless, for post-processing surface defects (eg. scratches, notches and indents) introduced during either sheet metal transportation, handling or storage (due to bad friction conditions between contact surfaces), such technological interventions are most likely untenable. Chances are that sheet metals with such post-processing induced surface defects may be rejected for forming operations where strict requirements for high quality sheet surface integrity are upheld. However, research directed at ascertaining the impact of post-processing induced surface defects on the room temperature forming capability of titanium sheets has not been extensively studied. To address these issues, two experimental trials were conducted in this chapter. The first aspect examined the impact of longitudinal scratch defects on the sheet bendability using press brake forming trials. The second aspect introduced an approach based on ex-situ uniaxial tensile deformation, SEM and a Matlab based DIC to compute the local strains at an indent defect surface at micro-level.

Most aspects of the results reported in this chapter have been published in a peer reviewed journal.

8.1 Localised strain measurement and the DIC approach

For a more detailed assessment of deformation behaviour, robust techniques based on the local mechanical strain evolution at micro scale level during plastic deformation are employed across various materials. DIC and microgrid techniques in conjunction with speckle pattern analysis are documented to have been employed in this respect. Ghadbeigi et al., compared DIC and microgrid methods during the in-situ tensile deformation of ferritic steels at micro level (Ghadbeigi, et al., 2012). Their work reported an overall error of 0-34% over the investigated

regions, indicating the efficacy of the DIC method for measuring at microstructure scale. Walley et al., in their work proposed using SEM based in-situ tests for high temperature deformation of nickel based superalloy by using hafnium oxide as the speckle particles (Walley, et al., 2012). According to their work electron beam lithography was employed for depositing the speckle particles, whose displacements were tracked by a commercial software during the deformation process. Paulsen et al., in their research also compared results obtained from DIC with an etched surface against a gold speckled surface during in-situ testing of two-phased steel (Paulsen, et al., 2019). The authors observed that DIC performed with gold speckles produces a spatial resolution of $0.096\mu\text{m}$ and was capable of resolving slip lines. This was compared to the results from an etched surface which gave a spatial resolution of $2.24\mu\text{m}$ and was capable of resolving grain level local stress. Lagattu et al., in their work examined the use of DIC for an in-situ SEM method which proved capable of achieving a spatial resolution of $1\mu\text{m}$ after process validation with Ti-6Al-4V (Lagattu, et al., 2006). According to the authors, the method was capable of accounting for deformation processes in a range of polycrystalline materials.

Other studies have relied on the usage of grey scale secondary electron (SE) images to correlate strains at the grain level without adopting the speckle particle or micro grid approaches. Kang et al., in their work utilised SEM images to correlate microscopic strain distribution and damage of dual phase steels at grain scale (Kang, et al., 2007). Ghadbeigi et al., in their work on high strength dual phase steels utilised DIC to examine localised plastic strain changes with SEM images (Ghadbeigi, et al., 2010). Tasan et al., in their research also used DIC with SEM images, to differentiate between band morphologies and phase features observed in dual phase steels during in-situ tensile testing (Tasan, et al., 2010).

Generally, conventional uniaxial tensile deformation provides useful information about material mechanical properties with a global strain distribution but offers limited information on localised strain evolution especially at sheet surface defect sites. Previous works conducted on the effect of surface damage on tensile properties was done in-situ. Li et al., in their work on the in-situ examination of the impact of scratch type on the tensile strength of Q235 low carbon steels reported that the depth and angle of scratches reduces the tensile strength of the material (Li, et al., 2017). Experimental proof showing the presence and magnitude of local strain evolution at sheet defect sites and their impact on local microstructure response thus becomes important towards understanding grain level plasticity mechanisms. According to Pinna et al., techniques targeted at identifying the evolution of local plastic flow are of

significant interest for validation of plasticity models (Pinna, et al., 2015). However, research directed at understanding the impact of surface defects in the form of indents on the in-plane strain evolution at microstructural level during plastic deformation has not been previously studied. Therefore, evaluating the strain field evolution at the micro- level will aid in providing vital information on the relationship between the material microstructure and the material response to deformation under various straining conditions.

An ex-situ uniaxial tensile test with an SEM and a Matlab based DIC was conducted on a notched tensile sample with an indent- defect surface in this chapter. The main aim was to compute the localised strain evolution at the indent defect and a defect free micro-surfaces in order to assess their role in the plastic deformation behaviour of the material.

8.2 Press brake forming

Press brake forming is a widely adopted sheet metal forming method used in the manufacturing industry for the fabrication of different geometry designs ranging from simple V-bends to more sophisticated shapes (Muderrisoglu, et al., 1996). Sheet metal bendability is usually evaluated as the ratio of the minimum die radius used to bend the material without failure to the sheet metal thickness (Datsko & Yang, 1960). Normally, a region of thickness strain gradient is created around zones of the die/sheet contact with the inside of the bend undergoing compression (compressive strain) and the outside of the bend also placed under tension (tensile strain). The parameters which influence sheet metal bendability includes; die opening width, shut height, punch nose radius and sheet thickness. Press brake forming is mainly utilised due to the versatility in terms of the ease and speed with which the tools can be changed over to a new setup, and the low tooling costs (Beal, et al., 2006). According to Ragab and Ch Saleh, sheet thickness unevenness, micro cracks, occurrence of shear bands and failure at sheet convex surfaces are some of the factors which hinder a bending operation. According to the authors, these defects are mainly attributed to anisotropy, hardening, cold workability as well as the width to thickness ratio of the material (Ragab & Ch Saleh, 2005).

In the present study, press brake forming trials were conducted on test coupons with longitudinal scratches oriented along the sheet rolling direction in order to establish a threshold value of scratch defect characteristics which may be considered acceptable for press brake forming operations.

8.3 Experimental procedure

8.3.1 The material

The material examined in this chapter was Ti-3Al-2.5V near alpha titanium alloy sheets with thicknesses of 1.25mm and 1.6mm for the ex-situ uniaxial tensile test and the press brake forming trials respectively. The chemical constituents of Ti-3Al-2.5V has been detailed in Table 7.1.

8.3.2 Surface preparation and mechanical properties of the ex-situ tensile material

Surface polishing was performed with a 0.02 μ m Microcloth using 0.02 μ m colloidal silica and hydrogen peroxide to reveal the phases. SEM was performed on a Quanta FEG 250 microscope. The SEM micrograph of the as-received material is shown in Figure 8.1a. Two main orientations of the alpha phase were identified; the α orientation-1 (dark region) and the α orientation-2 (light region).

Standard room temperature tensile testing in accordance with ISO 6892-1:2016 was performed on the material in three sheet rolling directions (0⁰RD, 45⁰RD and 90⁰RD with respect to the sheet rolling direction) at a constant strain rate of 0.001/s. The material exhibited high anisotropic tendencies, Figure 8.1b.

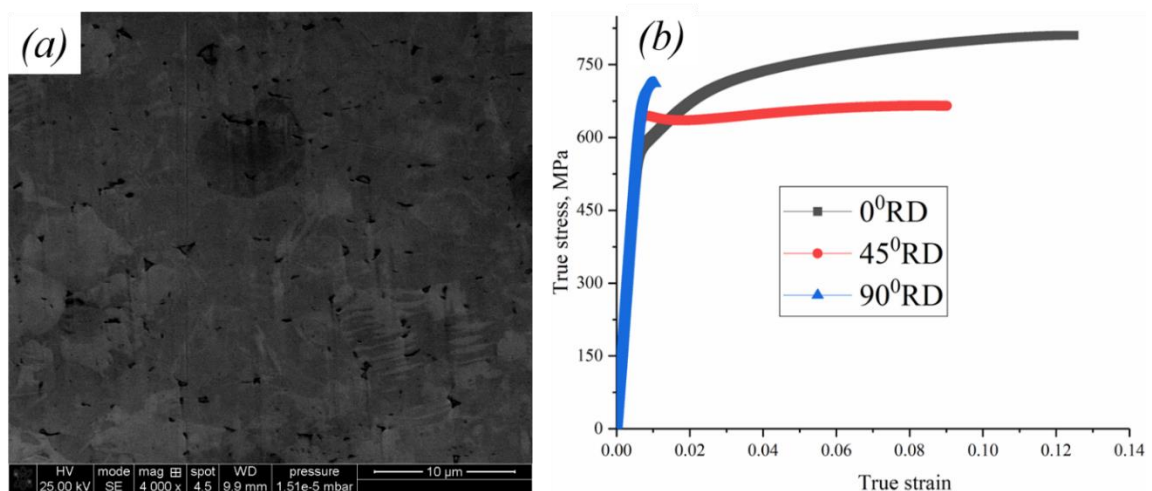


Figure 8. 1 Ti-3Al-2.5V alloy

(a) SEM microstructure and (b) tensile behaviour of an un-notched tensile sample of the as received material at room temperature

8.3.3 Nature of the surface defects on the as-received sheet

The main sheet post-processing surface defects observed in the titanium sheets studied in this chapter are shown in Figure 8.2. The most visible surface defects observed were predominantly surface scratches oriented at different angles with respect to the sheet rolling direction and randomly distributed with varied depths. Surface defects like scratches are mostly produced due to bad friction conditions between contact surfaces (Levaillant & Chenot, 1992).

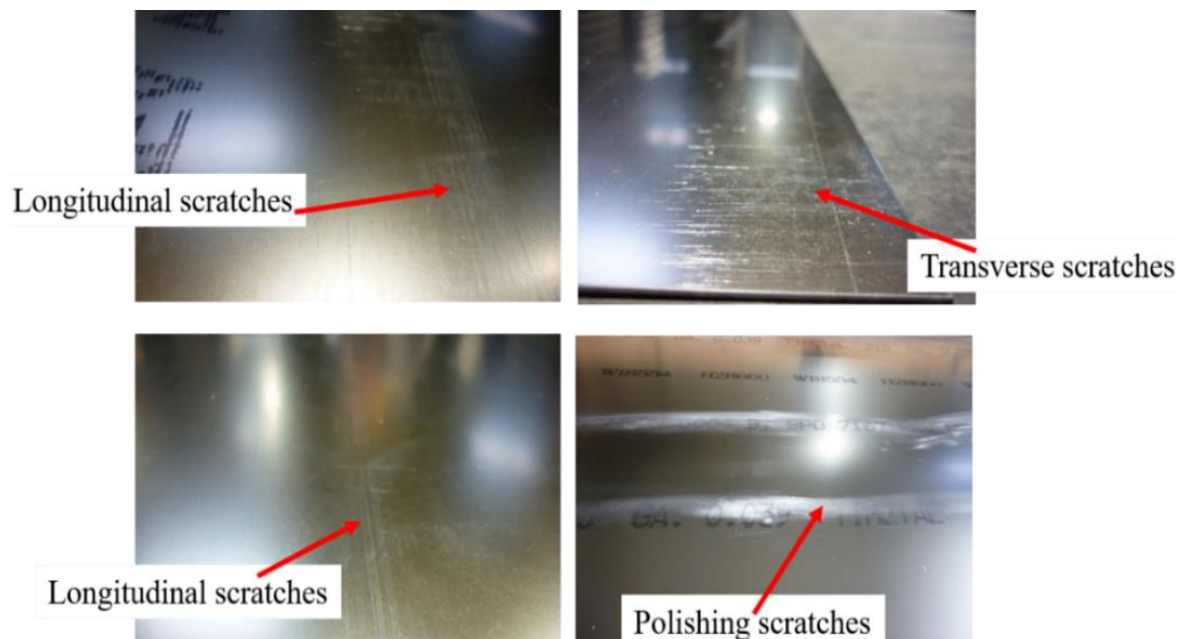


Figure 8. 2 Examples of different forms of post-processing defects on sheet surfaces

Table 8.1 shows the varied nature of the surface defects that may be observed on the Ti-3Al-2.5V titanium sheets. Three distinct surface zones were identified; the defect-free, scratched and indented defect surfaces. Alicona optical microscopy analysis was conducted to analyse as well as measure the profile of the three identified zones. The surface scratch defect morphology was characterised by surface depth and pile up heights. These surface scratch profiles (produced by virtue of bad friction conditions between contact surfaces typical of poor sheet handling) were varied across the supplied sheets with an accompanying varying surface depth and pile up heights. The indent- defect surface morphology generally featured surface depths with no pile up heights. A fairly flat and even surface morphology profile was observed for the defect-free surfaces.

Table 8. 1 Micrographs of defect types observed on the as-supplied Ti-3Al-2.5V sheets

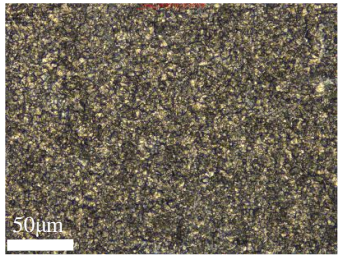
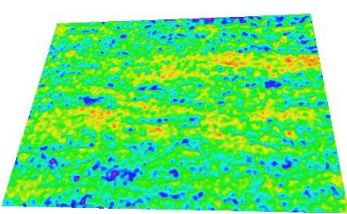
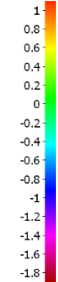
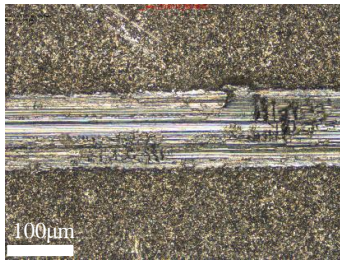
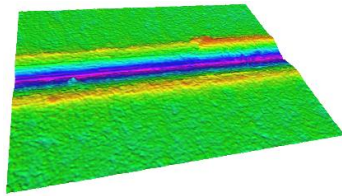
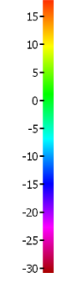
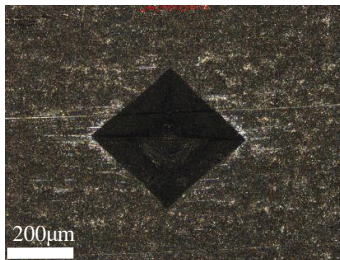
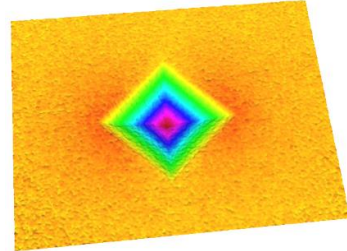
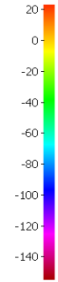
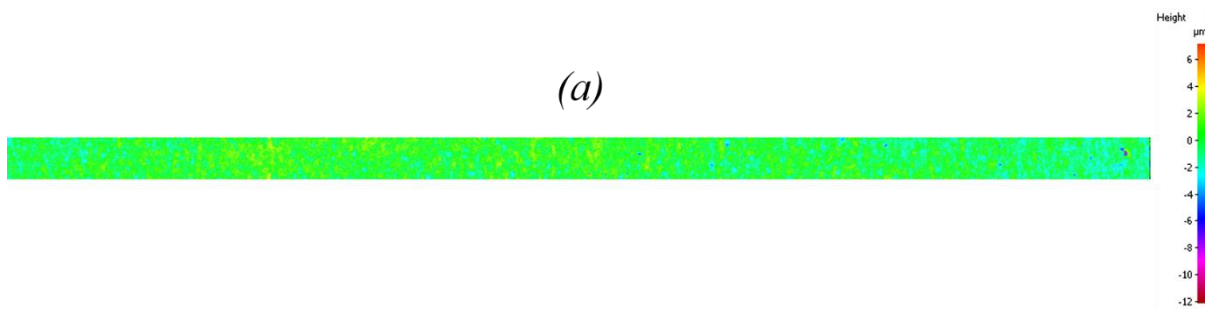
Defect type	Optical image	Alicona scan	Height, μm
Defect-free			
Scratch			
Indent			

Figure 8.3 shows the Alicona optical microscopy images of the three distinct areas identified for the as-received sheet surfaces measured over the full-length volume (1.6cm distance). A somewhat uniform sheet surface morphology was recorded for the defect-free surface zones over the measured length, Figure 8.3a. The surface scratch- defect zones observed over the measured full length featured surface depth and pile up heights stretching across the sheet surface, Figure 8.3b.



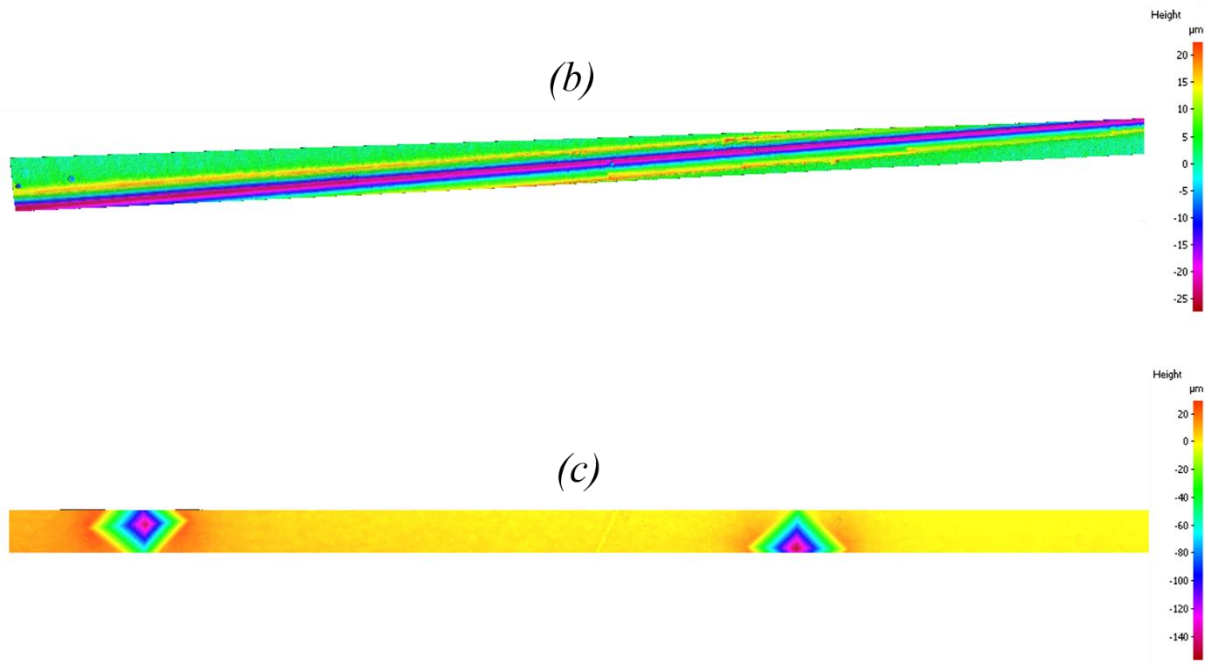


Figure 8. 3 Surface profilometry analysis at full-length measurement (1.6cm)

(a) Free surface, (b) scratch and (c) indent defect surfaces

The indent defect site for the measured full length was also characterised by its distinct surface depth region with a relatively flattened sheet surface at zones where no surface defect occurred, Figure 8.3c.

8.3.4 Surface scratch profile classification for the press brake forming trials

After the coupon preparation process, the profile of the surface scratches were measured using Alicona optical non-contact measurement system. For the surface scratch characteristics profiling, two main scratch parameters were considered for the classification; the scratch depth and the pile up heights, Figure 8.4. The coupons were then categorised into three distinct surface profile threshold ranges (scratch designations A, B and C) as shown in Table 8.2. Scratches on either side of the coupons were measured, however, only the highest defect profile values were considered. Only coupons with longitudinal scratches oriented along the material rolling direction was considered in the test trials. This was done to make certain that the potential effect of scratch orientation is not underestimated in the analysis of the test results. For the purposes of comparison and to ensure a proper appreciation of the material response to the scratch defects, the coupons with defect free surfaces were also examined but grouped with the low scratch profile value coupons. For each category of surface scratch profile range, 30 coupons were assessed during the press brake forming trials for each punch nose radius.

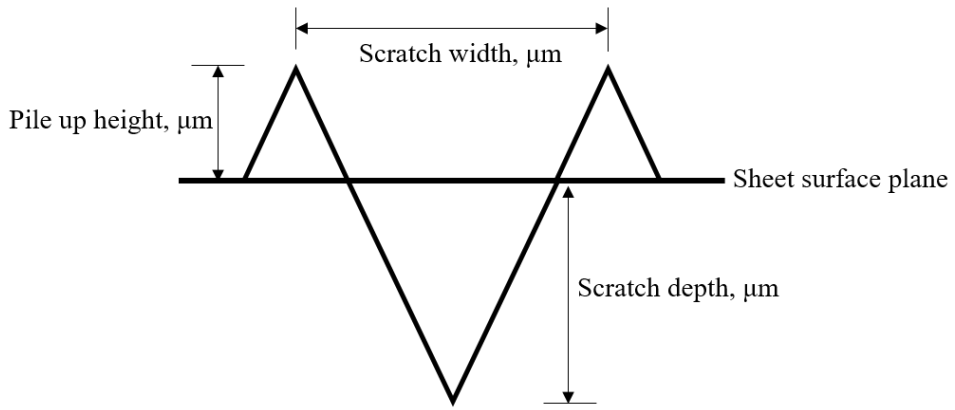


Figure 8. 4 Scratch characteristics profile parameters

Table 8. 2 Three ranges of scratch profiles examined during the press brake forming

Scratch designation	Alicona images	Scratch profile	
		Depth, μm	Pile up height, μm
A (Range including defect-free surfaces)		(-1 to -18)	(1 to 16)
B		(-18 to -35)	(16 to 35)
C		(-35 to -80)	(35 to 50)

8.3.5 Bending test trials

The press brake forming trials were conducted using a Jean Perrot Maneo 105/30 CNC hydraulic press-brake machine equipped with a maximum stroke of 250mm and a maximum capacity of 1000kN. A Wila made standard premium OZU-353 515 die with radius =3.5mm ($16 \times 30^\circ$), height = 100mm was used together with two different punch nose radii dimensions; a BIU-231 515 punch with radius =3mm (28°), height =200mm and a BIU-031 100 punch with radius =1mm (28°), height =200mm. In order to ensure that the coupons were formed to their optimum bending angle, the radius of the die was chosen to be slightly larger than the punch radii. Two different punch nose radii was chosen to compare the material response to two bending angles as well as to ensure the attainment of tighter radii prior to failure. For the press brake forming trials, 180 rectangular coupons of dimension 300×40mm with longitudinal scratches oriented along the sheet rolling direction were prepared using a guillotine metal cutter.

Figure 8.5 shows the experimental set-up for the press brake forming trials. Prior to the bend-test, the tool alignment was checked with a laser source. The coupon was then placed over the open die and aligned in position with the aid of a robotic arm. After setting the automated control on the computer numerical control (CNC) panel with the material and tool parameters, the coupon was then pressed by the punch to the optimum radius to execute the press forming manoeuvre.

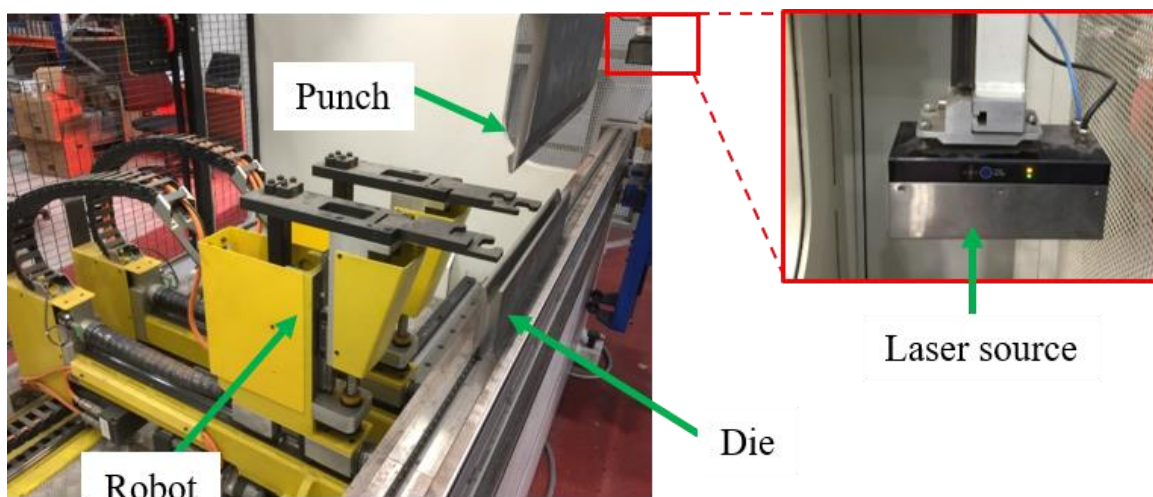


Figure 8. 5 Experimental set-up for the press brake forming trials

8.3.6 Ex-situ uniaxial tensile test and strain analysis of a notched tensile sample

A Zwick/Roell Z150 tensile testing machine was used to deform the sample at a crosshead speed of 0.002mm/s. A 100×19×1.25mm notched tensile sample with a 1mm radius notch was used in this work, Figure 8.6. A notched tensile sample was chosen to ensure that regions of high stress triaxiality (yellow dotted rectangle – Figure 8.7) are examined for consistent tracking of the critical strain field evolution.

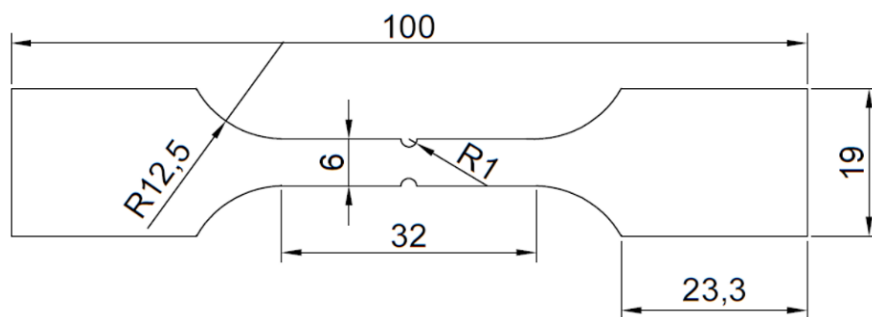


Figure 8. 6 Test sample dimensions

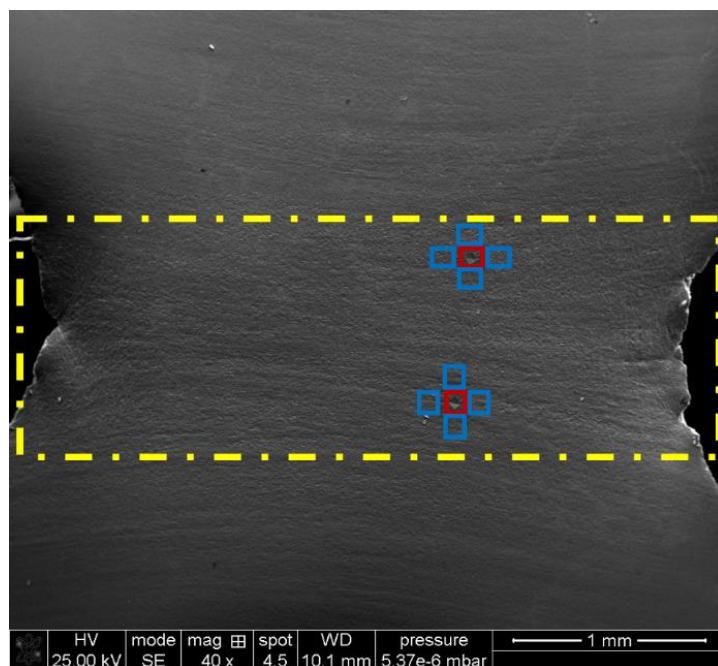


Figure 8. 7 Zones examined during ex-situ tensile testing. Indent regions (red regions) had an area of ~120µm×120µm and the free surface (blue regions) had an area of ~30µm×30µm

The two indent defects strategically sited at the critical strain zones of the sample did not only serve as the surface defect but also as a reference point for image capture during the ex-situ tensile test. The indent- defect micro surface possessed a surface depth of ~140µm. Two regions of interest were examined during the tensile testing; indent defect micro regions (red

regions) with an area of $\sim 120\mu\text{m} \times 120\mu\text{m}$ and the free micro surfaces (blue regions) with an area of $\sim 30\mu\text{m} \times 30\mu\text{m}$, Figure 8.7. The variations in magnification were accounted for during the calibration of the field displacement by ensuring that SEM images were acquired with the same contrast and brightness image qualities to make certain consistency in the grey level intensity.

The tensile test was interrupted at different strain values in order to capture the microstructural evolution images during the plastic working process. A low strain rate was used to ensure that the microstructure transformation as well as the micro damage process were sufficiently captured. The micrographs at the regions of interest were taken in SE mode. The most critical aspect of the ex-situ testing is the process of returning to and acquiring images at the same zones of interest after each image acquisition. For this, a DIC with a highly robust algorithm capable of capturing image discontinuities must be chosen. The Ncorr DIC software was employed in this EngD research for this purpose. The novel algorithms implemented in Ncorr DIC software enables for (Blaber, et al., 2015);

- Multithreaded version of reliability-guided DIC.
- Means of computing large strains via automatically updating the region of interest and adding displacement.
- Adopting Eulerian to Lagrangian conversion algorithm to evaluate discontinuous displacement fields.

The recorded SE microstructures for each interrupted deformation image were then loaded into the Matlab based Ncorr version 1.2.2 software for the onward correlation and evaluation of the field displacements and localised strain evolution at microstructure length scale.

8.3.7 Digital image correlation

The algorithm relies on the robust and computationally efficient Bing Pan's reliability-guided (RG) DIC framework (Pan, 2009). The improvement of the RG-DIC approach on the traditional DIC technique is based on its ability to correct wrongly calculated points, which may occur because of roughening of the surface during deformation. Normally, these errors would be carried on during image processing resulting in incorrect computation. The RG-DIC mainly employs the zero- mean normalised cross correlation (ZNCC) coefficient as the

reliability factor to compensate for such discontinuities. For a desired vector \mathbf{p} with respect to the displacement mapping function, the ZNCC is given by (Pan, 2009); (Pan, et al., 2007);

$$C_{ZNCC}(\mathbf{p}) = \frac{\sum_{x=-M}^M \sum_{y=-M}^M [f(x,y) - f_m] \times [g(x^t, y^t) - g_m]}{\sqrt{\sum_{x=-M}^M \sum_{y=-M}^M [f(x,y) - f_m]^2} \sqrt{\sum_{x=-M}^M \sum_{y=-M}^M [g(x^t, y^t) - g_m]^2}} = 1 - 0.5 \times C_{ZNSSD}(\mathbf{p}) \quad (8.1)$$

ZNSSD is the zero-normalised sum of squared differences also given by;

$$C_{ZNSSD}(\mathbf{p}) = \sum_{x=-M}^M \sum_{y=-M}^M \left[\frac{f(x,y) - f_m}{\sqrt{\sum_{x=-M}^M \sum_{y=-M}^M [f(x,y) - f_m]^2}} - \frac{g(x^t, y^t) - g_m}{\sqrt{\sum_{x=-M}^M \sum_{y=-M}^M [g(x^t, y^t) - g_m]^2}} \right]^2 \quad (8.2)$$

$$f_m = \frac{1}{(2M+1)^2} \sum_{x=-M}^M \sum_{y=-M}^M [f(x, y)] \quad (8.3)$$

$$g_m = \frac{1}{(2M+1)^2} \sum_{x=-M}^M \sum_{y=-M}^M [g(x^t, y^t)] \quad (8.4)$$

Where;

M - Subset dimension in pixels from a reference image

(x, y) - Reference subset

(x^t, y^t) - Target subset

$f(x, y)$ - Grey level intensity at reference coordinate (x, y) of reference image

$g(x^t, y^t)$ - Grey level intensity at target coordinate (x^t, y^t) of the target image

The fundamental principles governing the DIC process are illustrated in Appendix A5.

This algorithm is adopted by the DIC, and directed at correlating the localised displacement of the reference image surface location together with surface locations of the target (current) images acquired during the deformation process. Micrograph features were used to trace the patterns for which correlation is attained between subsequent loading steps. Seed placements are performed for the update and to obtain good correlation with the reference image. To ensure good seed placement in this work, a strong match location for the reference image and the subsequent current image locations was enforced. A striking similarity between the reference and the transformed current subsets was obtained in this research, Figure 8.8. Subsets are minute subsections of a reference image from the undeformed material, which is compared against subsequent deformed (current) images by evaluation of their subsequent positions in

the current configuration. Subsets enable the tracking of points on the grey scale SE images where the distinct grey scale within each subset serves as a specific point to track that subset. Subsets are fundamentally sets of coordinate points. The cell size that is utilised for correlating the reference and current images is the subset size. For two successive subsets, the distance between them is the subset spacing.

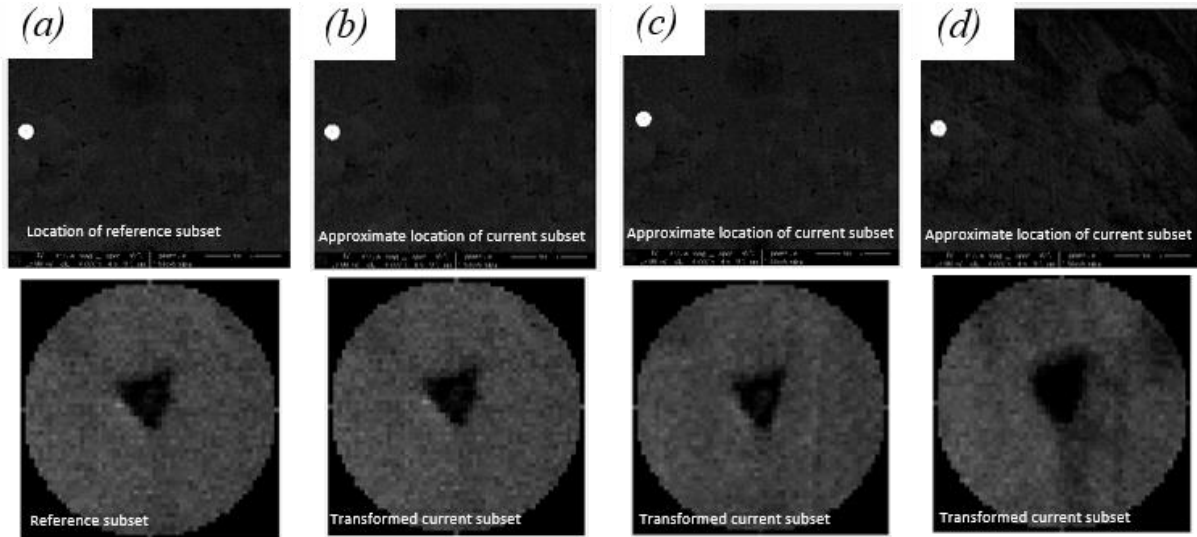


Figure 8. 8 Seed placement matching for reference and current images

(a) Reference image (Stage 0), (b) stage 0, (c) stage 1, (d) stage 2

8.4 Results and discussion

8.4.1 Effect of longitudinal scratch defect on the sheet bendability

Table 8.3 shows the results after press brake forming of the test coupons deformed with two different punch nose radii. The test criteria adopted in this research to ascertain the competence of the scratch characteristic profile is the failure or success of the test trial. Failed test coupons after the test trials were characterised by cracks at the summit of the V-bend, whereas successful trials were fully bent per the punch radius adopted without crack occurrence, Figure 8.9. Test trials for the coupons with no scratch defect (defect free surface) exhibited 100% forming success rate after bend forming with both punch radii. For longitudinal scratches deformed with a 3mm radius nose punch, scratches with a depth in the ranges of $-1\mu\text{m}$ to $-18\mu\text{m}$ and a pile up height in the ranges of $1\mu\text{m}$ to $16\mu\text{m}$ were successfully formed without failure. For scratch profiles with depth in the ranges of $-18\mu\text{m}$ to $-35\mu\text{m}$ and a pile up height between $16\mu\text{m}$ to $35\mu\text{m}$, the forming success rate reduced by half the initial threshold when deformed with the 3mm radius punch nose. Scratch profiles beyond the scratch designation ‘B’

were 100% unsuccessful, when deformed with both punch nose radii. The success rate for all scratch profile designations also reduced for coupons deformed with punch nose radius 1mm compared to punch nose radius 3mm.

Table 8. 3 Press brake forming trials for different longitudinal scratch profiles

Punch nose radius = 1mm						
Scratch designation	Scratch profile		Total trials	Pass	Fail	Success rate, %
	Depth, μm	Pile up height, μm				
A	(-1 to -18)	(1 to 16)	30	26	4	87
B	(-18 to -35)	(16 to 35)	30	12	18	40
C	(-35 to -80)	(35 to 50)	30	0	30	0
Punch nose radius = 3mm						
A	(-1 to -18)	(1 to 16)	30	30	0	100
B	(-18 to -35)	(16 to 35)	30	16	14	53
C	(-35 to -80)	(35 to 50)	30	0	30	0

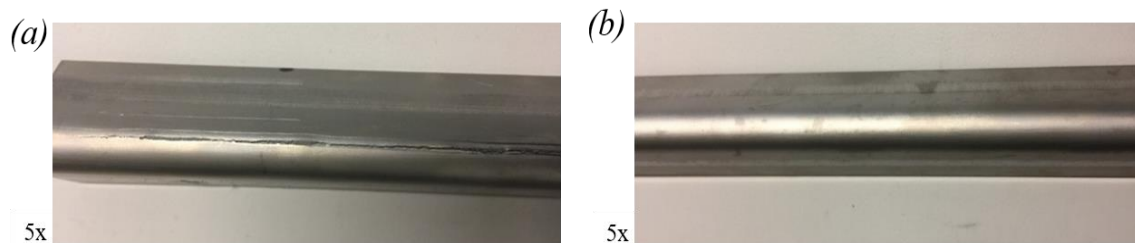


Figure 8. 9 Coupons after press brake trial

(a) Failed and (b) Unfailed V-bend coupons

This trend could be attributed to the variations in the geometrical dimensions of the punch nose radii adopted. Mostly, a smaller punch radius exerts more pressure on the contact sheet surface since it occupies a lesser surface area. This permits larger force per unit contact area leading to higher stress concentration and early material yielding, leading to early fracture. Conversely, a punch with larger nose radius produces a broader contact area with minimised force thereby resulting in delayed material yielding. Similar press brake forming test trials were conducted by Määttä et al., on ultra-high strength steels (direct quenched bainitic-martensitic steel DQ960 and abrasion resistant steel AR500- due to their sensitivity to surface defect e.g. scratches) with surface cracks produced with laser ablation in order to ascertain the critical surface defect size which results in failure during press brake forming. Their work found that the critical crack sizes attained were responsive to the material hardness and that about 36% reduction in the material hardness resulted in the critical crack size increasing by 138% (Määttä, et al., 2012).

8.4.2 Crack nucleation during the press brake forming trials

Material failure during the press brake forming trials occurred mainly at the longitudinal scratch defect sites. The macro-cracks (green arrows) were observed to develop away from the coupon machined edges, Figure 8.10a. The macro-cracks were also seen to have occurred along the trajectory of the longitudinal surface scratches. This indicates that the main cause of the coupon failure could be attributable to the effect of the longitudinal scratch defects (red arrows) in their role as stress raisers, Figure 8.10a. Analysis of the micro-features of the scratch surface (blue arrow) after the press brake forming trials revealed regions of micro-crack initiation (yellow arrow), Figure 8.10b. This is opposed to observations made by Reyes et al., on AA7108 T6 aluminium alloy during press forming, where the failure crack was observed to commence from the sample fabricated edges with traces of orange peel seen just outside the fracture region (Reyes, et al., 2009).

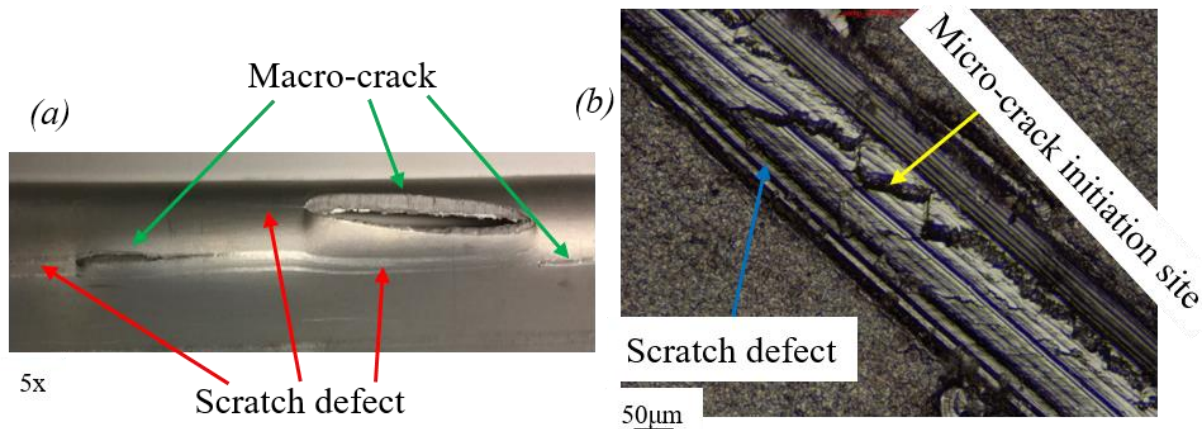


Figure 8. 10 Crack nucleation process

(a) Macro and (b) micro-crack occurrence

8.4.3 Evaluation of localised strain evolution at indent and defect-free micro-surfaces

A notched tensile sample oriented transverse (90° RD) to the sheet rolling direction was used in this investigation. The standard force- displacement curve after each stage of deformation during the interrupted tensile testing process is shown in Figure 8.11. The notched sample yielded after 0.13mm of travel after which a drop in load was observed. There was a continuous decrease in the load until micro-fracture nucleation sites were observed at the notch root after a displacement of 0.54mm. The maximum load occurred at just about the same value of the

yield point for this material when worked in the transverse direction (90° RD), consistent with the true stress- strain behaviour shown in Figure 8.1*b*.

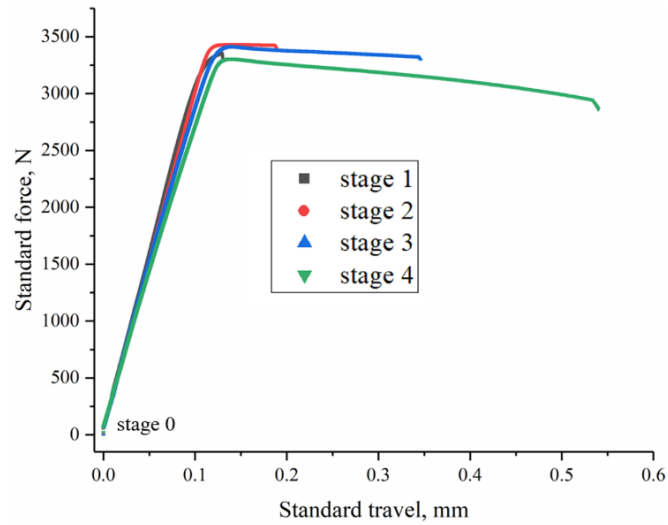


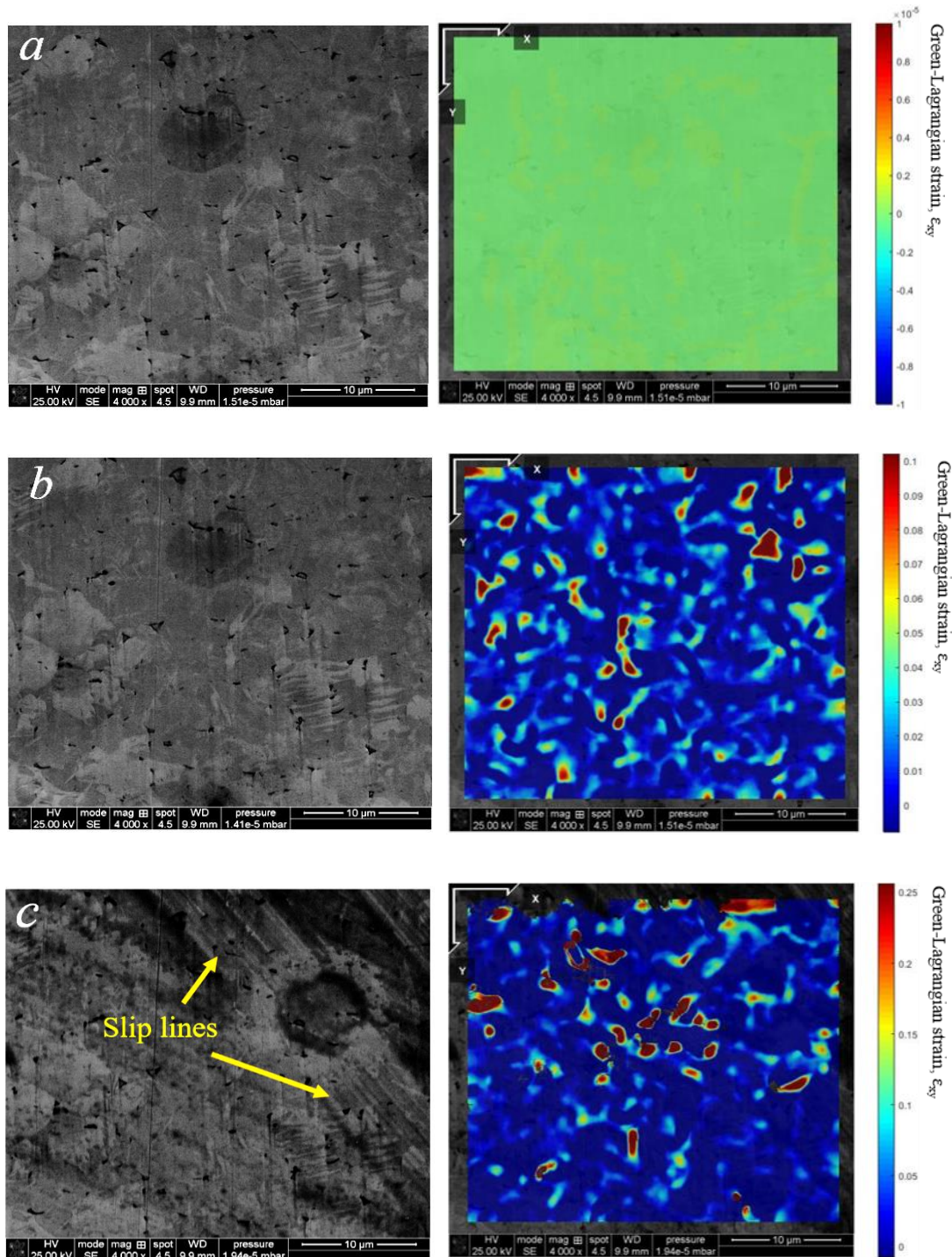
Figure 8. 11 Standard force- travel curve for the interrupted tensile deformation. The different stages of deformation (stage 0-4) correspond to micrographs labelled (*a-e*) respectively in Figures 8.12 and 8.16

8.4.4 Localised strain evolution at defect-free micro-surface

The micrographs captured during the interrupted tensile deformation of the notched sample with their corresponding DIC localised strain maps are shown in Figure 8.12. The as-received microstructure (Figure 8.12*a*) and those obtained at the material yield point (Figure 8.12*b*) showed very similar microstructure features. Further deformation beyond the material yield point resulted in significant microstructure transformation, (see Figure 8.12*c-e*). Slip lines (Figure 8.12*c, d*) were observed after the material yielded, followed by the formation of deformation bands and subsequently shear bands (Figure 8.12*e*) oriented at 45° to the tensile axis. Slip deformation was observed very early in this material because necking occurred abruptly as a result of the tensile strength being very close to the yield point for this sheet orientation. Slip deformation after yielding of Ti-6Al-4V is reported to evolve from single to multiple and subsequently cross-slip modes during in-situ tensile deformation (Zhang, et al., 2018). The deformation bands observed in Figure 8.12*d* became heavily deformed following further straining resulting in roughening of the surface (Figure 8.12*e*). A match of the slip traces (green line- Figure 8.12*d*) with the slip trace analysis graph (Wang, et al., 2016) are normally used to estimate the slip plane and direction as well as the accompanying schmid factor in order to determine the dominant activated deformation slip system. Other works done to ascertain

the active deformation slip system present in Ti-3Al-2.5V showed that 80% of the 128 active slip systems examined were prismatic slip (Li, et al., 2014).

The DIC analysed strain maps also revealed the main strain concentration sites attained during the deformation process. From the initial deformation up until the material yield point, the strains are seen to concentrate mostly in the α orientation-2 (light region) site (Figure 8.12b).



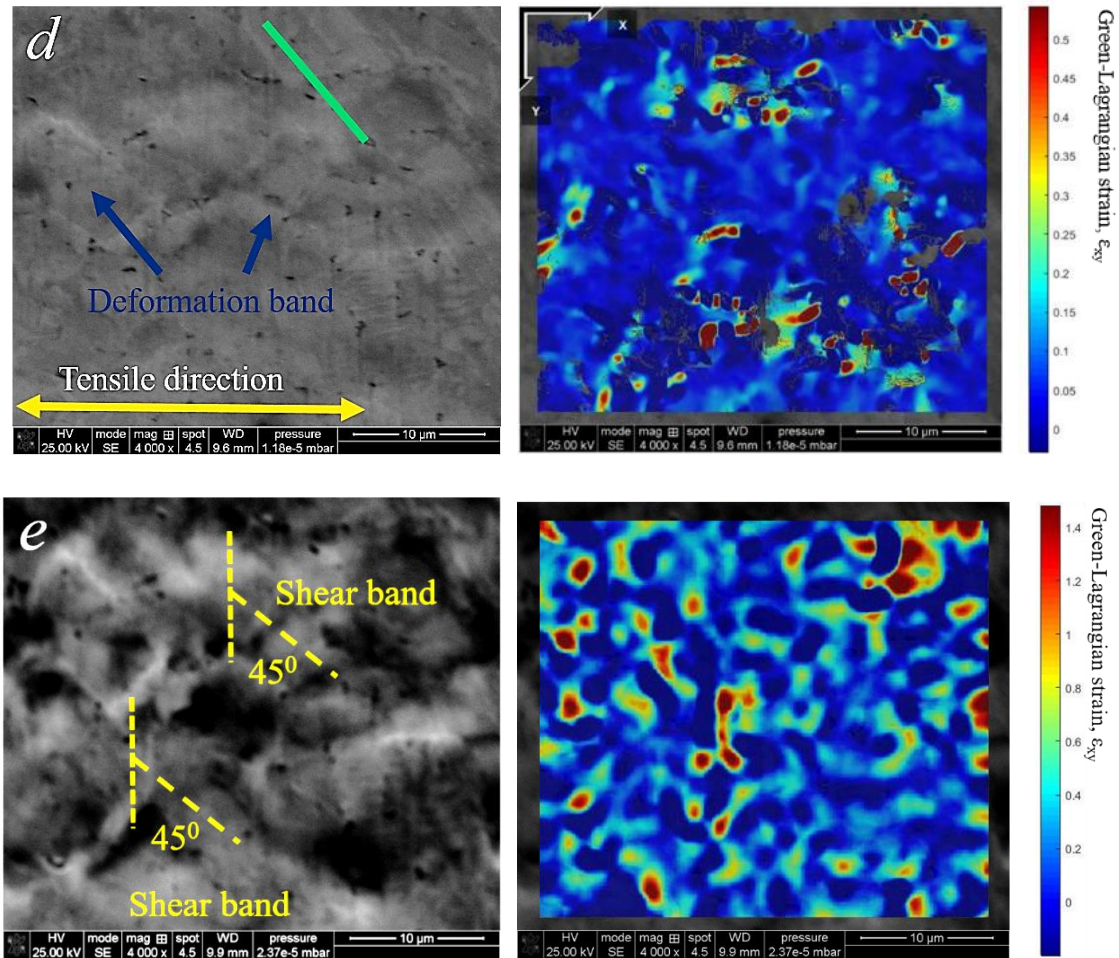


Figure 8. 12 SEM and DIC strain maps at the defect free micro surface

(a) stage 0, $\epsilon_{\text{global}}= 0\%$ (b) stage 1, $\epsilon_{\text{global}}= 0.41\%$ (c) stage 2, $\epsilon_{\text{global}}= 0.58\%$ (d) stage 3, $\epsilon_{\text{global}}= 1.1\%$ (e) stage 4 $\epsilon_{\text{global}}=1.7\%$

Where ϵ_{global} = global engineering strain.

Generally, grains of varied orientation will deform through different slip activities subject to the mechanisms which are most favourable. For polycrystalline materials, load distribution between neighbouring grains could also impact on slip activities (Dunne, et al., 2007). Subsequent straining beyond the yield point resulted in the strains concentrating mostly in the regions with slip bands as well as the emergent bands, Figure 8.12c, d. Further loading resulted in the formation of dense shear bands where the high strains continued to concentrate, Figure 8.12e. Emergent bands serving as zones of high stress concentration and acting as nucleation points for damage are reported in high strength dual phase steel (Kapp, et al., 2011) and ferrite-pearlite two-phase steels (Paulsen, et al., 2019), Figure 8.13.

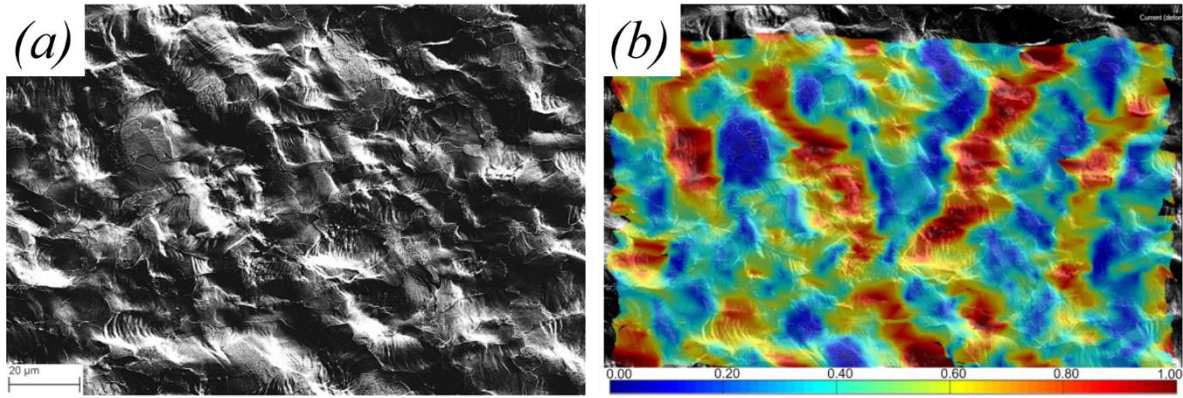


Figure 8.13 Strain concentration at heavily deformed bands during in-situ SEM tensile test of ferrite-pearlite two- phase steels (Paulsen, et al., 2019)

(a) SEM image of deformed bands, (b) corresponding DIC strain map

The localised strain field evolution within the critical zones identified were evaluated by identifying discrete points in the α phases as well as the emergent band regions. For the α phase region, two distinct zones were evaluated; the α orientation-1 (dark region) and the α orientation-2 (light region) –see Figure 8.12a. The regions of interest chosen, with the subset radius and spacing preview for the local phase strain field evolution during the deformation process is shown in Figure 8.14. For a given region of interest, imprints (location of subset zones to be tracked, shown as green cross in Figure 8.14b) were placed in the reference image for processing and onward correlation. A subset radius of 28 and subset spacing of 1 offered the best subset tracking for the DIC in this work, Figure 8.14c.

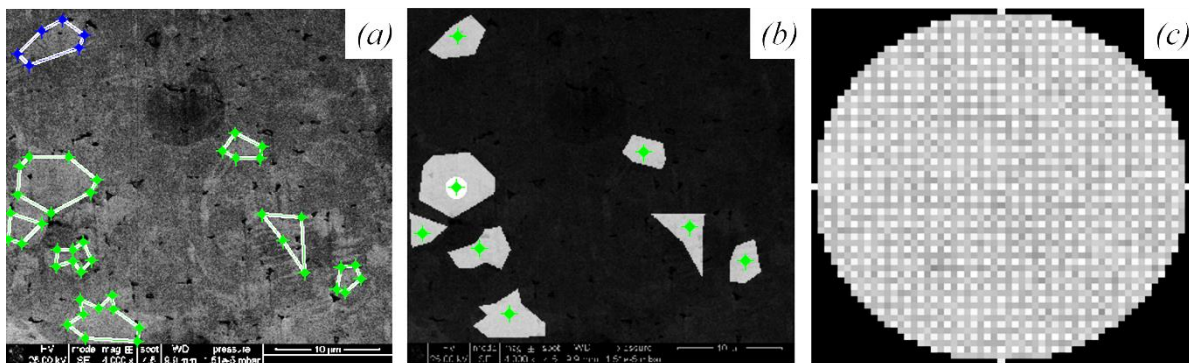


Figure 8.14 DIC parameters for localised phase strain evolution

(a) Regions of interest (b) Subset location, (b) subset spacing preview

A plot detailing the DIC analysed zones, created to quantify the phase field localised strain evolution during the deformation process is shown in Figure 8.15. The localised strains were highest for the corresponding global strains where the emergent bands began to appear. Initial straining to the yield point (global engineering strain, $\epsilon_{global} = 0.41\%$) resulted in most of the

strain concentrating in the α orientation-2 (light region) region. Primarily, the Al content as a phase stabiliser controls the strength and plasticity of the α phase. Thus, with respect to slip and twin inception, plasticity is initiated in the α phase. Beyond the yield point, both the α phases and the emergent bands exhibited similar strain distribution trends with slightly higher localised strains observed in the emergent band regions compared to the α phase regions at room temperature. This is mainly because, the emergent band regions tend to contain high dense network of dislocations. The localised strains obtained at the various α phase orientations were different with slightly higher strains obtained in the α orientation-2 (light region) compared to the α orientation-1 (dark region). The maximum localised strain attained for the α orientation-1, α orientation-2 and the emergent band regions were 80%, 170% and 320% respectively at a global strain of 1.7%, Figure 8.15.

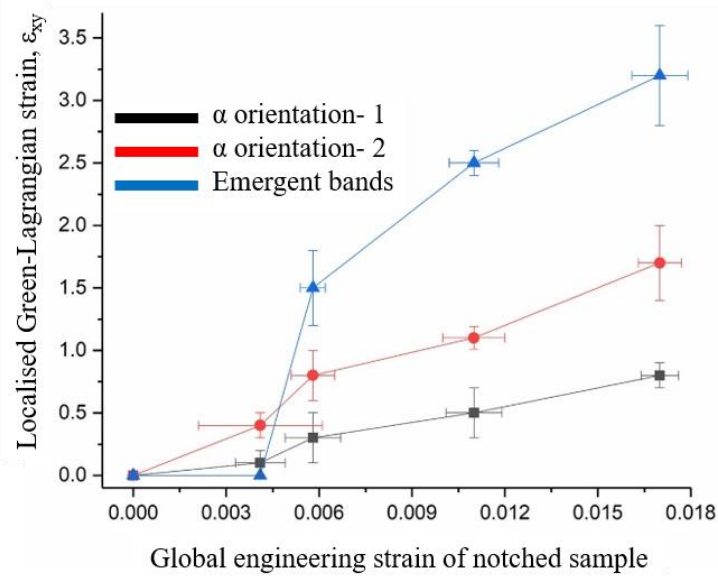


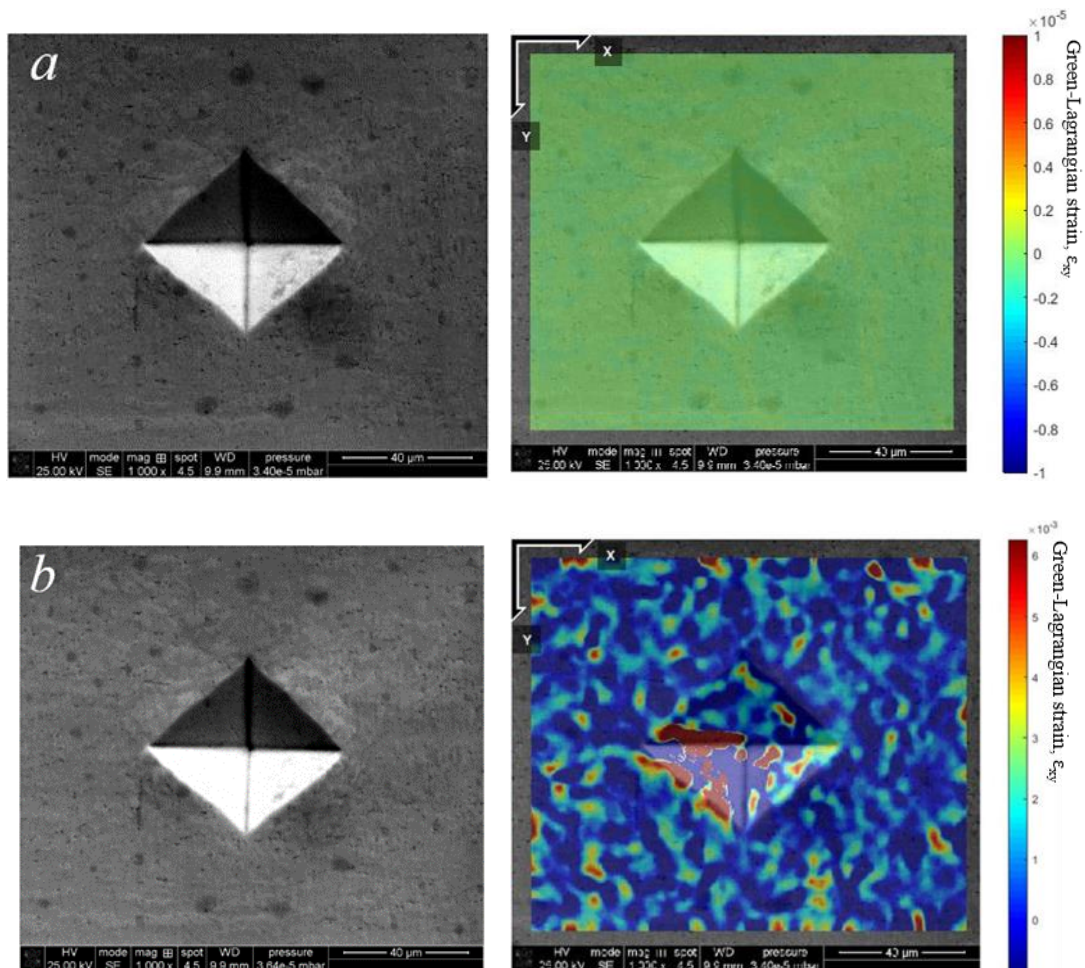
Figure 8. 15 Localised strain evolution in α phases and the emergent band regions

8.4.5 Localised strain evolution at indent defect micro-surface

The micrographs obtained for the indent defect zone with their corresponding DIC strain maps are shown in Figure 8.16. Again, there were a few differences in the micrographs between the as-received condition and those from the material yield point, Figure 8.16a, b. Deformation beyond the material yield point produced slip lines with subsequent straining resulting in the activation of shear bands (Figure 8.16c, d) oriented at 45° to the tensile axis. Further straining resulted in the formation of bands near the indent edge, Figure 8.16e. The most outstanding

feature of the deformation at the indent defect micro surface is the initiation and accumulation of the bands at the sharp tip of the defect along the tensile axis.

Initial evaluation of the DIC strain map at the yield point of the indent defect micro region revealed strains concentrating at the defect site and at the α orientation-2 (light region), Figure 8.16*b*. Further straining beyond the yield point, resulted in the strains concentrating both inside the indent defect site and at the sharp defect edge along the tensile axis, Figure 8.16*c*. This observation is a sharp departure from the strain concentration seen at zones around the slip line region of the defect free micro surface zone, for the same loading condition (see Figure 8.12*c*). Subsequent deformation resulted in increased localised strain concentration at the shear bands and the severely strained emergent bands near the indent defect edge tip along the tensile axis, Figure 8.16*d*. The strains at the indent defect edge tip increased with increasing deformation load to 40% localised strain for a global strain of 1.7%, Figure 8.16*e*.



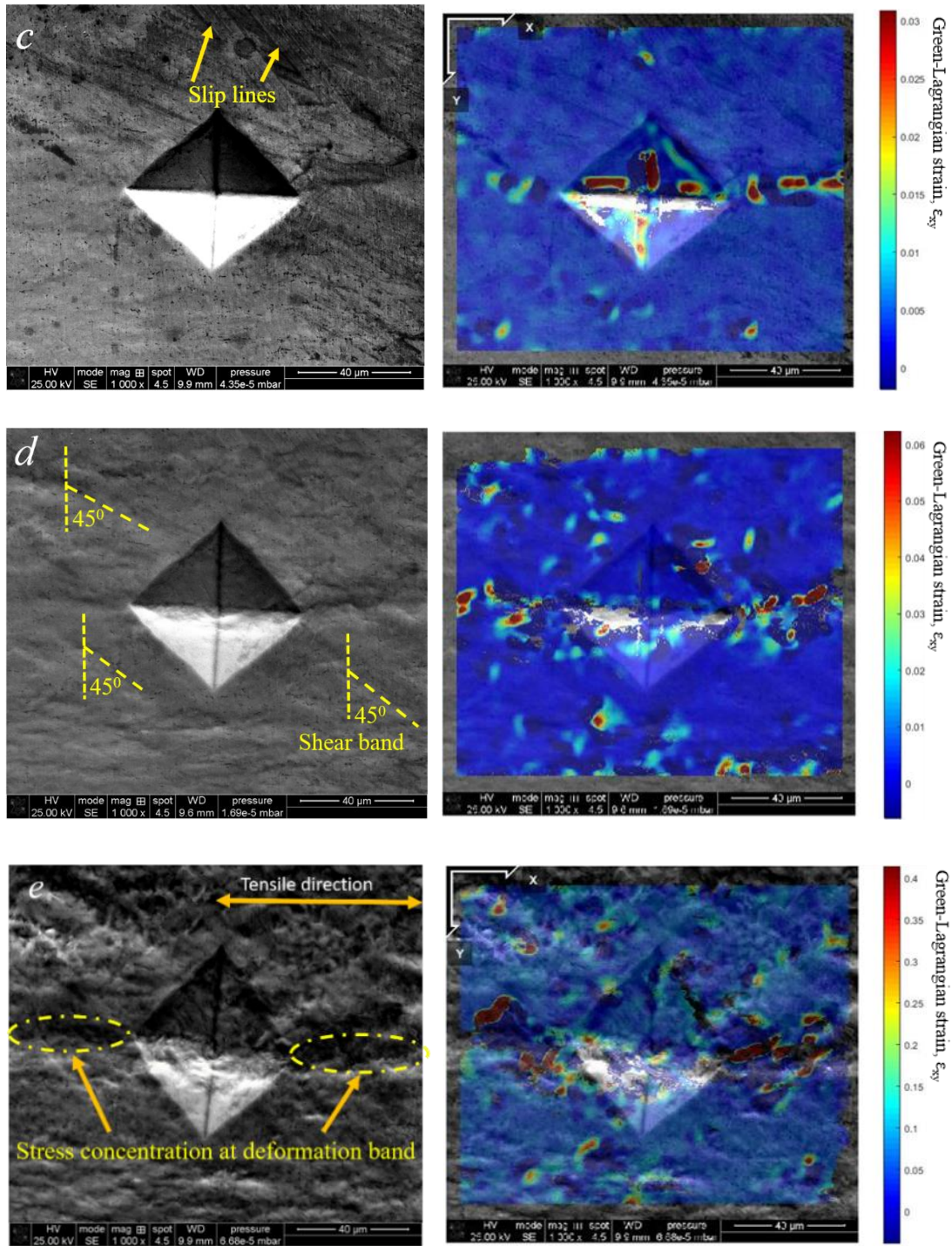


Figure 8. 16 SEM and DIC strain maps at the indent defect micro surface

(a) stage 0, $\epsilon_{\text{global}} = 0\%$ (b) stage 1, $\epsilon_{\text{global}} = 0.41\%$, (c) stage 2, $\epsilon_{\text{global}} = 0.58\%$ (d) stage 3, $\epsilon_{\text{global}} = 1.1\%$ (e) stage 4, $\epsilon_{\text{global}} = 1.7\%$

The indent defect tip aligned to the tensile axis experienced the highest localised deformation strain as a result of the actions of the high emergent band accumulation with little deformation observed at the indent defect edge tip oriented transverse to the tensile axis. This is probably because the indent defect edge tip along the tensile axis was under tensile stress whereas the

indent defect transverse to the tensile axis was under compressive stress. The localised strains observed at the emergent bands along the indent defect edge tip are significantly higher than those observed in zones away from the indent defect site.

Therefore, for a defect free micro surface the absence of artificial (defect) zones acting as high stress concentration site means strain aggregation at critical defect sites is minimised and the α - phase is able to accommodate the deformation reasonably well. The presence of these indent defects serve as an obstacle to the material plastic flow by restricting the movement of dislocations and creating zones of high energy absorption resulting in the reduced values of fracture strain at the indent defect micro surface. The impact of indentation on dislocation activities have been discussed in some works. Huang et al., in their studies at a nanometer length scale have shown that for situations where a grain is considered as a crystal, indents from controlled nanoindentation leads to the formation of atomic crystal steps, produced by dislocation glide along planes. According to their work, this results in coherent local crystal lattice movement and rotation. This causes deep dislocation movement into the crystal and irregular pile up at the edges of the indent surface. Thus, indents results in incoherent lattice movement, causing dislocation locking that inhibits their movement (Huang, et al., 2013). The deformation bands concentrating at the tip of the indent defect act as a nucleation site for early crack nucleation, propagation and growth hence the reduced localised fracture strain.

A comparative analysis was done for the localised strain evolution attained for both indent defect and defect-free micro-surfaces, Figure 8.17. Both the defect free micro surface and the indent defect micro zones exhibited higher localised strains albeit different at the emergent bands (140% and 40% respectively) at a global strain of 1.7% showing the heterogeneous nature of the deformation observed in the material. The disparity in the localised strain evolution observed in the emergent bands and those outside the band as well as their role in the deformation evolution in terms of damage nucleation observed on both micro surface conditions account for the heterogeneity in the plastic flow. The heterogeneity could also be attributed to the evolution in shear band formation oriented 45° to the tensile axis on the respective micro surface conditions and their role in the micro-surface damage process. Similar deformation trends of localised strain field distribution was observed for both sheet micro surface conditions over the examined global strain values, Figure 8.17.

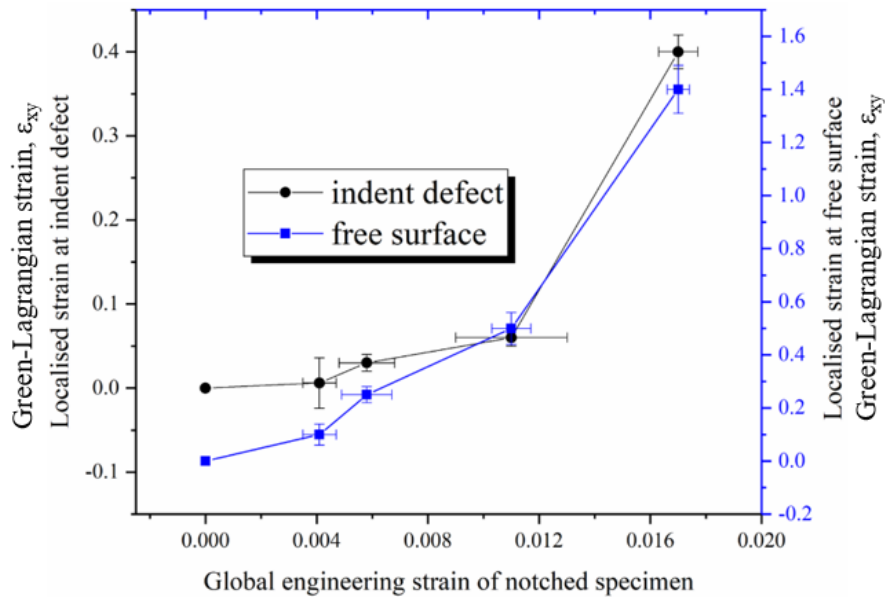


Figure 8. 17 Localised and global strain evolution at micro-surface conditions

8.4.6 Damage evolution of the notched tensile sample

At global strain of 1.7% (with the localised strain at the defect free and the indent defect micro-surfaces of 140% and 40% respectively), a high volume fraction of micropores with spherical morphology (size~1-3 μ m, Figure 8.18b), were observed in the mid-section of the notched tensile sample due to the high stress triaxiality (Peng, et al., 2019) of the region. Regions where the heavily deformed α phase intercepts the shear deformation bands (yellow dotted rectangle) produce tracks with minimised thickness, which could also promote micro crack propagation. This narrow zone of deformation bands act as critical point where localised fracture strains are highest. Micro-cracks initiating and propagating along phase boundaries and slip bands are observed in Ti-6Al-4V during in-situ tensile deformation (Zhang, et al., 2018). These micro pores act as nucleation sites for crack growth and coalescence resulting in damage, reminiscent of ductile fracture (Samei, et al., 2019); (Pineau, et al., 2016). At optimum values of the acting shear stress, the micro-cracks nucleated at the root of the notch are propagated along the interface with the through thickness-cracks oriented at 45⁰ to the tensile axis, Figure 8.18a. The global damage mechanism is ductile fracture. Assessment of the notch edge crack surface showed zones with a high volume fraction of fine dimple texture with accompanying long tearing ridges and the presence of micro voids, which are synonymous with a ductile fracture mechanism during plastic deformation, Figure 8.18c. The nucleation, growth and coalescence of the micro voids results in part failure.

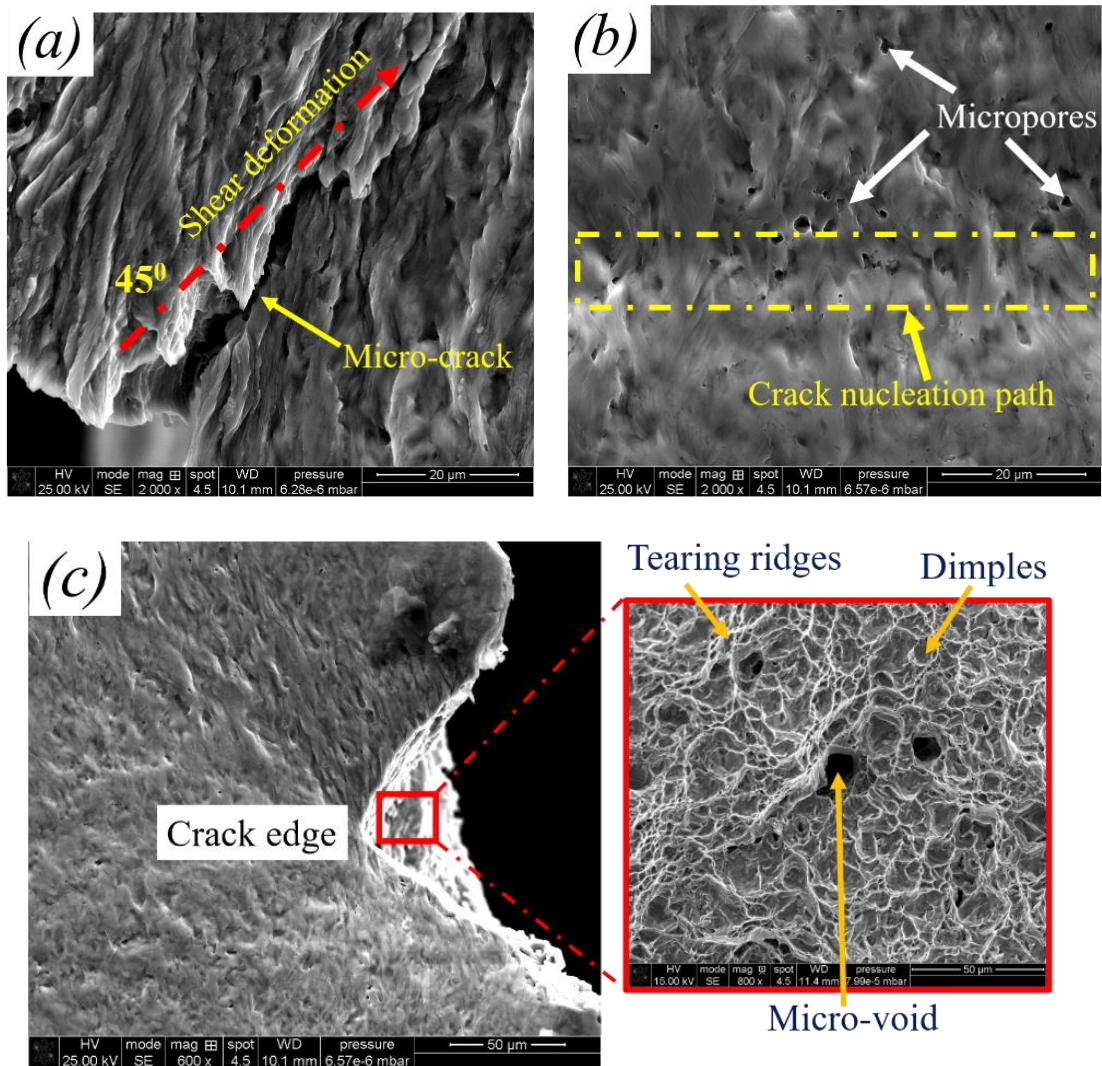


Figure 8. 18 Damage nucleation after 1.7% global strain

(a) microcrack at notch root, (b) micropore nucleation (c) fracture surface

Upon reflecting on the results obtained after the ex-situ tensile test, it became apparent that the software utilised during the DIC analysis wasn't quite able to resolve the slip lines and the shear angles during the strain computation process. Comparison of the software performance on other aerospace materials under the same testing as well as in-situ conditions could be conducted in future works. Also, the approach did not take into account the impact of stress triaxiality on the magnitude of the fracture strain evolution, considering the influence of notch radius on stress triaxiality (Peng, et al., 2019).

8.5 Summary

Post-manufacturing induced surface defects in the form of grooves, scratches and indents are sometimes inadvertently instituted onto sheet metal surfaces during either sheet metal handling, transportation or storage. For forming operations with uncompromising requirements on the integrity of supplied sheets, such defective sheets may be rejected. However, the actual influence of such post-processing induced surface defects on the forming capability of sheet metals have not been extensively investigated. Considering the high notch sensitivity of titanium, there is the need to understand the impact of the post-processing induced sheet surface defects on the room temperature forming performance on titanium. The research identified that;

For the influence of the micro- surface conditions (1.25mm sheet thickness);

- The sharp edges of the indent defects act as zones of high stress concentration. During the deformation process, the emergent localisation of deformation led to the formation of bands which accumulated at the sharp defect edges resulting in reduced localised fracture strain values. For a defect free micro surface, the absence of artificial (defect) zones acting as high stress concentration site means strain aggregation at critical defect sites is minimised and the α phase is able to accommodate the deformation reasonably well.
- For a global strain of 1.7%, the defect free micro-surface exhibited higher localised fracture strain values (140%) compared to the indent defect micro-surface (40%). The reduced fracture strain at the indent defect micro-surface was mainly as a result of the actions of the indent defect in their role as stress raisers.

For the influence of the longitudinal scratches on the sheet bendability (1.6mm sheet thickness);

- The press brake forming trials conducted on the coupons with defect free surface exhibited 100% forming success rate after V-bending with both punch nose radii. For longitudinal scratches oriented along the sheet rolling direction, scratch profiles with depth in the ranges of $-1\mu\text{m}$ to $-18\mu\text{m}$ and pile up height between $1\mu\text{m}$ to $16\mu\text{m}$ can be successfully formed under room temperature conditions. Also, scratch defects with the depth ranges of $-18\mu\text{m}$ to $-35\mu\text{m}$ and a pile up height between $16\mu\text{m}$ to $35\mu\text{m}$ could be formed to an appreciable extent with the probability of failure almost half the prior dimensions. However, scratch profile dimensions beyond the stated threshold values

resulted in formed part failure and may be rejected for use in press brake forming operations.

- The punch nose radius has a significant impact on the bendability of the sheet metal. Thus, the dimensioning of the tool geometry influences the bending capability as well as the sheet surface defect sensitivity of the material.
- Failure during the press brake forming trials occurred primarily at the longitudinal scratch defect zone in their role as stress raisers.

Chapter 9

Conclusions, recommendations and contributions to knowledge

9.1 Main conclusions

For the impact of machining induced edge surface defects on the hole flanging capability of titanium sheets;

- The EDM machined edges exhibited higher edge forming capability compared to AWJ and laser fabricated edges. EDM machining could therefore be adopted industrially as the preferred unconventional machining technique for preparing titanium sheet edges for hole flanging operations as opposed to either laser or AWJ machining.
- Machining induced edge surface defects influence the edge forming capability of titanium sheets in their role as stress raisers. The quality of the machined edge surface finishes are a function of the machining parameters and are responsive to the edge forming performance of the materials.
- The extent of sheet thinning and the dome height evolution attained during HET are major indicators of the hole edge flangeability of sheet metals.
- HET with a Nakajima punch offers the appropriate strains which could be used to evaluate the edge forming limit diagrams of sheet metals. The approach proposed could be implemented industrially as a technical guide during machining method and material selection processes for hole flanging operation.
- The Erichsen index number showed a high linear correlation with the HER values. The Erichsen index number of materials could provide a viable indication of the edge forming performance of sheet metals since they are derived from biaxial stretching which offers an avenue to assess the material ductility in all sheet orientations. The Erichsen index number could therefore be used to correlate the HER of sheet metals.

For the impact of post- processing induced surface defects on the room temperature formability of Ti-3Al-2.5V;

- Surface defects observed on the titanium sheet surfaces like scratches and indents influence their forming capabilities at room temperature in their role as stress raisers.

- For the micro-sheet conditions, the indent defects present on the titanium sheet altered the material plastic flow. The indent defect influenced the emergent deformation bands evolution and their role in the damage nucleation process during the uniaxial tensile loading.
- For sheets with thickness 1.6mm adopted in press brake forming operation, surface defects such as longitudinal scratch with characteristic profile parameters below depth ranges of $-18\mu\text{m}$ to $-35\mu\text{m}$ and a pile up height between $16\mu\text{m}$ to $35\mu\text{m}$ threshold values could be adopted for a successful forming operation. Sheet metals with scratch characteristic profile parameters beyond the stated thresholds values could be rejected.

9.2 Recommendations and future works

In view of the various observations made in this EngD research, the following additional studies could be undertaken to further advance the understanding of the impact of sheet conditions on the room temperature forming capability of titanium alloys;

- i. Investigate the influence of different laser machining parameters on the edge forming performance of titanium alloys.
- ii. Deploy finite element models capable of reproducing the sort of edge surface texture and morphology obtained after laser, EDM and AWJ machining which could be inculcated into material and fracture models to predict the HER values of titanium alloys.
- iii. Considering the high distribution of scratch defects on the supplied sheets, it could be instructive to conduct an in-situ test to understand the nature of the localised strain evolution at the scratch defect site and compare results with those observed at the indent defect sites and defect free micro-surfaces.
- iv. The statistical linear regression model expression proposed for predicting the HER of titanium alloys in this EngD research could be tested on different materials and machining methods. The proposed regression model expression could also be improved by inculcating the HER data for other titanium alloys with edges prepared with different machining methods in order to enhance its robustness.

- v. Conduct HET on titanium sheets for edges prepared with conventional machining methods (e.g. milling, piercing, punching, etc.) and compare the material edge forming performances to those with edges prepared with non-conventional machining methods (e.g. laser, EDM, AWJ, etc.).

9.3 Contributions to knowledge and industrial relevance

The usefulness and the industrial relevance of the proposed predictive linear regression model expression includes;

- *Economic viability*: The high predictability of the proposed regression model expression meant that the cost of machining materials, operator time and equipment time could be saved.
- *Convenient approach for calibration*: Most numerical models rely on heavy data set to provide appreciable levels of accuracy and predictability. The robustness of the proposed regression model expression was evident in its capability to calibrate as low as 5 data points for the onward generation of the appropriate regression model equations and the prediction of HER values.
- *Large data predictability*: The R scripts written and executed in this EngD research were built to accommodate large volumes of data for implementation ‘in one go’, thereby saving model execution time.
- *Material saving*: Generally, the size of the test samples employed in Erichsen cupping test are relatively small compared to most HET samples. In addition, less effort is put into material preparation for Erichsen cupping test as opposed to HET, which relies heavily on the pre-fabrication and the integrity of holes as the integral part. The cost incurred in procuring extra materials could therefore be saved.

Other contributions to knowledge derived from this EngD research includes;

- i. Provided information on the effect of sheet machining parameters on titanium hole edge flangeability. The research also provided data on the threshold values of scratch characteristic profiles which could be deemed acceptable for press brake forming operation. These information will be vital when clarifying requirements of supplied titanium sheet conditions for cold forming operations.

- ii. Titanium sheets prepared with EDM machining produces a higher edge forming performance compared to either AWJ or laser machined edges. The EDM machining method is proposed for preparing titanium sheet edges for hole flanging operation in an industrial setting. This contributes towards the fundamental understanding of titanium edge forming behaviour at room temperature under various manufacturing conditions.
- iii. The approach proposed to evaluate the edge FLD based on the traditional FLD if adopted industrially could assist in decision making during material and machining method selection processes for hole flanging operation.
- iv. The EngD research offered an experimental database, which could be linked to computer simulations for statistical, sensitivity analysis and material model formulation of the forming behaviour of titanium alloys by taking into account the defect factor. This could be instrumental towards optimising the cold forming regime of titanium sheets.
- v. The GOM Atos measurement technique proposed could be adopted as a viable supplementary characterisation technique for assessing the hole edge forming performance of sheet metals. This approach is particularly useful for cases where the hole edges become fully flanged with no edge cracks after the test termination. The GOM Atos method has an edge over current approaches which rely on edge crack emergence to determine the edge forming performance of sheet metals.

Specific areas, which are worth noting for the ex-situ studies on the influence of the supplied sheet micro surface conditions on titanium room temperature formability includes;

- i. *Main contribution to the field:* This research offered an experimental approach for computing the magnitude of local strain evolution at sheet defect sites at micro scale and ascertaining their influence on local microstructure response. This technique is critical towards the appreciation of the micro-level plasticity mechanisms.
- ii. *Novelty in theory and experimental techniques:* Studies pointed at comprehending the influence of post-processing induced surface defects in the form of indents on the in-plane strain changes at micro level during plastic deformation have not been previously researched. Hence, examining the strain field evolution at the micro-level will help in offering crucial information on the link between the material microstructure and the potential effect of surface defects under various straining conditions.

- iii. *Industrial relevance*: quantitative assessment of the localised strain evolution at micro-level for sheets with post-processing surface defects will offer crucial mechanistic understanding of the deformation parameters. The information obtained will be helpful for purposes of material selection for sheet metal forming where the surface integrity of sheets are of high significance, the generation of critical forming parameters for plasticity model validation and the formulation of roadmap for assessing the origin of failure in engineering components.

9.4 Project challenges and limitations

Even though this EngD project was not initially tailored at ascertaining the titanium sheet metal machinability and the effect of machining parameters on the edge surface integrity response, this facet became the main component which linked the material sensitivity to the defects attained thereof. The relationship between the machining parameters, the edge surface finish and the defects obtained as a consequence could have been examined further. Considering the extent of the material formability response to edge surface defects, a rigorous assessment of the impact of the machining parameters on the edge surface finish response would have provided a more exhaustive mechanistic correlation between the machining induced edge surface defects and the edge forming performances of the materials.

Challenges encountered during this project included the limited access to machine time. For instance, the longer machining time required to prepare the finished edge surface quality EDM samples meant that only limited amount of samples could be prepared for testing. The tight scheduling on machines in terms of operator time and machine availability meant that a more rigorous examination of the machining parameters that should have been done wasn't quite achieved. There were also challenges with changing the cutting parameters on machines for the sample preparation. This proved to be a herculean task particularly for the laser fabricated edges where the outsourced companies were reluctant to change the parameters on their machine for the job. Finding companies with laser cutting capability to machine samples with different edge surface finish qualities proved futile.

Furthermore, supplementary material characterisation techniques like residual stress analysis could have provided additional information on the response of the materials to a particular machining process.

References

- Abbassi, F., Pantalé, O., Mistou, S., Zghal, A. & Rakotomalala, R., 2010. Effect of ductile damage evolution in sheet metal forming: experimental and numerical investigations. *Key Engineering Materials*, Volume 446, pp. 157-169. <https://doi.org/10.4028/www.scientific.net/KEM.446.157>.
- Adamczyk, R. D. & Michal, G. M., 1986. Sheared edge extension of high-strength cold-rolled Steels. *Journal of Applied Metalworking*, 4(2), pp. 157-163. <https://doi.org/10.1007/BF02834379>.
- Adamus, J., 2006. Characteristics of shaping Titanium sheets by cold working methods. *International Journal of Applied Mechanics and Engineering*, 11(4), pp. 727-733.
- Adamus, J., 2007. The influence of cutting methods on the cut-surface quality of Titanium sheets. *Key Engineering Materials*, Volume 344, pp. 185-192. <https://doi.org/10.4028/www.scientific.net/KEM.344.185>.
- Ahmetoglu, M., Broek, T. R., Kinzel, G. & Altan, T., 1995. Control of blank holder force to eliminate wrinkling and fracture in deep-drawing rectangular parts. *CIRP Annals*, 44(1), pp. 247-250. [https://doi.org/10.1016/S0007-8506\(07\)62318-X](https://doi.org/10.1016/S0007-8506(07)62318-X).
- Akkurt, A., Kulekci, M. K., Seker, U. & Ercan, F., 2004. Effect of feed rate on surface roughness in abrasive waterjet cutting applications. *Journal of Materials Processing Technology*, 147(3), pp. 389-396. <https://doi.org/10.1016/j.jmatprotec.2004.01.013>.
- Alang, N. A., Razak, N. A. & Miskam, A. K., 2011. Effect of surface roughness on fatigue life of notched carbon steel. *International Journal of Engineering and Technology*, 11(1), pp. 160-163.
- Al-Qureshi, H. A., Klein, A. N. & Fredel, M. C., 2005. Grain size and surface roughness effect on the instability strains in sheet metal stretching. *Journal of Materials Processing Technology*, 170(1-2), pp. 204-210. <https://doi.org/10.1016/j.jmatprotec.2005.04.116>.
- Al-Shawk, A., Lu, P., Vedanti, P. & Wu, X., 2018. Topological Characterization of Machined Edges Prepared by Different Cutting Methods, and Edge Evolution in Tensile Deformation. *IOP Conference Series: Materials Science and Engineering*, Volume 418, pp. 1-7.
- Alsoufi, M. S., Suker, D. K., Alsabban, A. S. & Azam, S., 2016. Experimental study of surface roughness and micro hardness obtained by cutting carbon steel with abrasive waterjet and laser beam technologies. *American Journal of Mechanical Engineering*, 4(5), pp. 173-181. <https://doi.org/10.12691/AJME-4-5-2>.
- Anderson, T. L., 2005. *Fracture mechanics: Fundamentals and applications*. Third ed. Boca Raton: Taylor & Francis Group, LLC.
- Andersson, A., 2009. Evaluation and visualisation of surface defects on auto-body panels. *Journal of Materials Processing Technology*, 209(2), pp. 821-837. <https://doi.org/10.1016/j.jmatprotec.2008.02.078>.

- Antunes, R. A., Salvador, C. A. F. & Lopes de Oliveira, M. C., 2018. Materials selection of optimized Titanium alloys for aircraft applications. *Materials Research*, 21(2), pp. 1-9. <https://doi.org/10.1590/1980-5373-mr-2017-0979>.
- Armendia, M., Garay, A., Iriarte, L. M. & Arrazola, P. J., 2010. Comparison of the machinabilities of Ti-6Al-4V and TIMETAL 54M using uncoated WC-Co tools. *Journal of Materials Processing Technology*, Volume 210, pp. 197-203. <https://doi.org/10.1016/j.jmatprotec.2009.08.026>.
- Arola, D. & Ramulu, M., 1997. Material removal in abrasive waterjet machining of metals surface integrity and texture. *Wear*, 210(1-2), pp. 50-58. [https://doi.org/10.1016/S0043-1648\(97\)00087-2](https://doi.org/10.1016/S0043-1648(97)00087-2).
- Arrazola, P. J., Garay, A., Iriarte, L.-M., Armendia, M., Marya, S. & Le Maître, F., 2009. Machinability of titanium alloys (Ti-6Al-4V and Ti555.3). *Journal of Material Processing Technology*, Volume 209, pp. 2223-2230. <https://doi.org/10.1016/j.jmatprotec.2008.06.020>.
- ASM Metals Handbook, 1996. Fatigue and Fracture: Fatigue and Fracture Properties of Titanium Alloys. *ASM Metals Handbook*, Volume 19, pp. 2121-2190.
- ASM Handbook: Machining, 1989. Machining of Aluminum and Aluminum alloys. *ASM Handbook Committee*, Volume 16, pp. 761-804.
- Attar, H., Calin, M., Zhang, L. C., Scudino, S. & Eckert, J., 2014. Manufacture by selective laser melting and mechanical behavior of commercially pure titanium. *Materials Science and Engineering: A*, Volume 593, pp. 170-177. <https://doi.org/10.1016/j.msea.2013.11.038>.
- Attia, H., Tavakoli, S., Vargas, R. & Thomson, V., 2010. Laser-assisted high-speed finish turning of superalloy Inconel 718 under dry conditions. *CIRP Annals*, 59(1), pp. 83-88. <https://doi.org/10.1016/j.cirp.2010.03.093>.
- Atzema, E., Borsutzki, M., Braun, M., Brockmann, S., Butler, M., Carlsson, B., Larour, P. & Richter, A., 2012. A European round robin test for the hole expansion test according to ISO 16630. Fellbach, Proceedings of international conference: New development in sheet metal forming.
- Atzori, B., Lazzarin, P. & Meneghetti, G., 2003. Fracture mechanics and notch sensitivity. *Fatigue and Fracture of Engineering Materials and Structures*, Volume 26, pp. 257-267. <https://doi.org/10.1046/j.1460-2695.2003.00633.x>.
- AutoForm News, 2015. *Surface Defect Analysis*. [Online] Available at: <https://www.autoform.com/en/news-events/news/surface-defect-analysis/> [Accessed 27 February 2019].
- Ay, M., Caydas, U. & Hascalik, A., 2010. Effect of transverse speed on abrasive waterjet machining of age hardened Inconel 718 Nickel-based superalloy. *Materials and Manufacturing Processes*, 25(10), pp. 1160-1165. <https://doi.org/10.1080/10426914.2010.502953>.
- Badoniya, P., 2018. CO2 Laser Cutting of Different Materials – A Review. *International Research Journal of Engineering and Technology*, 5(6), pp. 2103-2115.

- Badr, O. M., Rolfe, B., Hodgson, P. & Weiss, M., 2015. Forming of high strength Titanium sheet at room temperature. *Materials and Design*, 66(Part B), pp. 618-626. <https://doi.org/10.1016/j.matdes.2014.03.008>.
- Badr, O. M., Rolfe, B. & Weiss, M., 2018. Effect of the forming method on part shape quality in cold roll forming high strength Ti-6Al-4V sheet. *Journal of Manufacturing Processes*, Volume 32, pp. 513-521. <https://doi.org/10.1016/j.jmapro.2018.03.022>.
- Bambach, M., Voswinckel, H. & Hirt, G., 2014. A new process design for performing hole-flanging operations by incremental sheet forming. *Procedia Engineering*, Volume 81, pp. 2305-2310. <https://doi.org/10.1016/j.proeng.2014.10.325>.
- Bathini, U., Srivatsan, T. S., Patnaik, A. & Quick, T., 2010. A study of the tensile deformation and fracture behavior of commercially pure Titanium and Titanium alloy: Influence of orientation and microstructure. *Journal of Materials Engineering and Performance*, 19(8), pp. 1172-1182. <https://doi.org/10.1007/s11665-010-9613-5>.
- Beal, J. D., Boyer, R. & Sanders, D., 2006. Forming of Titanium and Titanium Alloys. In: S. L. Semiatin, ed. *Metalworking: Sheet Forming*. ASM Handbook, Volume 14B: ASM International, pp. 656-669. <https://doi.org/10.31399/asm.hb.v14b.a0005146>.
- Becker, R., 1998. Effects of strain localization on surface roughening during sheet forming. *Acta Materialia*, 46(4), pp. 1385-1401. [https://doi.org/10.1016/S1359-6454\(97\)00182-1](https://doi.org/10.1016/S1359-6454(97)00182-1).
- Begic-Hajdarevic, D., Cekic, A., Mehmedovic, M. & Djelmic, A., 2015. Experimental study on surface roughness in abrasive water jet cutting. *Procedia Engineering*, Volume 100, pp. 394-399. <https://doi.org/10.1016/j.proeng.2015.01.383>.
- Behrens, B. A., Diaz-Infante, D., Altan, T., Yilkeran, D., Wolki, K. & Hubner, S., 2018. Improving hole expansion ratio by parameter adjustment in abrasive water jet operations for DP800. *SAE International Journal of Materials and Manufacturing*, 11(3), pp. 241-252. <https://doi.org/10.4271/05-11-03-0023>.
- Benzerga, A. A., Thomas, N. & Herrington, J., 2019. Plastic flow anisotropy drives shear fracture. *Scientific reports*, 9(1425), pp. 1-9. <https://doi.org/10.1038/s41598-018-38437-y>.
- Blaber, J., Adair, B. & Antoniou, A., 2015. Ncorr: Open-source 2D digital image correlation Matlab software. *Experimental Mechanics*, Volume 55, pp. 1105-1122. <https://doi.org/10.1007/s11340-015-0009-1>.
- Blaber, J., 2017. *Ncorr Version 1.2.2 Instruction Manual*, Georgia: Ncorr.
- Bloomfield, V. A., 2014. *Using R for numerical analysis in science and engineering*. First ed. Boca Raton: CRC Press, Taylor & Francis Group.
- Borrego, M., Morales-Palma, D., Martínez-Donaire, A. J., Centeno, G. & Vallellano, C., 2016. Experimental study of hole-flanging by single-stage incremental sheet forming. *Journal of Materials Processing Technology*, Volume 237, pp. 320-330. <https://doi.org/10.1016/j.jmatprotec.2016.06.026>.

- Boyer, R. R., 1992. New titanium applications on the Boeing 777 airplane. *JOM*, 44(5), pp. 23-25. <https://doi.org/10.1007/BF03223045>.
- Boyer, R. R., 1996. An overview on the use of titanium in the aerospace industry. *Materials Science and Engineering: A*, 213(1-2), pp. 103-114. [https://doi.org/10.1016/0921-5093\(96\)10233-1](https://doi.org/10.1016/0921-5093(96)10233-1)
- Brown, A. M., 2005. A new software for carrying out one-way ANOVA post hoc tests. *Computer Methods and Programs in Biomedicine*, 79(1), pp. 89-95. <https://doi.org/10.1016/j.cmpb.2005.02.007>.
- Bryson, W. E., 2009. *Heat treatment, selection, and application of tool Steels*. Second ed. Cincinnati: Hanser Publications.
- Buehler, 2015. Precision Cutting - The Science of the Cut. *Tech Notes*, 3(6), pp. 1-5.
- Buehler, 2017. Efficient Sample Preparation of Titanium Grade 2. *Tech Notes*, 7(9), pp. 1-2.
- Butcher, C., Anderson, D. & Worswick, M., 2013. Predicting failure during sheared edge stretching using a damage-based model for the shear-affected zone. *SAE International Journal of Materials and Manufacturing*, 6(2), pp. 304-312. <https://doi.org/10.4271/2013-01-1166>.
- Calamaz, M., Coupard, D. & Girot, F., 2008. A new material model for 2D numerical simulation of serrated chip formation when machining titanium alloy Ti-6Al-4V. *International Journal of Machine Tools and Manufacture*, 48(3-4), pp. 275-288. <https://doi.org/10.1016/j.ijmachtools.2007.10.014>.
- Cao, C., Zhang, X., Zha, X. & Dong, C., 2014. Surface integrity of tool steels multi-cut by wire electrical discharge machining. *Procedia Engineering*, Volume 81, pp. 1945-1951. <https://doi.org/10.1016/j.proeng.2014.10.262>.
- Cao, T., Lu, B., Ou, H., Long, H. & Chen, J., 2016. Investigation on a new hole-flanging approach by incremental sheet forming through a featured tool. *International Journal of Machine Tools & Manufacture*, Volume 110, pp. 1-17. <https://doi.org/10.1016/j.ijmachtools.2016.08.003>.
- Cattin, P., 1980. Estimation of the predictive power of a regression model. *Journal of Applied Psychology*, 65(4), pp. 407-414. <https://doi.org/10.1037/0021-9010.65.4.407>.
- Caydas, U. & Hascalik, A., 2008. A study on surface roughness in abrasive waterjet machining process using artificial neural networks and regression analysis method. *Journal of Materials Processing Technology*, 202(1-3), pp. 574-582. <https://doi.org/10.1016/j.jmatprotec.2007.10.024>.
- Centeno, G., Silva, M. B., Cristino, V. A. M., Vallellano, C. & Martins, P. A. F., 2012. Hole-flanging by incremental sheet forming. *International Journal of Machine Tools and Manufacture*, Volume 59, pp. 46-54. <https://doi.org/10.1016/j.ijmachtools.2012.03.007>.
- Chao, J., Zhou, G., Leu, M. C. & Geskin, E., 1995. Characteristics of abrasive water jet generated surfaces and effects of cutting parameters and structure vibration. *Transactions of*

ASME: *Journal of Manufacturing Science and Engineering*, 117(4), pp. 516-525. <https://doi.org/10.1115/1.2803529>.

Che-Haron, C. H. & Jawaid, A., 2005. The effect of machining on surface integrity of Titanium alloy Ti-6%Al-4%V. *Journal of Materials Processing Technology*, 166(2), pp. 188-192. <https://doi.org/10.1016/j.jmatprotec.2004.08.012>.

Chen, F. K. & Chiu, K. H., 2005. Stamping formability of pure Titanium sheets. *Journal of Materials Processing Technology*, 170(1-2), pp. 181-186. <https://doi.org/10.1016/j.jmatprotec.2005.05.004>.

Chen, F. L. & Siores, E., 2003. The effect of cutting jet vibration on surface striation formation in abrasive water jet cutting. *Journal of Materials Processing Technology*, 135(1), pp. 1-5. [https://doi.org/10.1016/S0924-0136\(01\)00579-9](https://doi.org/10.1016/S0924-0136(01)00579-9).

Chen, F. L., Wang, J., Lemma, E. & Siores, E., 2003. The mechanism of surface striation formation in abrasive waterjet machining. *Journal of Materials Processing Technology*, 141(2), pp. 213-218. [https://doi.org/10.1016/S0924-0136\(02\)01120-2](https://doi.org/10.1016/S0924-0136(02)01120-2).

Chen, S. L., Yan, B. H. & Huang, F. Y., 1999. Influence of kerosene and distilled water as dielectrics on the electric discharge machining characteristics of Ti-6Al-4V. *Journal of Materials Processing Technology*, 87(1-3), pp. 107-111. [https://doi.org/10.1016/S0924-0136\(98\)00340-9](https://doi.org/10.1016/S0924-0136(98)00340-9).

Chen, X., McKune, P. & Prince, D., 2003. *Automotive applications of stretch flange high strength Steel*, Warrendale: SAE Technical Paper. <https://doi.org/10.4271/2003-01-0690>.

Chen, X., Jiang, H., Cui, Z., Lian, C. & Lu, C., 2014. Hole expansion characteristics of ultra-high strength Steels. *Procedia Engineering*, Volume 81, pp. 718-723. <https://doi.org/10.1016/j.proeng.2014.10.066>.

Chow, C. L. & Jie, M., 2004. Forming limits of Al 6022 sheets with material damage consideration—theory and experimental validation. *International Journal of Mechanical Sciences*, 46(1), pp. 99-122. <https://doi.org/10.1016/j.ijmecsci.2004.02.003>.

Chuahan, S. R. & Dass, K., 2012. Optimisation of machining parameters in turning of titanium (Grade 5) alloy using response surface methodology. *Materials and Manufacturing Processes*, 27(5), pp. 531-537. <https://doi.org/10.1080/10426914.2011.593236>.

Chung, K., Ma, N., Park, T., Kim, D., Yoo, D. & Kim, C., 2011. A modified damage model for advanced high strength steel sheets. *International Journal of Plasticity*, 27(10), pp. 1485-1511. <https://doi.org/10.1016/j.ijplas.2011.01.007>.

Churi, N. J., Pei, Z. J. & Treadwell, C., 2007. Rotary ultrasonic machining of Titanium alloy (Ti-6Al-4V): Effects of tool variables. *International Journal of Precision Technology*, 1(1), pp. 85-96. <https://doi.org/10.1504/IJPTECH.2007.015347>.

Claves, S. R. & Deal, A., 2005. Orientation dependence of EBSD pattern quality. *Microscopy and Microanalysis*, 11(S02), pp. 514-515. <https://doi.org/10.1017/S1431927605507347>.

- Colafemina, J. P., Jasinevicius, R. G. & Duduch, J. G., 2007. Surface integrity of ultra precision diamond turned Ti (commercially pure) and Ti alloy (Ti-6Al-4V). *Proc.IMEchE Part B: Journal of Engineering Manufacture*, Volume 221, pp. 999-1006. <https://doi.org/10.1243/09544054JEM798>.
- Cui, Z. & Gao, L., 2010. Studies on hole-flanging process using multistage incremental forming. *CIRP Journal of Manufacturing Science and Technology*, 2(2), pp. 124-128. <https://doi.org/10.1016/j.cirpj.2010.02.001>.
- Cusanelli, G., Hessler-Wyser, A., Bobard, F., Demellayer, R., Perez, R. & Flükigera, R., 2004. Microstructure at submicron scale of the white layer produced by EDM technique. *Journal of Materials Processing Technology*, 149(1-3), pp. 289-295. <https://doi.org/10.1016/j.jmatprotec.2003.11.047>.
- Datsko, J. & Yang, C. T., 1960. Correlation of bendability of materials with their tensile properties. *Transactions of the ASME: Journal of Engineering for Industry*, 82(4), pp. 309-313. <https://doi.org/10.1115/1.3664236>.
- Dieter, G. E., 1961. *Mechanical Metallurgy: Metallurgy and Metallurgical Engineering Series*. First ed. New York: McGraw-Hill book company, Inc.
- Dixit, P. M. & Dixit, U. S., 2008. *Modeling of Metal Forming and Machining Processes by Finite Element and Soft Computing Methods*. 1st ed. London: Springer.
- Dixit, U. S., Joshi, S. N. & Davim, J. P., 2011. Incorporation of material behavior in modeling of metal forming and machining processes: A review. *Materials & Design*, 32(7), pp. 3655-3670. <https://doi.org/10.1016/j.matdes.2011.03.049>.
- Donachie, M. J., 1988. *Titanium: A technical guide*. Ohio: ASM International, Metals Park, OH 44073.
- Dong, Y. L. & Pan, B., 2017. A review of speckle pattern fabrication and assessment for digital image correlation. *Experimental Mechanics*, Volume 57, pp. 1161-1181. <https://doi.org/10.1007/s11340-017-0283-1>.
- Dubey, A. K. & Yadava, V., 2008. Laser beam machining: a review. *International Journal of Machine Tools and Manufacture*, 48(6), pp. 609-628. <https://doi.org/10.1016/j.ijmachtools.2007.10.017>.
- Dunne, F. P. E., Rugg, D. & Walker, A., 2007. Lengthscale-dependent, elastically anisotropic, physically-based hcp crystal plasticity: Application to cold-dwell fatigue in Ti alloys. *International Journal of Plasticity*, 23(6), pp. 1061-1083. <https://doi.org/10.1016/j.iplas.2006.10.013>.
- Dykeman, J., Malcolm, S., Yan, B., Chintamani, J., Huang, G., Ramiseti, N. & Zhu, H., 2011. *Characterization of edge fracture in various types of advanced high strength Steel*, East Chicago: SAE technical paper series. <https://doi.org/10.4271/2011-01-1058>.

- Ekmekci, B., Elkoca, O., Tekkaya, A. & Erden, A., 2005. Residual stress state and hardness depth in electric discharge machining: Deionized water as dielectric liquid. *Machining Science and Technology*, 9(1), pp. 39-61. <https://doi.org/10.1081/MST-200051244>.
- Ekmekci, B., 2009. White layer composition, heat treatment and crack formation in electric discharge machining process. *Metallurgical and Materials Transaction B*, 40(1), pp. 70-81. <https://doi.org/10.1007/s11663-008-9220-0>.
- Ellis, D. L., 2007. *Effects of long term thermal exposure on chemically pure (CP) Titanium grade 2 room temperature tensile properties and microstructure*. NASA Glenn Research Center; Cleveland, OH, United States, Patent No. NASA/TM-2007-214968, E-16121.
- El-Hofy, H., 2014. *Fundamentals of machining processes: Conventional and nonconventional processes*. Second ed. Boca Raton: CRC Press: Taylor & Francis.
- Ezugwe, E. O., Bonney, J. & Yamane, Y., 2003. An overview of the machinability of aeroengine alloys. *Journal of Materials Processing Technology*, Volume 143, pp. 233-253. [https://doi.org/10.1016/S0924-0136\(02\)01042-7](https://doi.org/10.1016/S0924-0136(02)01042-7).
- Ezugwu, E. O. & Wang, Z. M., 1997. Titanium alloys and their machinability-A review. *Journal of Materials Processing Technology*, 68(3), pp. 262-274. [https://doi.org/10.1016/S0924-0136\(96\)00030-1](https://doi.org/10.1016/S0924-0136(96)00030-1).
- Fang, X., Ralph, B., Evans, P. & Underhill, R., 2003. The relationships between tensile properties and hole expansion property of C-Mn Steels. *Journal of Materials Science*, Volume 38, pp. 3877-3882. <https://doi.org/10.1023/A:1025913123832>.
- Farnaz, N., Rajurkar, K. P., Malshe, A. P. & Cao, J., 2013. Wire Electro-Discharge machining of Titanium alloy. *Procedia CIRP*, Volume 5, pp. 13-18. <https://doi.org/10.1016/j.procir.2013.01.003>.
- Fukuda, M., Yamaguchi, K., Takakura, N. & Sakano, Y., 1974. Roughening phenomenon on free surface of products in sheet metal forming. *Journal of the Japan Society for Technology of Plasticity*, Volume 15, p. 994.
- Fukui, Y. & Nakanishi, K., 1988. Effects of sheet thickness on the in-plane stretch forming limit in an Aluminum sheet. *JSME international journal. Ser. 1, Solid Mechanics, Strength of Materials*, 31(4), pp. 679-685. https://doi.org/10.1299/jsmea1988.31.4_679.
- Gadelmawla, E. S., Koura, M. M., Maksoud, T. M. A., Elewa, I. M. & Soliman, H. H., 2002. Roughness parameter. *Journal of Material Processing Technology*, Volume 123, pp. 133-145. [https://doi.org/10.1016/S0924-0136\(02\)00060-2](https://doi.org/10.1016/S0924-0136(02)00060-2).
- Geiger, M. & Vollertsen, F., 1993. The Mechanisms of Laser Forming. *CIRP Annals*, 42(1), pp. 301-304. [https://doi.org/10.1016/S0007-8506\(07\)62448-2](https://doi.org/10.1016/S0007-8506(07)62448-2).
- George Dieter, J. R. E., 1961. *Mechanical Metallurgy, Metallurgy and Metallurgical Engineering Series*. First ed. New York: McGraw-Hill book company, Inc.

- Ghadbeigi, H., Pinna, C., Celotto, S. & Yates, J. R., 2010. Local plastic strain evolution in a high strength dual-phase Steel. *Materials Science and Engineering: A*, 527(18-19), pp. 5026-5032. <https://doi.org/10.1016/j.msea.2010.04.052>.
- Ghadbeigi, H., Pinna, C. & Celotto, S., 2012. Quantitative strain analysis of the large deformation at the scale of microstructure: comparison between digital image correlation and microgrid techniques. *Experimental Mechanics*, Volume 52, pp. 1483-1492. <https://doi.org/10.1007/s11340-012-9612-6>.
- Ghanem, F., Braham, C. & Sidhom, H., 2003. Influence of steel type on electrical discharge machined surface integrity. *Journal of Materials Processing Technology*, 142(1), pp. 163-173. [https://doi.org/10.1016/S0924-0136\(03\)00572-7](https://doi.org/10.1016/S0924-0136(03)00572-7).
- Ghanem, F., Sidhom, H., Braham, C. & Fitzpatrick, M. E., 2002. Effect of near surface residual stress and microstructure modification from machining on the fatigue endurance of a tool steel. *Journal of Materials Engineering and Performance*, 11(6), pp. 631-639. <https://doi.org/10.1361/105994902770343629>.
- Ghany, K. A. & Newishy, M., 2005. Cutting of 1.2 mm thick austenitic stainless steel sheet using pulsed and CW Nd:YAG laser. *Journal of Materials Processing Technology*, 168(3), pp. 438-447. <https://doi.org/10.1016/j.jmatprotec.2005.02.251>.
- Gläsner, T., Schneider, M., Troitzsch, M. & Westhäuser, S., 2016. Considering the edge-crack sensitivity of a hot-rolled steel in forming simulation. *IOP Conference Series: Materials Science and Engineering*, 159(1), pp. 1-17.
- Greger, M., Mašek, V. & Snášel, V., 2011. *Mechanical properties of commercially pure Titanium grade 2 after severe plastic deformation*. Brno, Metal 2011.
- Gurao, N. P., Kapoor, R. & Suwas, S., 2011. Deformation behaviour of commercially pure titanium at extreme strain rates. *Acta Materialia*, 59(9), pp. 3431-3446. <https://doi.org/10.1016/j.actamat.2011.02.018>.
- Guu, Y. H., 2005. AFM surface imaging of AISI D2 tool steel machined by the EDM process. *Applied Surface Science*, Volume 242, pp. 245-250. <https://doi.org/10.1016/j.apsusc.2004.08.028>.
- Guu, Y. H. & Hocheng, H., 2001. Effects of workpiece rotation on machinability during electrical discharge machining. *Materials and Manufacturing Processes*, 16(1), pp. 91-101. <https://doi.org/10.1081/AMP-100103699>.
- Guu, Y. H., Hocheng, H., Chou, C. Y. & Deng, C. S., 2003. Effect of electrical discharge machining on surface characteristics and machining damage of AISI D2 tool steel. *Materials Science and Engineering A*, Volume 358, pp. 37-43. [https://doi.org/10.1016/S0921-5093\(03\)00272-7](https://doi.org/10.1016/S0921-5093(03)00272-7).
- Guu, Y. H. & Hou, M. T. K., 2007. Effect of machining parameters on surface textures in EDM of Fe-Mn-Al alloy. *Materials Science and Engineering A*, Volume 466, pp. 61-67. <https://doi.org/10.1016/j.msea.2007.02.035>.

- Harada, Y. & Ueyama, M., 2015. Multi-stage cold deep drawing of pure titanium square cup. *Key Engineering Materials*, Volume 651-653, pp. 1072-1077. <https://doi.org/10.4028/www.scientific.net/KEM.651-653.1072>.
- Harel, O., 2009. The estimation of R^2 and adjusted R^2 in incomplete data sets using multiple imputation. *Journal of Applied Statistics*, 36(10), pp. 1109-1118. <https://doi.org/10.1080/02664760802553000>.
- Hascalik, A. & Caydas, U., 2007. A comparative study of surface integrity of Ti-6Al-4V alloy machined by EDM and AECG. *Journal of Materials Processing Technology*, 190(1-3), pp. 173-180. <https://doi.org/10.1016/j.jmatprotec.2007.02.048>.
- Hascalik, A. & Caydas, U., 2007. Electrical discharge machining of titanium alloy (Ti-6Al-4V). *Applied Surface Science*, 253(22), pp. 9007-9016. <https://doi.org/10.1016/j.apsusc.2007.05.031>.
- Hascalik, A., Caydas, U. & Gurun, H., 2007. Effect of transverse speed on abrasive waterjet machining of Ti-6Al-4V alloy. *Materials and Design*, 28(6), pp. 1953-1957. <https://doi.org/10.1016/j.matdes.2006.04.020>.
- Hasegawa, K., Kawamura, K., Urabe, T. & Hosoya, Y., 2004. Effects of microstructure on stretch- flange- formability of 980MPa grade cold- rolled ultra high strength steel sheets. *ISIJ International*, 44(3), pp. 603-609. <https://doi.org/10.2355/isijinternational.44.603>.
- Hashemi, A., Mashhadi, M., Bakhshi-Jooybari, M. & Gorji, A., 2012. Study of the effect of material properties and sheet thickness on formability of conical parts in hydro-mechanical deep drawing assisted by radial pressure. *Advanced Materials Research*, Volume 445, pp. 149-154. <https://doi.org/10.4028/www.scientific.net/AMR.445.149>.
- Hashish, M., 1984. A modeling study of metal cutting with abrasive waterjets. *Trans of ASME: Journal of Engineering Materials and Technology*, 106(1), pp. 88-100. <https://doi.org/10.1115/1.3225682>.
- Hashish, M., 1991. Characteristics of Surfaces Machined With Abrasive-Waterjets. *Transactions of the ASME: Journal of Engineering Materials and Technology*, 113(3), pp. 354-362. <https://doi.org/10.1115/1.2903418>.
- Hayashi, H. & Nakagawa, T., 1994. Recent trends in sheet metals and their formability in manufacturing automotive panels. *Journal of Materials Processing Technology*, 46(3-4), pp. 455-487. [https://doi.org/10.1016/0924-0136\(94\)90128-7](https://doi.org/10.1016/0924-0136(94)90128-7).
- Hiroi, T. & Nishimura, H., 1997. The influence of surface defects on the forming-limit diagram of sheet metal. *Journal of Materials Processing Technology*, 72(1), pp. 102-109. [https://doi.org/10.1016/S0924-0136\(97\)00136-2](https://doi.org/10.1016/S0924-0136(97)00136-2).
- Hu, X. H., Sun, X. & Golovashchenko, S. F., 2016. An integrated finite element-based simulation framework: From hole piercing to hole expansion. *Finite Elements in Analysis and Design*, Volume 109, pp. 1-13. <https://doi.org/10.1016/j.finel.2015.09.005>.

- Huang, J. Y., Ponce, F. A., Caldas, P. G., Prioli, R. & Almeida, M. C., 2013. The effect of nanoscratching direction on the plastic deformation and surface morphology of InP crystals. *Journal of Applied Physics*, 114(203503), pp. 1-9. <https://doi.org/10.1063/1.4833237>.
- Hussain, G., Al-Ghamdi, K. A., Khalatbari, H., Iqbal, A. & Hashemipour, M., 2014. Forming parameters and forming defects in incremental forming process: Part B. *Materials and Manufacturing Processes*, 29(4), pp. 454-460. <https://doi.org/10.1080/10426914.2014.880457>.
- Hussain, G., Gao, L. & Hayat, N., 2011. Forming parameters and forming defects in incremental forming of an Aluminium sheet: Correlation, empirical modelling and optimization: Part A. *Materials and Manufacturing Processes*, 26(12), p. 1546–1553. <https://doi.org/10.1080/10426914.2011.552017>.
- Hussain, G., Gao, L. & Zhang, Z. Y., 2008. Formability evaluation of a pure titanium sheet in the cold incremental forming process. *The International Journal of Advanced Manufacturing Technology*, 37(9-10), pp. 920-926. <https://doi.org/10.1007/s00170-007-1043-7>.
- Hyun, D. I., Oak, S. M., Kang, S. S. & Moon, Y. H., 2002. Estimation of hole flangeability for high strength Steel plates. *Journal of Materials Processing Technology*, Volume 130-131, pp. 9-13. [https://doi.org/10.1016/S0924-0136\(02\)00793-8](https://doi.org/10.1016/S0924-0136(02)00793-8).
- InfiniteFocus, 2017. *Optical 3D surface metrology*, Graz: Alicona G4-21-050704.
- Jäger, A., Gärtnerova, V. & Tesař, K., 2015. Microstructure and anisotropy of the mechanical properties in commercially pure titanium after equal channel angular pressing with back pressure at room temperature. *Materials Science and Engineering: A*, Volume 644, pp. 114-120. <https://doi.org/10.1016/j.msea.2015.07.038>.
- Jain, M., Lloyd, D. J. & MacEwen, S. R., 1996. Hardening laws, surface roughness and biaxial tensile limit strains of sheet aluminium alloys. *International Journal of Mechanical Sciences*, 38(2), pp. 219-232. [https://doi.org/10.1016/0020-7403\(95\)00038-Y](https://doi.org/10.1016/0020-7403(95)00038-Y).
- Jin, H. & Bruck, H. A., 2005. A new method for characterizing nonlinearity in scanning probe microscopes using digital image correlation. *Nanotechnology*, 16(9), pp. 1849-1855.
- Jones, W. R., 1996. *Vacuum heat treating for M2 high speed and D2 tool Steels*. Cincinnati, Proceedings of 16th ASM heat treating society conference and exposition.
- Jones, O., Maillardet, R. & Robinson, A., 2014. *Introduction to scientific programming and simulation using R*. Second ed. Boca Raton: CRC Press, Taylor & Francis Group.
- Jurendić, S. & Gaiani, S., 2013. Numerical Simulation of Cold Forming of α -Titanium Alloy Sheets. *Strojniški Vestnik - Journal of Mechanical Engineering*, 59(3), pp. 148-155. <https://doi.org/10.5545/sv-jme.2012.415>.
- Kacem, A., Krichen, A., Manach, P. Y., Thuillier, S. & Yoon, Y. W., 2013. Failure prediction in the hole-flanging process of Aluminium alloys. *Engineering Fracture Mechanics*, Volume 99, pp. 251-265. <https://doi.org/10.1016/j.engfracmech.2012.12.018>.

- Kacher, J., Landon, C., Adams, B. L. & Fullwood, D., 2009. Bragg's law diffraction simulations for electron backscatter diffraction analysis. *Ultramicroscopy*, 109(9), pp. 1148-1156. <https://doi.org/10.1016/j.ultramic.2009.04.007>.
- Kaebnick, H., Jeromin, A. & Mathew, P., 1998. Adaptive control for laser cutting using striation frequency analysis. *CIRP Annals*, 47(1), pp. 137-140. [https://doi.org/10.1016/S0007-8506\(07\)62802-9](https://doi.org/10.1016/S0007-8506(07)62802-9).
- Kai, C. & Lawrence, Y. Y., 1999. Striation formation and melt removal in the laser cutting process. *Journal of Manufacturing Processes*, 1(1), pp. 43-53. [https://doi.org/10.1016/S0278-6125\(99\)80025-9](https://doi.org/10.1016/S0278-6125(99)80025-9).
- Kang, J., Jain, M., Wilkinson, D. S. & Embury, J. D., 2005. Microscopic strain mapping using scanning electron microscopy topography image correlation at large strain. *The Journal of Strain Analysis for Engineering Design*, 40(6), pp. 559-570. <https://doi.org/10.1243/030932405X16151>.
- Kang, J., Ososkov, Y., Embury, J. D. & Wilkinson, D. S., 2007. Digital image correlation studies for microscopic strain distribution and damage in dual phase Steels. *Scripta Materialia*, 56(11), pp. 999-1002. <https://doi.org/10.1016/j.scriptamat.2007.01.031>.
- Kapp, M., Hebesberger, T. & Kolednik, O., 2011. A micro-level strain analysis of a high-strength dual-phase Steel. *International Journal of Materials Research*, 102(6), pp. 687-691. <https://doi.org/10.3139/146.110522>.
- Karellova, A., Kremaszky, C., Werner, E., Tsipouridis, P., Hebesberger, T. & Pichler, A., 2009. Hole Expansion of dual-phase and complex-phase AHS Steels - Effect of edge conditions. *Materials Technology*, 80(1), pp. 71-77. <https://doi.org/10.2374/SRI08SP110>.
- Keskin, Y., Halkaci, H. S. & Kizil, M., 2006. An experimental study for determination of the effects of machining parameters on surface roughness in electric discharge machining (EDM). *The International Journal of Advanced Manufacturing Technology*, 28(11), pp. 1118-1121. <https://doi.org/10.1007/s00170-004-2478-8>.
- Kim, B. J., Choi, K. H., Park, K. S., van Tyne, C. J. & Moon, Y. H., 2007. Effect of the surface defects on hydroformability of Aluminium alloys. *Key Engineering Materials*, Volume 340-341, pp. 587-592. <https://doi.org/10.4028/www.scientific.net/KEM.340-341.587>.
- Kim, B. -C., Kim, T.-H., Jang, Y. & Chung, K.-H., 2001. Investigation of striation formation in thin Stainless Steel tube during pulsed Nd:YAG laser cutting process by numerical simulation. *Metallurgical and Materials Transaction A*, Volume 32A, pp. 2623-2632. <https://doi.org/10.1007/s11661-001-0052-7>.
- Kim, Y. & Son, Y., 2000. Study on wrinkling limit diagram of anisotropic sheet metals. *Journal of Materials Processing Technology*, 97(1-3), pp. 88-94. [https://doi.org/10.1016/S0924-0136\(99\)00346-5](https://doi.org/10.1016/S0924-0136(99)00346-5).

- Kim, J. H., Kwon, Y. J., Lee, T., Lee, K. -A., Kim, H. S. & Lee, C. S., 2018. Prediction of hole expansion ratio for various steel sheets based on uniaxial tensile properties. *Metals and Materials International*, Volume 24, p. 187–194. <https://doi.org/10.1007/s12540-017-7288-2>.
- Kiyak, M. & Cakir, O., 2007. Examination of machining parameters on surface roughness in EDM of tool steel. *Journal of Materials Processing Technology*, Volume 191, pp. 141-144. <https://doi.org/10.1016/j.jmatprotec.2007.03.008>.
- Komanduri, R., 1982. Some clarifications on the mechanics of chip formation when machining Titanium alloys. *Wear*, 76(1), pp. 15-34. [https://doi.org/10.1016/0043-1648\(82\)90113-2](https://doi.org/10.1016/0043-1648(82)90113-2).
- Konieczny, A. & Henderson, T., 2007. *On formability limitations in stamping involving sheared edge stretching*, Warrendale: SAE technical paper series.
- Kotkunde, N., Krishnamurthy, H. N., Puranik, P., Gupta, A. K. & Singh, S. K., 2014. Microstructure study and constitutive modeling of Ti–6Al–4V alloy at elevated temperatures. *Materials & Design (1980-2015)*, Volume 54, pp. 96-103. <https://doi.org/10.1016/j.matdes.2013.08.006>.
- Kotkunde, N., Krishnamurthy, H. N., Singh, S. K. & Jella, G., 2018. Experimental and numerical investigations on hot deformation behavior and processing maps for ASS 304 and ASS 316. *High Temperature Materials and Processes*, 37(9-10), pp. 873-888. <https://doi.org/10.1515/http-2017-0047>.
- Krahmer, D. M., Polvorosa, R., López de Lacalle, L. N., Alonso-Pinillos, U., Abate, G. & Riu, F., 2016. Alternatives for specimen manufacturing in tensile testing of Steel plates. *Experimental Techniques*, Volume 40, pp. 1555-1565. <https://doi.org/10.1007/s40799-016-0134-5>.
- Krieger-Lassen, N. C., Juul-Jensen, D. & Conradsen, K., 1992. Image processing procedures for analysis of electron back scattering patterns. *Scanning Microscopy*, 6(1), pp. 115-121.
- Krajcarz, D., 2014. Comparison of metal water jet cutting with laser and plasma cutting. *Procedia Engineering*, Volume 69, pp. 838-843. <https://doi.org/10.1016/j.proeng.2014.03.061>.
- Krempaszky, C., Larour, P., Freudenthaler, J. & Werner, E., 2014. *Towards more efficient hole expansion testing*. Paris, IDDRG Conference Proceedings - Innovations for the sheet metal industry.
- Kumar, A., Kumar, V. & Kumar, J., 2013. Investigation of machining parameters and surface integrity in wire electric discharge machining of pure titanium. *Journal of Engineering Manufacture*, 227(7), pp. 972-992. <https://doi.org/10.1177/0954405413479791>.
- Kumar, A., Kumar, V. & Kumar, J., 2016. Investigation of micro-cracks susceptibility on machined pure Titanium surface in WEDM process. *Journal for Manufacturing Science and Production*, 16(2), pp. 123-139. <https://doi.org/10.1515/jmsp-2016-0013>.
- Kumar, S., Singh, R., Singh, T. P. & Sethi, B. L., 2009. Surface modification by electrical discharge machining: A review. *Journal of Materials Processing Technology*, 209(8), pp. 3675-3687. <https://doi.org/10.1016/j.jmatprotec.2008.09.032>.

- Kumar De, S., Deva, A., Mukhopadhyay, S. & Kumar Jha, B., 2011. Assessment of formability of hot-rolled Steel through determination of hole-expansion ratio. *Materials and Manufacturing Processes*, 26(1), pp. 37-42. <https://doi.org/10.1080/10426914.2010.531240>.
- Kurra, S. & Regalla, S. P., 2014. Experimental and numerical studies on formability of extra-deep drawing steel in incremental sheet metal forming. *Journal of Materials Research and Technology*, 3(2), pp. 158-171. <https://doi.org/10.1016/j.jmrt.2014.03.009>.
- Lagattu, F., Bridier, F., Villechaise, P. & Brillaud, J., 2006. In-plane strain measurements on a microscopic scale by coupling digital image correlation and an in situ SEM technique. *Materials Characterization*, 56(1), pp. 10-18. <https://doi.org/10.1016/j.matchar.2005.08.004>.
- Larour, P., Freudenthaler, J., Grünsteidl, A. & Wang, K., 2014. *Evaluation of alternative stretch flangeability testing methods to ISO 16630 standard*. Paris, IDDRG Conference Proceedings - Innovations for the sheet metal industry.
- Larour, P., Schauer, H., Lackner, J. & Till, E. T., 2016. *Edge crack Simulation with the modular "smiley" forming tool*. Linz, IDDRG 2016 International Conference.
- Lee, E. H., Mallett, R. L. & Yang, W. H., 1977. Stress and deformation analysis of the metal extrusion process. *Computer Methods in Applied Mechanics and Engineering*, 10(3), pp. 339-353. [https://doi.org/10.1016/0045-7825\(77\)90077-9](https://doi.org/10.1016/0045-7825(77)90077-9).
- Lee, H. -T., Hsu, F. -C. & Tai, T.-Y., 2004. Study of surface integrity of using the small area EDM process with copper-tungsten electrode. *Material Science and Engineering A*, Volume 364, pp. 346-356. <https://doi.org/10.1016/j.msea.2003.08.046>.
- Lee, H. T. & Yur, J. P., 2000. Characteristic analysis of EDMed surfaces using the Taguchi approach. *Materials and Manufacturing Processes*, 15(6), pp. 781-806. <https://doi.org/10.1080/10426910008913021>.
- Lee, S. H. & Li, X., 2003. Study of the surface integrity of the machined workpiece in the EDM of tungsten carbide. *Journal of Materials Processing Technology*, 139(1-3), pp. 315-321. [https://doi.org/10.1016/S0924-0136\(03\)00547-8](https://doi.org/10.1016/S0924-0136(03)00547-8).
- Lee, S. H. & Li, X. P., 2001. Study of the effect of machining parameters on the machining characteristics in electric discharge machining of tungsten carbide. *Journal of Materials Processing Technology*, Volume 115, pp. 334-358. [https://doi.org/10.1016/S0924-0136\(01\)00992-X](https://doi.org/10.1016/S0924-0136(01)00992-X).
- Lee, H. T. & Tai, T. Y., 2003. Relationship between EDM parameters and surface crack formation. *Journal of Materials Processing Technology*, 142(3), pp. 676-683. [https://doi.org/10.1016/S0924-0136\(03\)00688-5](https://doi.org/10.1016/S0924-0136(03)00688-5).
- Leskovar, P. & Grum, J., 1986. The metallurgical aspects of machining. *CIRP Annals*, 35(2), pp. 537-550. [https://doi.org/10.1016/S0007-8506\(07\)60199-2](https://doi.org/10.1016/S0007-8506(07)60199-2).
- Leu, D. K., 1996. Finite-element simulation of hole-flanging process of circular sheets of anisotropic materials. *International Journal of Mechanical Sciences*, 38(8-9), pp. 917-933. [https://doi.org/10.1016/0020-7403\(95\)00090-9](https://doi.org/10.1016/0020-7403(95)00090-9).

- Levaillant, C. & Chenot, J. L., 1992. Physical modelling and numerical prediction of defects in sheet metal forming. *Journal of Materials Processing Technology*, 32(1-2), pp. 383-397. [https://doi.org/10.1016/0924-0136\(92\)90195-X](https://doi.org/10.1016/0924-0136(92)90195-X).
- Lin, Y. C., Yan, B. H. & Chang, Y. S., 2000. Machining characteristics of titanium alloy (Ti-6Al-4V) using a combination process of EDM with USM. *Journal of Materials Processing Technology*, Volume 104, pp. 171-177. [https://doi.org/10.1016/S0924-0136\(00\)00539-2](https://doi.org/10.1016/S0924-0136(00)00539-2).
- Lin, Y. C., Yan, B. H. & Huang, F. Y., 2001. Surface improvement using a combination of electric discharge machining with ball burnish machining based on the Taguchi method. *The International Journal of Advanced Manufacturing Technology*, 18(9), pp. 673-682.
- Lin Prakash, P. S., Rajak, B., Panda, S. K., Roy, G. G., Jha, M. N. & Mascarenhas, M., 2017. Mechanical properties and stretch forming behaviour of electron beam welded Titanium sheets of Grade-2 and Grade-5. *Materials Today: Proceedings*, Volume 4, pp. 908-916. <https://doi.org/10.1016/j.matpr.2017.01.102>.
- Liu, Z., Liu, S., Li, Y. & Meehan, P. A., 2014. Modeling and optimization of surface roughness in incremental sheet forming using a multi-objective function. *Materials and Manufacturing Processes*, 29(7), p. 808–818. <https://doi.org/10.1080/10426914.2013.864405>.
- Li, Y., Liu, Z., Daniel, W. J. T. B. & Meehan, P. A., 2014. Simulation and experimental observations of effect of different contact interfaces on the incremental sheet forming process. *Materials and Manufacturing Processes*, 29(2), pp. 121–128. <https://doi.org/10.1080/10426914.2013.822977>.
- Li, H., Boehlert, C. J., Bieler, T. R. & Crimp, M. A., 2014. Analysis of the deformation behavior in tension and tension-creep of Ti-3Al-2.5V (wt pct) at 296 K and 728 K (23 °C and 455 °C) using in situ SEM experiments. *Metallurgical and Materials Transactions A*, 45A(13), pp. 6053-6066. <https://doi.org/10.1007/s11661-014-2576-7>.
- Li, N., Zhao, H., Jin, M., Li, J., Dai, X., Huo, Z., Wang, S, Yang, L. & Sun, X., 2017. Influence of scratch type on tensile strength in in situ tensile test. *Advances in Mechanical Engineering*, 9(6), pp. 1-8. <https://doi.org/10.1177/1687814017707130>.
- Lohade, D. M. & Chopade, P. B., 2016. *Metal inspection for surface defect detection by image thresholding*. Pune, International Journal of Electrical, Electronics and Computer Systems.
- Lou, Y., Yoon, J. W. & Huh, H., 2014. Modeling of shear ductile fracture considering a changeable cut-off value for stress triaxiality. *International Journal of Plasticity*, Volume 54, pp. 56-80. <https://doi.org/10.1016/j.ijplas.2013.08.006>.
- Määttä, A., Järvenpää, A., Jaskari, M. & Mäntyjärvi, K., 2012. Influence of predetermined surface defect to the bendability of ultra-high-strength Steel. *Key Engineering Materials*, Volume 504-506, pp. 901-906. <https://doi.org/10.4028/www.scientific.net/KEM.504-506.901>.
- Marciniak, Z., Duncan, J. L. & Hu, S. J., 2002. *Mechanics of sheet metal forming*. 2nd ed. Oxford: Butterworth-Heinemann.

- Marciniak, Z. & Kuczyński, K., 1967. Limit strains in the processes of stretch-forming sheet metal. *International Journal of Mechanical Sciences*, 9(9), pp. 609-612. [https://doi.org/10.1016/0020-7403\(67\)90066-5](https://doi.org/10.1016/0020-7403(67)90066-5).
- Matloff, N., 2011. *The art of R programming; A tour of statistical software design*. First ed. San Francisco: William Pollock.
- Maurice, C. & Fortunier, R., 2008. A 3D Hough transform for indexing EBSD and Kossel patterns. *Journal of Microscopy*, 230(Part 3), pp. 520-529. <https://doi.org/10.1111/j.1365-2818.2008.02045.x>.
- McCarron, T. J., Kain, K. E., Hahn, G. T. & Flanagan, W. F., 1988. Effect of geometrical defects in forming sheet steel by biaxial stretching. *Metallurgical Transactions A*, 19(8), p. 2067–2074. <https://doi.org/10.1007/BF02645209>.
- Mendricky, R., 2016. Determination of measurement accuracy of optical 3D scanners. *MM Science Journal*, pp. 1565-1572. https://doi.org/10.17973/MMSJ.2016_12_2016183.
- Merdan, M. A. E. R. & Arnell, R. D., 1989. Surface integrity of a die steel after electrodischarge machining: structure, composition and hardness. *Surface Engineering*, 5(2), pp. 158-164. <https://doi.org/10.1179/sur.1989.5.2.158>.
- Meurling, F., Melander, A., Linder, J. & Larsson, M., 2001. The influence of mechanical and laser cutting on the fatigue strengths of carbon and stainless sheet steels. *Scandinavian Journal of Metallurgy*, Volume 30, pp. 309-319. <https://doi.org/10.1034/j.1600-0692.2001.300506.x>.
- Meyer, P. & Waas, A. M., 2015. Measurement of in situ-full-field strain maps on ceramic matrix composites at elevated temperature using digital image correlation. *Experimental Mechanics*, Volume 55, pp. 795-802. <https://doi.org/10.1007/s11340-014-9979-7>.
- Miraoui, I., Boujelbene, M. & Bayraktar, 2014. Analysis of roughness and heat affected zone of steel plates obtained by laser cutting. *Advanced Material Research*, Volume 974, pp. 169-173. <https://doi.org/10.4028/www.scientific.net/AMR.974.169>.
- Miraoui, I., Boujelbene, M. & Bayraktar, E., 2013. Effects of laser cutting main parameters on microhardness and microstructure changes of Stainless Steel. *Advanced Materials Research*, Volume 664, pp. 811-816. <https://doi.org/10.4028/www.scientific.net/AMR.664.811>.
- Miraoui, I., Boujelbene, M. & Zaied, M., 2016. High-power laser cutting of Steel plates: Heat affected zone analysis. *Advances in Materials Science and Engineering*, Volume 2016, pp. 1-8. <https://doi.org/10.1155/2016/1242565>.
- Mišičko, R., Kvačkaj, T., Vlado, M., Gulová, L., Lupták, M. & Bidulská, J., 2009. Defects Simulations of Rolling Strip. *Materials Engineering*, 16(3), pp. 7-12.
- Monno, M. & Ravasio, C., 2005. The effect of cutting head vibrations on the surfaces generated by waterjet cutting. *International Journal of Machine Tools and Manufacture*, 45(3), pp. 335-363. <https://doi.org/10.1016/j.ijmachtools.2004.07.010>.

- Montanari, L., Cristino, V. A., Silva, M. B. & Martins, P. A. F., 2013. A new approach for deformation history of material elements in hole-flanging produced by single point incremental forming. *The International Journal of Advanced Manufacturing Technology*, 69(5-8), pp. 1175-1183. <https://doi.org/10.1007/s00170-013-5117-4>.
- Mori, K. I., Abe, Y. & Suzui, Y., 2010. Improvement of stretch flangeability of ultra high strength steel sheet by smoothing of sheared edge. *Journal of Materials Processing Technology*, 210(4), pp. 653-659. <https://doi.org/10.1016/j.jmatprotec.2009.11.014>.
- MTD CNC, 2020. *Is Optical Measurement of surface finish the best option?*. [Online] Available at: <https://mtdcnc.com/news/mtdcnc/is-optical-measurement-of-surface-finish-the-best-option> [Accessed 24 10 2020].
- Muderrisoglu, A., Murata, M., Ahmetoglu, M. A., Kinzel, G. & Altan, T., 1996. Bending, flanging, and hemming of Aluminum sheet-an experimental study. *Journal of Materials Processing Technology*, 59(1-2), pp. 10-17. [https://doi.org/10.1016/0924-0136\(96\)02281-9](https://doi.org/10.1016/0924-0136(96)02281-9).
- Murakami, S., Ozaki, K., Ono, K. & Itsumi, Y., 2011. Effect of alloying elements on machinability and hot workability of α - β Titanium alloy containing Fe and C. *Kobelco Technology Review*, Volume 30, pp. 13-18.
- Nagasaka, A., Kubota, Y., Sugimoto, K.-i., Mio, A., Hojo, T., Makii, K., Kawajiri, M. & Kitayama, M., 2010. Effect of YAG Laser cutting on stretch-flangeability of ultra high strength TRIP sheet Steel with Bainitic Ferrite matrix. *ISIJ International*, 50(10), pp. 1441-1446. <https://doi.org/10.2355/isijinternational.50.1441>.
- Nasiri-Abarbekoh, H., Ekrami, A. & Ziaei-Moayyed, A. A., 2012. Impact of phase transformation on mechanical properties anisotropy of commercially pure titanium. *Materials and Design*, Volume 37, pp. 223-227. <https://doi.org/10.1016/j.matdes.2011.12.040>.
- Nasiri-Abarbekoh, H., Ekrami, A., Ziaei-Moayyed, A. A. & Shohani, M., 2012. Effects of rolling reduction on mechanical properties anisotropy of commercially pure titanium. *Materials and Design*, Volume 34, pp. 268-274. <https://doi.org/10.1016/j.matdes.2011.06.024>.
- Nasiri-Abarbekoh, H., Ekrami, A. & Ziaei-Moayyed, A. A., 2013. Effects of thickness and texture on mechanical properties anisotropy of commercially pure titanium thin sheets. *Materials & Design*, Volume 44, pp. 528-534. <https://doi.org/10.1016/j.matdes.2012.08.046>.
- Neimeyer, R., Smith, R. N. & Kaminski, D. A., 1993. Effects of operating parameters on surface quality for laser cutting of Mild Steel. *Journal of Engineering for Industry: Technical Brief*, 115(3), pp. 359-362. <https://doi.org/10.1115/1.2901673>.
- Nouari, M. & Makich, H., 2013. Experimental investigation on the effect of the material microstructure on tool wear when machining hard titanium alloys: Ti-6Al-4V and Ti-555. *International Journal of Refractory Metals and Hard Materials*, Volume 41, pp. 259-269. <https://doi.org/10.1016/j.ijrmhm.2013.04.011>.
- Obermeyer, E. J. & Majlessi, S. A., 1998. A review of recent advances in the application of blank-holder force towards improving the forming limits of sheet metal parts. *Journal of*

Materials Processing Technology, 75(1-3), pp. 222-234. [https://doi.org/10.1016/S0924-0136\(97\)00368-3](https://doi.org/10.1016/S0924-0136(97)00368-3).

Ogawa, K., 2007. Temperature and strain rate effects on plastic deformation of Titanium alloys. *Materials Science Forum*, Volume 539-543, pp. 3619-3624. <https://doi.org/10.4028/www.scientific.net/MSF.539-543.3619>.

Ogórek, A. & Stachowicz, F., 2005. Determination of forming limits of thin aluminium sheets. *Scientific Bulletin Series C: Fascicle Mechanics, Tribology, Machine Manufacturing Technology; Baia Mare*, Volume 19, pp. 1-6.

Orbanic, H. & Junkar, M., 2008. Analysis of striation formation mechanism in abrasive water jet cutting. *Wear*, 265(5-6), pp. 821-830. <https://doi.org/10.1016/j.wear.2008.01.018>.

Osakada, K. & Oyane, M., 1971. On the roughening of free surface in deformation processes. *Bulletin of JSME*, 14(68), pp. 171-177. <https://doi.org/10.1299/jsme1958.14.171>.

Palmer, P. B. & O'Connell, D., 2009. Regression analysis for prediction: Understanding the process. *Cardiopulmonary Physical Therapy Journal*, 20(3), pp. 23-26.

Pan, B., 2009. Reliability-guided digital image correlation for image deformation measurement. *Applied Optics*, 48(8), pp. 1535-1542. <https://doi.org/10.1364/AO.48.001535>.

Pan, B., Qian, K., Xie, H. & Asundi, A., 2009. Two-dimensional digital image correlation for in-plane displacement and strain measurement: a review. *Measurement Science and Technology*, 20(6), pp. 1-17.

Pan, B., Xie, H., Guo, Z. & Hua, T., 2007. Full-field strain measurement using a two dimensional Savitzky-Golay digital differentiator in digital image correlation. *Optical Engineering*, 46(3), pp. 1-10. <https://doi.org/10.1117/1.2714926>.

Park, S., Jung, J., Kim, S., Seo, S.- J., Lee, M. -G. & Han, H. N., 2018. Prediction of fracture behaviour in hole expansion test using microstructure based dual-scale model. *Journal of Physics: Conference Series*, Volume 1063, pp. 1-6.

Pathak, N., Butcher, C. & Worswick, M., 2016. Assessment of the critical parameters influencing the edge stretchability of advanced high-strength Steel sheet. *Journal of Materials Engineering and Performance*, 25(11), pp. 4919-4932. <https://doi.org/10.1007/s11665-016-2316-9>.

Paul, S. K., Mukherjee, M., Kundu, S. & Chandra, S., 2014. Prediction of hole expansion ratio for automotive grade Steels. *Computational Materials Science*, Volume 89, pp. 189-197. <https://doi.org/10.1016/j.commatsci.2014.03.040>.

Paulsen, C. O., Fagerholt, E., Børvik, T. & Westermann, I., 2019. Comparing In situ DIC results from an etched surface with a gold speckled surface. *Metals*, 9(8), pp. 1-23. <https://doi.org/10.3390/met9080820>.

Peng, R. D., 2015. *Exploratory data analysis with R*. First ed. British Columbia: Lean Publishing.

- Peng, R. D., 2018. *R programming for data science*. First ed. British Columbia: Lean Publishing.
- Peng, J., Wang, Y., Dai, Q., Liu, X., Liu, L. & Zhang, Z., 2019. Effect of stress triaxiality on plastic damage evolution and failure mode for 316L notched specimen. *Metals*, 9(1067), pp. 1-17. <https://doi.org/10.3390/met9101067>.
- Pervaiz, S., Rashid, A., Deiab, I. & Nicolescu, M., 2014. Influence of tool materials on machinability of titanium and nickel based alloys: a review. *Materials and manufacturing processes*, 29(3), pp. 219-252. <https://doi.org/10.1080/10426914.2014.880460>.
- Peters, M., Kumpfert, J., Ward, C. H. & Leyens, C., 2003. Titanium alloys for aerospace applications. *Advanced Engineering Materials*, 5(6), pp. 419-427. <https://doi.org/10.1002/adem.200310095>.
- Pinna, C., Lan, Y., Kiu, M. F., Efthymiadis, P., Lopez-Pedrosa, M. & Farrugia, D., 2015. Assessment of crystal plasticity finite element simulations of the hot deformation of metals from local strain and orientation measurements. *International Journal of Plasticity*, Volume 73, pp. 24-38. <https://doi.org/10.1016/j.ijplas.2015.05.015>.
- Pineau, A., Benzerga, A. A. & Pardoën, T., 2016. Failure of metals I: brittle and ductile fracture. *Acta Materialia*, Volume 107, pp. 424-483. <https://doi.org/10.1016/j.actamat.2015.12.034>.
- Pramanik, A. & Littlefair, G., 2015. Machining of titanium alloy (Ti-6Al-4V): Theory to application. *Machining Science and Technology*, 19(1), pp. 1-49. <https://doi.org/10.1080/10910344.2014.991031>.
- Qamar, S. Z., Arif, A. F. M. & Sheikh, A. K., 2004. Analysis of product defects in a typical Aluminum extrusion facility. *Materials and Manufacturing Processes*, 19(3), pp. 391-405. <https://doi.org/10.1081/AMP-120038650>.
- Radovanovic, M. & Dašić, P., 2006. Research on surface roughness by laser cut. *The Annals of University Dunarea de Jos of Galati Fascicle VIII, Tribology*, Volume 12, p. 84-88.
- Ragab, A. R. & Ch Saleh, A., 2005. Evaluation of bendability of sheet metals using void coalescence models. *Materials Science and Engineering: A*, 395(1-2), pp. 102-109. <https://doi.org/10.1016/j.msea.2004.12.011>.
- Raghavan, K. S. & Garrison-Jr, W. M., 2010. An investigation of the relative effects of thickness and strength on the formability of steel sheet. *Materials Science and Engineering: A*, 527(21-22), pp. 5565-5574. <https://doi.org/10.1016/j.msea.2010.05.004>.
- Rajaram, N., Sheikh-Ahmad, J. & Cheraghi, S. H., 2003. CO₂ laser cut quality of 4130 Steel. *International Journal of Machine Tools and Manufacture*, 43(4), pp. 351-358. [https://doi.org/10.1016/S0890-6955\(02\)00270-5](https://doi.org/10.1016/S0890-6955(02)00270-5).
- Ramesh, S., Karunamoorthy, L. & Palanikumar, K., 2008. Fuzzy modelling and analysis of machining parameters in machining Titanium alloy. *Materials and Manufacturing Processes*, 23(4), pp. 439-447. <https://doi.org/10.1080/10426910801976676>.

- Ramesh, S., Karunamoorthy, L. & Palanikumar, K., 2008. Surface roughness analysis in machining titanium alloy. *Materials and Manufacturing Processes*, 23(2), pp. 174-181. <https://doi.org/10.1080/10426910701774700>.
- Ramulu, M., Kunaporn, S., Arola, D., Hashish, M. & Hopkins, J., 2000. Waterjet machining and peening of metals. *Trans of ASME: Journal of Pressure Vessel Technology*, 122(1), pp. 90-95. <https://doi.org/10.1115/1.556155>.
- Rebeloa, J. C., Diasa, A. M., Kremerb, D. & Lebrunb, J. L., 1998. Influence of EDM pulse energy on the surface integrity of martensitic steels. *Journal of Materials Processing Technology*, 84(1-3), pp. 90-96. [https://doi.org/10.1016/S0924-0136\(98\)00082-X](https://doi.org/10.1016/S0924-0136(98)00082-X).
- Reyes, A., Eriksson, M., Lademo, O. -G., Hopperstad, O. S. & Langseth, M., 2009. Assessment of yield and fracture criteria using shear and bending tests. *Materials and Design*, Volume 30, pp. 596-608. <https://doi.org/10.1016/j.matdes.2008.05.045>.
- Roberts, G., Krauss, G. & Kennedy, R., 1998. *Tool Steels*. Fifth ed. Cleveland: ASM International.
- Rosenberg, H. W., 1983. Ti-15-3: A new cold-formable sheet Titanium alloy. *Journal of Metals*, 35(11), pp. 30-34. <https://doi.org/10.1007/BF03339165>.
- Sally, A. L., 2019. *Applied statistical inference with MINITAB®*. Second ed. Boca Raton: CRC Press, Taylor & Francis Group.
- Samei, J., Zhou, L., Kang, J. & Wilkinson, D. S., 2019. Microstructural analysis of ductility and fracture in fine-grained and ultrafine-grained vanadium-added DP1300 Steels. *International Journal of Plasticity*, Volume 117, pp. 58-70. <https://doi.org/10.1016/j.iplas.2017.12.009>.
- Sánchez-Arévalo, F. M. & Pulos, G., 2008. Use of digital image correlation to determine the mechanical behavior of materials. *Materials Characterization*, 59(11), pp. 1572-1579. <https://doi.org/10.1016/j.matchar.2008.02.002>.
- Sárosi, Z., Knapp, W., Kunz, A. & Wegener, K., 2010. *Detection of surface defects on sheet metal parts by using one-shot deflectometry in the infrared range*. Las Vegas, InfraMation Proceedings.
- Schneider, M., Geffert, A., Peshekhodov, I., Bouguecha, A. & Behrens, B. -A., 2015. Overview and comparison of various test methods to determine formability of a sheet metal cut-edge and approaches to the test results application in forming analysis. *Materials Science and Engineering Technology*, 46(12), pp. 1196-1217. <https://doi.org/10.1002/mawe.201500446>.
- Schneider, M., Peshekhodov, I., Bouguecha, A. & Behrens, B. A., 2016. A new approach for user-independent determination of formability of a steel sheet sheared edge. *Production Engineering*, 10(3), p. 241–252. <https://doi.org/10.1007/s11740-016-0677-4>.
- Schuöcker, D., 1986. Dynamic phenomena in laser cutting and cut quality. *Applied Physics B*, 40(1), pp. 9-14. <https://doi.org/10.1007/BF00697221>.

Schuöcker, D. & Muller, P., 1987. Dynamic Effects In Laser Cutting And Formation Of Periodic Striations. *SPIE Proceedings: High power lasers*, Volume 801, pp. 258-264. <https://doi.org/10.1117/12.941250>.

Şeker, U., Çiftçi, I. & Hasirci, H., 2003. The effect of alloying elements on surface roughness and cutting forces during machining of ductile iron. *Materials & Design*, 24(1), pp. 47-51. [https://doi.org/10.1016/S0261-3069\(02\)00081-X](https://doi.org/10.1016/S0261-3069(02)00081-X).

Semenova, I. P., Salimgareeva, G. Kh., Latysh, V. V., Lowe, T. & Valiev, R. Z., 2009. Enhanced fatigue strength of commercially pure Ti processed by severe plastic deformation. *Materials Science and Engineering: A*, 503(1-2), pp. 92-95. <https://doi.org/10.1016/j.msea.2008.07.075>.

Sergueeva, A. V., Stolyarov, V. V., Valiev, R. Z. & Mukherjee, A. K., 2001. Advanced mechanical properties of pure Titanium with ultrafine grained structure. *Scripta Materialia*, 45(7), pp. 747-752. [https://doi.org/10.1016/S1359-6462\(01\)01089-2](https://doi.org/10.1016/S1359-6462(01)01089-2).

Shanjin, L. & Yang, W., 2006. An investigation of pulsed laser cutting of Titanium alloy sheet. *Optics and Lasers in Engineering*, 44(10), pp. 1067-1077. <https://doi.org/10.1016/j.optlaseng.2005.09.003>.

Shanmugam, D. K., Chen, F. L., Siores, E. & Brandt, M., 2002. Comparative study of jetting machining technologies over laser machining technology for cutting composite materials. *Composite structures*, 57(1-4), pp. 289-296. [https://doi.org/10.1016/S0263-8223\(02\)00096-X](https://doi.org/10.1016/S0263-8223(02)00096-X).

Shi, M. F. & Chen, X., 2007. *Prediction of stretch flangeability limits of advanced high strength Steels using the hole expansion test*, Warrendale: SAE Technical Paper Series. <https://doi.org/10.4271/2007-01-1693>.

Shi, X., Chen, J., Peng, Y. & Ruan, X., 2004. A new approach of die shape optimization for sheet metal forming processes. *Journal of Materials Processing Technology*, 152(1), pp. 35-42. <https://doi.org/10.1016/j.jmatprotec.2004.02.033>.

Silva, M. B., Teixeira, P., Reis, A. & Martins, P. A. F., 2013. On the formability of hole-flanging by incremental sheet forming. *Proceedings of the Institution of Mechanical Engineers, Part L: Journal of Materials Design and Applications*, 227(2), pp. 91-99. <https://doi.org/10.1177/1464420712474210>.

Simbi, D. J. & Scully, J. C., 1996. The effect of residual interstitial elements and iron on mechanical properties of commercially pure Titanium. *Materials Letters*, 26(1-2), pp. 35-39. [https://doi.org/10.1016/0167-577X\(95\)00204-9](https://doi.org/10.1016/0167-577X(95)00204-9).

Siqueira, R. H. M., Carvalho, S. M., Kam, I. K. L., Riva, R. & Lima, M. S. F., 2016. Non-contact sheet forming using lasers applied to a high strength Aluminium alloy. *Journal of Materials Research and Technology*, 5(3), pp. 275-281. <https://doi.org/10.1016/j.jmrt.2016.02.002>.

- Song, H., Wang, Z.-J. & Gao, T.-J., 2007. Effect of high density electropulsing treatment on formability of TC4 Titanium alloy sheet. *Transactions of Nonferrous Metals Society of China*, 17(1), pp. 87-92. [https://doi.org/10.1016/S1003-6326\(07\)60053-3](https://doi.org/10.1016/S1003-6326(07)60053-3).
- Song, H., Wang, Z. J. & He, X. D., 2013. Improving in plasticity of orthorhombic Ti₂AlNb based alloy sheet by high density electropulsing. *Transactions of Nonferrous Metals Society of China*, 23(1), pp. 32-37. [https://doi.org/10.1016/S1003-6326\(13\)62425-5](https://doi.org/10.1016/S1003-6326(13)62425-5).
- Stournaras, A., Stavropoulos, P., Salonitis, K. & Chryssolouris, G., 2009. An investigation of quality in CO₂ laser cutting of Aluminium. *CIRP Journal of Manufacturing Science and Technology*, 2(1), pp. 61-69. <https://doi.org/10.1016/j.cirpj.2009.08.005>.
- Strasky, J., Janeček, M., Harcuba, P., Bukovina, M. & Wagner, L., 2011. The effect of microstructure on fatigue performance of Ti-6Al-4V alloy after EDM surface treatment for applications in orthopaedics. *Journal of the Mechanical Behavior of Biomedical Materials*, 4(8), pp. 1955-1962. <https://doi.org/10.1016/j.jmbbm.2011.06.012>.
- Suraratchai, M., Limido, J., Mabru, C. & Chieragatti, R., 2008. Modelling the influence of machined surface roughness on the fatigue life of aluminium alloy. *International Journal of Fatigue*, 30(12), pp. 2119-2126. <https://doi.org/10.1016/j.ijfatigue.2008.06.003>.
- Suresh, S. & Ritchie, R. O., 1982. A geometric model for fatigue crack closure induced by fracture surface roughness. *Metallurgical Transaction*, 13(9), pp. 1627-1631. <https://doi.org/10.1007/BF02644803>.
- Szacinski, A. M. & Thomson, P. F., 1984. The effect of mechanical properties on the wrinkling behaviour of sheet materials in the Yoshida test. *Journal of Mechanical Working Technology*, 10(1), pp. 87-102. [https://doi.org/10.1016/0378-3804\(84\)90081-0](https://doi.org/10.1016/0378-3804(84)90081-0).
- Szacinski, A. M. & Thomson, P. F., 1991. Comparison of effect of material properties on growth of wrinkles in sheet metal during forming and their removal. *Materials Science and Technology*, 7(3), pp. 224-227. <https://doi.org/10.1179/mst.1991.7.3.224>.
- Tabatchikova, T. I., Tereshchenko, N. A., Yakovleva, I. L. & Gudnev, N. Z., 2017. Effect of abrasive water jet on the structure of the surface layer of Al-Mg alloy. *Physics of Metals and Metallography*, 118(9), pp. 879-889. <https://doi.org/10.1134/S0031918X17090095>.
- Tadros, A. K. & Mellor, P. B., 1978. An experimental study of the in-plane stretching of sheet metal. *International Journal of Mechanical Sciences*, 20(2), pp. 121-133. [https://doi.org/10.1016/0020-7403\(78\)90073-5](https://doi.org/10.1016/0020-7403(78)90073-5).
- Takakura, N., Yamaguchi, K. & Fukuda, M., 1987. Improvement of the Forming Limit of Sheet Metals by Removal of Surface Roughening with Plastic Strain. *JSME International Journal*, 30(270), pp. 2034-2039. <https://doi.org/10.1299/jsme1987.30.2034>.
- Tang, J., 2013. Effects of surface roughness microtopography on formability in cold rolled steel sheet. *Advanced Materials Research*, Volume 690-693, pp. 2232-2235. <https://doi.org/10.4028/www.scientific.net/AMR.690-693.2232>.

- Tao, X., Zhang, D., Ma, W., Liu, X. & Xu, D., 2018. Automatic metallic surface defect detection and recognition with convolutional neural networks. *Applied Sciences*, 1575(8), pp. 1-15. <https://doi.org/10.3390/app8091575>.
- Tasan, C. C., Hoefnagels, J. P. M. & Geers, M. G. D., 2010. Microstructural banding effects clarified through micrographic digital image correlation. *Scripta Materialia*, 62(11), pp. 835-838. <https://doi.org/10.1016/j.scriptamat.2010.02.014>.
- Tekkaya, A. E., 2000. State-of-the-art of simulation of sheet metal forming. *Journal of Materials Processing Technology*, 103(1), pp. 14-22. [https://doi.org/10.1016/S0924-0136\(00\)00413-1](https://doi.org/10.1016/S0924-0136(00)00413-1).
- Thawari, G., Sarin Sundar, J. K., Sundararajan, G. & Joshi, S. V., 2005. Influence of process parameters during pulsed Nd:YAG laser cutting of nickel-base superalloys. *Journal of Materials Processing Technology*, 170(1-2), pp. 229-239. <https://doi.org/10.1016/j.jmatprotec.2005.05.021>.
- Thipprakmas, S., Jin, M. & Murakawa, M., 2007. Study on flanged shapes in fineblanked-hole flanging process (FB-hole flanging process) using finite element method (FEM). *Journal of Materials Processing Technology*, Volume 192-193, pp. 128-133. <https://doi.org/10.1016/j.jmatprotec.2007.04.040>.
- Thomas, D. J., 2009. Characteristics of abrasive water jet cut edges and the effect on formability and fatigue performance of high strength steels. *Journal of Manufacturing Processes*, 11(2), pp. 97-105. <https://doi.org/10.1016/j.jmapro.2009.12.001>.
- Tian, S. & Xu, K., 2017. An algorithm for surface defect identification of Steel plates based on genetic algorithm and extreme learning machine. *Metals*, 7(311), pp. 1-11. <https://doi.org/10.3390/met7080311>.
- Tomita, Y. & Shindo, A., 1988. Onset and growth of wrinkles in thin square plates subjected to diagonal tension. *International Journal of Mechanical Sciences*, 30(12), pp. 921-931. [https://doi.org/10.1016/0020-7403\(88\)90074-4](https://doi.org/10.1016/0020-7403(88)90074-4).
- Tsoupis, I. & Merklein, M., 2016. Edge crack sensitivity of lightweight materials under different load conditions. *IOP Conference Series: Materials Science and Engineering*, Volume 159, pp. 1-8.
- Veiga, C., Davim, J. P. & Loureiro, A. J. R., 2013. Review on machinability of Titanium alloys: the process perspective. *Reviews on Advanced Materials Science*, Volume 34, pp. 148-164.
- Verzani, J., 2014. *Using R for introductory statistics*. Second ed. New York: CRC Press, Taylor & Francis Group.
- Vicanek, M., Simon, G., Urbassek, H. M. & Decker, I., 1987. Hydrodynamical instability of melt flow in laser cutting. *Journal of Physics D: Applied Physics*, 20(1), pp. 140-145.
- Walley, J. L., Wheeler, R., Uchic, M. D. & Mills, M. J., 2012. In-situ mechanical testing for characterizing strain localization during deformation at elevated temperatures. *Experimental Mechanics*, Volume 52, pp. 405-416. <https://doi.org/10.1007/s11340-011-9499-7>.

- Wang, C. -T., Kinzel, G. & Altan, T., 1994. Wrinkling criterion for an anisotropic shell with compound curvatures in sheet forming. *International Journal of Mechanical Sciences*, 36(10), pp. 945-960. [https://doi.org/10.1016/0020-7403\(94\)90056-6](https://doi.org/10.1016/0020-7403(94)90056-6).
- Wang, K., Luo, M. & Wierzbicki, T., 2014. Experiments and modeling of edge fracture for an AHSS sheet. *International Journal of Fracture*, 187(2), pp. 245-268. <https://doi.org/10.1007/s10704-014-9937-5>.
- Wang, N. M. & Wenner, M. L., 1974. An analytical and experimental study of stretch flanging. *International Journal of Mechanical Sciences*, 16(2), pp. 135-143. [https://doi.org/10.1016/0020-7403\(74\)90082-4](https://doi.org/10.1016/0020-7403(74)90082-4).
- Wang, Z. -J., Song, H. & Wang, Z., 2008. Deformation behavior of TC1 titanium alloy sheet under double-sided pressure. *Transactions of Nonferrous Metals Society of China*, 18(1), pp. 72-76. [https://doi.org/10.1016/S1003-6326\(08\)60013-8](https://doi.org/10.1016/S1003-6326(08)60013-8).
- Wang, H., Boehlert, C. J., Wang, Q. D., Yin, D. D. & Ding, W. J., 2016. In-situ analysis of the tensile deformation modes and anisotropy of extruded Mg-10Gd-3Y-0.5Zr (wt.%) at elevated temperatures. *International Journal of Plasticity*, Volume 84, pp. 255-276. <https://doi.org/10.1016/j.ijplas.2016.06.001>.
- Wilby, A. J. & Neale, D. P., 2009. Defects introduced into metals during fabrication and Service. In: A. J. Wilby & D. P. Neale, eds. *Materials Science and Engineering*. Paris: Encyclopedia of Life Support Systems, pp. 48–75.
- Wilson, D. V., Roberts, W. T. & Rodrigues, P. M. B., 1981. Effect of grain anisotropy on limit strains in biaxial stretching: Part I. Influence of sheet thickness and grain size in weakly textured sheets. *Metallurgical Transactions A*, 12(9), p. 1595–1602. <https://doi.org/10.1007/BF02643565>.
- Wu, H. B. & To, S., 2016. Effects of electropulsing treatment on material properties and ultra precision machining of titanium alloy. *The International Journal of Advanced Manufacturing Technology*, 82(9-12), pp. 2029-2036. <https://doi.org/10.1007/s00170-015-7379-5>.
- Xavierarockiaraj, S. & Kuppan, P., 2014. Investigation of Cutting Forces, Surface Roughness and Tool Wear during Laser Assisted Machining of SKD11 Tool Steel. *Procedia Engineering*, Volume 97, pp. 1657-1666. <https://doi.org/10.1016/j.proeng.2014.12.316>.
- Xu, L., Barlat, F., Lee, M. G., Choi, K. S. & Sun, X., 2012. Hole expansion of dual phase Steels. In: W. P. De Wilde, C. A. Brebbia & S. Hernandez, eds. *High Performance Structure and Materials VI*. Southampton: WITpress, pp. 75-83.
- Yagami, T., Manabe, K. & Yamauchi, Y., 2007. Effect of alternating blank holder motion of drawing and wrinkle elimination on deep-drawability. *Journal of Materials Processing Technology*, Volume 187–188, pp. 187-191. <https://doi.org/10.1016/j.jmatprotec.2006.11.180>.
- Yamaguchi, K., Takakura, N. & Imatani, S., 1995. Increase in forming limit of sheet metals by removal of surface roughening with plastic strain (Balanced biaxial stretching of Aluminium

- sheets and foils). *Journal of Materials Processing Technology*, 48(1-4), pp. 27-34. [https://doi.org/10.1016/0924-0136\(94\)01629-F](https://doi.org/10.1016/0924-0136(94)01629-F).
- Yan, B. H., Tsai, H. C. & Huang, F. Y., 2005. The effect of EDM of a dielectric of a urea solution in water on modifying the surface of titanium. *International journal of machine tools and manufacture*, Volume 45, pp. 194-200. <https://doi.org/10.1016/j.ijmachtools.2004.07.006>.
- Yang, X. & Liu, C. R., 1999. Machining Titanium and its alloys. *Machining Science and Technology*, 3(1), pp. 107-139. <https://doi.org/10.1080/10940349908945686>.
- Ye, X., Tse, Z. T. H., Tang, G. & Song, G., 2015. Effect of high energy electropulsing on the phase transition and mechanical properties of two-phase titanium alloy strips. *Advanced Engineering Materials*, 17(7), pp. 995-1007. <https://doi.org/10.1002/adem.201400273>.
- Yi, N., Hama, T., Kobuki, A., Fujimoto, H. & Takuda, H., 2016. Anisotropic deformation behavior under various strain paths in commercially pure titanium Grade 1 and Grade 2 sheets. *Materials Science and Engineering: A*, Volume 655, pp. 70-85. <https://doi.org/10.1016/j.msea.2015.12.081>.
- Yilbaş, B. S., 1996. Experimental investigation into CO₂ laser cutting parameters. *Journal of Materials Processing Technology*, 58(2-3), pp. 323-330. [https://doi.org/10.1016/0924-0136\(95\)02094-2](https://doi.org/10.1016/0924-0136(95)02094-2).
- Yoon, J. I., Jung, J., Lee, H. H., Kim, G.- S. & Kim, H. S., 2016. Factors governing hole expansion ratio of Steel sheets with sheared edge. *Metals and Materials International*, 22(6), pp. 1009-1014. <https://doi.org/10.1007/s12540-016-6346-5>.
- Yu, H., Tieu, K., Lu, C., Lou, Y., Liu, X., Godbole, A. & Kong, C., 2014. Tensile fracture of ultrafine grained aluminum 6061 sheets by asymmetric cryorolling for microforming. *International Journal of Damage Mechanics*, 23(8), pp. 1077-1095. <https://doi.org/10.1177/1056789514538083>.
- Yuri, T., Ono, Y. & Ogata, T., 2003. Effects of surface roughness and notch on fatigue properties for Ti-5Al-2.5Sn ELI alloy at cryogenic temperatures. *Science and Technology of Advanced Materials*, 4(4), pp. 291-299. [https://doi.org/10.1016/S1468-6996\(03\)00058-5](https://doi.org/10.1016/S1468-6996(03)00058-5).
- Zaefferer, S., 2003. Computer-aided crystallographic analysis in the TEM. *Advances in Imaging and Electron Physics*, Volume 125, pp. 355-415. [https://doi.org/10.1016/S1076-5670\(02\)80019-2](https://doi.org/10.1016/S1076-5670(02)80019-2).
- Zeid, O. A. A., 1997. On the effect of electrodischarge machining parameters on the fatigue life of AISI D6 tool steel. *Journal of Materials Processing Technology*, 68(1), pp. 27-32. [https://doi.org/10.1016/S0924-0136\(96\)02523-X](https://doi.org/10.1016/S0924-0136(96)02523-X).
- Zeilmann, R. P., Bordin, F. M. & Vacaro, T., 2015. Surface integrity of electrodischarge machined cavities for different depths and radii. *Journal of the Brazilian Society of Mechanical Sciences and Engineering*, 37(1), pp. 93-104. <https://doi.org/10.1007/s40430-014-0159-6>.

- Zeilmann, R. P., Vacaro, T., Zanotto, F. M. & Czarnobay, M., 2013. Metallurgical alterations in the surface of steel cavities machined by EDM. *Revista Matéria*, 18(4), pp. 1541 – 1548. <http://dx.doi.org/10.1590/S1517-70762013000400014>.
- Zeleňák, M., Valíček, J., Klich, J. & Židková, P., 2012. Comparison of surface roughness quality created by abrasive water jet and CO2 laser beam cutting. *Technicki Vjesnik*, 19(3), pp. 481-485.
- Zhang, X.-H., Tang, B., Zhang, X.-Lu., Kou, H.-C., Li, J.-S. & Zhou, L., 2012. Microstructure and texture of commercially pure Titanium in cold deep drawing. *Transactions of Nonferrous Metals Society of China*, 22(3), pp. 496-502. [https://doi.org/10.1016/S1003-6326\(11\)61204-1](https://doi.org/10.1016/S1003-6326(11)61204-1).
- Zhang, Y., Liu, Y. & Wu, X., 2007. *Fracture behaviour of a dual phase sheet steel in hole expansion test*. Washington, Proceedings of IMECE2007: 2007 ASME International Mechanical Engineering Congress and Exposition. <https://doi.org/10.1115/IMECE2007-42974>.
- Zhang, X., Zhang, S., Zhao, Q., Zhao, Y., Li, R. & Zeng, W., 2018. In-situ observations of the tensile deformation and fracture behavior of a fine-grained Titanium alloy sheet. *Journal of Alloys and Compounds*, Volume 740, pp. 660-668. <https://doi.org/10.1016/j.jallcom.2018.01.009>.
- Zheng, H. & Liu, K., 2015. Machinability of engineering materials. In: Y. C. N. Andrew, ed. *Handbook of Manufacturing Engineering and Technology*. First ed. London: Springer-Verlag, pp. 901-938.
- Zhao, Z., Radovitzky, R. & Cuitiño, A., 2004. A study of surface roughening in FCC metals using direct numerical simulation. *Acta Materialia*, 52(20), pp. 5791-5804. <https://doi.org/10.1016/j.actamat.2004.08.037>.
- Zhao, Z., Ramesh, M., Raabe, D., Cuitiño, A. M. & Radovitzky, R., 2008. Investigation of three-dimensional aspects of grain-scale plastic surface deformation of an Aluminium Oligocrystal. *International Journal of Plasticity*, 24(12), pp. 2278-2297. <https://doi.org/10.1016/j.ijplas.2008.01.002>.
- Zhoa, W. & Guo, C., 2014. Topography and microstructure of the cutting surface machined with abrasive waterjet. *The International Journal of Advanced Manufacturing Technology*, 73(5-8), pp. 941-947. <https://doi.org/10.1007/s00170-014-5869-5>.
- Zhou, W. & Wang, Z. L., 2006. *Scanning microscopy for nanotechnology, techniques and applications*. First ed. New York: Springer Science and Business Media, LLC.

Appendices

Appendix A

A1 Metallurgical surface preparation

Pure titanium Grade 2 is quite soft and relatively ductile hence, sectioning it for metallurgical examinations must be done with optimum care by employing the appropriate cutting tools and coolant to avoid twinning and thermal damage (Buehler, 2017).

The test samples for microstructure investigation were machined out using a Buehler Isomet 5000 linear precision saw machine, Figure A1a. This machine was furnished with a standard 7inch MetAbrase cut-off abrasive wheel suitable for the sectioning of titanium. The sample was firmly held in place with a single saddle chuck prior to the sectioning process. The abrasive wheel was operated at a speed of 4000rpm with the linear feed of the wheel manually controlled into the test sample and retracted post sectioning. The manual control was utilised to quash damage to the sample and the abrasive wheel. Water was used as a coolant during the cutting process.

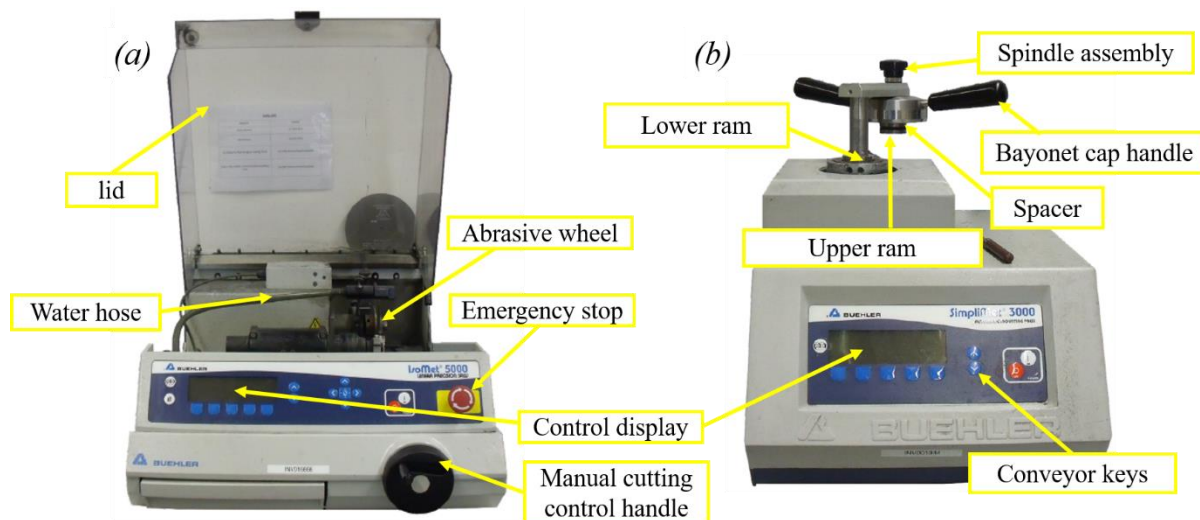


Figure A. 1 Apparatus for sample cutting and mounting for onward metallurgical preparation

(a) Abrasive wheel cutting machine, (b) sample mounting machine

The main functions of the coolant includes; the lubrication of the wheel/sample interface, conveying away the heat generated during sectioning and the carrying away of swarf/chips (Buehler, 2015). The machine was connected to an external recirculation system to ensure high coolant mineral concentration (ppm) and effectiveness during the cutting process. The water quality and coolant concentration have significant impact on the efficiency of the abrasive wheel (Buehler, 2015). During the sectioning process, the water delivery system flooded the

test sample from either sides of the abrasive wheel at a flowrate of 0.7gal/min while tracking the wheel manoeuvre.

A Buehler Simplimet 3000 mounting press machine was used to mount the sectioned samples, Figure A1*b*. The sectioned samples were mounted in an EpoMet compression mounting compound by pressing at a pressure of 29MPa and heating for 1.5minutes before cooling for 6minutes to cure. For each mounting cycle the edge of the mold assembly, the lower and the upper rams were cleaned thoroughly of any residue compound using a scrapper tool and brush. The spindle assembly and the spacer were then adjusted to ensure that they were properly tightened. A release agent was then applied to both the upper and lower rams. Prior to the sample mounting, all burrs were removed and the sample thoroughly cleaned in acetone to ensure that no gaps existed between the sample and the conductive compound. This was done to make certain that all possible spaces which could serve as collection point for contaminants during the sample preparation process were eliminated. The deburred sample was then placed centrally on the lower ram and lowered to about halfway down the mold cylinder. After adding the mounting compound, the lower ram was further lowered. The upper ram was then lowered into the mold cylinder and locked by twisting the bayonet cap handles clockwise to about 45° angle. The mounting cycle was then commenced until the cured mounted sample was produced. The mounted samples in the conductive compound were then readied for onward grinding and polishing.

The grinding and polishing process was done on a Buehler Automet 300 Pro grinder – polisher machine, Figure A2*a*. CP-Ti (Grade 2) is susceptible to deformation during preparation hence, employing aggressive grinding in the bid to reduce preparation time could result in smearing, gross deformation and twinning (Buehler, 2017). For the grinding process, silica-carbide abrasive disc grinding papers with varied grit sizes including; P600, P1200 and P2500 respectively were utilised for each subsequent step to flatten the sample surface. In addition, complementary head rotation mode was adopted for the grinding process with a platen speed of 150rpm, head speed of 60rpm, single force of 25N and a grinding time of 1minute. Sufficient water supply was ensured for cooling and cleaning purposes during the grinding period due to the vulnerability of titanium to local overheating which could result in localised structural changes (Buehler, 2017). For the polishing stage, a 20ml 0.02µm silica (MasterMet 2 non-crystalizing colloidal Silica) was added to a 100ml distilled water to form a colloidal suspension which was used to polish the samples on a 0.02µm polishing Microcloth.

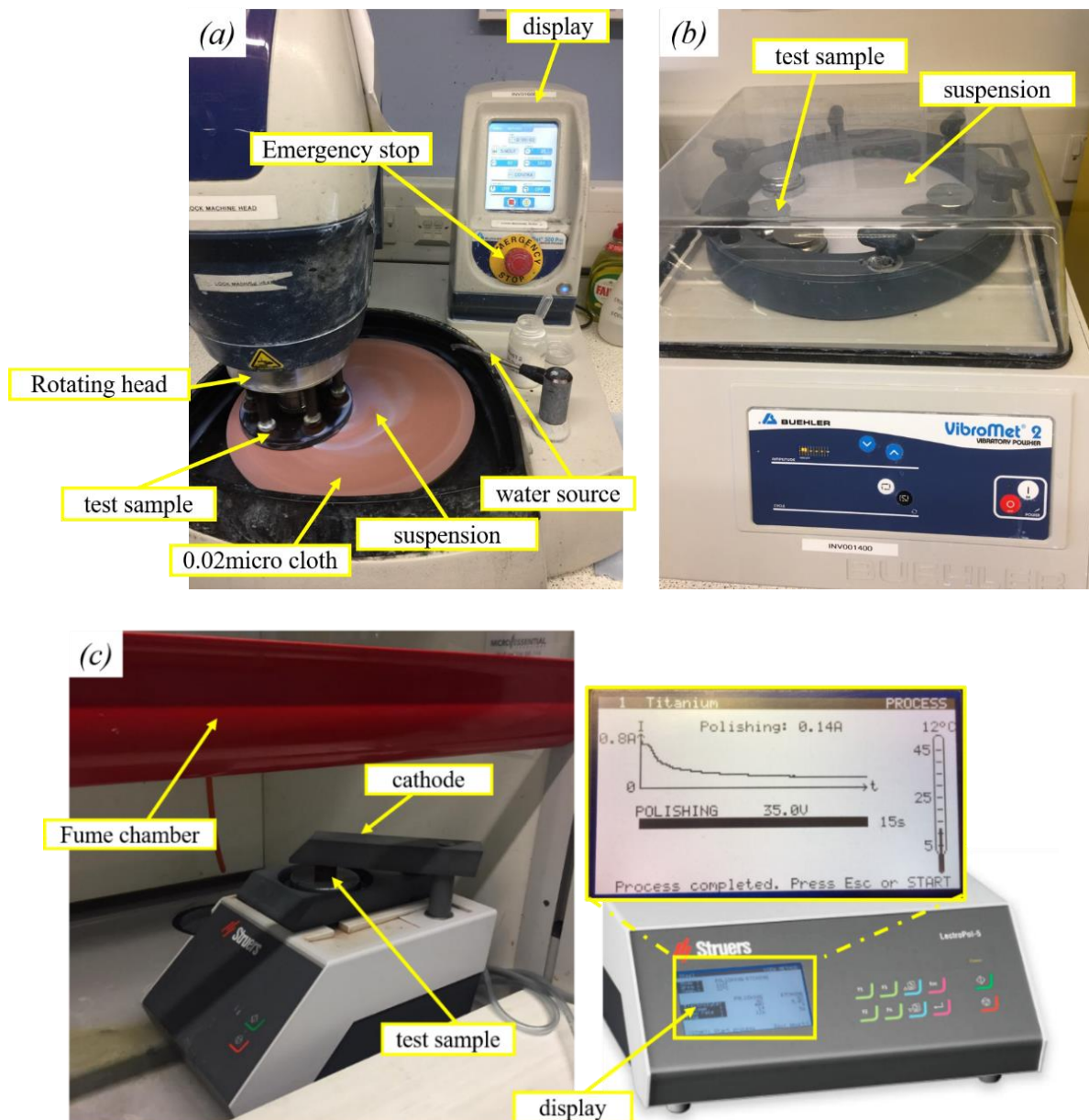


Figure A. 2 Apparatus for metallurgical surface preparation

(a) Grinding and polishing, (b) vibratory polishing (c) electro polishing set-up

For the Ti-3Al-2.5V tensile test samples used for the ex-situ test analysis, hydrogen peroxide was added during the polishing process to reveal the phases. A contra head- rotation mode was adopted for the polishing with a single force application head speed of 60rpm and a platen speed of 150rpm. A three stage polishing regime was used with intermittent addition of the colloidal suspension during the polishing process. Each polishing step lasted for 6minutes with a corresponding reduction in the polishing single forces from 20N to 15N and 10N for each subsequent step respectively. A Buehler Vibromet 2 vibratory polishing machine with a MasterMet 2 colloidal silica suspension were employed to chemo-mechanically polish the

originally polished test samples to enhance the surface finish quality, Figure A2*b*. A vibratory amplitude of 20% was utilised for the final polishing stage for 12 hours to attain mirror-finished surfaces. For surfaces prepared for electron backscatter diffraction (EBSD), an additional electro-polishing step was done to ensure a high indexing rate. A Struers LectroPol-5 automatic electrolytic polishing and etching machine was used to electropolish the samples, Figure A2*c*. A mixture of 600ml methanol + 360ml butoxy-ethanol + 60ml perchloric acid solution (A3 electrolyte) was used as an electrolyte for the electropolishing process. A 1cm² round area aperture transparent mask was utilised to ensure an adequate tracking of the electrolyte level and an effective regulation of the electrolyte flow. A polishing current of 0.14A with a voltage of 35V was utilised to polish a 1cm² area by holding for 15s at a temperature of 12^oC and a flowrate of 16m³/s. The electropolished surfaces were devoid of scratches but were mostly characterised by waviness (red arrows) and some level of pitting (yellow arrows), Figure A3. The electrolyte was stored under low temperature and the polishing time kept at 15s to avoid burning of the polished surface.

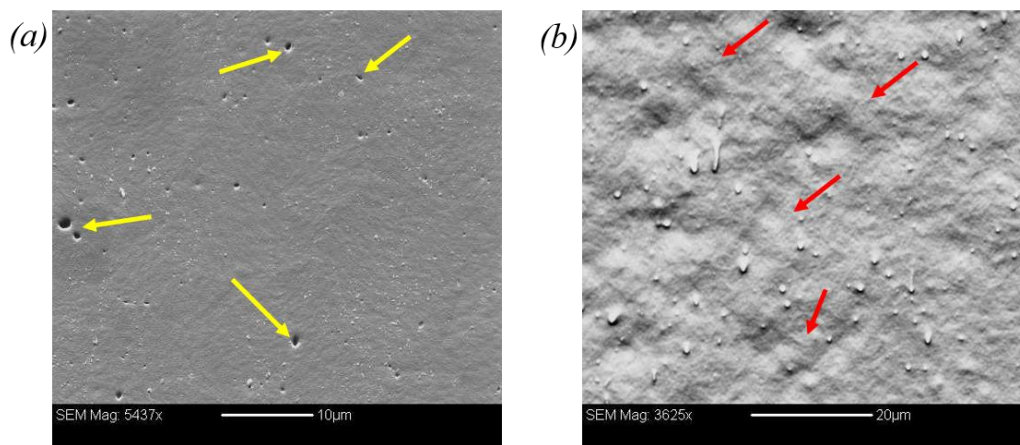


Figure A. 3 Characteristic surfaces of CP-Ti (Grade 2) after electropolishing

(a) Pitting and (b) waviness features

A2 Microscopy analysis

A2.1 Microstructure characterisation

A Leica DM 12000M light microscope was utilised to examine the microstructural morphology of the machined edges of CP-Ti (Grade 2) prepared with either EDM, laser or AWJ cutting. Scanning electron microscopy (SEM) examination of the machining induced edge surface micro-features, material microstructure and material failure modes (fractographs) were conducted on a Quanta FEG 250 microscope via acquisition of secondary electron (SE) images.

EBSD analysis was conducted for the onward determination of CP-Ti (Grade 2) grain structure and texture. The SEM analysis was conducted using an accelerating voltage of 20kV with a spot size of 4.5. A working distance of 10mm between the lens and the loaded position of the polished sample surface was employed during the SEM analysis. The edges of the hole expansion test samples and tensile testing samples after failure were examined using SE in SEM. The samples prepared for fractography examination were cut equidistant to the zone where the fracture occurred and cleaned thoroughly in acetone solution. The treated test specimens were then mounted in a stainless steel SamplKlip support clip on a flat platform and the edges coated with conductive silver suspension, Figure A4. The treated test specimens with the fractured zones of interest facing the lens were then examined under the microscope. High magnifications were adopted in order to appreciate the fracture modes as well as the fine level nature of the failed surfaces for the onward identification of the fracture initiation zones during plastic deformation.



Figure A. 4 Prepared specimen for fractography analysis in SEM

A2.2 Surface profile parameter measurement

The edge and surface integrity of the test samples were studied using Alicona 3D infinite focus optical microscope furnished with an Alicona measure suite 5.3.1 software and operational with a vertical resolution of up to 10nm, Figure A5. The microscope is furnished with 5×, 10×, 20× and 50× objective magnification for the onward assessment of the edge surface texture and

roughness. The surface characterization capabilities of this device stems from its functionality as both an optical profiler and a micro coordination measurement system. The main principle governing the operation of this optical 3D surface metrology system is the combination of small depth of focus with vertical scanning in order to obtain the topography of the region of focus (InfiniteFocus, 2017). Measurements done on Alicona 3D InfiniteFocus optical microscope conforms to ISO 4287 and ISO 4288 metrology standards. For surface roughness examination, a lateral resolution of $293\mu\text{m}$ was used. The vertical resolution was set by dividing the root-mean-square deviation of the profile by 3. After each round of roughness measurement, the calculated vertical resolution was compared with the input figure. The difference between the calculated vertical resolution and the input figure must be less than 100nm . Checks were done after every scan to ensure that the evaluation length and the sampling length were consistent with the ISO standards.

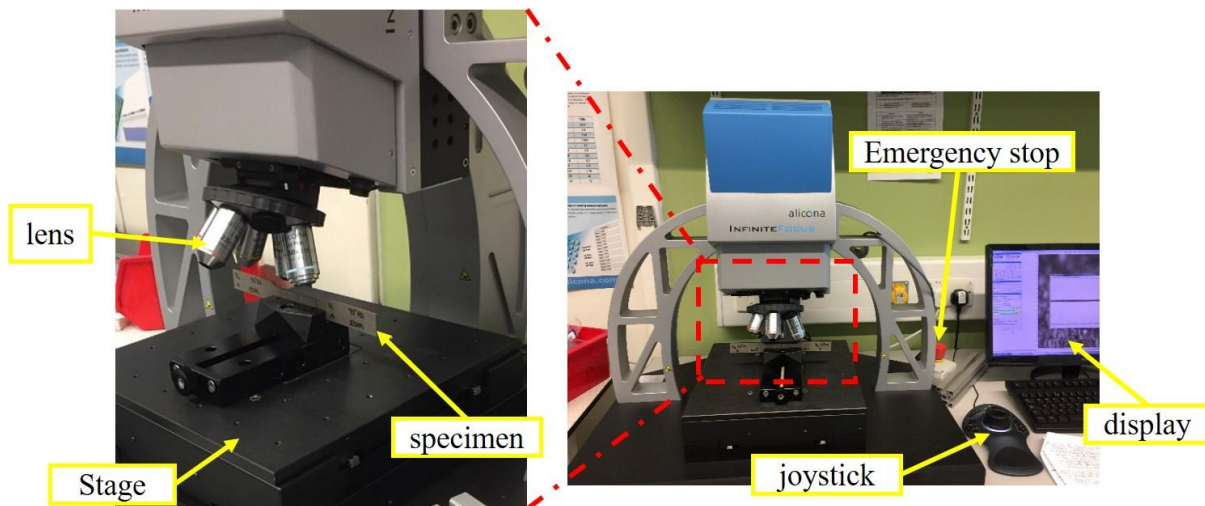


Figure A. 5 Alicona 3D InfiniteFocus optical microscope

The optical 3D measurement was preferred in this research since it provides more information on the surface texture rather than just the surface roughness values. The traditional diamond stylus tactile measurement method wasn't considered since (MTD CNC, 2020);

- They offer 2D data information which varies in size (though could be $\sim 2\mu\text{m}$) and describe only lines and do not account for the surface.
- The results are impacted by position as well as the operator. Positions as low as 0.5mm away from the line could alter the measurement.
- The contact nature of the measurement could cause damage to the material surface.

A3 Fundamental principles of EBSD

EBSD technique involves the combination of SEM with an EBSD detector and forms an important facet of material characterisation via orientation mapping. The detector comprises a phosphor screen as well as a charge-coupled device (CCD) camera, which are linked to a computer system for the onward processing of images. The schematic of an EBSD system set-up is shown in Figure A6.

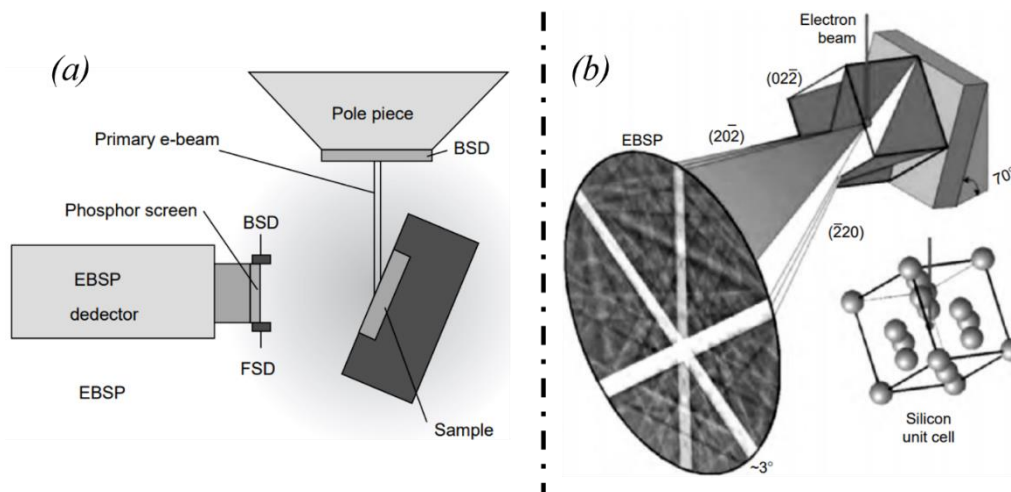


Figure A. 6 Schematic of EBSD set-up (Zhou & Wang, 2006)

(a) Specimen orientation in SEM, (b) electron interaction with crystalline material

For an interaction of the primary electron beams with material crystal lattice, low energy loss backscattered electrons are funnelled and exposed to path differences resulting in constructive and destructive interference, Figure A6b (Zhou & Wang, 2006).

A given EBSD map is a function of (Zhou & Wang, 2006);

- The lattice parameter of the crystal subjected to the electron beam.
- Crystallographic orientation.
- Incident electron beam wavelength.
- Detector proximity to the mounted sample.

For a given beam of electrons striking a polished sample surface, the electron emanating from the crystals within the solid material are scattered and diffracted into a pattern format in accordance with Bragg's law (Kacher, et al., 2009). For two cones of a given angle θ which bound the diffraction band from the hkl plane for a given electron wavelength λ , Bragg's law is expressed as equation (A.1) (Kacher, et al., 2009);

$$Z\lambda = 2d_{hkl} \sin \theta \quad (A.1)$$

Where; Z = an integer representing the order of the diffraction band; d_{hkl} = interplanar spacing
 The electron wavelength λ is a function of the accelerating voltage.

Figure A7 shows an illustration of the Bragg's law. The electron diffraction processes are defined by a wave vector \mathbf{k} . Thus, \mathbf{k} is transverse to the wave front length $\frac{1}{\lambda}$. The diffraction vector $\Delta\mathbf{k}$ describes the difference vector between the primary and the diffracted wave vector, $\Delta\mathbf{k} = \mathbf{k} - \mathbf{k}' = \mathbf{g}$. In essence, the \mathbf{g} acts transverse to the diffracting planes, which is parallel to the reciprocal vector \mathbf{h}_{hkl} of the diffracting planes. The diffracting vector \mathbf{g} equals to the reciprocal lattice vector \mathbf{h} . Thus, the length of diffraction is defined as (Zaefferer, 2003);

$$\text{Given that; } |\mathbf{g}| = 2 \sin \theta |\mathbf{k}| = 2 \sin \theta \frac{1}{\lambda} \quad (A.2)$$

$$\text{Then, equation (A.1) can be rewritten as; } |\mathbf{g}| = \frac{1}{d_{hkl}} \quad (A.3)$$

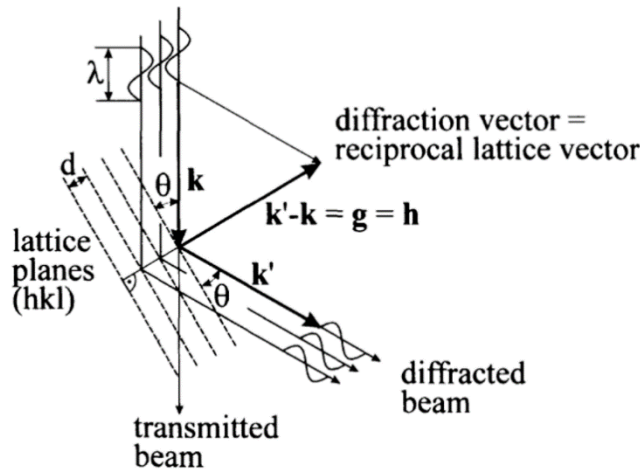


Figure A. 7 Illustration of Bragg's law (Zaefferer, 2003)

The vector \mathbf{h}_{hkl} forms the reciprocal lattice of a crystal lattice, which are transverse to the crystal lattice plane hkl with length and equates to the reciprocal interplanar distance of the crystal lattice plane, $|\mathbf{h}_{hkl}| = \frac{1}{d_{hkl}}$. However, the electron diffraction geometry is defined by equation (A.1) (Zaefferer, 2003).

Optimized Hough transform algorithms developed in specialized computer software are utilised to examine the acquired EBSD map via the detection of the amount of Kikuchi bands. Krieger-Lassen et al., were among the pioneers to introduce the Hough transform for the onward detection of Kikuchi bands, which are adopted in commercially supplied EBSD

software packages. Their approach employed two-dimensional (2D) parameterisation of the Hough space for the onward detection of the Kikuchi bands (Krieger-Lassen, et al., 1992). Maurice & Fortunier in their work suggested an extension to the 2D parameterisation of the Hough space by proposing a 3D space, which includes the K lines (created by the ‘*gnomonic projection of diffraction cones obeying Bragg’s law*’) as a novel parameter (Maurice & Fortunier, 2008).

A4 Fundamental principle of DIC in GOM Aramis

Digital image correlation enables the computation of displacement fields on test sample surfaces during deformation. Normally, grey level analysis are utilised to measure the displacement fields on the test sample planar surface. The DIC compares the reference and target images, which are obtained at various stages of the deformation process. The measurement is done by selecting two subsets from the reference and target images for the calculation process (Abbassi, et al., 2010). Digital images taken during the deformation process are analysed using GOM Aramis software. The grey level analysis is adopted by GOM Aramis software to track corresponding points of an image taken from a surface with a sufficient random speckle pattern. An example is given in Figure A8; the perimeter within the dotted yellow circle encompasses the region of interest while the blue shaded areas are discarded when analysing the HET test samples.

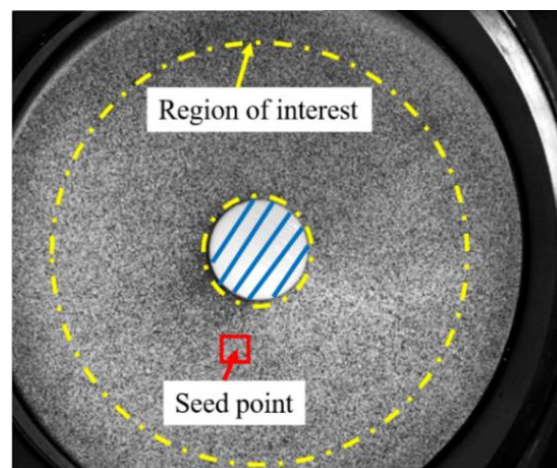


Figure A. 8 Random grey level on HET test sample

Each pixel in a charge-coupled device camera sensor corresponds to grey level coded on 8 or 12 bits. A grey level sequence is formed when various subsequent pixels align on the same line as a result of no changes in the distribution variation during deformation. This occurrence is

vital in order to obtain the corresponding points. This could be attained by adopting the correlation domains for a given pixel gathering zones (Abbassi, et al., 2010).

Figure A9 shows the relationship which exist between the reference and target images. Consider G to be a point at the subset centre of the reference image and G^* to be a point at the subset centre of the target image. The coordinates of G and G^* are related by (Abbassi, et al., 2010);

$$x^* = x + u(x, y) \quad (A.4)$$

$$y^* = y + v(x, y) \quad (A.5)$$

Where $u(x, y)$ and $v(x, y)$ are homogenous displacement fields for one pattern

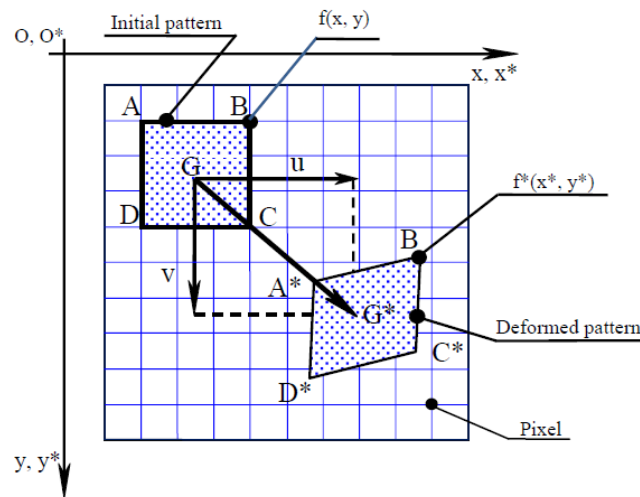


Figure A. 9 Positions of reference and target image patterns (Abbassi, et al., 2010)

The displacement field utilised in GOM Aramis software are homogeneous and bilinear with respect to x and y (Abbassi, et al., 2010);

$$u(x, y) = a_1x + a_2y + a_3xy + a_4 \quad (A.6)$$

$$v(x, y) = b_1x + b_2y + b_3xy + b_4 \quad (A.7)$$

Where; a_4, b_4 – rigid body motion terms

a_1, a_2, b_1, b_2 – elongation terms

a_3, b_3 – shearing terms

Since the reference point in the reference image must be same as the reference point in the target images, the grey values of these two reference points are related by (Kang, et al., 2005);

$$g_1(x, y) = g_2(x_t, y_t) \quad (A.8)$$

Where; g_1 and g_2 are grey values of the reference and target images respectively.

(x_t, y_t) is the transformation of (x, y)

The correlation coefficient, C for the reference and target image subsets is given by (Kang, et al., 2005);

$$C = 1 - \frac{\sum[g_1(x, y)g_2(x_t, y_t)]}{\sqrt{[\sum g_1^2(x, y) \sum g_2^2(x_t, y_t)]}} \quad (A.9)$$

A5 Fundamental principle of DIC in Ncorr version 2.1.1 software

In order to perform the DIC, a region of interest ought to be identified in the reference image, which are split into virtual grids. Natural or artificial speckle patterns are utilised to attain full field surface displacement by tracking the identified subset over the entire deformation process. The full field deformation are then accounted for by calculating the displacements at each location of the virtual grids. The virtual grids ensure high spatial resolution of the displacement field.

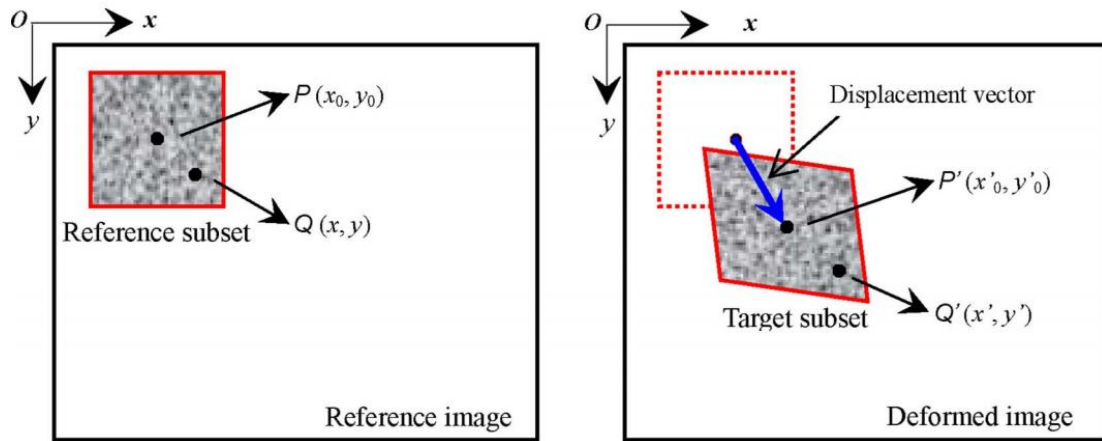


Figure A. 10 Fundamental principles of DIC (Pan, 2009)

For the displacement field evaluated at the respective locations of the virtual grid, the grid step adopted are usually between 2 and 10 pixels (Pan, et al., 2007). The fundamental principle governing the DIC is shown in Figure A10. For a reference subset, $(2M + 1) \times (2M + 1)$ pixels positioned at the centre point $P(x_0, y_0)$ from the reference image can be selected and utilised to locate its corresponding position in the deformed image. The displacement

component for the reference and target subset centres are computed upon identification of the position of the target subset in the target image (Pan, 2009).

A5.1 Displacement mapping

Figure A11 shows the positions of investigated subsets of reference and target images. Assume that the points tracked in the reference subset are the same as the points in the target subset. For a small enough reference subset, each neighbouring point $Q(x, y)$ situated around the centre $P(x_0, y_0)$ of the reference subset can be tracked to $Q'(x', y')$ in the target subset. The displacement mapping function can be defined as (Pan, et al., 2007);

$$x' = x_0 + \Delta x + u + \frac{\partial u}{\partial x} \Delta x + \frac{\partial u}{\partial y} \Delta y \quad (A.10)$$

$$y' = y_0 + \Delta y + v + \frac{\partial v}{\partial x} \Delta x + \frac{\partial v}{\partial y} \Delta y \quad (A.11)$$

Where; u, v – displacement components in the x and y directions respectively

$\Delta x, \Delta y$ – distance from subset centre P to point $Q(x, y)$

u_x, u_y, v_x, v_y – displacement gradient components for subset in Figure A11

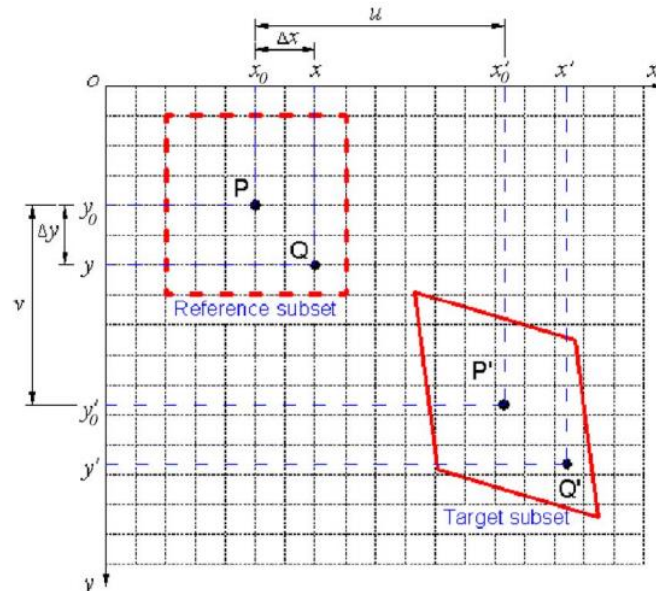


Figure A. 11 Position of deformed and undeformed subsets (Pan, et al., 2007)

A5.2 Correlation function

Consider $f(x, y)$ to denote the grey intensity distribution for the reference subset and $g(x', y')$ to denote that for the target subset. Then a normalised least square correlation function can be utilised to compute the similarity between them (Pan, et al., 2007);

$$C_{f,g}(\vec{P}) = \sum_{x=-M}^M \sum_{y=-M}^M \left[\frac{f(x, y) - f_m}{\sqrt{\sum_{x=-M}^M \sum_{y=-M}^M [f(x, y) - f_m]^2}} - \frac{g(x', y') - g_m}{\sqrt{\sum_{x=-M}^M \sum_{y=-M}^M [g(x', y') - g_m]^2}} \right]^2 \quad (A.12)$$

Where; f_m, g_m are ensemble averages for reference and target subsets respectively

$\vec{P}_{i=1\dots 6} = (u, u_x, u_y, v, v_x, v_y)^T$ are vectors apropos 6 preferred displacement mapping parameters

Then, f_m and g_m can be defined as;

$$f_m = \frac{1}{(2M + 1)} \sum_{x=-M}^M \sum_{y=-M}^M f(x, y) \quad (A.13)$$

$$g_m = \frac{1}{(2M + 1)} \sum_{x=-M}^M \sum_{y=-M}^M g(x', y') \quad (A.14)$$

Appendix B

B1 Heat treatment cycle of D2 tool steel billet for fabricating the HET tool set

Generally, tool steels are either alloyed, carbon or high-speed steels, which have the ability to be hardened or tempered. The choice of tool steel selection for any manufacturing process is a function of their predicted performance and the limitations associated with the tool steel (Roberts, et al., 1998). According to Bryson, the Advisor in Metals (AIM) Tool Steel Selector can be employed as a guide for tool steel selection and is governed by four design features; heat resistance, shock resistance, wear resistance and machinability (Bryson, 2009). A D2 tool steel billet with a dimension of $\text{Ø}102 \times 130\text{mm}$ was employed in this EngD research to fabricate the conical punch with its accompanying die set in accordance with BS ISO 16630:2017.

Figure B1 shows the heat treatment cycle adopted for improving the hardness of the D2 tool steel billet in order to ensure its compliance with the required standard (minimum of 55HRC) for the tool set fabrication. Prior to the heat treatment process, the billet was cleaned thoroughly with acetone to ensure a minimised potential contamination of the furnace. In order to relieve stress possibly inherited during either the manufacturing phase or machining, minimize distortions and precondition the material for structural transformation, the billet was pre-heated to a temperature of 650°C (Bryson, 2009), for a period of 42minutes and then held for another 30minutes. The temperature in the furnace was then increased to 850°C for 13minutes and held for 30minutes. Austenite structure was attained by heating the billets to the temperature of 1020°C for 11minutes and soaking at the same temperature for 120minutes. The soaking of the billet during the heat treatment is also referred to as the austenizing process (Bryson, 2009). The billet was then quenched to room temperature using nitrogen gas (2-6bars) (Jones, 1996). It was ensured that the billet was protected from atmospheric contact to prevent deep outer surface decarburization layer formation (Bryson, 2009). The billet was tempered by heating to a temperature of 270°C and holding for 90minutes. The billet was furnace cooled for 20minutes to 35°C . The billet was then re-tempered to a temperature of 270°C for 16minutes and held for 90minutes. Finally, the billet was again furnace cooled to a temperature of 35°C for 20minutes after which, it was allowed to recover to room temperature (20°C).

The summary of the heat treatment cycle adopted to harden the D2 tool steel billet for the onward adoption in the fabrication of the conical punch and its accompanying die sets is enumerated in Table B1. Upon attaining the austenite structure at the austenizing temperature

(soaking stage), the quenching results in the formation of a hardened martensitic structure, which offers the wear properties. Normally, about 95-96% of martensitic transformation occurs with some amount of retained austenite (Bryson, 2009).

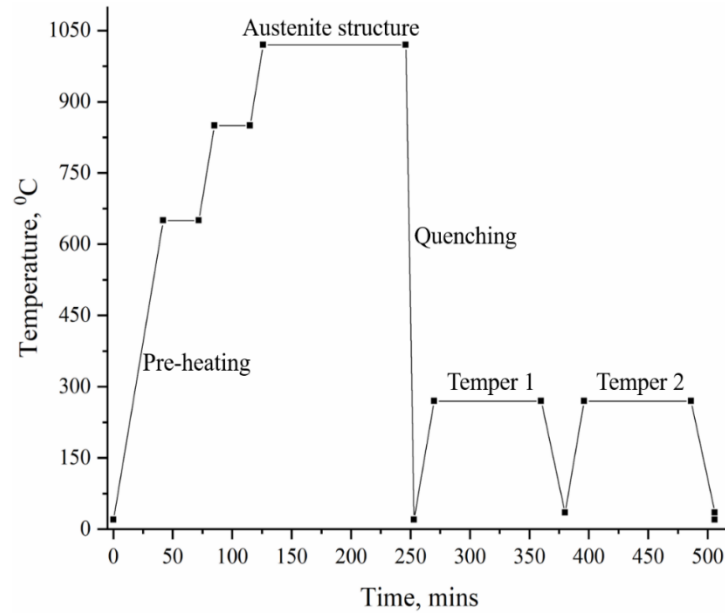


Figure B. 1 Heat treatment cycle adopted for the D2 tool steel

Table B. 1 Heat treatment steps for hardening the D2 tool steel billet

Stage	Time (minutes)	Temperature (°C)	Notes
	0	20	
Preheating	42	650	
	30	650	Ramp: 0.5 min/mm OR 30°C/min - used 15°C/min
	13	850	
	30	850	
	11	1020	Austenizing temperature
	120	1020	
Quench/ Hardening	7	20	Gas: 2-6 bar N ₂ (Nitrogen)
Temper 1	0	20	
	17	270	1h / 20min but minimum 2hours
	90	270	

	20	35	
Temper 2	0	35	
	16	270	
	90	270	
	20	35	
	0	20	

B2 Tool set Fabrication

The D2 tool steel billet was cleaned thoroughly in acetone after the heat treatment process. The hardness value was examined on a Zwick ZHV1 –micro Vickers hardness testing machine. The attained hardness value of 58.46 ± 0.17 HRC was consistent with the required hardness standard (minimum of 55HRC) for fabricating tools for HET. A schematic tool set-up with the requisite tool dimensions adopted for fabricating the bottom die, top die and the conical punch are shown in Figure B2. The fabricated punch had an outer diameter of 30mm with a 60° angled conical head with an overall height of 80mm. The top die also has inner and outer diameters of 50-52mm (diameters from bottom to top) and 95mm respectively with a height of 20mm. The bottom die has inner and outer diameters of 32mm and 89.96mm respectively with a height of 20mm. A more detailed engineering drawing with the appropriate dimensioning are provided in subsequent subsections B5.

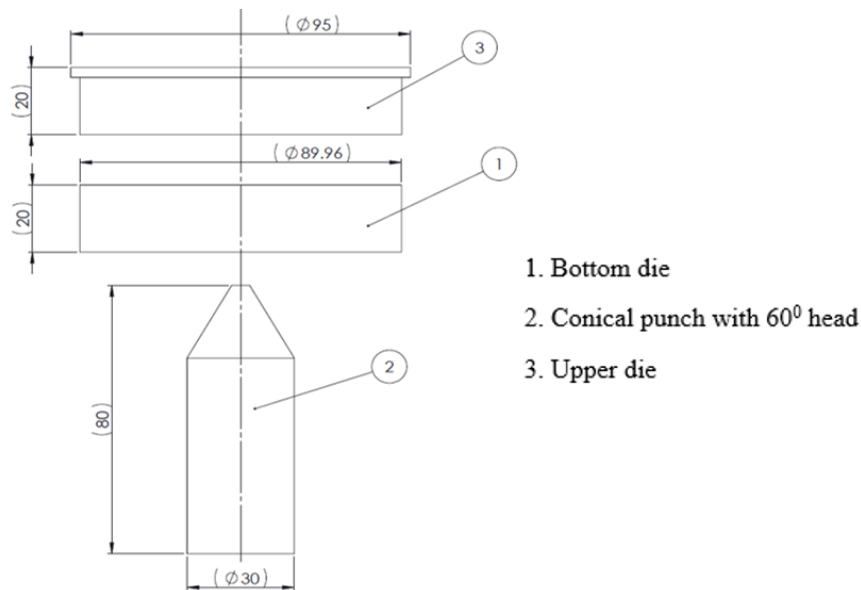


Figure B. 2 Schematic of the tool set-up and dimensioning

Figure B3 shows the fabricated tool-set adopted for the onward HET examination of the titanium sheets. An M18 threaded hole size with a 6H tolerance was created at the base of the conical punch in order to ensure firm fixture to the BUP machine, Figure B3a. The tool set assembly as deployed in the sheet clamping position during the HET is also shown in Figure B3b. The tool set assembly orientation is such that the punch emerges from beneath the clamped sheet with a centre hole. The apex of the conical punch head was deliberately flattened as a safety feature. The dimensioning for the conical punch head-apex flattening was carefully chosen to ensure that the diameter was smaller than the sheet hole centre diameter investigated.

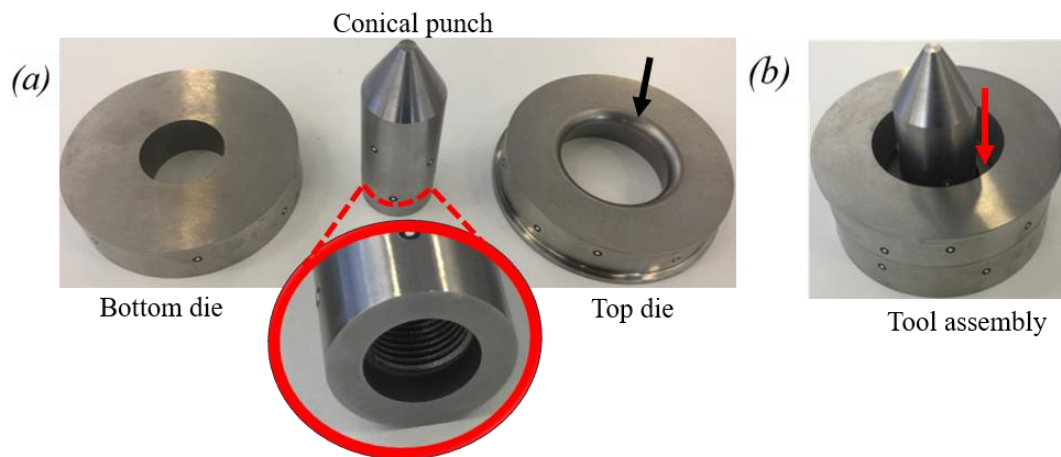


Figure B. 3 Manufactured die set with conical punch for HET trials
 (a) Fabricated tool set, (b) tool assembly

Special detailed features were included in the tool design to ensure accurate HER test results. A fillet radius of 5mm used at the base of the top die (black arrow) ensures free curvature flow of the material during the HET, Figure B3a. The bottom die inner diameter was fabricated small enough to accommodate the punch diameter as well as ensure straightened trajectory of the punch movement. The widening inner diameter of the top die (red arrow) permits material flow within the dimensional limits of BS ISO 16630:2017, Figure B3b.

B3 GOM Atos analysis of the tool integrity before HET trials

Figure B4 shows the GOM Atos measurement of the bottom die prior to the HET. An initial thickness of 20mm was recorded for the bottom die, consistent with the fabricated thickness value, Figure B4a,b. The inner and outer diameter measurements were also consistent with the required dimensions, Figure B4c.

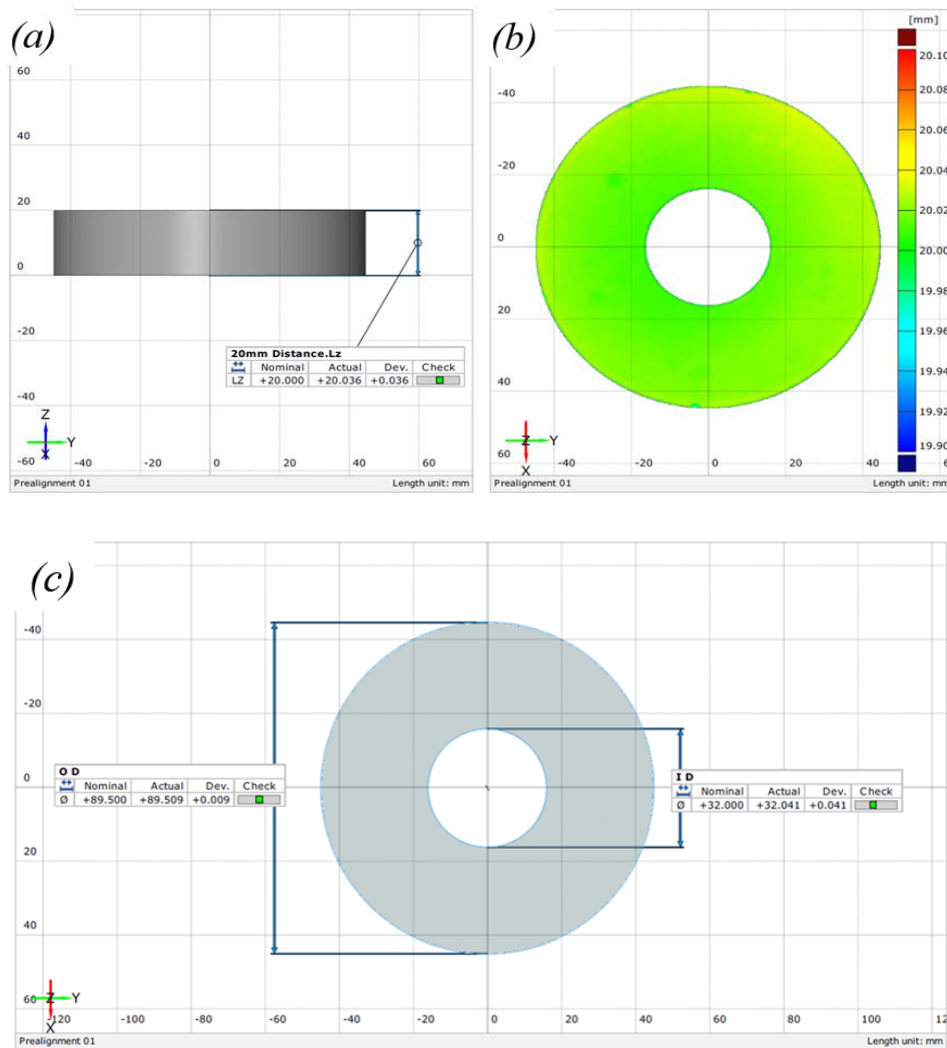


Figure B. 4 GOM Atos measurement of the bottom die prior to the HET
 (a)Side view measurement, (b) measurement scale, (c) plan view measurement

Figure B5 shows the GOM Atos measurement of the top die prior to the HET trials. The side view measurements showed dimensions consistent with the fabricated values, Figure B5a. Both the actual and nominal measurement values were recorded during the evaluation process. A fillet radius of 5mm was also recorded for the side view measurement. The outer and the inner diameters including the fillet starting point were captured in the plan view measurement, Figure B5b.

Figure B6 shows the GOM Atos measurement of the punch prior to the HET trial. The outer diameter of 30mm and the 60° conical head values obtained were consistent with the manufactured measurement values. The apex of the conical head was reduced by 5mm diameter as a safety feature as captured in the fabricated measurement. Measurements for both the actual and nominal values were considered during the evaluation process.

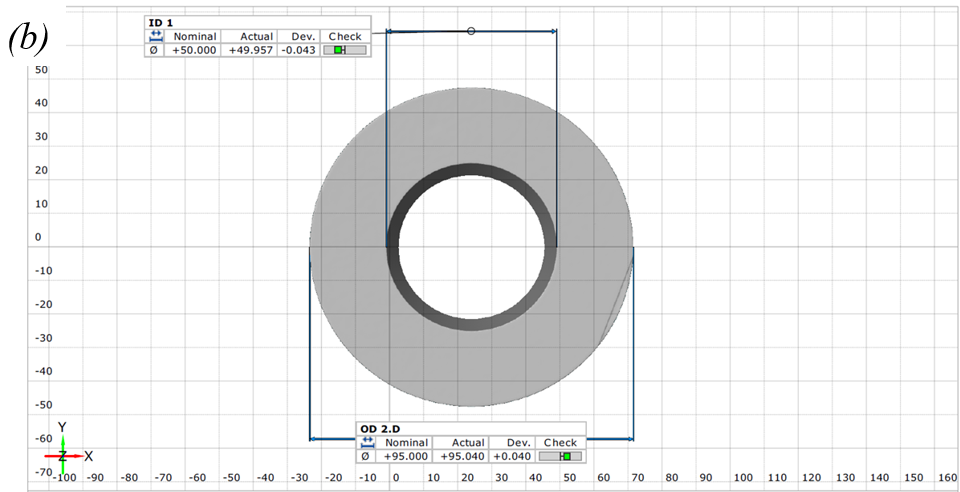
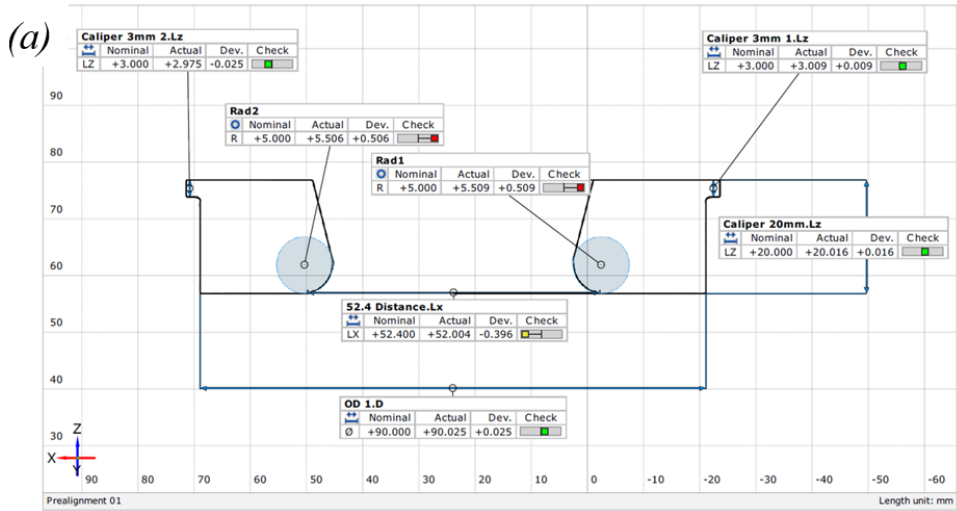


Figure B. 5 GOM Atos measurement of the top die prior to the HET
(a)Side view measurement, (b) plan view measurement

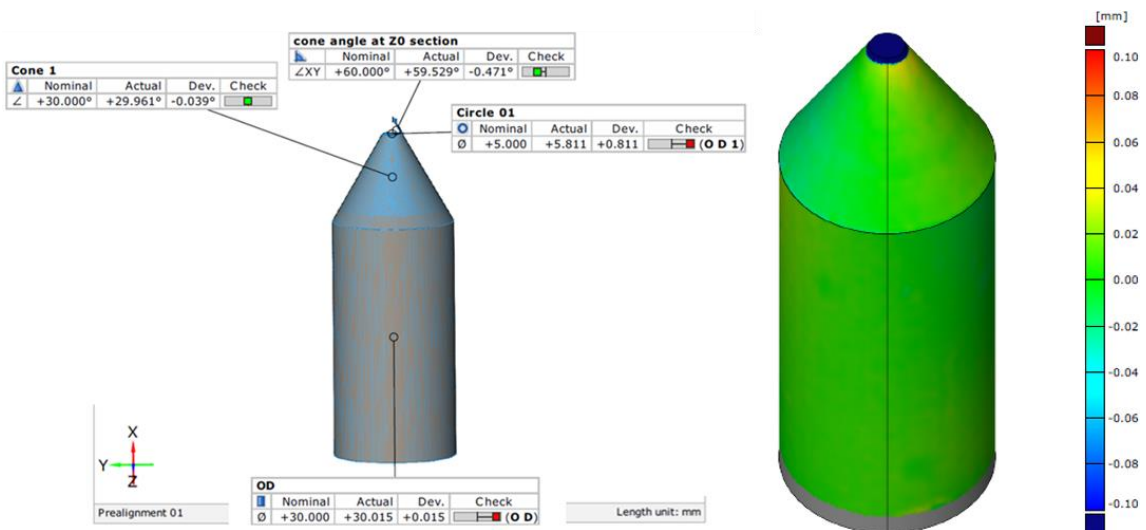


Figure B. 6 GOM Atos measurement of the conical punch prior to the HET

B4 GOM Atos analysis of the tool integrity after HET trials

Figure B7 shows the GOM Atos measurement of the bottom die after the HET trials. Overall, no significant dimensional variations in the tool geometry integrity was recorded after the HET trials.

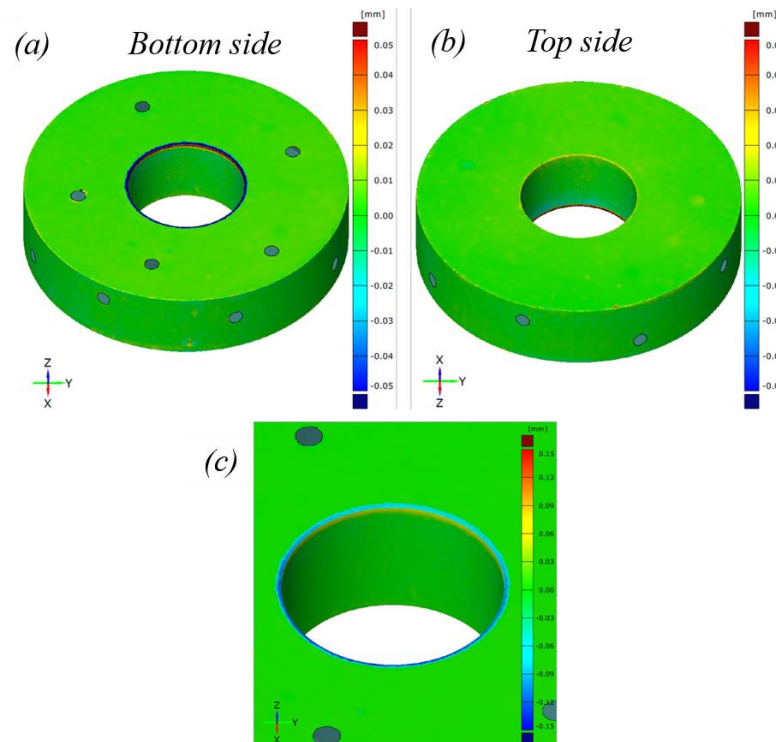


Figure B. 7 GOM Atos measurement of the bottom die after HET
(a) Bottom side, (b) top side and (c) higher magnification of hole areas in (a)

Further analysis of the inner hole area of the bottom side of the bottom die was conducted to ascertain the geometrical integrity of the tool, Figure B7c. A slight notch was observed, which was recorded as a slight reduction in the thickness value. This occurred due to a collision between the bottom of the punch holder and the die inner hole area during the HET test trials for the EDM finished edge samples. The high edge forming performance of the EDM finished edge samples resulted in a fully flanged edge without fracture. The absence of fracture occurrence during the HET rendered the crack sensitivity sensor on the BUP machine inert. This occurrence permitted the punch to run through the die thereby damaging the inner hole edge of the bottom die. However, this occurrence had no impact on the HER values recorded in this EngD research.

Figure B8 shows the GOM Atos measurement of the top die after the HET trial. Examination of both the top and the bottom sides of the die revealed no significant dimensional changes in the tool geometrical integrity. An insignificant reduction in thickness observed around the

holder region for zones, which holds the top die in position to the die holder might be due to reduced friction conditions during the testing process. Overall, the top die geometrical integrity was intact after the HET trial.

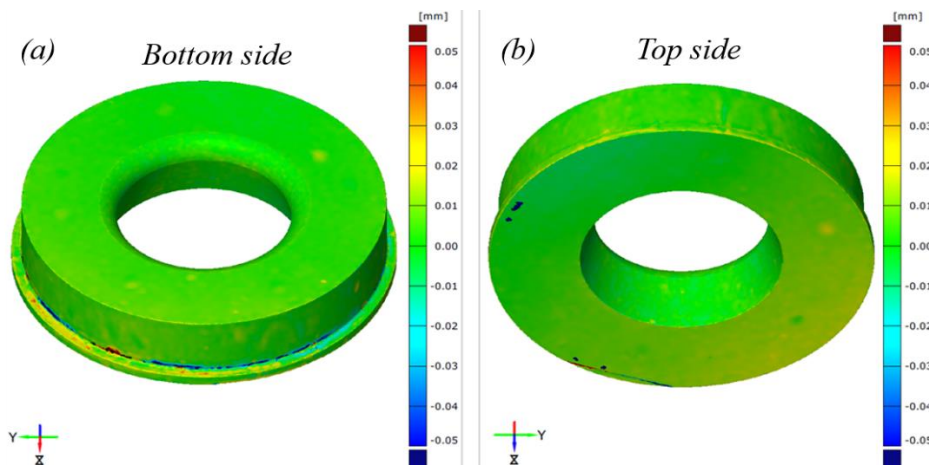


Figure B. 8 GOM Atos measurement of the top die after HET

(a) Bottom side, (b) top side

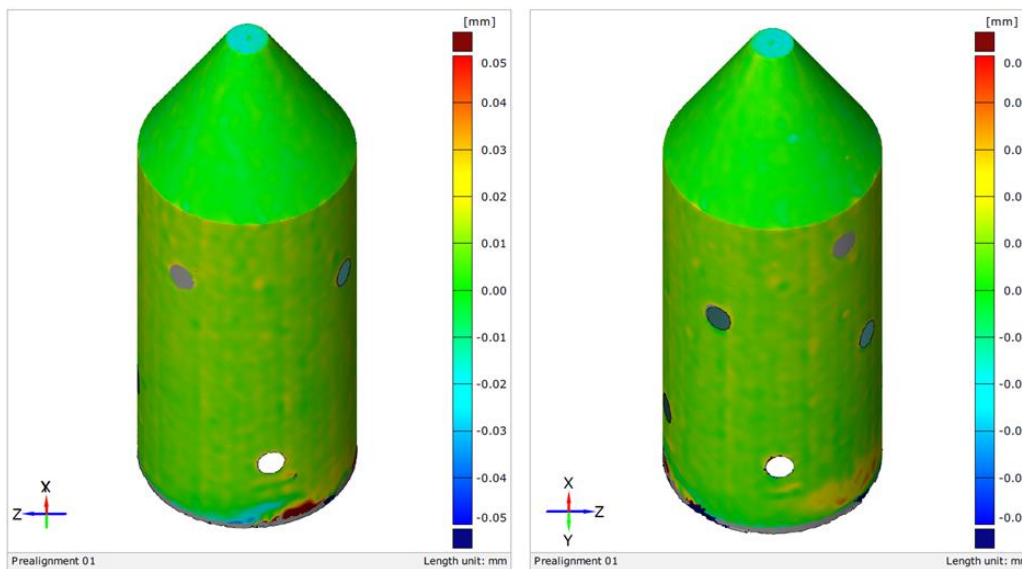


Figure B. 9 GOM Atos measurement of the conical punch after HET

Figure B9 shows the GOM Atos measurement of the conical punch after the HET trials. No significant variations in the conical punch geometrical integrity was observed at the conical head region after the HET. This observation could be attributed to the fact that no serious contact occurred between the hole area of the blank and the punch due to the use of lubricants during the HET. Overall, there was no significant dimensional variations observed in the punch geometrical integrity after the HET trials.

B5 Engineering drawing of the tool set design

Figure B10 shows the approved engineering drawing and the dimensioning used to fabricate the top die

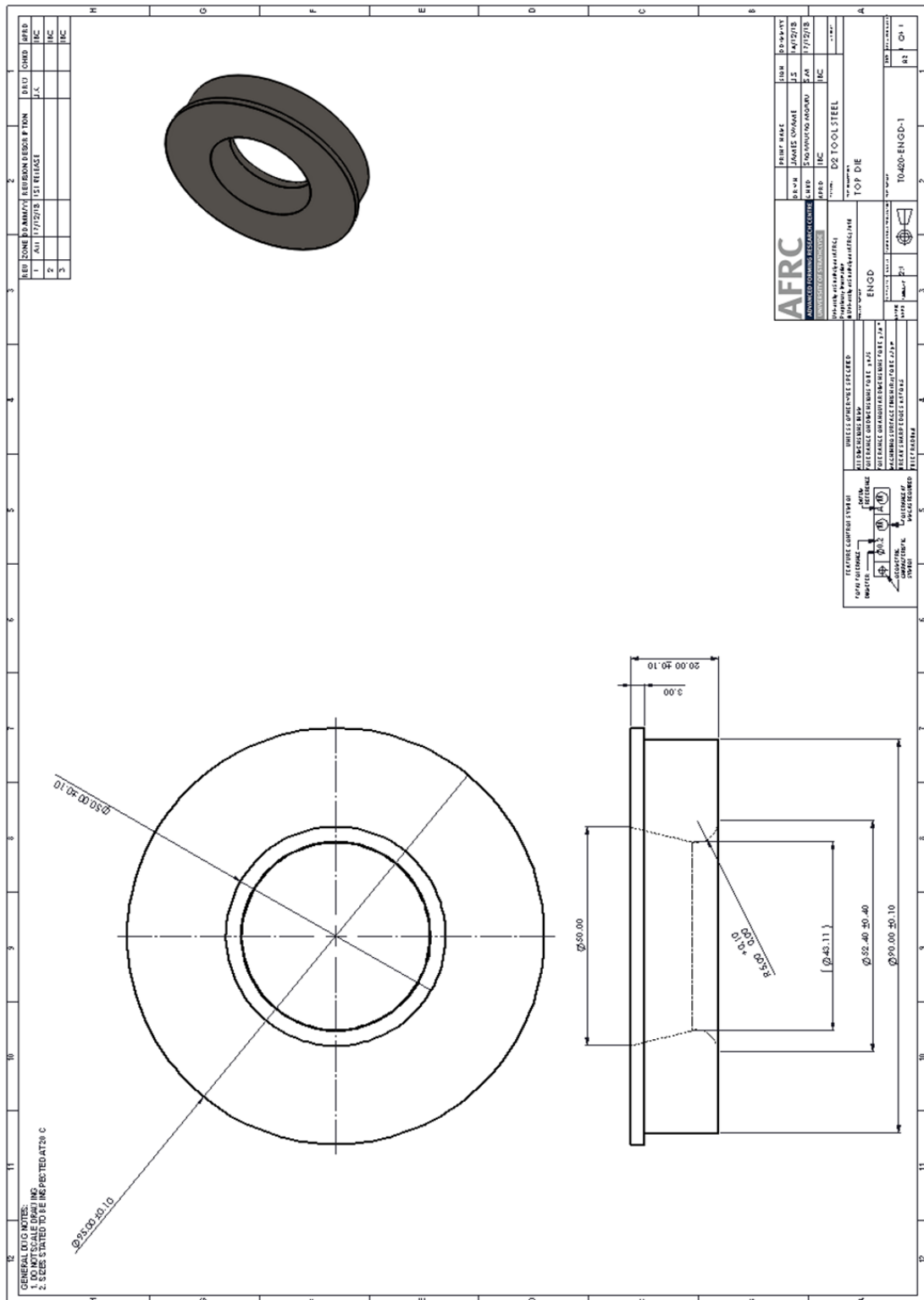


Figure B. 10 AFRC approved engineering drawing of the top die

Figure B11 shows the approved engineering drawing and the dimensioning used to fabricate the conical punch. Dimensioning for the threading used to ensure a firm fixture of the punch during the HET was also included in the design.

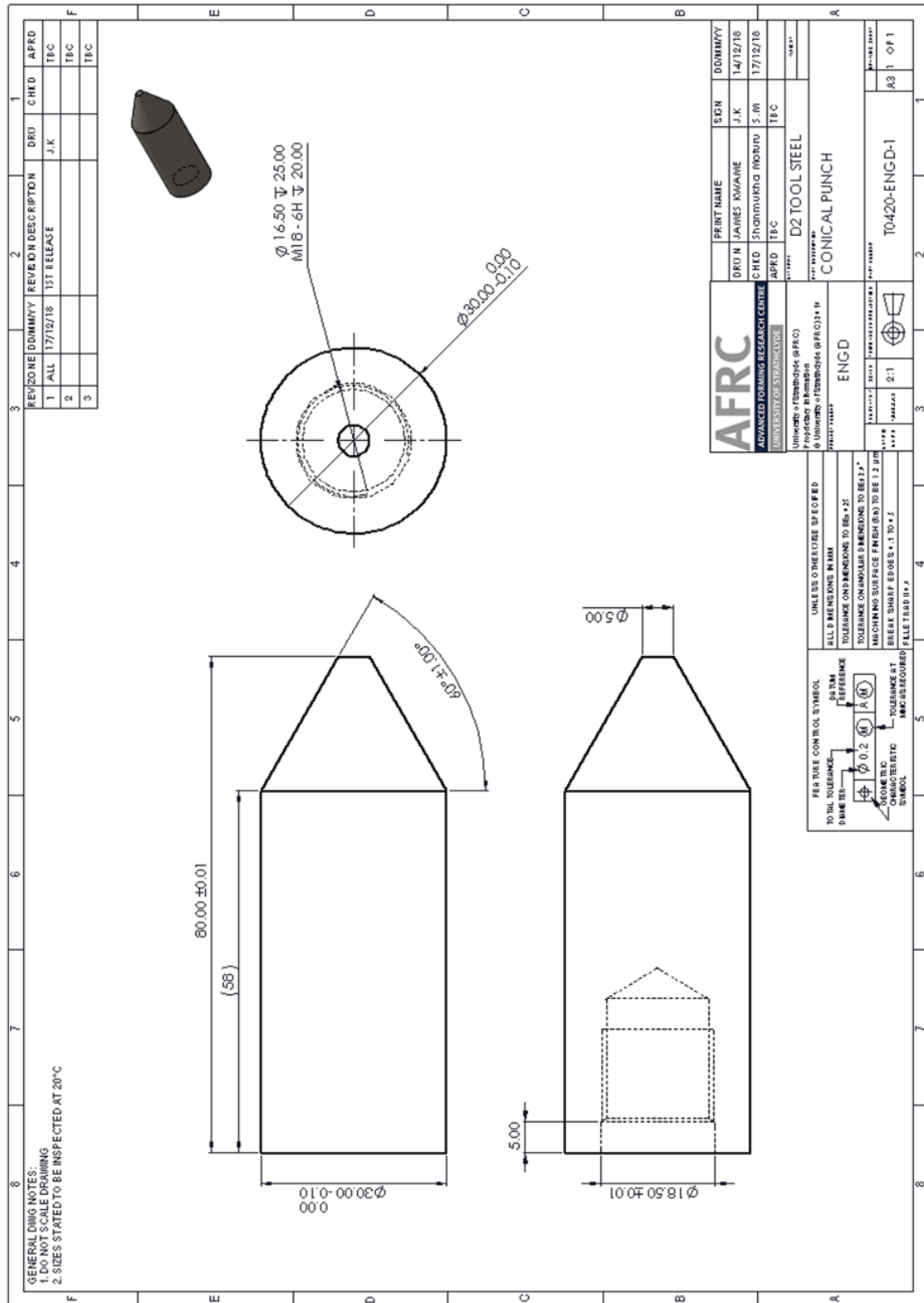


Figure B. 11 AFRC approved engineering drawing of the conical punch

Figure B12 shows the approved engineering drawing and the dimensioning used to fabricate the bottom die.

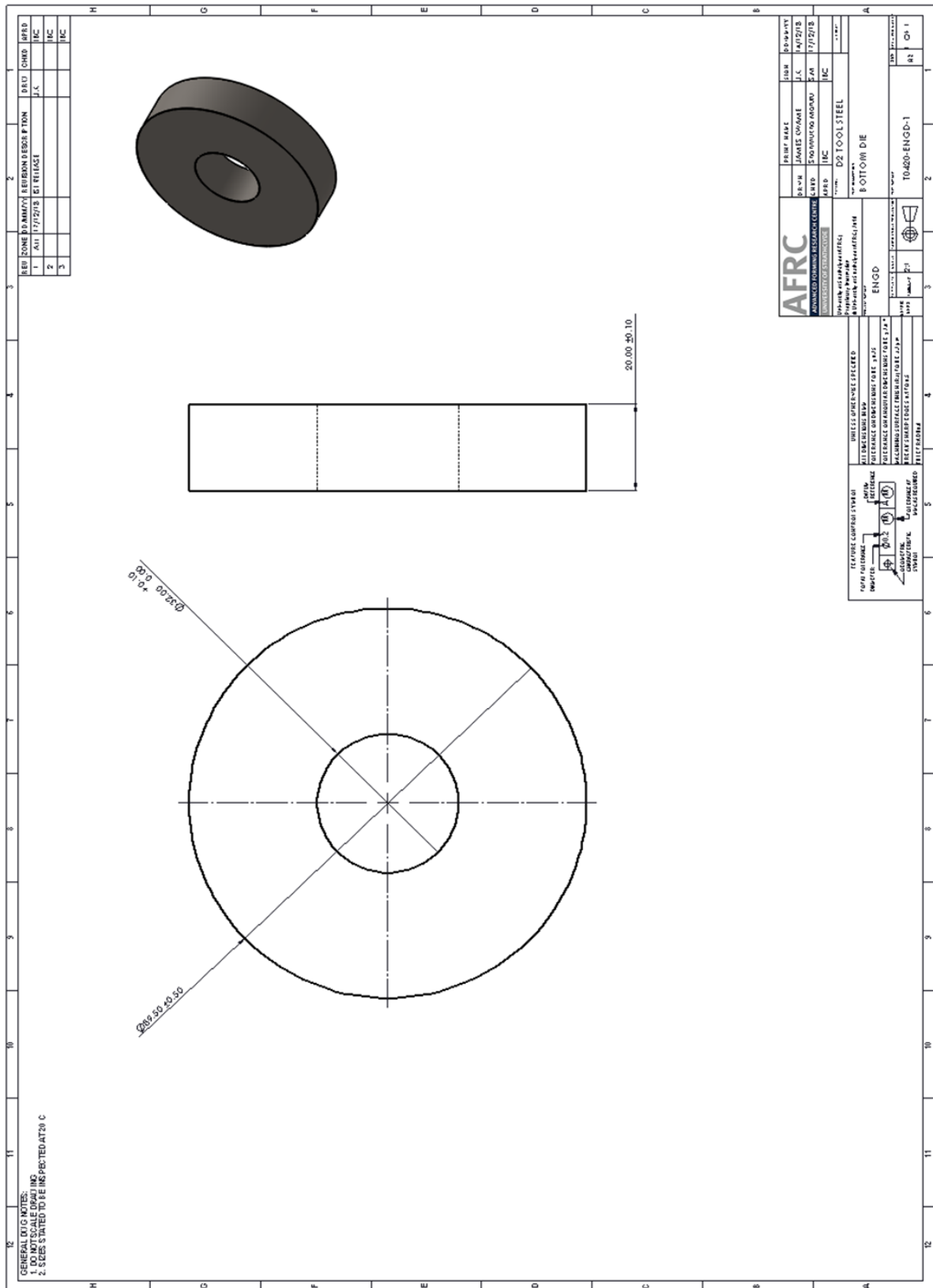


Figure B. 12 AFRC approved engineering drawing of the bottom die

Appendix C

C1 GOM Atos measurement of tensile sample thinning

Figure C1 shows the GOM Atos measurement of zones via the mid-section of the gage length over the reduced section of the specimens evaluated at 1mm interval after tensile deformation of CP-Ti (Grade 2).

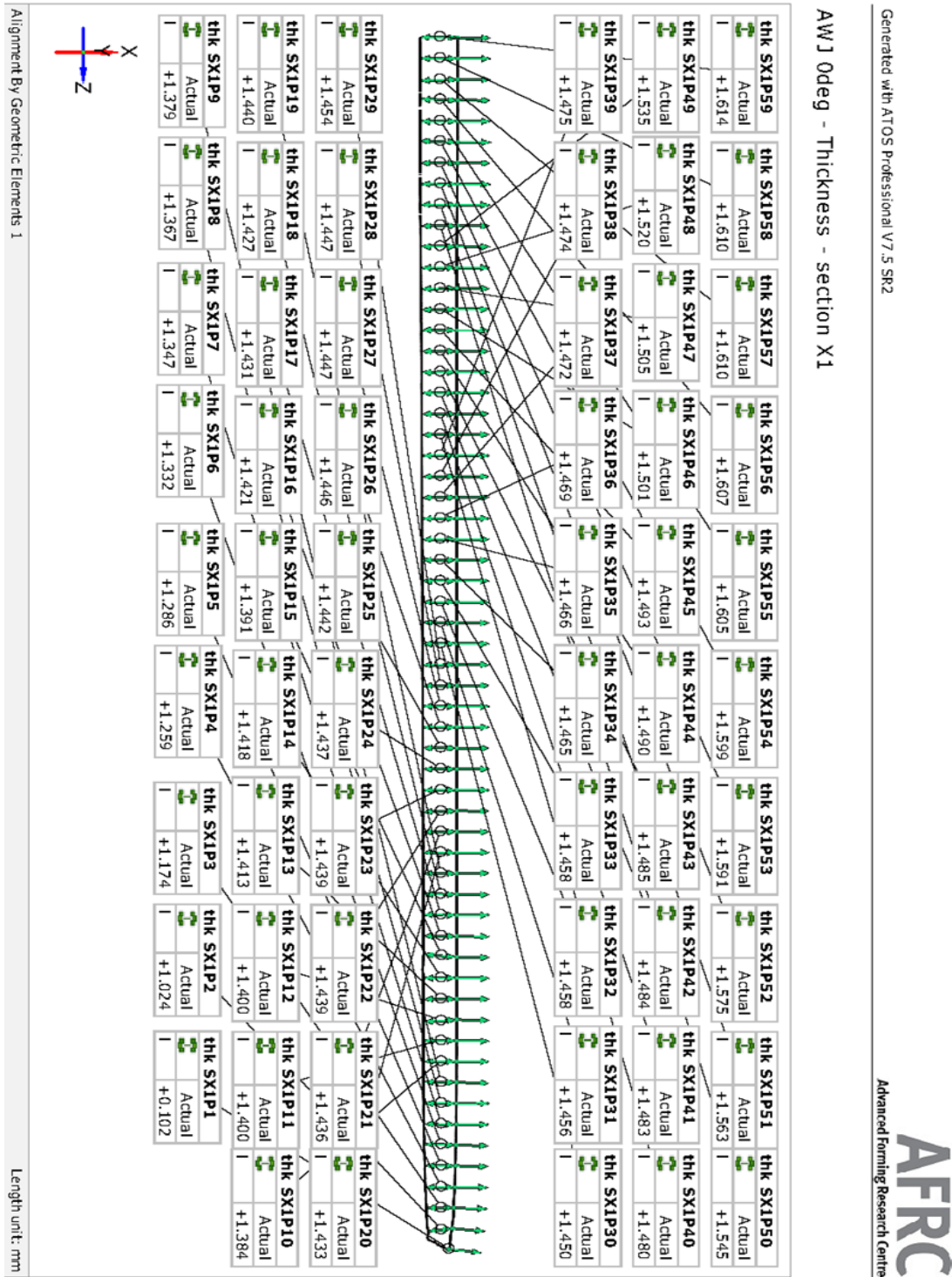


Figure C. 1 GOM Atos measurement of thinning along a tensile sample gage section

Appendix D

D1 Prediction of HER using the proposed regression model expression

Figure D1 shows the predicted HER of Ti-6Al-4V. The generated regression model equation based on cross validation for the onward prediction of the HER value is given by equation D.1

$$HER = e^{2.085+0.228EI-0.234t+0.393t^2} \quad (D.1)$$

The figure displays two screenshots of the RStudio interface. The top screenshot shows the R script editor with the following code:

```
1 rm(list=ls())
2 cat("\014")
3
4 # upload data
5 old_data<-read.csv(file.choose())
6
7 # model fitting
8 model<-lm(log(HER)~Index+poly(Thickness,2), data=old_data)
9 summary(model)
10
11 # creating new data
12 new_data<-data.frame("Index"=c(4.014444), "Thickness"=c(1.6))
13 new_data
14
15 # predicting with new data
16 log_HER<-predict(model,new_data)
17 HER<-exp(log_HER)
18 HER
19
20
```

The bottom screenshot shows the RStudio console output for the same script. A yellow box labeled "Display on console" points to the console window. The output includes the model summary and the predicted HER value:

```
> # upload data
> old_data<-read.csv(file.choose())
> # model fitting
> model<-lm(log(HER)~Index+poly(Thickness,2), data=old_data)
> summary(model)

Call:
lm(formula = log(HER) ~ Index + poly(Thickness, 2), data = old_data)

Residuals:
    1      2      3      4      5
0.0020451 -0.0031794  0.0031223 -0.0021253  0.0001374

Coefficients:
            Estimate Std. Error t value Pr(>|t|)
(Intercept)  2.084901   0.012466  167.24  0.00381 **
Index        0.228383   0.001433  159.37  0.00399 **
poly(Thickness, 2)1 -0.234035   0.006029  -38.82  0.01640 *
poly(Thickness, 2)2  0.393102   0.006341   61.99  0.01027 *
---
Signif. codes:  0 '***' 0.001 '**' 0.01 '*' 0.05 '.' 0.1 ' ' 1

Residual standard error: 0.005346 on 1 degrees of freedom
Multiple R-squared:  1, Adjusted R-squared:  0.9999
F-statistic: 2.407e+04 on 3 and 1 DF, p-value: 0.004738

> # creating new data
> new_data<-data.frame("Index"=c(4.014444), "Thickness"=c(1.6))
> new_data
  Index Thickness
1 4.014444      1.6
> # predicting with new data
> log_HER<-predict(model,new_data)
> HER<-exp(log_HER)
> HER
[1] 19.57396
```

A yellow box labeled "Predicted HER value" points to the output value 19.57396.

Figure D. 1 R-script computation on the user interface for Ti-6Al-4V

Figure D2 shows the predicted HER of Ti-3Al-2.5V. The generated regression model equation based on cross validation for the onward prediction of the HER value is given by equation D.2

$$HER = e^{2.001+0.237EI-0.243t+0.361t^2} \quad (D.2)$$

The image displays two screenshots of the RStudio interface. The top screenshot shows the source editor with the following R code:

```

1 rm(list=ls())
2 cat("\014")
3
4 # upload data
5 old_data<-read.csv(file.choose())
6
7 # model fitting
8 model<-lm(log(HER)~Index+poly(Thickness,2), data=old_data)
9 summary(model)
10
11 # creating new data
12 new_data<-data.frame("Index"=c(5.889118),"Thickness"=c(1.6))
13 new_data
14
15 # predicting with new data
16 log_HER<-predict(model,new_data)
17 HER<-exp(log_HER)
18 HER
19
20

```

The bottom screenshot shows the console output of the above code. A red box highlights the 'Console' tab, and a yellow box labeled 'Display on console' points to it. The console output is as follows:

```

> # upload data
> old_data<-read.csv(file.choose())
> # model fitting
> model<-lm(log(HER)~Index+poly(Thickness,2), data=old_data)
> summary(model)

Call:
lm(formula = log(HER) ~ Index + poly(Thickness, 2), data = old_data)

Residuals:
    1     2     3     4     5
0.0091863 -0.0090213 -0.0041435  0.0043755 -0.0003969

Coefficients:
            Estimate Std. Error t value Pr(>|t|)
(Intercept)  2.000910   0.024539   81.54  0.00781 **
Index        0.237032   0.002903   81.64  0.00780 **
poly(Thickness, 2)1 -0.242505   0.016498  -14.70  0.04324 *
poly(Thickness, 2)2  0.361009   0.015312   23.58  0.02699 *
---
Signif. codes:  0 '***' 0.001 '**' 0.01 '*' 0.05 '.' 0.1 ' ' 1

Residual standard error: 0.01422 on 1 degrees of freedom
Multiple R-squared:  0.9999,    Adjusted R-squared:  0.9997
F-statistic: 4753 on 3 and 1 DF,  p-value: 0.01066

> # creating new data
> new_data<-data.frame("Index"=c(5.889118),"Thickness"=c(1.6))
> new_data
  Index Thickness
1 5.889118     1.6
> # predicting with new data
> log_HER<-predict(model,new_data)
> HER<-exp(log_HER)
> HER
[1] 28.72558

```

A red dashed box highlights the predicted HER value '28.72558' in the console output, with a yellow box labeled 'Predicted HER value' pointing to it.

Figure D. 2 R-script computation on the user interface for Ti-3Al-2.5V ($t=1.6\text{mm}$)

Figure D3 shows the predicted HER of Ti-3Al-2.5V. The generated regression model equation based on cross validation for the onward prediction of the HER value is given by equation D.3.

$$HER = e^{2.033+0.236EI-0.268t+0.311t^2} \quad (D.3)$$

```

1 rm(list=ls())
2 cat("\014")
3
4 # upload data
5 old_data<-read.csv(file.choose())
6
7 # model fitting
8 model<-lm(log(HER)~Index+poly(Thickness,2), data=old_data)
9 summary(model)
10
11 # creating new data
12 new_data<-data.frame("Index"=c(6.2175),"Thickness"=c(1.25))
13 new_data
14
15 # predicting with new data
16 log_HER<-predict(model,new_data)
17 HER<-exp(log_HER)
18 HER
19
20

```

Source

Console

Terminal

Jobs

```

> # upload data
> old_data<-read.csv(file.choose())
> # model fitting
> model<-lm(log(HER)~Index+poly(Thickness,2), data=old_data)
> summary(model)

Call:
lm(formula = log(HER) ~ Index + poly(Thickness, 2), data = old_data)

Residuals:
    1      2      3      4      5
3.049e-02  1.214e-17 -2.138e-02 -9.108e-03 -1.388e-17

Coefficients:
            Estimate Std. Error t value Pr(>|t|)
(Intercept)  2.033223   0.070266  28.936  0.0220 *
Index        0.236434   0.008415  28.095  0.0226 *
poly(Thickness, 2)1 -0.267915   0.051478  -5.204  0.1208
poly(Thickness, 2)2  0.311301   0.038383   8.110  0.0781 .
---
Signif. codes:  0 '***' 0.001 '**' 0.01 '*' 0.05 '.' 0.1 ' ' 1

Residual standard error: 0.03833 on 1 degrees of freedom
Multiple R-squared:  0.9995,    Adjusted R-squared:  0.9979
F-statistic: 638.5 on 3 and 1 DF,  p-value: 0.02908

> # creating new data
> new_data<-data.frame("Index"=c(6.2175),"Thickness"=c(1.25))
> new_data
  Index Thickness
1 6.2175      1.25
> # predicting with new data
> log_HER<-predict(model,new_data)
> HER<-exp(log_HER)
> HER
[1] 27.88676

```

Display on console

Predicted HER value

Figure D. 3 R-script computation on the user interface for Ti-3Al-2.5V ($t=1.25\text{mm}$)

Figure D4 shows the predicted HER of CP-Ti (Grade 2). The generated regression model equation based on cross validation for the onward prediction of the HER value is given by equation D.4.

$$HER = e^{1.987+0.240EI-0.206t+0.368t^2} \quad (D.4)$$

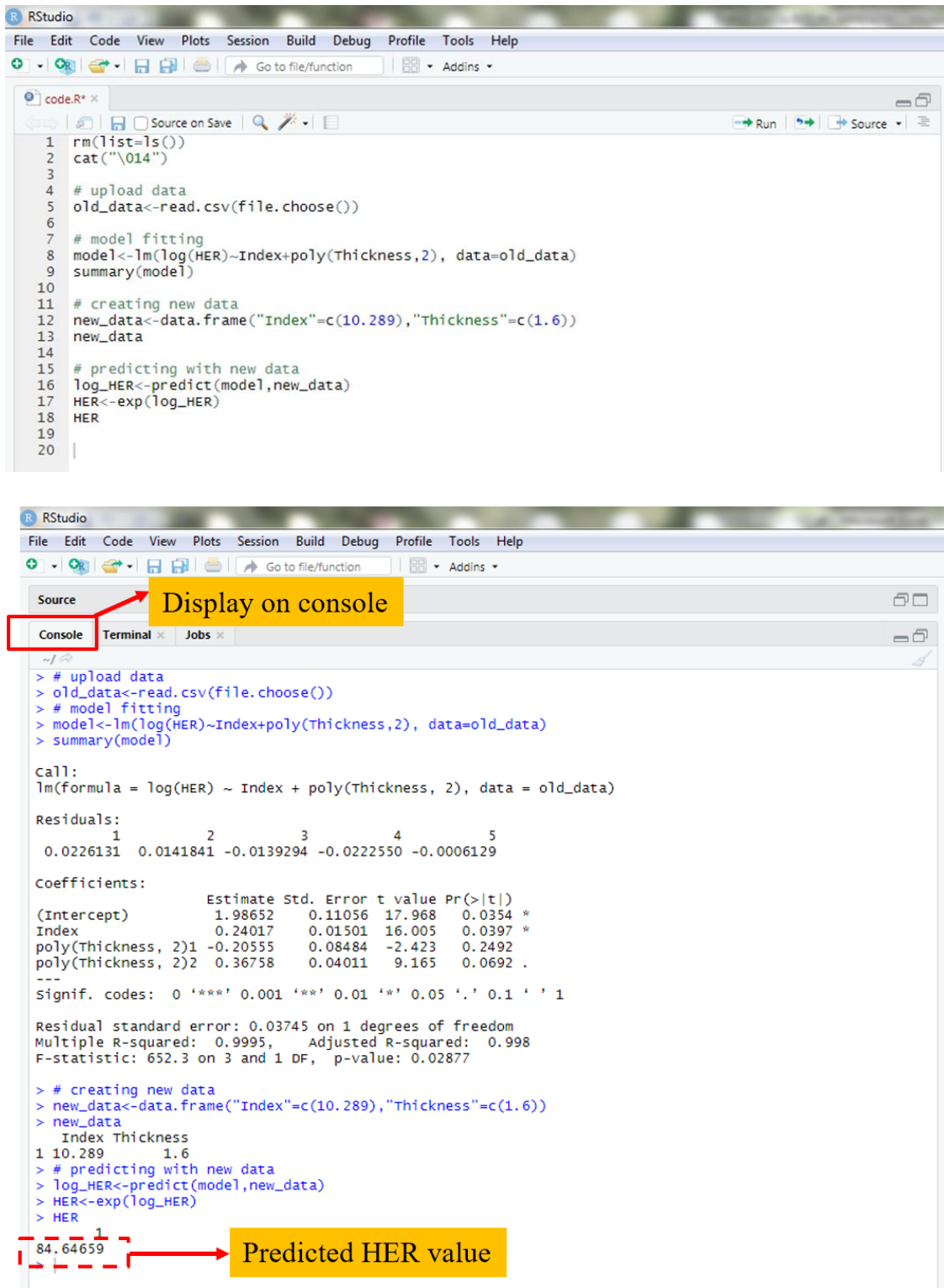


Figure D. 4 R-script computation on the user interface for CP-Ti (Grade 2)

Figure D5 shows the predicted HER of Ti-35A. The generated regression model equation based on cross validation for the onward prediction of the HER value is given by equation D.5.

$$HER = e^{1.932+0.236EI+0.136t+0.031t^2} \quad (D.5)$$

```

1 rm(list=ls())
2 cat("\014")
3
4 # upload data
5 old_data<-read.csv(file.choose())
6
7 # model fitting
8 model<-lm(log(HER)~Index+poly(Thickness,2), data=old_data)
9 summary(model)
10
11 # creating new data
12 new_data<-data.frame("Index"=c(11.3133),"Thickness"=c(1))
13 new_data
14
15 # predicting with new data
16 log_HER<-predict(model,new_data)
17 HER<-exp(log_HER)
18 HER
19
20

```

```

> # upload data
> old_data<-read.csv(file.choose())
> # model fitting
> model<-lm(log(HER)~Index+poly(Thickness,2), data=old_data)
> summary(model)

call:
lm(formula = log(HER) ~ Index + poly(Thickness, 2), data = old_data)

Residuals:
    1      2      3      4      5
3.049e-02  4.163e-17 -3.990e-17 -2.138e-02 -9.108e-03

Coefficients:
              Estimate Std. Error t value Pr(>|t|)
(Intercept)   1.931510   0.061983  31.162  0.0204 *
Index          0.236434   0.008415  28.095  0.0226 *
poly(Thickness, 2)1 0.135855  0.039036   3.480  0.1781
poly(Thickness, 2)2 0.031093  0.041826   0.743  0.5930
---
Signif. codes:  0 '***' 0.001 '**' 0.01 '*' 0.05 '.' 0.1 ' ' 1

Residual standard error: 0.03833 on 1 degrees of freedom
Multiple R-squared:  0.9989,    Adjusted R-squared:  0.9957
F-statistic:  308 on 3 and 1 DF,  p-value: 0.04186

> # creating new data
> new_data<-data.frame("Index"=c(11.3133),"Thickness"=c(1))
> new_data
  Index Thickness
1 11.3133        1
> # predicting with new data
> log_HER<-predict(model,new_data)
> HER<-exp(log_HER)
> HER
[1] 231.597

```

Figure D. 5 R-script computation on the user interface for Ti-35A